

Spring 1-1-2017

# Molecular Dynamics in Mesoscopic Equilibrium and Nonequilibrium Systems with Applications in Sustainability

Steven Earl Strong  
*University of Colorado at Boulder*, StevenE.Strong@gmail.com

Follow this and additional works at: [https://scholar.colorado.edu/chem\\_gradetds](https://scholar.colorado.edu/chem_gradetds)



Part of the [Physical Chemistry Commons](#)

---

## Recommended Citation

Strong, Steven Earl, "Molecular Dynamics in Mesoscopic Equilibrium and Nonequilibrium Systems with Applications in Sustainability" (2017). *Chemistry & Biochemistry Graduate Theses & Dissertations*. 213.  
[https://scholar.colorado.edu/chem\\_gradetds/213](https://scholar.colorado.edu/chem_gradetds/213)

This Dissertation is brought to you for free and open access by Chemistry & Biochemistry at CU Scholar. It has been accepted for inclusion in Chemistry & Biochemistry Graduate Theses & Dissertations by an authorized administrator of CU Scholar. For more information, please contact [cuscholaradmin@colorado.edu](mailto:cuscholaradmin@colorado.edu).

**Molecular Dynamics in Mesoscopic Equilibrium and  
Nonequilibrium Systems with Applications in Sustainability**

by

**Steven E. Strong**

B.S., Colorado School of Mines, 2012

A thesis submitted to the  
Faculty of the Graduate School of the  
University of Colorado in partial fulfillment  
of the requirements for the degree of  
Doctor of Philosophy, Chemical Physics  
Department of Chemistry and Biochemistry

2017

This thesis entitled:

Molecular Dynamics in Mesoscopic Equilibrium and Nonequilibrium Systems with Applications in  
Sustainability

written by Steven E. Strong

has been approved for the Department of Chemistry and Biochemistry

---

Prof. Joel D. Eaves

---

Prof. Sandeep Sharma

Date \_\_\_\_\_

The final copy of this thesis has been examined by the signatories, and we find that both the content and the form meet acceptable presentation standards of scholarly work in the above mentioned discipline.

Strong, Steven E. (Ph.D., Chemical Physics)

Molecular Dynamics in Mesoscopic Equilibrium and Nonequilibrium Systems with Applications in  
Sustainability

Thesis directed by Prof. Joel D. Eaves

As the Earth's population grows, it becomes increasingly important to use our limited resources sustainably. Among our most important natural resources are fossil fuels and fresh water, but fossil fuel use is driving climate change and water security is under threat. This thesis uses molecular simulation, statistical mechanics, and molecular hydrodynamics to explore fundamental processes and develop tools and concepts for new classes of materials that have applications in water and energy sustainability.

Reverse osmosis, a water desalination process that removes salt from water using a semipermeable membrane, is one solution to the water security problem. Current membrane technology suffers from low throughput, however, necessitating high capital expenditures and large energy footprints for desalination plants. Membranes made from atomically thin two-dimensional crystals, like porous graphene, could increase throughput by orders of magnitude. This filtration process is difficult to understand and model, however, without the molecular dynamics method developed here. Our method is theoretically rigorous and faithful to both statistical mechanics and hydrodynamics. We apply this method to study atomically thin reverse osmosis membranes and find that the permeability of a membrane is not a simple function of the membrane's hydrophobicity. Quantifying the hydrophobic effect is a major area in theoretical chemistry, and this thesis contributes to our understanding by exploring the hydrophobic effect away from equilibrium.

Solar energy has the potential to compete with nonrenewable fossil fuels, but single junction cells are theoretically limited to 34% power conversion efficiency. Singlet fission, a photophysical process that occurs in some organic chromophores and splits high energy excitations into two lower energy ones, can make more efficient use of the solar spectrum and overcome this limit.

Singlet fission rates depend very sensitively on the relative orientation of neighboring chromophores. Historically, singlet fission research has focused on the energetics of the photophysical process. In this thesis, we approach the problem, for the first time, through the dynamics and statistics of chromophore aggregation. We find that the aggregates do form crystal-like structures known to undergo fast singlet fission, making singlet fission compatible with simple and inexpensive solar devices like dye sensitized solar cells.

## **Dedication**

To Larry Strong

## Acknowledgements

To say the least, this thesis would not have been possible without the support I have received from many different corners of my life, as well as a good bit of luck. My teachers have fostered creativity and a thirst for discovery from an early age. Craig Munsart, Rebecca Gorrell, Ken Gabaldon, and Terry Bridgman are standout examples, but by no means an exhaustive list. My high school chemistry teacher Suzanne McClung ignited my interest in chemistry and introduced me to my mentors at USGS: Geoff Plumlee, Todd Hoefen, and Phil Hageman. They provided me with excellent guidance and my first experience as a chemist in the real world. At the School of Mines, Mark Eberhart's phenomenal lectures steered my interests towards physical chemistry and Mark Seger gave me my first taste of research. At CU, my success has been due in large part to the creativity and support of my adviser, Joel Eaves. He has been a continuous source of excellent advice. My friends at CU and my fellow Eaves group members have helped me with both science and sanity. Bridge games with Russell Perkins, Becky Rapf, Jay Kroll, and Alyssa Landin have been especially fruitful on both counts.

I am grateful for the support of my good friends Alex Daniluk, Nick Haase, Joey Gardner, Anna Shea, Barbie Noyes, Scott Thullen, Michael Taylor, Travis Weisse, Erik Schaefer, and Cody Daigneault. They have put up with a lot. I am thankful for the love and support of Sara Chmelka and her family. She has put up with a lot more, and spent countless hours helping me edit writing and listening to practice talks, and her advice is always excellent. My Thanksgiving family and my real family have always been interested and supportive of anything I try to do. Especially Joan Kenney, who I'm sure would still be willing to build a fort under a table with me now, if I asked. The people without which this thesis would certainly not have been possible are my parents, two of the kindest and smartest people I know.

## Contents

### Chapter

<b>1</b>	<b>Introduction</b>	<b>1</b>
1.1	Water Security . . . . .	4
1.2	Renewable Energy . . . . .	5
<b>2</b>	<b>Atomistic Hydrodynamics: Molecular Dynamics Simulation of Steady-State Flow</b>	<b>10</b>
2.1	Abstract . . . . .	10
2.2	Background . . . . .	11
2.3	Derivation of Gaussian Dynamics . . . . .	12
2.4	Methods . . . . .	17
2.4.1	Pump Method . . . . .	17
2.4.2	Steady State and Current . . . . .	18
2.4.3	Reynolds Number . . . . .	20
2.4.4	Pore Dimensions . . . . .	21
2.4.5	Simulation Details . . . . .	22
2.4.6	Convergence with Respect to Box Length . . . . .	22
2.5	Nonequilibrium Definition of Temperature . . . . .	23
2.6	Comparison of Hydrodynamic Profiles . . . . .	23
2.7	Pressure Profile Adjustment and Pressure Drops . . . . .	26
2.8	Effective Viscosity . . . . .	30

2.9	Slip Length . . . . .	31
2.10	Conclusion . . . . .	34
<b>3</b>	<b>The Dynamics of Water in Porous Two-dimensional Crystals</b>	<b>43</b>
3.1	Abstract . . . . .	43
3.2	Background . . . . .	44
3.3	Methods . . . . .	47
3.3.1	Permeability . . . . .	47
3.3.2	Membranes . . . . .	48
3.3.3	Pore Dimensions . . . . .	50
3.3.4	Markov Model . . . . .	51
3.3.5	Reynolds Number . . . . .	51
3.3.6	Simulation Details . . . . .	51
3.4	Tuning the Hydrophobicity . . . . .	53
3.5	Polar Interactions . . . . .	54
3.5.1	H-bond Survival Time . . . . .	57
3.5.2	Pore Functionalization: Local versus Nonlocal Polar Interactions . . . . .	57
3.6	van der Waals Interactions . . . . .	59
3.7	Flexible Membranes . . . . .	64
3.8	Bursty Transport . . . . .	69
3.9	Linear Response Theory in Dry Nanopores . . . . .	76
3.10	Conclusion . . . . .	86
<b>4</b>	<b>Tetracene Aggregation on Polar and Nonpolar Surfaces</b>	<b>101</b>
4.1	Abstract . . . . .	101
4.2	Background . . . . .	102
4.3	Methods . . . . .	104
4.4	Results and Discussion . . . . .	106

<b>5</b>	Complete Bibliography	<b>124</b>
----------	-----------------------	------------

## **Appendix**

<b>A</b>	Derivation of Gaussian Dynamics with an Isokinetic Thermostat	<b>150</b>
<b>B</b>	Funding and Computer Resources	<b>154</b>
<b>C</b>	Hagen-Poiseuille Law	<b>155</b>
C.1	Derivation of Hagen-Poiseuille Law in 2d . . . . .	156

## Tables

### Table

2.1	Simulation parameters for very long and/or narrow channels . . . . .	23
3.1	Thermodynamic prediction of the critical wetting contact angle . . . . .	62

## Figures

### Figure

1.1	Schematic of reverse osmosis . . . . .	4
1.2	Singlet fission can increase power conversion in solar cells . . . . .	6
2.1	Spatial binning is used to compute the streaming velocity . . . . .	14
2.2	Schematic of the pump method . . . . .	17
2.3	Velocity distributions generated by Gaussian dynamics . . . . .	24
2.4	Comparison of the pump method and Gaussian dynamics . . . . .	25
2.5	Comparison of hydrodynamic profiles in the pump region . . . . .	26
2.6	Pressure adjustment for comparing the pump method and Gaussian dynamics . . . .	29
2.7	Effective viscosity of 2d Lennard-Jones fluids . . . . .	31
2.8	Effective viscosity: profile-unbiased thermostat and errors . . . . .	32
2.9	Slip length of a 2d Lennard-Jones fluid . . . . .	33
3.1	Geometry of pores in atomically thin membranes . . . . .	49
3.2	Permeability as a function of applied voltage . . . . .	54
3.3	Markov model of the transport mechanism . . . . .	55
3.4	Explicit hydrogen-bond breaking rates corroborate the Markov model . . . . .	58
3.5	Permeability as a function of local polar interactions at the pore edge . . . . .	59
3.6	Permeability as a function of van der Waals interaction strength . . . . .	60
3.7	Disagreement between pump method and Gaussian dynamics permeabilities . . . . .	64

3.8	Permeability of flexible membranes . . . . .	66
3.9	Dynamic correlation and reorientation on a flexible membrane . . . . .	67
3.10	Bursty passage . . . . .	70
3.11	Waiting-time distributions for the bursty passage process . . . . .	71
3.12	Burst-size distributions for the bursty passage process . . . . .	75
3.13	Nonlinear pressure drop–flux relationship on hydrophobic membranes . . . . .	77
3.14	Schematic of the two step passage process in dry pores . . . . .	78
3.15	A two step process for transport: permeabilities in the wet state . . . . .	79
3.16	Nonequilibrium pressure thresholds and equilibrium pore occupation . . . . .	80
3.17	Thermodynamic wetting pressures in nanopores . . . . .	85
4.1	Herringbone and $\pi$ -stacked structures in tetracene clusters . . . . .	108
4.2	Clustering of tetracene as a function of surface polarity . . . . .	110
4.3	Tetracene cluster size distributions . . . . .	111
4.4	Diffusion of tetracene on disordered polar surfaces . . . . .	113

## Chapter 1

### Introduction

At equilibrium, the thermodynamic state of a simple box of gas is a function of just a few variables, like temperature and pressure. Yet such a box contains around  $10^{23}$  particles, and its microscopic state is specified by the three-dimensional positions and momenta of every particle. How do the  $\sim 10^{23}$  degrees of freedom in a box of gas get distilled into only a few important thermodynamic ones? This is the central question of statistical mechanics, which forms the framework that connects the complex microscopic picture to the simple macroscopic one. In contrast to dilute gases, interparticle interactions in liquids are strong, yet there is no long range order or symmetry as one finds in a crystal. These properties make phenomena in the liquid phase much more difficult to understand from a microscopic perspective. Problems are often analytically intractable, and researchers must turn to numerical solutions.

The computer is indispensable in the field of liquid phase statistical mechanics because it can simulate classical systems with many degrees of freedom, giving the researcher a window directly into the microscopic system to an extent that experiment often cannot. The computer was first used in this way during the 1940s to sample equilibrium configurations of simple interacting fluids by Monte Carlo simulation.<sup>1</sup> This allows macroscopic observables to be calculated from the microscopic details of an equilibrium system. These methods shed no light, however, on the dynamics of a system. Shortly after the introduction of Monte Carlo, molecular dynamics (MD) simulation was developed to study the dynamics of complex interacting systems.<sup>2–4</sup> It is hard to overstate the impact that these methods have had on understanding chemical systems. The 2013 Nobel Prize in

Chemistry partially recognizes these remarkable achievements.<sup>5</sup>

MD simulations operate in a regime where the nuclei move in the classical limit and the dynamics of a system are given by Newton's law,  $\mathbf{F}_i = m_i \ddot{\mathbf{r}}_i$ , where  $\mathbf{F}_i$  is the force on particle  $i$ ,  $m_i$  is its mass, and  $\ddot{\mathbf{r}}_i$  is its acceleration. In principle, the force  $\mathbf{F}_i$  is a function of complex many-body quantum mechanical interactions, but in practice, empirical force fields are adequate. Even with this simplification, Newton's law still describes a system of coupled nonlinear second-order differential equations that must be solved numerically.

There are countless models that approximate the interactions between particles in real systems. They are parametrized to match various experimental observables, but no single model matches every experimental observable. For example, in this thesis, we make use of the extended simple point charge (SPC/E) model for liquid water. This model is a nearly optimal trade-off between computational accuracy and conceptual simplicity. It was parametrized to match energetic data such as the heat of vaporization,<sup>6,7</sup> and it performs very well for liquid water over a wide range of conditions, but it does not freeze until about  $-60^{\circ}\text{C}$ .<sup>8</sup> Countless person-hours have been spent tweaking potential parameters for water models to fix problems like this. This thesis instead focuses on the use of simple models to predict qualitative trends rather than quantitative features.

While the choice of model for a particular problem may seem like an art, it is important that the mechanics of the simulation are firmly rooted in theory. Simulations based on Newton's laws conserve energy and generate the exact dynamics of systems in the equilibrium microcanonical ensemble. Newtonian mechanics is restricted, however, to closed and isolated systems. Systems at constant temperature and pressure, for example, are ubiquitous in the real world but are not described by Newtonian mechanics. Variables like temperature and pressure are statistical in nature, and the equilibrium static properties of such systems are well understood in terms of statistical mechanics, but there is no unique description of their microscopic dynamics. The equations of motion used in MD simulations can be modified to generate exact equilibrium averages in the canonical and isothermal-isobaric ensembles,<sup>9–11</sup> as well as many others, but the many different thermostats and barostats that do this generate different dynamics. Away from equilibrium, even less is understood.

One usually turns to hydrodynamic theories, which are essentially Newton's equations of motion for a fluid, but these theories are continuous, and cannot be trusted on atomistic length scales. Atomistic MD simulations of nonequilibrium systems require both a driving force and a dissipation mechanism like a thermostat to maintain steady state. These two competing components interact with each other and can produce unphysical results.<sup>12–15</sup>

A major contribution of this thesis is the development of a new method for nonequilibrium MD simulation of systems under steady-state flow (Chapter 2). Unlike many other nonequilibrium MD techniques, our method has a rigorous theoretical foundation in Gauss's principle of least constraint, which generates the nonequilibrium dynamics that are mathematically as close as possible to unconstrained Newtonian dynamics. Our method, called Gaussian dynamics (GD) is faithful to both hydrodynamics and statistical mechanics, theories that are usually applicable at vastly different length and time scales. In GD, the flux through a system is fixed, and all other relevant hydrodynamic fields arise naturally. This is a significant step forward in the simulation and understanding of such systems.

This new method has allowed us to make considerable progress toward understanding the hydrophobic effect in nonequilibrium systems. The hydrophobic effect in static equilibrium systems explains diverse phenomena from protein folding to the partitioning of oil and water.<sup>16</sup> But many important physical and biological systems are nonequilibrium ones, and the hydrophobic effect is poorly understood in these contexts. Here, by studying water flow through atomically thin porous membranes, we extend our understanding of the hydrophobic effect to nonequilibrium systems. Away from equilibrium, well known equilibrium phenomena like dewetting are still important, but nonequilibrium effects like friction and detailed molecular transport mechanisms also become important. We even observe evidence of a clogging or jamming transition, like that seen in granular flows. Extending the concept of hydrophobicity to dynamic scenarios is a key scientific contribution of this thesis.

The development of GD was motivated, as is most science, by the desire to improve human lives. To this end, we study two specific problems regarding environmental sustainability using

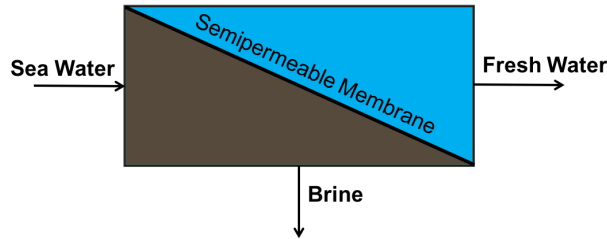


Figure 1.1: In RO, an applied pressure forces water through a semipermeable membrane that blocks salt ions, producing fresh water. The ideal osmotic pressure that must be opposed is given by the difference in solute concentration between the fresh water output and the concentrated brine output.

the tools described above: water security (Chapter 3) and renewable energy (Chapter 4). A brief motivation for these problems follows in Sections 1.1 and 1.2.

## 1.1 Water Security

In 2010, over 80% of the world’s population lived with high risk of water insecurity.<sup>17</sup> The wide availability of salt water, especially in densely populated areas, makes water desalination a promising solution to the water security problem.<sup>18</sup> Reverse osmosis (RO) is a water desalination technique in which water is forced through a semipermeable membrane that allows the water through but not the salt (Figure 1.1). Current RO facilities operate close to the thermodynamic limit. Applied pressures only 15% higher than the osmotic pressure of the concentrated brine output (40 atm) are not uncommon.<sup>19</sup> Increasing the permeability of RO membranes is still a worthwhile goal, however, because energy consumption is at least 50% of the cost of an RO facility.<sup>18</sup> Further, membranes with increased permeability require less surface area, thereby decreasing both membrane replacement costs and facility size.<sup>18</sup> Porous two-dimensional (2d) crystals offer a new paradigm of atomically thin semipermeable membranes for gas and liquid separations,<sup>20–24</sup> and could have important applications in water desalination through RO.<sup>24–30</sup> Semipermeable RO membranes made from an atomically thin material like graphene would offer much less resistance to flow than conventional membranes, reducing energy lost to friction.

This is a difficult problem to study with computer simulation, and was entirely intractable

until our development of GD, discussed in detail in Chapter 2. We apply GD to study the dynamics of water during flow through atomically thin membranes in Chapter 3. We explore the effects of membrane hydrophobicity, membrane flexibility, and pore functionalization. The permeability of these porous membranes is not a simple function of the hydrophobicity, and even depends on the details of the intermolecular interactions. We study both van der Waals and electrostatic interactions. This system exhibits a competition between phenomena that occur on vastly different scales and give rise to qualitatively different transport mechanisms.

## 1.2 Renewable Energy

The modern world is built on an energy economy of nonrenewable fossil fuels. Not only are inexpensive fossil fuels running out,<sup>31</sup> but their continued use is also a major driver in global climate change.<sup>32</sup> According to the most recent IPCC report, in the best case scenario global temperatures will increase 2.5°C by 2100.<sup>32</sup> This will have far reaching and unpredictable consequences on virtually every government, industry, and human life. As glaciers melt, sea level rise alone will displace 10% of the world's population by 2100, creating a billion climate refugees.<sup>33,34</sup> Renewable carbon-neutral energy resources are the only option to maintain modern living standards for an increasingly populous and economically vibrant world.

Solar energy is a particularly promising renewable resource. Solar energy conversion efficiencies have increased dramatically since 1976,<sup>36</sup> but the theoretical upper limit on the efficiency of a single-junction solar cell, known as the Shockley-Queisser limit, is only 34%.<sup>37</sup> One of the limiting factors is that solar materials can only absorb photons with equal or greater energy than the material's band gap. Photons with an energy above the band gap are also used inefficiently, because their excess energy is dissipated as heat (Figure 1.2).

One way to overcome the Shockley-Queisser limit is to make more efficient use of the solar spectrum. Singlet fission (SF) is one way to accomplish this. SF is a photophysical process in which a singlet excited state relaxes into two triplet excited states, each with half the energy. Used in conjunction with conventional solar devices, SF can raise the theoretical efficiency limit

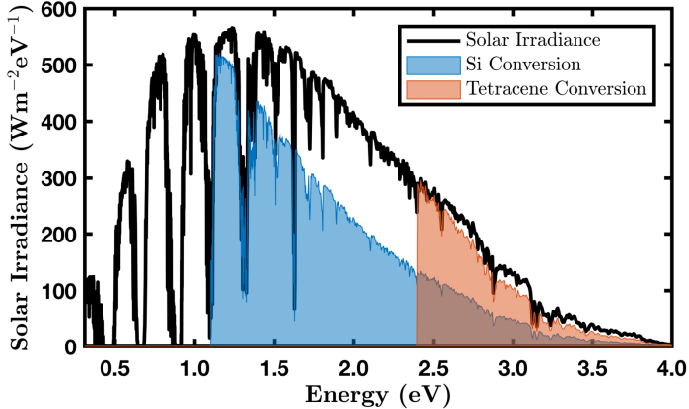


Figure 1.2: A conventional silicon (Si) solar cell, with a band gap of 1.1 eV wastes much of the high energy part of the solar spectrum because those photons only produce power at the band gap. A SF chromophore, like tetracene, in conjunction with a conventional solar absorber, makes more efficient use of this part of the spectrum by absorbing high energy photons and splitting them into two excitations each with half the energy. The blue area shows the fraction of the solar spectrum that is usable in a silicon solar cell. The orange area shows the usable fraction in a solar cell using tetracene, a canonical SF chromophore with a band gap of 2.4 eV. The total solar irradiance at sea level is shown in black.<sup>35</sup>

to 45% (Figure 1.2). However, SF is an intermolecular, or inter-chromophore, process. Its efficiency is very sensitive to intermolecular couplings, which are strong functions of intermolecular configuration.

The original picture for a solar cell device that incorporates SF is a dye-sensitized solar cell (DSSC), or Grätzel cell. In this architecture, both conventional and SF chromophores are haphazardly mixed with semiconducting nanoparticles, commonly  $\text{TiO}_2$ .<sup>38,39</sup> This avoids the high-cost manufacturing processes required to fabricate thin-film or crystalline solar absorbers. However, as described above, the efficiency of such a device depends very sensitively on the intermolecular configurations present in the chromophore aggregates formed. Historically, SF researchers have searched for candidate chromophores that have favorable energetic properties.<sup>40</sup> This thesis approaches the problem, for the first time, from a statistical standpoint. We use MD to study the aggregation of tetracene, a canonical SF chromophore, on surfaces of varying polarity, and for both ordered and disordered polar surfaces (Chapter 4).

## Bibliography

- [1] Metropolis, N.; Ulam, S. The Monte Carlo method. *J. Am. Stat. Assoc.*, 44(247):335–341, **1949**.
- [2] Fermi, E.; Pasta, J.; Ulam, S. Studies of non linear problems. Technical Report LA-1940, Los Alamos National Laboratory, **1955**.
- [3] Alder, B. J.; Wainwright, T. E. Studies in molecular dynamics. I. General method. *J. Chem. Phys.*, 31(2):459–466, **1959**.
- [4] Rahman, A. Correlations in the motion of atoms in liquid argon. *Phys. Rev.*, 136(2A):A405–A411, **1964**.
- [5] Karplus, M.; Levitt, M.; Warshel, A. Nobel prize in chemistry 2013. [http://www.nobelprize.org/nobel\\_prizes/chemistry/laureates/2013/](http://www.nobelprize.org/nobel_prizes/chemistry/laureates/2013/), **2013**. Accessed: 2017-03-25.
- [6] Berendsen, H. J. C.; Postma, J. P. M.; van Gunsteren, W. F.; Hermans, J. Interaction models for water in relation to protein hydration. In Pullman, B., ed., *Intermolecular Forces*, volume 14 of *The Jerusalem Symposia on Quantum Chemistry and Biochemistry*, pages 331–342. Springer, Netherlands, **1981**.
- [7] Berendsen, H. J. C.; Grigera, J. R.; Straatsma, T. P. The missing term in effective pair potentials. *J. Phys. Chem.*, 91(24):6269–6271, **1987**.
- [8] Vega, C.; Sanz, E.; Abascal, J. L. F.; Noya, E. G. Determination of phase diagrams via computer simulation: Methodology and applications to water, electrolytes and proteins. *J. Phys.: Condens. Matter*, 20(15):153101, **2008**.
- [9] Nosé, S. A molecular dynamics method for simulations in the canonical ensemble. *Mol. Phys.*, 52(2):255–268, **1984**.
- [10] Hoover, W. G. Canonical dynamics: Equilibrium phase-space distributions. *Phys. Rev. A*, 31(3):1695–1697, **1985**.
- [11] Martyna, G. J.; Tobias, D. J.; Klein, M. L. Constant pressure molecular dynamics algorithms. *J. Chem. Phys.*, 101(5):4177–4189, **1994**.
- [12] Evans, D. J.; Morriss, G. P. Shear thickening and turbulence in simple fluids. *Phys. Rev. Lett.*, 56(20):2172–2175, **1986**.
- [13] Harvey, S. C.; Tan, R. K.-Z.; Cheatham, T. E. The flying ice cube: Velocity rescaling in molecular dynamics leads to violation of energy equipartition. *J. Comput. Chem.*, 19(7):726–740, **1998**.
- [14] Bernardi, S.; Todd, B. D.; Searles, D. J. Thermostating highly confined fluids. *J. Chem. Phys.*, 132(24):244706, **2010**.
- [15] Heyes, D. M.; Morriss, G. P.; Evans, D. J. Nonequilibrium molecular dynamics study of shear flow in soft disks. *J. Chem. Phys.*, 83(9):4760–4766, **1985**.

- [16] Chandler, D. Interfaces and the driving force of hydrophobic assembly. *Nature*, 437(7059):640–647, **2005**.
- [17] Vörösmarty, C. J.; McIntyre, P. B.; Gessner, M. O.; Dudgeon, D.; Prusevich, A.; Green, P.; Glidden, S.; Bunn, S. E.; Sullivan, C. A.; Liermann, C. R.; et al. Global threats to human water security and river biodiversity. *Nature*, 467(7315):555–561, **2010**.
- [18] Lee, K. P.; Arnot, T. C.; Mattia, D. A review of reverse osmosis membrane materials for desalination—Development to date and future potential. *J. Membrane Sci.*, 370(1–2):1–22, **2011**.
- [19] Zhu, A.; Christofides, P. D.; Cohen, Y. On RO membrane and energy costs and associated incentives for future enhancements of membrane permeability. *J. Membrane Sci.*, 344(1–2):1–5, **2009**.
- [20] Koenig, S. P.; Wang, L.; Pellegrino, J.; Bunch, J. S. Selective molecular sieving through porous graphene. *Nat. Nanotechnol.*, 7(11):728–732, **2012**.
- [21] Schrier, J. Helium separation using porous graphene membranes. *J. Phys. Chem. Lett.*, 1(15):2284–2287, **2010**.
- [22] Nair, R. R.; Wu, H. A.; Jayaram, P. N.; Grigorieva, I. V.; Geim, A. K. Unimpeded permeation of water through helium-leak-tight graphene-based membranes. *Science*, 335(6067):442–444, **2012**.
- [23] Drahushuk, L. W.; Wang, L.; Koenig, S. P.; Bunch, J. S.; Strano, M. S. Analysis of time-varying, stochastic gas transport through graphene membranes. *ACS Nano*, 10(1):786–795, **2016**.
- [24] Jain, T.; Rasera, B. C.; Guerrero, R. J. S.; Boutilier, M. S. H.; O'Hern, S. C.; Idrobo, J.-C.; Karnik, R. Heterogeneous sub-continuum ionic transport in statistically isolated graphene nanopores. *Nat. Nanotechnol.*, 10(12):1053–1057, **2015**.
- [25] Surwade, S. P.; Smirnov, S. N.; Vlassiouk, I. V.; Unocic, R. R.; Veith, G. M.; Dai, S.; Mahurin, S. M. Water desalination using nanoporous single-layer graphene. *Nat. Nanotechnol.*, 10(5):459–464, **2015**.
- [26] Kalra, A.; Garde, S.; Hummer, G. Osmotic water transport through carbon nanotube membranes. *Proc. Nat. Acad. Sci. U. S. A.*, 100(18):10175–10180, **2003**.
- [27] Suk, M. E.; Aluru, N. R. Water transport through ultrathin graphene. *J. Phys. Chem. Lett.*, 1(10):1590–1594, **2010**.
- [28] Wang, E. N.; Karnik, R. Water desalination: Graphene cleans up water. *Nat. Nanotechnol.*, 7(9):552–554, **2012**.
- [29] Cohen-Tanugi, D.; Grossman, J. C. Water desalination across nanoporous graphene. *Nano Lett.*, 12(7):3602–3608, **2012**.
- [30] Heiranian, M.; Farimani, A. B.; Aluru, N. R. Water desalination with a single-layer MoS<sub>2</sub> nanopore. *Nat. Commun.*, 6:8616, **2015**.

- [31] Abdul-Hamid, O. S.; Odulaja, A.; Hassani, H.; Christodoulides, P.; Stöger, K.; Kalirai, H.; Moudassir, M.; Pospiech, R.; Gredinger, A.; Hamamciyan, L.-S.; et al. OPEC annual statistical bulletin. Technical Report ESA/P/WP.242, OPEC, **2016**.
- [32] Summary for policymakers. In Edenhofer, O.; Pichs-Madruga, R.; Farahani, E.; Kadner, S.; Seyboth, K.; Adler, A.; Baum, I.; Brunner, S.; Eickemeier, P.; Kriemann, B.; et al., eds., *Climate Change 2014: Mitigation of Climate Change. Contribution of Working Group III to the Fifth Assessment Report of the Intergovernmental Panel on Climate Change*, pages 1–30. Cambridge University Press, Cambridge, **2014**.
- [33] Church, J.; Clark, P.; Cazenave, A.; Gregory, J.; Jevrejeva, S.; Levermann, A.; Merrifield, M.; Milne, G.; Nerem, R.; Nunn, P.; et al. Sea level change. In Stocker, T.; Qin, D.; Plattner, G.-K.; Tignor, M.; Allen, S.; Boschung, J.; Nauels, A.; Xia, Y.; Bex, V.; Midgley, P., eds., *Climate Change 2013: The Physical Science Basis. Contribution of Working Group I to the Fifth Assessment Report of the Intergovernmental Panel on Climate Change*, pages 1137–1216. Cambridge University Press, Cambridge, **2013**.
- [34] Department of Economic and Social Affairs, Population Division. World population prospects: The 2015 revision, methodology of the United Nations population estimates and projections. Technical Report ESA/P/WP.242, United Nations, **2015**.
- [35] Standard tables for reference solar spectral irradiances: Direct normal and hemispherical on 37° tilted surface. Technical Report G173–03, ASTM International, **2012**.
- [36] Green, M. A.; Emery, K.; Hishikawa, Y.; Warta, W.; Dunlop, E. D. Solar cell efficiency tables (version 48). *Prog. Photovoltaics*, 24(7):905–913, **2016**.
- [37] Shockley, W.; Queisser, H. J. Detailed balance limit of efficiency of  $p - n$  junction solar cells. *J. Appl. Phys.*, 32(3):510–519, **1961**.
- [38] O'Regan, B.; Grätzel, M. A low-cost, high-efficiency solar cell based on dye-sensitized colloidal  $TiO_2$  films. *Nature*, 353(6346):737–740, **1991**.
- [39] Hanna, M. C.; Nozik, A. J. Solar conversion efficiency of photovoltaic and photoelectrolysis cells with carrier multiplication absorbers. *J. Appl. Phys.*, 100(7):074510–8, **2006**.
- [40] Smith, M. B.; Michl, J. Singlet fission. *Chem. Rev.*, 110(11):6891–6936, **2010**.

## Chapter 2

### Atomistic Hydrodynamics: Molecular Dynamics Simulation of Steady-State Flow

The contents of this chapter are reprinted, with permission, from

Strong, S. E.; Eaves, J. D. Atomistic hydrodynamics and the dynamical hydrophobic effect in porous graphene. *J. Phys. Chem. Lett.*, 7(10):1907–1912, **2016**

and

Strong, S. E.; Eaves, J. D. The dynamics of water in porous two-dimensional crystals. *J. Phys. Chem. B*, 121(1):189–207, **2017**

#### 2.1 Abstract

Mirroring their role in electrical and optical physics, 2d crystals are emerging as novel platforms for fluid separations and water desalination, which are hydrodynamic processes that occur in nanoscale environments. For numerical simulation to play a predictive and descriptive role, one must have theoretically sound methods that span orders of magnitude in physical scales, from the atomistic motions of particles inside the channels to the large-scale hydrodynamic gradients that drive transport. Here, we use constraint dynamics to derive a nonequilibrium MD method for simulating steady-state mass flow of a fluid moving through the nanoscopic spaces of a porous solid. This method, called GD, has a rigorous foundation in theory, unlike many other common methods used for nonequilibrium simulation. We thoroughly test GD using a simple 2d LJ fluid flowing through channels and pores of various geometries. Unlike the pump method, a common method for

the simulation of steady-state flow, GD generates results compatible with both statistical mechanics and hydrodynamics.

## 2.2 Background

Numerical techniques, rooted in theory, are indispensable tools in the study of liquids and fluids. On microscopic length and time scales, statistical mechanics underpins the MD methods for systems at thermal equilibrium.<sup>3</sup> On macroscopic scales, continuum hydrodynamics can describe fluids driven away from equilibrium.<sup>4</sup> But it remains unclear how one should simulate an atomistic system away from equilibrium.<sup>5–10</sup> This gap in knowledge makes it difficult to model processes on the mesoscale, such as water desalination, gas separation, and cellular transport. In these systems, gradients in continuous fields, like density and pressure, drive flow through bottlenecks that admit only a few particles at a time.<sup>5,11–23</sup> These processes require computational models to be theoretically rigorous and accurate across orders of magnitude in physical scales.

Hydrodynamic approaches are rooted in continuum models that inherently break down on atomic scales.<sup>4</sup> Conversely, microscopic MD simulations only generate rigorously accurate dynamics for closed and isolated systems.<sup>24</sup> These systems can be coupled to a heat bath to generate static averages consistent with the canonical ensemble, but the thermostats that do this are not unique.<sup>3</sup> The dynamics generated under various thermostating schemes can be quite different, even at thermal equilibrium.<sup>3,24</sup> In nonequilibrium MD simulations, both an external force and a thermostat counterbalance to maintain steady state.<sup>25,26</sup> The implementation of these two components is likewise not unique. Away from equilibrium, the interaction between the thermostat and an external driving force can produce results that are manifestly unphysical.<sup>27–30</sup>

In this Chapter, we develop a method for simulating atomistic systems in nonequilibrium steady states of mass flow. Our method, which we call GD, finds the equations of motion that are consistent with a minimal set of constraints, much like early system-bath coupling schemes devised in MD methods.<sup>26</sup> We constrain only the total mass current and kinetic temperature. Gradients in hydrodynamic fields such as velocity, density, temperature, and pressure, arise naturally (Fig-

ure 2.7a). Section 2.3 presents a thorough derivation of the method.

We then subject GD to a variety of tests and comparisons to validate and benchmark it, using a simple 2d liquid as a test system. The simulation methods are presented in Section 2.4. In Section 2.6, we discuss the similarities and differences between GD and the pump method for both Poiseuille flow and flow through porous walls. These two methods do not always give the same results for the permeability, and the deviations between the two are rooted in the fluctuations that each method allows. Because GD admits density and pressure fluctuations, it permits flow through pores in superhydrophobic membranes where the pump method does not. In Section 2.7, we present a thorough discussion of the calculation of the pressure profile and pressure drop, which are used to compute the permeability. In Section 2.8 we compare the pump and GD methods in more detail for a variety of channel geometries and at various Reynolds numbers ( $Re$ ). Finally, in Section 2.9, we investigate the hydrodynamic slip length, which measures the deviation from the idealized “no-slip” boundary condition.<sup>31</sup> The slip length in simulations of water in carbon nanotubes (CNTs) has been a topic of controversy, with different simulation methods yielding different results.<sup>12,32–37</sup> Our results show that the slip length depends sensitively on how one holds the membrane atoms in place, either through a rigid constraint or with harmonic springs. The slip length depends much less sensitively on whether the membrane atoms or the fluid atoms are thermostatted. These observations have not been discussed in the literature, and may be at least partly responsible for some apparent disagreement between different studies. We address this issue directly in Chapter 3.7 with simulations of water flow through porous membranes.

## 2.3 Derivation of Gaussian Dynamics

GD is rooted in Gauss’s principle of least constraint, which finds the equations of motion that strictly obey a set of constraints but that generate dynamics as mathematically close as possible to unconstrained Newtonian mechanics.<sup>26,38</sup> This is similar in spirit to other constraint methods, like Euler-Lagrange constraint dynamics and extended Lagrangian ensembles, that have a long history in MD simulations.<sup>3</sup> We start by first discussing the constraints, and then discuss Gauss’s method

for satisfying them. It is trivial to constrain the positions of atoms that are fixed in space, so we do not include them in this discussion. For a system of  $N$  atoms with masses  $\{m\}$  at positions  $\{\mathbf{r}\}$ , the constraint that holds the total mass flux constant, written as a level set  $\mathbf{g}_f$ , is

$$\mathbf{g}_f(\{\dot{\mathbf{r}}\}) = \frac{1}{M} \sum_{i=1}^N m_i \dot{\mathbf{r}}_i - \mathbf{u}_{\text{COM}} = 0, \quad (2.1)$$

where  $M \equiv \sum_{i=1}^N m_i$  is the total mass of the system, overdots denote time derivatives, and  $\mathbf{u}_{\text{COM}}$  is the center-of-mass (COM) velocity of the fluid to be held constant. For compactness of notation, we suppress time dependence. While out of equilibrium, the flows we study are at steady state. To satisfy the constraint in eq. 2.1, an external force will drive the system and heat it. A thermostat must dissipate this heat to maintain steady state, which requires another constraint.

To develop a thermostat one needs a working definition of temperature. Following previous work,<sup>26</sup> we assume that the velocity of an atom in the lab frame,  $\dot{\mathbf{r}}_i$ , can be decomposed into a thermal part,  $\mathbf{v}_i$ , and streaming part,  $\mathbf{u}(\mathbf{r}_i)$ ,

$$\dot{\mathbf{r}}_i = \mathbf{v}_i + \mathbf{u}(\mathbf{r}_i), \quad (2.2)$$

which implies that the flows are not turbulent. With this decomposition, we assume local equilibrium and define the kinetic temperature with respect to the thermal, or peculiar, velocities  $\mathbf{v}_i$ .<sup>25,26</sup> The thermal velocities have zero mean and a standard deviation given by equipartition. The streaming velocities

$$\mathbf{u}(\mathbf{r}) = \frac{\sum_i^N m_i \dot{\mathbf{r}}_i \delta(\mathbf{r}_i - \mathbf{r})}{\sum_i^N m_i \delta(\mathbf{r}_i - \mathbf{r})}, \quad (2.3)$$

must be determined self-consistently, which we achieve by spatial averaging. Figure 2.1 depicts the resolution of the Dirac  $\delta$ -functions in eq. 2.3 by spatial binning. These considerations lead to the following temperature constraint

$$g_T(\{\mathbf{r}, \dot{\mathbf{r}}\}) = \frac{1}{2} \sum_{i=1}^N m_i (\dot{\mathbf{r}}_i - \mathbf{u}(\mathbf{r}_i))^2 - \frac{d(N - N_u) k_B T}{2} = 0, \quad (2.4)$$

where  $k_B$  is Boltzmann's constant,  $T$  is the temperature set-point,  $d$  is the dimensionality, and  $N_u$  is the number of bins used to compute the streaming velocity profile (Figure 2.1). At equilibrium,

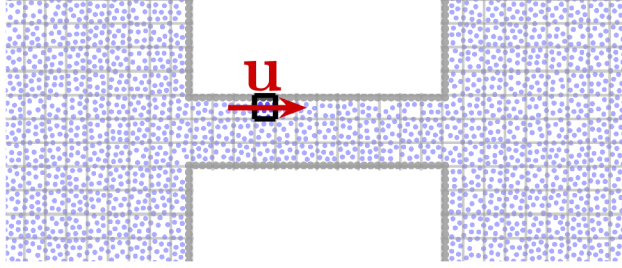


Figure 2.1: Image of a 2d Lennard-Jones simulation illustrating the calculation of the streaming velocity profile,  $\mathbf{u}(\mathbf{r})$ . The blue points are fluid atoms and the gray points are wall atoms. The gray boxes, fixed in the lab frame, represent the resolution for  $\mathbf{u}(\mathbf{r})$ , with a linear dimension typically on the order of a few atomic diameters. The streaming velocity within each bin is the COM velocity of the atoms in that cell.

this constraint (eq. 2.4) generates the well-known Gaussian isokinetic thermostat.<sup>26,38–40</sup> Since the form of the velocity profile is not assumed a priori, but is determined self-consistently a posteriori, the constraint in eq. 2.4 leads to a profile-unbiased thermostat (Figure 2.1).<sup>27</sup> Equation 2.4 pertains to the situation where only the fluid atoms are thermostatted. In general, the thermostatted atoms may or may not be the same as the fluid atoms constrained in eq. 2.1. For example, when a system consists of a fluid flowing between walls, if the wall atoms are mobile, then either the fluid, the walls, or both can be thermostatted. If both the fluid and the walls are thermostatted, then the thermostat constraint will couple the momenta of the fluid atoms to the momenta of wall atoms, rendering the COM momentum of the fluid unconserved. However, both the wall and fluid atoms can be thermostatted simultaneously with a separate thermostat for each.

The constraints in eqs. 2.1 and 2.4 depend on the velocities, making them nonholonomic constraints.<sup>41</sup> It is difficult to satisfy nonholonomic constraints using Euler-Lagrange constraint dynamics,<sup>42,43</sup> so we turn instead to Gauss's principle of least constraint, which finds the accelerations that minimize the cost function

$$C(\{\mathbf{r}, \dot{\mathbf{r}}, \ddot{\mathbf{r}}\}) = \frac{1}{2} \sum_{i=1}^N m_i \left( \ddot{\mathbf{r}}_i - \frac{\mathbf{F}_i}{m_i} \right)^2 + \lambda_T \dot{g}_T(\{\mathbf{r}, \dot{\mathbf{r}}, \ddot{\mathbf{r}}\}) + \boldsymbol{\lambda}_f \cdot \dot{\mathbf{g}}_f(\{\ddot{\mathbf{r}}\}), \quad (2.5)$$

where  $\mathbf{F}_i = -\nabla_i U$  is force on atom  $i$  from the intermolecular potential  $U$ , and the  $\lambda$ s are Gaussian multipliers. In the absence of the constraints, the accelerations that minimize eq. 2.5 follow Newton's law,  $m_i \ddot{\mathbf{r}}_i = \mathbf{F}_i$ . The constraints given in eqs. 2.1 and 2.4 do not depend on the accelerations,

so to minimize eq. 2.5 with respect to the accelerations, we write the constraints as functions of the accelerations by differentiating them with respect to time.<sup>26</sup> Including geometry constraints, such as rigid bonds, is trivial because those constraints are holonomic; they depend only on positions and separate completely. Here, we ignore the temperature constraint to illustrate the solution process. For the full treatment, see Appendix A. The time derivative of eq. 2.1 is

$$\dot{\mathbf{g}}_f = \sum_{i=1}^N m_i \ddot{\mathbf{r}}_i = 0, \quad (2.6)$$

which gives the cost function

$$C(\{\ddot{\mathbf{r}}\}) = \frac{1}{2} \sum_{i=1}^N m_i \left( \ddot{\mathbf{r}}_i - \frac{\mathbf{F}_i}{m_i} \right)^2 + \boldsymbol{\lambda}_f \cdot \sum_{i=1}^N m_i \ddot{\mathbf{r}}_i. \quad (2.7)$$

We now find the accelerations that minimize the cost function

$$\frac{\partial}{\partial \ddot{\mathbf{r}}_i} C(\{\ddot{\mathbf{r}}\}) = m_i \left( \ddot{\mathbf{r}}_i - \frac{\mathbf{F}_i}{m_i} \right) + \boldsymbol{\lambda}_f m_i = 0. \quad (2.8)$$

This gives the equation of motion

$$m_i \ddot{\mathbf{r}}_i = \mathbf{F}_i - \boldsymbol{\lambda}_f m_i. \quad (2.9)$$

We solve for  $\boldsymbol{\lambda}_f$  by summing eq. 2.9 over all atoms:

$$\sum_{i=1}^N m_i \ddot{\mathbf{r}}_i = \sum_{i=1}^N \mathbf{F}_i - \boldsymbol{\lambda}_f \sum_{i=1}^N m_i. \quad (2.10)$$

The term on the left-hand side is zero due to eq. 2.6, so we find

$$\boldsymbol{\lambda}_f = \frac{1}{M} \sum_{i=1}^N \mathbf{F}_i. \quad (2.11)$$

The resulting equation of motion is

$$m_i \ddot{\mathbf{r}}_i = \mathbf{F}_i - m_i \mathbf{I}, \quad (2.12)$$

where we have defined the vector

$$\mathbf{I} \equiv \boldsymbol{\lambda}_f = \frac{1}{M} \sum_{i=1}^N \mathbf{F}_i. \quad (2.13)$$

$\mathbf{I}$  is an acceleration, not the identity matrix.

Including the Gaussian isokinetic thermostat and molecular geometry constraints would simply add more terms to the equation of motion (Appendix A)

$$m_i \ddot{\mathbf{r}}_i = \mathbf{F}_i - m_i \mathbf{I} - m_i \xi (\dot{\mathbf{r}} - \mathbf{u}(\mathbf{r}_i)) + \mathbf{f}_i, \quad (2.14)$$

where, for molecules,  $\mathbf{f}_i$  is the force of constraint that fixes the intramolecular geometry,<sup>44,45</sup> and  $\xi$  is the drag coefficient associated with a profile-unbiased Gaussian isokinetic thermostat,<sup>26,27,38–40</sup>

$$\xi \equiv \frac{\sum_{i=1}^N (\dot{\mathbf{r}}_i - \mathbf{u}(\mathbf{r}_i)) \cdot \mathbf{F}_i}{\sum_{i=1}^N m_i (\dot{\mathbf{r}}_i - \mathbf{u}(\mathbf{r}_i))^2}. \quad (2.15)$$

Instead of exactly satisfying the temperature constraint at each time step, we fix the average kinetic temperature using a profile-unbiased Nosé-Hoover thermostat.<sup>26,27,46,47</sup> This greatly improves computational speed. Note that the final equation of motion (eq. 2.14) does not depend on the COM momentum set point  $\mathbf{u}_{\text{COM}}$ . This means that GD only preserves the initial COM momentum. As such, one must initialize the system with a non-zero COM momentum to simulate steady-state flow. Section 2.4.2 discusses this and the equilibration to steady state in detail.

The flow constraint applies a driving force to each fluid atom equal to  $-m_i \mathbf{I}$ . Physically,  $\mathbf{I}$  is a gravitational field that fluctuates in time to maintain the mass flux through the system, counteracting the virtual work required to hold a set of wall or membrane atoms fixed in space. In practical applications,  $\mathbf{I}$  is weak. In 2d Lennard-Jones (LJ) simulations, even at Re around 10, the average applied force is approximately equal to the force between two LJ atoms separated by  $3 \sigma$ . This force is so weak that it is beyond the cutoff distance typically employed in simulations.

Equation 2.12 is the basis of the GD method. While simple, it is theoretically rooted in constraint dynamics and stands in contrast to ad hoc approaches that employ some mixture of external forces, particle swaps, and thermostats.<sup>5–10,31,48</sup> Computing  $\mathbf{I}$  scales as  $\mathcal{O}(N)$ , so it adds little computational burden. GD also consistently averages more quickly than both the pump method and linear response theory (Figure 3.2).

Our implementation of GD is publicly available through LAMMPS as `fix flow/gauss`.

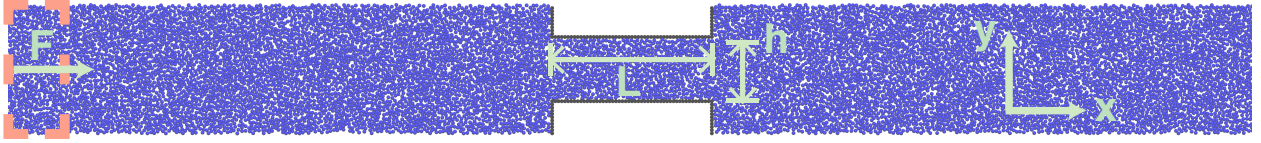


Figure 2.2: Snapshot from a 2d simulation using the pump method, with the pump region outlined in orange. An external force, applied only to the atoms in the pump region, creates a pressure drop across the pore, situated in the middle of the image. The simulation box must be long enough so that the bulk fluid can equilibrium the pressure and spatially discontinuous force applied in the pump region. In our simulations, the pump region is  $5 \sigma$  wide and is centered on the periodic boundary. For clarity, the pump region shown here is shifted and not drawn to scale. The length  $L$  and width  $h$  of the pore are labeled for reference.

## 2.4 Methods

### 2.4.1 Pump Method

To understand some of the differences between GD and another common method for the simulation of steady-state flow, we perform some comparisons using a 2d LJ test system. We compare GD to the “pump method”, in which a force is applied only to atoms in a “pump region”, which is a region far from the region of interest, such as a pore (Figure 2.2).<sup>5</sup> In the pump method, the pressure drop is given by the total force applied to the simulation divided by the cross-sectional area (length in 2d) over which it is applied:

$$\Delta P = \frac{F}{A}. \quad (2.16)$$

In 2d,  $A = L_y$ , and in 3d,  $A = L_y L_z$ , where the flow is in the  $x$ -direction. In some applications of the pump method, the force per atom is constant in time. In our implementation, the total force on the pump region is constant in time, which results in a constant pressure drop  $\Delta P$  across the system. Provided the pump region is large enough that the particle number fluctuations in its volume are small, the differences between these two implementations are negligible. In many respects, the pump method is a constant gradient complement to GD, which is a constant current method.

### 2.4.2 Steady State and Current

Just as equilibrium simulations require equilibration time to “forget” their initial conditions, both GD and the pump method require “stabilization” time to reach steady state. Further, GD only maintains the COM momentum that is already present in a system. As such, a nonequilibrium simulation must be initialized by giving the system a total COM momentum. We do this by first equilibrating the system at thermal equilibrium and then adding a velocity in the direction of flow to all fluid atoms. During the stabilization time, this uniform velocity profile relaxes into the natural steady-state velocity profile. The flux profile,

$$\mathbf{J}(\mathbf{r}, t) = \rho(\mathbf{r}, t)\mathbf{u}(\mathbf{r}, t), \quad (2.17)$$

measures whether or not the system has achieved steady state, where

$$\rho(\mathbf{r}, t) = \sum_i m_i \delta(\mathbf{r}_i(t) - \mathbf{r}) \quad (2.18)$$

is the mass density field.

Mass conservation implies the continuity equation

$$\nabla \cdot \mathbf{J}(\mathbf{r}, t) = -\frac{\partial \rho(\mathbf{r}, t)}{\partial t}, \quad (2.19)$$

which requires that the flux profile is constant in both space and time when the system is at steady state,  $\partial_t \rho = 0 \implies \nabla \cdot \mathbf{J}(\mathbf{r}) = 0$ . In the 2d LJ simulations, we use this criterion directly to ensure the system is at steady state (Figure 2.4c,d). In the water simulations discussed in Chapter 3, however, the low flow rates make the flux profiles too noisy to give a good test of steady state, so we use a coarser criterion on the flux. We compare the current inside the pore with the global current,  $q$ , defined below, to test that the flux profile is constant in space. A simulation is at steady state when the current inside the pore is equal to the global current, within the noise.

The computation of the global current requires that we develop relationships between the total mass flux,  $\mathbf{J}_{\text{tot}}$ , the COM velocity,  $\mathbf{u}_{\text{COM}}$ , and the global particle current,  $q$ , at steady state. The total mass flux,  $\mathbf{J}_{\text{tot}}$ , is defined as a spatial average of the flux profile  $\mathbf{J}(\mathbf{r}, t)$  over the entire

simulation box,

$$\mathbf{J}_{\text{tot}} \equiv \frac{\int_{\text{box}} d^d \mathbf{r} \mathbf{J}(\mathbf{r}, t)}{\int_{\text{box}} d^d \mathbf{r}}, \quad (2.20)$$

where  $\int_{\text{box}} d^d \mathbf{r}$  denotes an integral over a  $d$ -dimensional simulation box. The denominator in eq. 2.20 is simply the  $d$ -dimensional volume of the simulation, including any volume excluded by obstacles. Inserting eqs. 2.3 and 2.18 into eq. 2.17 and performing the integration in eq. 2.20 yields

$$\mathbf{J}_{\text{tot}} = \rho_{\text{tot}} \mathbf{u}_{\text{COM}}, \quad (2.21)$$

where  $\mathbf{u}_{\text{COM}}$  is the COM velocity of the fluid and in three dimensions

$$\rho_{\text{tot}} = \frac{M}{L_x L_y L_z} \quad (2.22)$$

is the *total* mass density in the simulation and  $L_x$ ,  $L_y$ , and  $L_z$  are the simulation box dimensions along the appropriate axes.  $\rho_{\text{tot}}$  is *not* the same as the bulk fluid density,  $\rho_0$ , which is the average fluid density in the homogeneous part of the fluid far from the membrane.

In what follows, for the sake of clarity, we specify our discussion to three dimensions, though the derivation in two dimensions appropriate for the LJ simulations reported here is straightforward. In our simulations, only the  $x$ -component of  $\mathbf{u}_{\text{COM}}$  is non-zero on average, so eq. 2.21 simplifies to  $J_{\text{tot},x} = \rho_{\text{tot}} u_{\text{COM},x}$ . The global particle current through a system with cross-sectional area  $A$  normal to the current is

$$q = \frac{J_{\text{tot},x} A}{m_p}, \quad (2.23)$$

where  $m_p$  is the mass per particle. For a three dimensional box with flow along the  $x$ -axis,  $A = L_y L_z$ , and eqs. 2.21, 2.22, and 2.23 yield the desired relationship between the global particle current,  $q$ , and  $u_{\text{COM},x}$ .

$$u_{\text{COM},x} = \frac{q L_x}{N}. \quad (2.24)$$

To simulate a given current, one uses eq. 2.24 to find the initial set-point velocity  $u_{\text{COM},x}$  for the simulation. Choosing an appropriate value of  $q$  is a balancing act. If  $q$  is too large, the equilibration time to steady state becomes too long and the requisite value of  $L_x$  too large to be computationally

feasible. If  $q$  is too small, more simulations are required to achieve statistically significant data. The particulars depend on the specific system, but for the water simulations reported in Chapter 3  $q$  is on the order of 10 molecules/ns.

We now turn to the calculation of the current inside the pore, which at steady state must be equal to the global current. To compute the current through the pore we use the collective variable  $n(t)$  defined by Zhu et al. in the context of collective diffusion.<sup>49</sup>  $n(t)$  is the appropriate collective variable for the linear response theory of particles flowing through channels.<sup>49</sup> The variable  $n(t)$  is simply a continuous variable that counts net passage events, and is defined by integrating

$$dn = \sum_i^{\text{in pore}} \frac{dx_i}{L}, \quad (2.25)$$

forward in time with  $n(0) = 0$ , where the sum goes over particles inside some region defined as the “pore”, and  $L$  is the length of the pore region. The definition of  $L$  is described in Section 2.4.4 and Figure 2.2 for a 2d fluid, and in Chapter 3.3.3 and Figure 3.1e for water. A particle that moves forwards across the pore has  $dx = L$ , so will increment  $n$  by exactly 1. A particle that moves backwards across the pore will have  $dx = -L$  and will increment  $n$  by exactly  $-1$ . The current is therefore given by the slope of  $n(t)$ , which we compute by linear regression with zero intercept. The choice of the pore region is discussed in Section 2.4.5.

### 2.4.3 Reynolds Number

The Reynolds number ( $\text{Re}$ ) is

$$\text{Re} = \frac{u_{\text{in}} L \rho_0}{\eta}, \quad (2.26)$$

where  $u_{\text{in}}$  is the velocity of the fluid inside the pore,  $L$  is the length of the pore,  $\rho_0$  is the bulk density of the fluid, and  $\eta$  is the bulk viscosity of the fluid. Conservation of momentum for an incompressible fluid says that the flow velocity inside the pore increases relative to the total flux proportionally to the reduction in cross-sectional area available to the flow. In 2d, this is a cross-sectional length, and the flow velocity in the pore is

$$u_{\text{in}} = \frac{J_{\text{tot}} L_y}{h \rho_{\text{tot}}}, \quad (2.27)$$

where  $h$  is the width of the pore defined in Figure 2.2. Using eq. 2.26, we have

$$\text{Re} = \frac{JL_y L}{\eta h}. \quad (2.28)$$

To calculate  $\text{Re}$ , we need to know  $\eta$ . We measure the viscosity for a bulk 2d system with no channel at the relevant conditions of  $T = 2 \epsilon/k_B$ , and  $\rho_0 = 0.8 \sigma^{-2}$  using the Green-Kubo relation,<sup>3</sup>

$$\eta = \frac{1}{V k_B T} \int_0^\infty dt \langle \sigma_{xy}(0) \sigma_{xy}(t) \rangle, \quad (2.29)$$

where  $\sigma_{xy}$  is the off-diagonal element of the 2d stress tensor, and  $V$  is the volume of the system (area, in 2d). We find no evidence that this integral diverges as discussed in Refs. 50–52; the autocorrelation function does not decay as  $t^{-1}$ , it decays as  $e^{-t}$ . We also find no system size dependence of the viscosity for systems from  $20 \times 20 \sigma^2$  to  $100 \times 100 \sigma^2$ . We find  $\eta = 2.2 \pm 0.1 \sqrt{m\epsilon}/\sigma$ .

#### 2.4.4 Pore Dimensions

The calculations of the current through the pore (Section 2.4.2) and the pressure drop (Section 2.7) both require the definition of the length of the pore,  $L$ , or a “pore region”, where  $L$  is the length of the pore region in the direction of flow (Figures 2.2 and 3.1e). The pore region is symmetric about the plane  $x = 0$ , so the edges of the pore are defined by the length of the pore,  $x_{\text{edge}} = \pm L/2$ . The length of the pore is defined as  $L = L_c + 2^{7/6}\sigma$ , where  $L_c$  is the center-to-center distance of wall atoms at the ends of the pore, and  $\sigma$  is the LJ parameter for wall-fluid interactions. The width of the pore is similarly defined as  $h = h_c - 2^{7/6}\sigma$ .

We use mechanical definitions of the pore size, which account for the excluded volume of the wall particles according to where the pairwise force goes to zero, at  $2^{1/6}\sigma$ . An alternative is a statistical definition based on, for example, the theory of Weeks, Chandler, and Andersen.<sup>53</sup> In this context the difference between the mechanical and statistical definition is irrelevant, so we opt for the simpler mechanical definition.

#### 2.4.5 Simulation Details

We study flows in two different geometries: Poiseuille flow and flow through a porous wall. The simulation geometry for flow through a porous wall is illustrated in Figures 2.2 and 2.4b. The simulations are periodic in both dimensions. Poiseuille flow is flow between two parallel infinite walls (Figure 2.4a), and the simulations are only periodic in the direction of flow. The wall and fluid atoms are identical. We make the wall-fluid interaction purely repulsive by cutting the force off where it goes to zero, at  $2^{1/6}\sigma$ .<sup>53</sup> The wall atoms are fixed in space during the simulations.

The simulations are composed of three parts,  $10\tau$  of equilibration time,  $1000\tau$  of stabilization time, and  $1000\tau$  of data collection, with  $\tau \equiv \sqrt{m\sigma^2/\epsilon}$ . The time step is  $0.001\tau$ . All simulations are at constant number, volume, and temperature (NVT). We use a Nosé-Hoover thermostat with a  $0.1\tau$  damping time.<sup>46,47</sup> The thermostat is profile-unbiased and uses boxes that contain an average of 8 atoms (Figure 2.1).<sup>27</sup> We choose the size of the boxes to be large enough so that the COM velocity in the box is not dominated by individual atoms entering or leaving the box, but small enough so that a realistic flow profile can develop. With the pump method, the thermostat does not correct for the flow profile, because this is how the method is usually implemented.<sup>5,6,9,54–56</sup> The bulk density of fluid atoms is  $\rho_0 = 0.8\sigma^{-2}$ , the temperature is  $T = 2\epsilon/k_B$ , and the flow is in the  $x$ -direction. The wall atoms are separated by  $1\sigma$ . For Poiseuille flow, the simulation box is  $200 \times 60\sigma^2$ . The Poiseuille simulations presented in Section 2.9 use a simulation box that is  $200 \times 30\sigma^2$ . For the porous wall flow simulations, the simulation box is  $400 \times 60\sigma^2$  with some exceptions presented in Section 2.4.6.

For each set of parameters, we run 96 simulations. Appendix B describes the software and computational resources used.

#### 2.4.6 Convergence with Respect to Box Length

We must verify that the reservoirs on each side of the channel are large enough. Here, “large enough” means that diffusive motion should dissipate the high velocity of a particle leaving the

$L_c (\sigma)$	$h_c (\sigma)$	Time to reach steady state ( $\tau$ )	$L_x (\sigma)$
70	6	3000	600
70	10	1000	500
70	20	1000	500
80	16	1000	600
90	10	1000	600
90	20	1000	600

Table 2.1: Exceptions to the general procedure presented for especially long and/or narrow channels.

channel before the particle wraps through the periodic boundary and enters the channel again. We run simulations at varying box lengths and look for convergence of the effective viscosity. This is not straight-forward, because longer boxes require longer time to reach steady state. In a larger simulation, the density profile is longer ranged and requires more time to develop. One must increase the box length and simultaneously ensure that the simulations are still at steady state.

Some of the especially long and narrow channels require longer simulation boxes and longer time to reach steady state (Table 2.1).

## 2.5 Nonequilibrium Definition of Temperature

The GD method requires that one has a self consistent definition of the temperature. This definition requires that the local velocity in the fluid separates into a streaming part and a fluctuating thermal part (eq. 2.2). In Figure 2.3, we show that these two requirements hold over many decades in the Gaussian velocity distribution.

## 2.6 Comparison of Hydrodynamic Profiles

To validate GD, we compare it to the pump method using two different 2d systems: planar Poiseuille flow and flow through a porous wall (Figure 2.4a,b). We first illustrate some of the similarities and differences between GD and the pump method. In the context of nonequilibrium statistical mechanics, GD is a constant current protocol, or a Norton ensemble method.<sup>26</sup> The pump

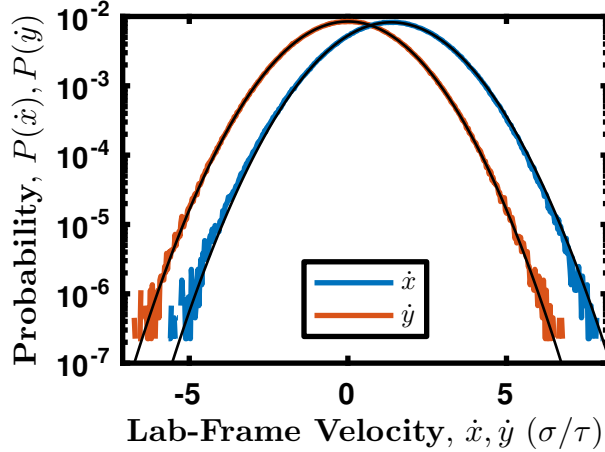


Figure 2.3: The probability distributions of the lab-frame velocity in the  $x$ - and  $y$ -directions for a 2d LJ system at steady state in GD. The flow is in the  $x$ -direction. Both components are Boltzmann distributed (black) over several decades and the  $x$ -component is centered at the streaming velocity. This illustrates the self-consistent separation between the thermal and streaming velocities used to define the temperature (eq. 2.2).

method is its conjugate Thévenin ensemble, or fixed gradient method. That is, in GD one applies a fixed current and measures the resulting pressure drop, while in the pump method, one applies a pressure drop and measures the resulting current. Both methods allow all other relevant fields to develop naturally. However, the spatial discontinuity in the pump method's force field leads to some differences in these fields for the two methods (Figure 2.4). The effects of the discontinuity can be emphasized by plotting the relevant spatial profiles across the periodic boundary, where the pump region lies (Figure 2.5). Since they are conjugate methods, one expects that at the same mass flux, they will both predict the same pressure drop, and vice versa. At the same mass flux (Figure 2.4c,d), the pressure profiles are clearly different (Figure 2.4e,f). This is simply because the pump method and GD simulate different physical situations. When the pressure profiles are adjusted according to eq. 2.32, they are nearly identical (Section 2.7 and Figure 2.6a). The density and temperature profiles, on the other hand, are different (Figures 2.4g–j). It is not surprising that the differences are largest in the pump region, but perhaps unexpectedly, the differences extend throughout the entire bulk fluid. The system is heated in the pump region, and this heat influences the entire system (Figure 2.5).

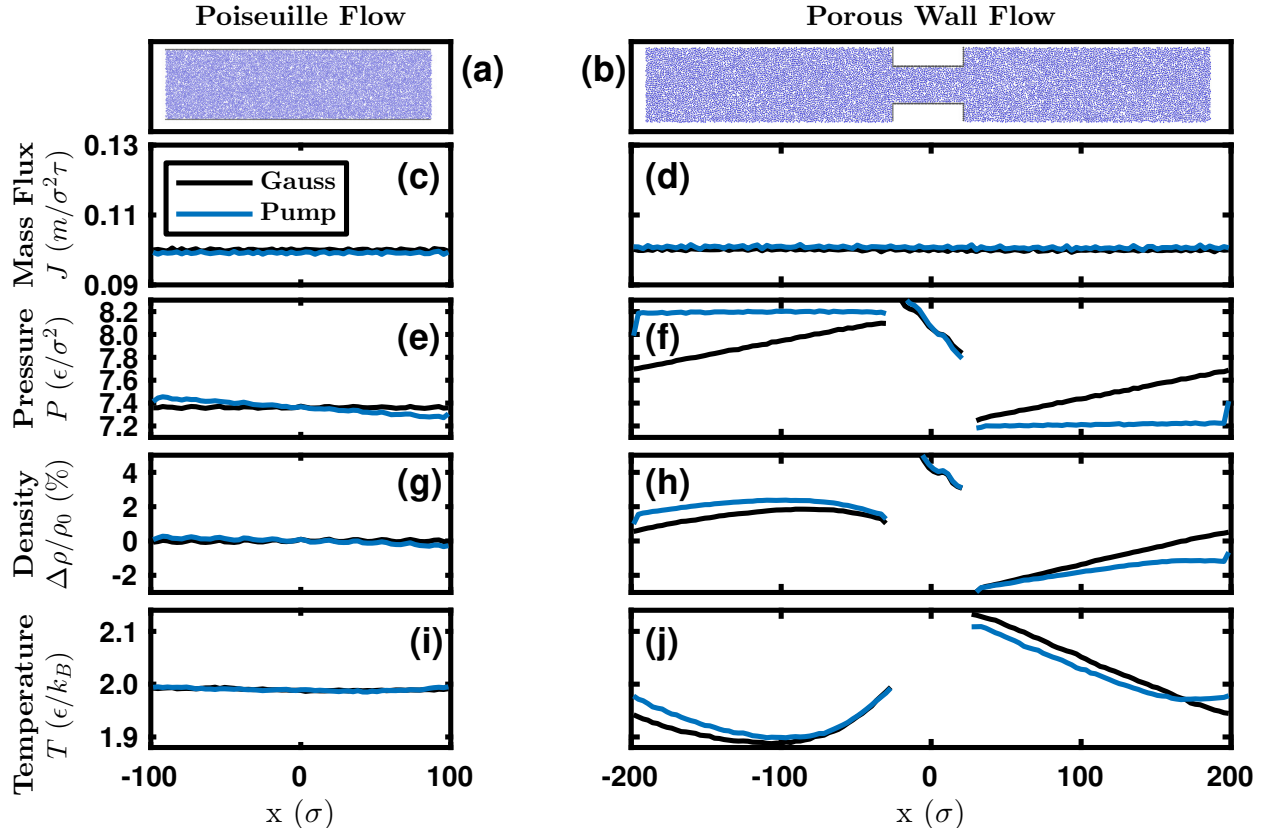


Figure 2.4: A comparison of the pump method (blue lines) and GD (black lines) in two different geometries, planar Poiseuille flow (left), and flow through a porous wall (right), both in 2d. Panels (a) and (b) show snapshots from the simulations. The wall atoms are black and the fluid atoms are blue. The flow is in the  $+x$ -direction. We compare the flux (c,d) and the intensive thermodynamic variables, pressure (e,f), density (g,h), and temperature (i,j). The simulations are all at the same mass flux, and are at steady state (c,d). The pressure profiles (e,f) must be adjusted according to the discussion in Section 2.7 before being used to compute permeabilities. For porous wall flow, the pump region introduces a discontinuity that has lasting effects for the density (g,h) and temperature (i,j) far from the pump region. The densities (g,h) are normalized by the bulk fluid density,  $\rho_0$ , with  $\Delta\rho \equiv \rho - \rho_0$ .

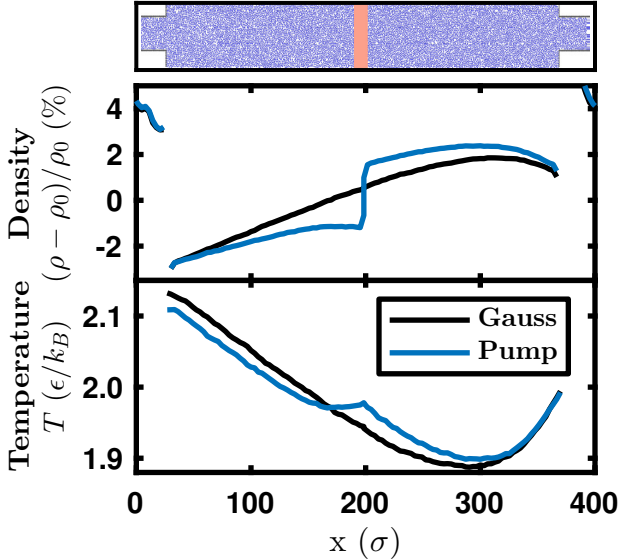


Figure 2.5: The same density and temperature profile for the simulation shown in Figure 2.4h,j. The boundaries are periodically shifted so that the pump region (orange) is centered in the figure at  $x = 200 \sigma$ , as shown in the simulation snapshot at the top. The effects of the pump region are clearly visible throughout the entire simulation, even though the pump region is almost two orders of magnitude smaller than the simulation box length. The pore and its periodic replica are centered at  $x = 0 \sigma$  and  $x = 400 \sigma$ .

## 2.7 Pressure Profile Adjustment and Pressure Drops

To make comparisons between the pressure profiles computed from GD and the pump method, one must make an adjustment to the GD pressure profile, as described here. Consider the hydrodynamic momentum conservation equations for GD and the pump method. In the pump method, far enough from the pump region, we have a fluid moving under a constant applied pressure gradient,  $\nabla P_{\text{app}}(\mathbf{r})$ . The momentum conservation equation is<sup>26</sup>

$$\rho(\mathbf{r}, t) \frac{D\mathbf{u}(\mathbf{r}, t)}{Dt} + \nabla \cdot \mathbf{P}(\mathbf{r}, t) = -\nabla P_{\text{app}}(\mathbf{r}), \quad (2.30)$$

where  $\mathbf{P}$  is the pressure tensor and  $\frac{D}{Dt}$  is a total time derivative. In GD, the fluid moves under an external applied acceleration,  $-\mathbf{I}(t)$ , which is uniform in space and fluctuating in time. The momentum conservation equation is<sup>26</sup>

$$\rho(\mathbf{r}, t) \frac{D\mathbf{u}(\mathbf{r}, t)}{Dt} + \nabla \cdot \mathbf{P}(\mathbf{r}, t) = -\rho(\mathbf{r}, t)\mathbf{I}(t). \quad (2.31)$$

Equations 2.30 and 2.31 are the equivalents of Newton's law for a fluid, where the terms on the right hand side of the equality are the external forces and  $\nabla \cdot \mathbf{P}$  arises from the internal forces. The pressure profile measured in a simulation is the sum of an internal pressure and an applied pressure  $P(\mathbf{r}) = P_{\text{int}}(\mathbf{r}) + P_{\text{app}}(\mathbf{r})$ , where  $P_{\text{int}} = \text{Tr}(\mathbf{P})/d$  and  $d$  is the dimensionality of the system. The full hydrodynamic description of a system is contained in  $\rho(\mathbf{r}, t)$ ,  $u(\mathbf{r}, t)$ , and  $\mathbf{P}(\mathbf{r}, t)$ , so when the hydrodynamics are identical,  $P_{\text{int}}(\mathbf{r})$  is the same for GD and the pump method. But the applied pressure,  $P_{\text{app}}(\mathbf{r})$ , is zero in GD while in the pump method it is nonzero. Thus, the pressure profiles measured with GD and the pump method will be different, even when the hydrodynamics are the same. To compare the pressure profiles generated by the two methods, we require that identical hydrodynamic situations yield the same pressure profile. We achieve this by adding an adjustment term  $P_{\text{adj}}(\mathbf{r})$  to the GD pressure profile. We enforce that the hydrodynamics are the same by setting the left hand sides of eqs. 2.30 and 2.31 equal,

$$\nabla P_{\text{app}}(\mathbf{r}, t) = \rho(\mathbf{r}, t)\mathbf{I}(t). \quad (2.32)$$

The pressure adjustment comes from the requirement  $\nabla P_{\text{adj}} = \nabla P_{\text{app}}$  in eq. 2.32. We emphasize that this is an adjustment applied to the data generated in a GD simulation, not a pressure that is applied during a GD simulation. To find the pressure profile adjustment, we integrate eq. 2.32

$$P_{\text{adj}}(x, t) - P_{\text{adj}}(-L_x/2, t) = I_x(t) \int_{-L_x/2}^x \rho(x', t) dx', \quad (2.33)$$

where we have set  $\mathbf{I} = (I_x, 0, 0)$ , as is the case in our simulations. Since only gradients in pressure drive flow, we can set  $P_{\text{adj}}(-L_x/2, t) = 0$ . This translation to an absolute pressure is a choice of gauge. The result is

$$P_{\text{adj}}(x, t) = I_x(t) \int_{-L_x/2}^x \rho(x', t) dx', \quad (2.34)$$

where  $L_x$  is the length of the simulation box in the  $x$ -direction. The lower bound of the integral,  $-L_x/2$ , is the left edge of the simulation box. Since the box is periodic in the  $x$ -direction, the choice of this lower bound is arbitrary. When the density is approximately constant, as it is in our

simulations (Figure 2.4g,h), the pressure adjustment can be approximated as

$$P_{\text{adj}}(x, t) \approx I_x(t)\rho(x, t)x. \quad (2.35)$$

Note that when the flow is in the  $+x$ -direction,  $I_x(t)$  is negative on average, but the applied acceleration,  $-I_x(t)$ , is in the positive direction. Equation 2.35 is equivalent to the hydrostatic pressure generated by a gravitational field,  $-\mathbf{I}$ . This hydrostatic pressure should be removed from the calculated pressure because the pressure tensor only depends on internal forces. Previous work has not applied this adjustment, resulting in erroneous reports of disagreement between the pump method and other methods.<sup>5,6</sup>

This discussion presupposes that the hydrodynamics in the pump method and GD can be made equivalent. In a simulation large enough to equilibrate the local pressure jump and sudden gradients in other intensive thermodynamic variables that the pump method generates, GD and the pump method would generate equivalent hydrodynamics. But for finite simulations, even very large ones, we find that this does not hold (Figure 2.5).

We compute the pressure profile in the simulations using the zeroth order Irving-Kirkwood approximation (IK1)<sup>57,58</sup> and add the pressure adjustment (eq. 2.35) to it,

$$P(x) = P_{\text{IK1}}(x) + P_{\text{adj}}(x). \quad (2.36)$$

We discard the pressure profile within  $19\sigma$  of the wall atoms because the IK1 method is only valid in homogeneous fluids (Figure 2.6b).<sup>57,58</sup> Used in this way, the IK1 method is convenient and accurate, but not unique.<sup>57–61</sup> We use the pressure profile to compute the pressure drop across a porous wall or membrane,  $\Delta P$ , which we use to calculate the permeability or effective viscosity of the pore (eq. 3.3 or 2.39). The pressure drop is, however, a macroscopic quantity that has no unique microscopic definition in terms of the pressure profile. We compute  $\Delta P$  by extrapolating the pressure profile in the bulk fluid to the edges of the pore (Figure 2.6b). This definition of  $\Delta P$  gives good agreement between GD and the pump method at low Re.

The pressure profiles shown in Figures 2.4e,f and 2.6 are time averaged. The time average of

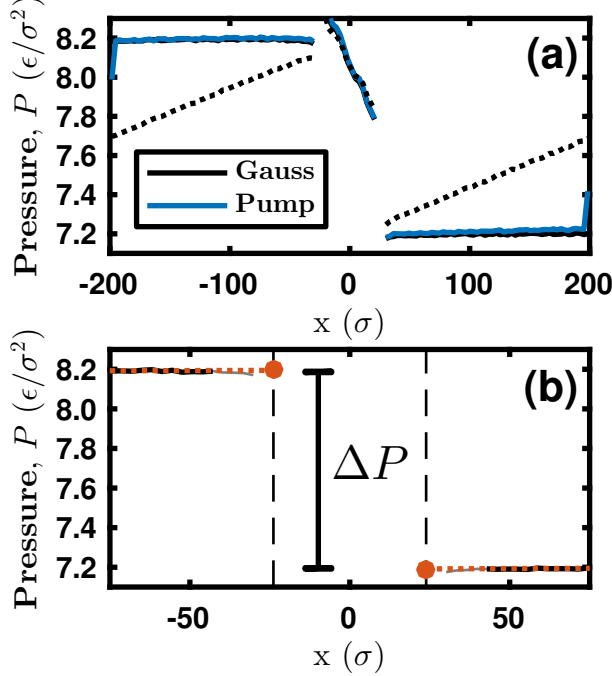


Figure 2.6: (a) The unadjusted GD pressure profile,  $P_{\text{IK1}}(x)$  (dotted black), the adjusted GD pressure profile,  $P_{\text{IK1}}(x) + P_{\text{adj}}(x)$  (solid black), and the pump method pressure profile,  $P_{\text{IK1}}(x)$  (blue), from simulations of flow through a porous wall. (b) The adjusted GD pressure profile for flow through a porous wall (black and gray). To compute the pressure drop, we fit the pressure profile on each side of the pore to a line (orange), and extrapolate that line to the edge of the pore (dashed black, see text). For the purposes of fitting, the pressure profile within  $19 \sigma$  of the wall is discarded (gray). The pressure drop,  $\Delta P$ , is then computed as shown by the annotation.

eq. 2.35 is

$$\overline{P_{\text{adj}}(x, t)} \approx -\overline{I_x(t)\rho(x, t)}x, \quad (2.37)$$

where an overbar denotes a time average. Here, we use the approximate eq. 2.35 for simplicity, but all the following results easily generalize to eq. 2.34. In principle the time dependence of  $I_x(t)$  does not decouple from the time dependence of  $\rho(x, t)$ , but in practice fluids at high densities are incompressible, so that the fluctuations of  $\rho(x, t)$  are small. So, we can make the approximation

$$\overline{P_{\text{adj}}(x, t)} \approx -\overline{I_x(t)} \cdot \overline{\rho(x, t)}x, \quad (2.38)$$

which can simplify simulation data output and save storage space. Using eq. 2.37 would require either the output of  $I_x(t)$  and  $\rho(x, t)$  at every sample time step or the premeditated on-the-fly

computation of  $\overline{I_x(t)\rho(x,t)}$ . Alternatively, eq. 2.38 only requires the output of a single time-averaged profile  $\overline{\rho(x,t)}$ , and the scalar time-average  $\overline{I_x(t)}$ .

## 2.8 Effective Viscosity

To compare the GD and pump methods in a wider range of channel geometries, we draw on the Hagen-Poiseuille (HP) law from hydrodynamics to calculate an effective viscosity,  $\eta_{\text{eff}}$ ,

$$\eta_{\text{eff}} = \frac{h^2 \rho_0 \Delta P}{12 L J}, \quad (2.39)$$

which relates the mass flux (Section 2.4.2), to the pressure drop applied across a channel of length  $L$  and diameter  $h$  (Figure 2.7a). Here, we have simplified the notation of Section 2.4.2 so that  $J = J_{\text{tot},x}$  is the total mass flux in the  $x$  direction. We certainly do not expect the HP law to be quantitative on these length scales, but merely use it as a practical means to discuss the relationship between the current and the pressure drop for channels of various geometries in a consistent way (Figure 2.7c). The Norton and Thévenin ensembles should give similar results for the effective viscosity  $\eta_{\text{eff}}$ , regardless of the fundamental inaccuracy of the HP law (Appendix C).

We compare GD and the pump method over a range of  $\text{Re}$ , computed as described in Section 2.4.3. The effective viscosity (eq. 2.39) computed using GD compares well with that computed from the pump method, particularly at low  $\text{Re}$  (Figure 2.7d). At larger  $\text{Re}$  ( $\text{Re} > 5$ ) there is more disagreement. It would be informative to simulate higher  $\text{Re}$  and narrower channels, but these regimes take a prohibitive amount of computational time to reach steady state (Section 2.4.6). Some, but not all, of the disagreement at higher  $\text{Re}$  is due to the thermostat conventionally used in the pump method, which is not Galilean-invariant.<sup>5–7</sup> To correct for this, we have amended the original pump method to include a profile-unbiased thermostat. This increases the agreement between the two methods at higher  $\text{Re}$ , but it does not fully account for the discrepancies observed (Figure 2.8). Note that GD consistently averages more quickly than the pump method, when all other simulation details are the same (Figure 2.8).

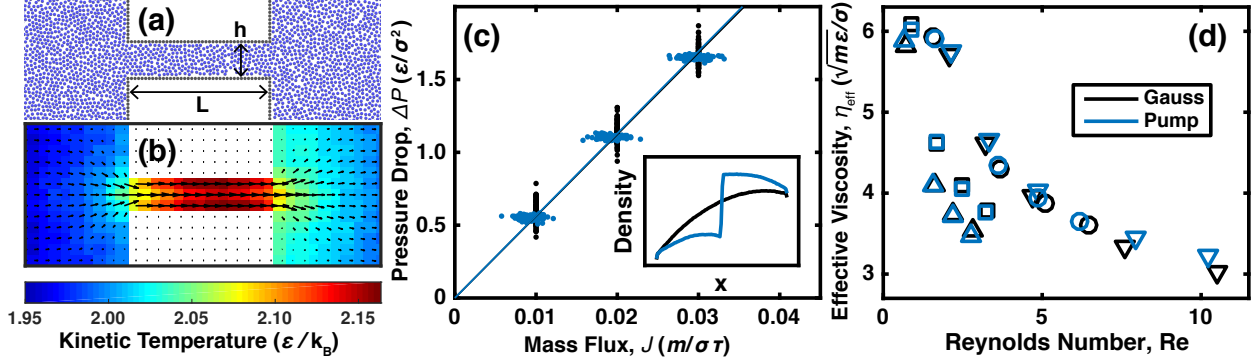


Figure 2.7: (a) A closeup of a snapshot from a 2d LJ simulation evolving under GD, including variables for the length ( $L$ ) and diameter ( $h$ ) of the channel. (b) The steady-state kinetic temperature (color) and velocity field (vectors),  $\mathbf{u}(\mathbf{r})$ , averaged over time at  $Re = 3$ . Hydrodynamic variables, like  $\mathbf{u}(\mathbf{r})$ , and associated gradients in density, temperature, and pressure, develop naturally under the imposed constraints. (c) The pressure drop as a function of the mass flux,  $J$ , for both GD and the pump method in 2d LJ simulations at various flow rates, with 96 trials at each flow rate. The slope of these data determines the effective viscosity,  $\eta_{\text{eff}}$  (eq. 2.39). Panel (d) compares  $\eta_{\text{eff}}$  for the two methods at various  $L$  and  $h$ , plotted as a function of  $Re$  at maximum  $J$ . The symbol shape indicates the diameter ( $h$ ) of the channel:  $\triangle$  ( $h = 18 \sigma$ ),  $\square$  ( $h = 14 \sigma$ ),  $\circ$  ( $h = 8 \sigma$ ),  $\nabla$  ( $h = 4 \sigma$ ). The computed  $\eta_{\text{eff}}$  of the two methods match well at low  $Re$ , but show increasing differences for narrow channels ( $\nabla$ ) as  $Re$  increases.

## 2.9 Slip Length

Continuum hydrodynamics cannot be trusted on atomistic length scales, but here we use it on systems large enough that a continuum approximation should be accurate. In hydrodynamic models, the microscopic interactions between the fluid and the walls of the system give rise to boundary conditions. In ideal hydrodynamics, the velocity of the fluid goes to zero at the fluid-solid boundary. This is the so-called no-slip boundary condition on the velocity. Figure 2.9a shows that GD generates the parabolic velocity profile that continuum hydrodynamics predicts, but the no-slip boundary condition is not satisfied. The deviation from no-slip behavior is quantified by the size of the slip length,  $L_s$ , as defined by Kannam et al.<sup>35</sup> and illustrated in Figure 2.9a.

In CNTs, water passage rates have been observed in both simulations<sup>12,32–37</sup> and experiments<sup>36,62–65</sup> that are much faster than the no-slip Hagen-Poiseuille predictions. This is thought to be the result of almost frictionless flow, which gives rise to very large slip lengths. However, estimates of the slip length and the flow enhancement vary by several orders of magnitude among

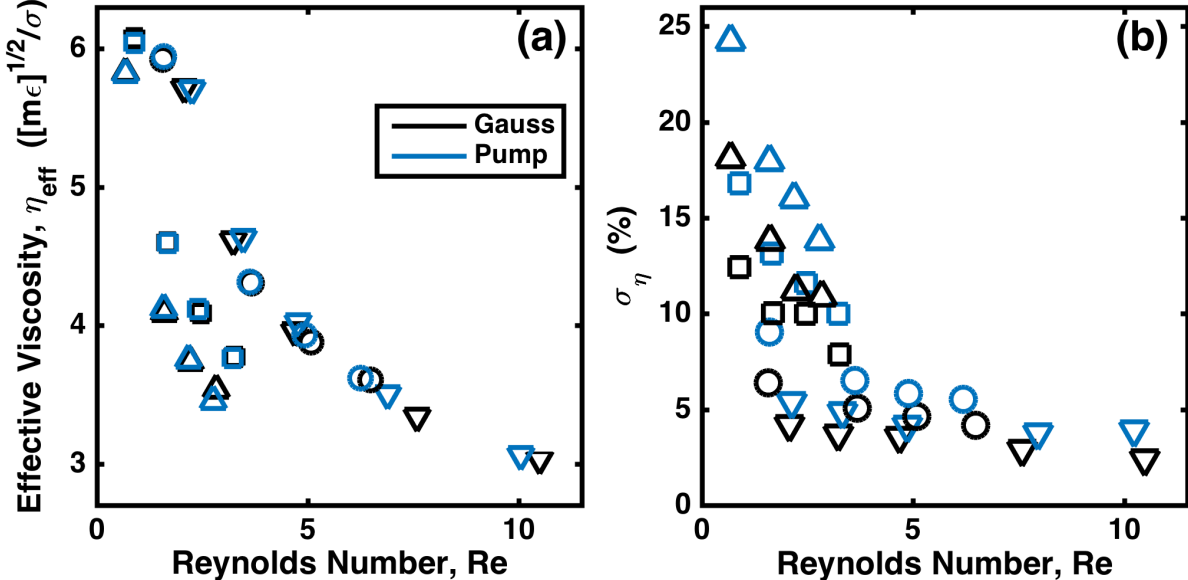


Figure 2.8: Panel (a) shows the effective viscosity calculated with the pump method modified to use a profile-unbiased thermostat. The agreement between the two methods is better at  $Re > 5$  than in Figure 2.7d, but there is still disagreement, especially for the narrowest channel ( $\nabla$ ). Panel (b) shows the relative error  $\sigma_\eta$  on the values of the effective viscosity plotted in Figure 2.7d. For a given channel diameter (symbol shape), GD always has smaller error than the pump method. The symbols used here correspond to channel diameter in the same way as described in Figure 2.7d.

both experiment and simulation.<sup>35</sup> The disagreement of simulation results is, at least in part, likely due to the wide variety of water models and surface-water potentials used, as well as the rigidity of the surface.<sup>31–33,66–70</sup> Another important aspect is the type of thermostat used in the simulations, which can affect the measured slip length.<sup>35,70,71</sup> Here, we use the simple 2d LJ fluid in Poiseuille flow as a test system to study the effects of wall rigidity and thermostating. When the walls are rigid, the system can only be thermostatted through the fluid. When the walls are flexible, however, either the walls or the fluid can be thermostatted.

In the rigid wall simulations, the wall atoms are fixed in space. In the flexible wall simulations, the wall atoms are harmonically bound to their initial position,  $\mathbf{r}_0$ , by the potential  $U(\mathbf{r}) = K(\mathbf{r} - \mathbf{r}_0)^2/2$ , with  $K = 25 \epsilon/\sigma^2$ . This value of  $K$  is large enough to prevent fluid atoms from penetrating the wall, but small enough to allow significant energy transfer between the wall and the fluid. We place an extra layer of fixed wall atoms behind the harmonic ones to stop the

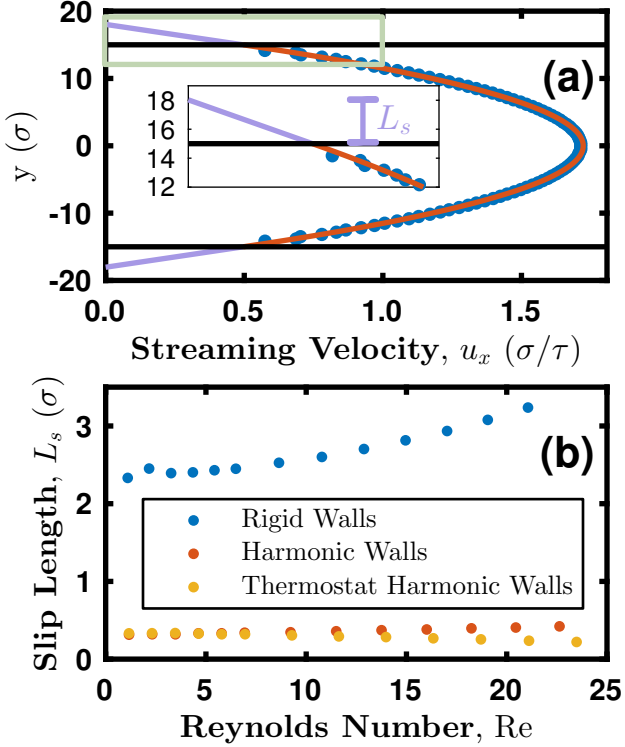


Figure 2.9: The slip length,  $L_s$ , from GD simulations of a 2d LJ fluid in steady-state planar Poiseuille flow. (a) The  $x$ -component of the velocity profile along  $y$ ,  $u_x(y)$  (blue), is fit to a parabola (red). We take a linear extrapolation of the parabolic fit to the vertical intercept,  $u_x = 0$  (purple).  $L_s$  is the distance between the edge of the pipe (black) and the vertical intercept. The inset shows a close-up of the region in the light green box. (b)  $L_s$  is an order of magnitude larger with rigid walls (blue) than with flexible walls (red and yellow). When the walls are flexible, we thermostat the system through either the walls (yellow) or the fluid (red), but not both.

few fluid atoms that do penetrate the wall. We also place an extra layer of atoms behind the rigid wall, for consistency with the flexible walls. We find that  $L_s$  is an order of magnitude larger on rigid walls (Figure 2.9b). This is because the flexible walls can absorb kinetic energy from the fluid, while the rigid walls cannot. With flexible walls,  $L_s$  is smaller than the radius of an atom, so the flow is effectively no-slip. We also measure  $L_s$  as a function of the Reynolds number,

$$\text{Re} = \frac{u_{\max} d \rho_0}{\eta} \quad (2.40)$$

where  $u_{\max}$  is the maximum velocity in the flow,  $d = 30 \sigma$  is the distance between the walls,  $\rho_0 = 0.8 \sigma^{-2}$  is the bulk fluid density, and  $\eta \approx 2.2 \epsilon \tau / \sigma$  is the bulk viscosity measured at equilibrium using the Green-Kubo relation.<sup>3</sup> We find no evidence of the divergence of  $\eta$  that others have reported

for the diffusion constant in 2d.<sup>26,50–52</sup> We tune Re by increasing the flux through the channel, thereby increasing  $u_{\max}$ . For reference,  $\text{Re} = 25$  corresponds to a mass flux of about  $J = 1 \text{ m}/\sigma\tau$  and a shear rate of about  $\dot{\gamma} = 0.15 \tau^{-1}$ . When the walls are flexible, we thermostat the system through either the fluid or the walls. When the fluid is thermostatted,  $L_s$  increases as a function of Re (Figure 2.9b), a trend that has been observed before in simulations.<sup>35,72</sup> When the wall atoms are thermostatted instead of the fluid,  $L_s$  changes only slightly, but the qualitative trend is reversed at high Re (Figure 2.9b). The slip length averages very slowly, especially in nonequilibrium simulations,<sup>31</sup> so this discrepancy may not be statistically significant, but would be an interesting topic for future study. Both the wall rigidity and application of the chosen thermostat could be a factor in the large scatter of simulation and experimental slip lengths in CNTs.<sup>35</sup>

## 2.10 Conclusion

In this Chapter, we describe a simulation method for atomistic systems under flow that is firmly rooted in constraint dynamics. We show that GD is capable of satisfying expectations for velocity distributions from statistical mechanics, and, when the atomic degrees of freedom can be sensibly coarse-grained into a continuum description, reproduces results consistent with hydrodynamics. In the low Re limit studied here, GD performs similarly when compared to the closely related pump method. But from a practical perspective, simulations using GD consistently yield smaller standard errors for both permeabilities and effective viscosities when all other variables are the same. It is not at all obvious that the methods studied here will give similar results for other observables, particularly at high Re ( $\text{Re} > 10$ ). Indeed, GD always dissipates less heat than the pump method for the same mass flux. Further, the nonequilibrium spatial distributions of intensive thermodynamic variables, like temperature and density, can be different between these two methods. These effects are likely due to heating at the discontinuity in the applied force used in the pump method. While the focus in this Chapter was on mass transport, other transport behaviors, like heat transport, might be significantly different between these two methods. This also calls into question the assumption of local equilibrium.<sup>25,26</sup> These artifacts in the pump method

may make GD more accurate at high Re and for other observables more sensitive to heat flux.

As far as hydrodynamic quantities are concerned, we find that the slip length can vary by an order of magnitude if the solid surface in contact with the fluid is rigid or if it is flexible. This observation connects to controversies in the literature about the slip length of water in CNTs and calls for further systematic investigation, though we do not endorse the concept of a slip length for single-file water as being even conceptually accurate. We explore this further in Chapter 3.7.

## Bibliography

- [1] Strong, S. E.; Eaves, J. D. Atomistic hydrodynamics and the dynamical hydrophobic effect in porous graphene. *J. Phys. Chem. Lett.*, 7(10):1907–1912, **2016**.
- [2] Strong, S. E.; Eaves, J. D. The dynamics of water in porous two-dimensional crystals. *J. Phys. Chem. B*, 121(1):189–207, **2017**.
- [3] Frenkel, D.; Smit, B. *Understanding Molecular Simulation: From Algorithms to Applications*. Academic Press, San Diego, 2<sup>nd</sup> edition, **2001**.
- [4] Bird, R. B.; Stewart, W. E.; Lightfoot, E. N. *Transport Phenomena*. John Wiley & Sons, Inc., New York, 2<sup>nd</sup> edition, **2006**.
- [5] Zhu, F.; Tajkhorshid, E.; Schulten, K. Pressure-induced water transport in membrane channels studied by molecular dynamics. *Biophys. J.*, 83(1):154–160, **2002**.
- [6] Huang, C.; Choi, P. Y. K.; Kostiuk, L. W. A method for creating a non-equilibrium NT(P<sub>1</sub>–P<sub>2</sub>) ensemble in molecular dynamics simulation. *Phys. Chem. Chem. Phys.*, 13(46):20750, **2011**.
- [7] Frentrup, H.; Avendaño, C.; Horsch, M.; Salih, A.; Müller, E. A. Transport diffusivities of fluids in nanopores by non-equilibrium molecular dynamics simulation. *Mol. Simulat.*, 38(7):540–553, **2012**.
- [8] Takaba, H.; Onumata, Y.; Nakao, S.-I. Molecular simulation of pressure-driven fluid flow in nanoporous membranes. *J. Chem. Phys.*, 127(5):054703, **2007**.
- [9] Huang, C.; Nandakumar, K.; Choi, P. Y. K.; Kostiuk, L. W. Molecular dynamics simulation of a pressure-driven liquid transport process in a cylindrical nanopore using two self-adjusting plates. *J. Chem. Phys.*, 124(23):234701, **2006**.
- [10] Müller-Plathe, F. A simple nonequilibrium molecular dynamics method for calculating the thermal conductivity. *J. Chem. Phys.*, 106(14):6082–6085, **1997**.
- [11] Hummer, G.; Rasaiah, J. C.; Noworyta, J. P. Water conduction through the hydrophobic channel of a carbon nanotube. *Nature*, 414(6860):188–190, **2001**.

- [12] Kalra, A.; Garde, S.; Hummer, G. Osmotic water transport through carbon nanotube membranes. *Proc. Nat. Acad. Sci. U. S. A.*, 100(18):10175–10180, **2003**.
- [13] Corry, B. Designing carbon nanotube membranes for efficient water desalination. *J. Phys. Chem. B*, 112(5):1427–1434, **2008**.
- [14] Suk, M. E.; Aluru, N. R. Water transport through ultrathin graphene. *J. Phys. Chem. Lett.*, 1(10):1590–1594, **2010**.
- [15] Cohen-Tanugi, D.; Grossman, J. C. Water desalination across nanoporous graphene. *Nano Lett.*, 12(7):3602–3608, **2012**.
- [16] Wang, E. N.; Karnik, R. Water desalination: Graphene cleans up water. *Nat. Nanotechnol.*, 7(9):552–554, **2012**.
- [17] Konatham, D.; Yu, J.; Ho, T. A.; Striolo, A. Simulation insights for graphene-based water desalination membranes. *Langmuir*, 29(38):11884–11897, **2013**.
- [18] Xu, L.; Tsotsis, T. T.; Sahimi, M. Nonequilibrium molecular dynamics simulation of transport and separation of gases in carbon nanopores. I. Basic results. *J. Chem. Phys.*, 111(7):3252–3264, **1999**.
- [19] Vieira-Linhares, A. M.; Seaton, N. A. Non-equilibrium molecular dynamics simulation of gas separation in a microporous carbon membrane. *Chem. Eng. Sci.*, 58(18):4129–4136, **2003**.
- [20] Skouidas, A. I. Molecular dynamics simulations of gas diffusion in metal-organic frameworks: Argon in CuBTC. *J. Am. Chem. Soc.*, 126(5):1356–1357, **2004**.
- [21] Koenig, S. P.; Wang, L.; Pellegrino, J.; Bunch, J. S. Selective molecular sieving through porous graphene. *Nat. Nanotechnol.*, 7(11):728–732, **2012**.
- [22] Schrier, J. Helium separation using porous graphene membranes. *J. Phys. Chem. Lett.*, 1(15):2284–2287, **2010**.
- [23] Nair, R. R.; Wu, H. A.; Jayaram, P. N.; Grigorieva, I. V.; Geim, A. K. Unimpeded permeation of water through helium-leak-tight graphene-based membranes. *Science*, 335(6067):442–444, **2012**.
- [24] Nosé, S. A molecular dynamics method for simulations in the canonical ensemble. *Mol. Phys.*, 52(2):255–268, **1984**.
- [25] Evans, D. J.; Morriss, G. P. Non-Newtonian molecular dynamics. *Comput. Phys. Rep.*, 1(6):297–343, **1984**.
- [26] Evans, D. J.; Morriss, G. *Statistical Mechanics of Nonequilibrium Liquids*. Cambridge University Press, Cambridge, 2<sup>nd</sup> edition, **2008**.
- [27] Evans, D. J.; Morriss, G. P. Shear thickening and turbulence in simple fluids. *Phys. Rev. Lett.*, 56(20):2172–2175, **1986**.
- [28] Harvey, S. C.; Tan, R. K.-Z.; Cheatham, T. E. The flying ice cube: Velocity rescaling in molecular dynamics leads to violation of energy equipartition. *J. Comput. Chem.*, 19(7):726–740, **1998**.

- [29] Bernardi, S.; Todd, B. D.; Searles, D. J. Thermostating highly confined fluids. *J. Chem. Phys.*, 132(24):244706, **2010**.
- [30] Heyes, D. M.; Morriss, G. P.; Evans, D. J. Nonequilibrium molecular dynamics study of shear flow in soft disks. *J. Chem. Phys.*, 83(9):4760–4766, **1985**.
- [31] Kannam, S. K.; Todd, B. D.; Hansen, J. S.; Daivis, P. J. Slip length of water on graphene: Limitations of non-equilibrium molecular dynamics simulations. *J. Chem. Phys.*, 136(2):024705, **2012**.
- [32] Joseph, S.; Aluru, N. R. Why are carbon nanotubes fast transporters of water? *Nano Lett.*, 8(2):452–458, **2008**.
- [33] Liu, L.; Patey, G. N. Simulated conduction rates of water through a (6,6) carbon nanotube strongly depend on bulk properties of the model employed. *J. Chem. Phys.*, 144(18):184502, **2016**.
- [34] Thomas, J. A.; McGaughey, A. J. H. Reassessing fast water transport through carbon nanotubes. *Nano Lett.*, 8(9):2788–2793, **2008**.
- [35] Kannam, S. K.; Todd, B. D.; Hansen, J. S.; Daivis, P. J. How fast does water flow in carbon nanotubes? *J. Chem. Phys.*, 138(9):094701, **2013**.
- [36] Walther, J. H.; Ritos, K.; Cruz-Chu, E. R.; Megaridis, C. M.; Koumoutsakos, P. Barriers to superfast water transport in carbon nanotube membranes. *Nano Lett.*, 13(5):1910–1914, **2013**.
- [37] Falk, K.; Sedlmeier, F.; Joly, L.; Netz, R. R.; Bocquet, L. Molecular origin of fast water transport in carbon nanotube membranes: Superlubricity versus curvature dependent friction. *Nano Lett.*, 10(10):4067–4073, **2010**.
- [38] Evans, D. J.; Hoover, W. G.; Failor, B. H.; Moran, B.; Ladd, A. J. C. Nonequilibrium molecular dynamics via Gauss's principle of least constraint. *Phys. Rev. A*, 28(2):1016–1021, **1983**.
- [39] Hoover, W. G.; Ladd, A. J. C.; Moran, B. High-strain-rate plastic flow studied via nonequilibrium molecular dynamics. *Phys. Rev. Lett.*, 48(26):1818–1820, **1982**.
- [40] Evans, D. J. Computer “experiment” for nonlinear thermodynamics of Couette flow. *J. Chem. Phys.*, 78(6):3297–3302, **1983**.
- [41] Goldstein, H.; Poole, C. P., Jr.; Safko, J. L. *Classical Mechanics*. Pearson, San Francisco, 3<sup>rd</sup> edition, **2001**.
- [42] Cronström, C.; Raita, T. On nonholonomic systems and variational principles. *J. Math. Phys.*, 50(4):042901, **2009**.
- [43] Flannery, M. R. The elusive d'Alembert-Lagrange dynamics of nonholonomic systems. *Am. J. Phys.*, 79(9):932–944, **2011**.
- [44] Edberg, R.; Evans, D. J.; Morriss, G. P. Constrained molecular dynamics: Simulations of liquid alkanes with a new algorithm. *J. Chem. Phys.*, 84(12):6933–6939, **1986**.

- [45] Morriss, G. P.; Evans, D. J. A constraint algorithm for the computer simulation of complex molecular liquids. *Comput. Phys. Commun.*, 62(2–3):267–278, **1991**.
- [46] Nosé, S. A unified formulation of the constant temperature molecular dynamics methods. *J. Chem. Phys.*, 81(1):511–519, **1984**.
- [47] Hoover, W. G. Canonical dynamics: Equilibrium phase-space distributions. *Phys. Rev. A*, 31(3):1695–1697, **1985**.
- [48] Ying-Hua, Q.; Kun, L.; Wei-Yu, C.; Wei, S.; Qi-Yan, T.; Yun-Fei, C. Ion and water transport in charge-modified graphene nanopores. *Chinese Phys. B*, 24(10):108201, **2015**.
- [49] Zhu, F.; Tajkhorshid, E.; Schulten, K. Collective diffusion model for water permeation through microscopic channels. *Phys. Rev. Lett.*, 93(22):224501, **2004**.
- [50] Alder, B. J.; Wainwright, T. E. Velocity autocorrelations for hard spheres. *Phys. Rev. Lett.*, 18(23):988–990, **1967**.
- [51] Alder, B. J.; Wainwright, T. E. Decay of the velocity autocorrelation function. *Phys. Rev. A*, 1(1):18–21, **1970**.
- [52] Pomeau, Y.; Resibois, P. Time dependent correlation functions and mode-mode coupling theories. *Phys. Rep.*, 19(2):63–139, **1975**.
- [53] Weeks, J. D.; Chandler, D.; Andersen, H. C. Role of repulsive forces in determining the equilibrium structure of simple liquids. *J. Chem. Phys.*, 54(12):5237–5247, **1971**.
- [54] Zhu, F.; Tajkhorshid, E.; Schulten, K. Theory and simulation of water permeation in aquaporin-1. *Biophys. J.*, 86(1):50–57, **2004**.
- [55] Turgman-Cohen, S.; Araque, J. C.; Hoek, E. M. V.; Escobedo, F. A. Molecular dynamics of equilibrium and pressure-driven transport properties of water through LTA-type zeolites. *Langmuir*, 29(40):12389–12399, **2013**.
- [56] Docherty, S. Y.; Nicholls, W. D.; Borg, M. K.; Lockerby, D. A.; Reese, J. M. Boundary conditions for molecular dynamics simulations of water transport through nanotubes. *Proc. Inst. Mech. Eng. C*, 228(1):186–195, **2014**.
- [57] Irving, J. H.; Kirkwood, J. G. The statistical mechanical theory of transport processes. IV. The equations of hydrodynamics. *J. Chem. Phys.*, 18(6):817–829, **1950**.
- [58] Todd, B. D.; Evans, D. J.; Daivis, P. J. Pressure tensor for inhomogeneous fluids. *Phys. Rev. E*, 52(2):1627–1638, **1995**.
- [59] Hafskjold, B.; Ikeshoji, T. Microscopic pressure tensor for hard-sphere fluids. *Phys. Rev. E*, 66(1):011203, **2002**.
- [60] Heinz, H. Calculation of local and average pressure tensors in molecular simulations. *Mol. Simulat.*, 33(9–10):747–758, **2007**.
- [61] Zimmerman, J. A.; Webb, E. B., III; Hoyt, J. J.; Jones, R. E.; Klein, P. A.; Bammann, D. J. Calculation of stress in atomistic simulation. *Model. Simul. Mater. Sci. Eng.*, 12(4):S319, **2004**.

- [62] Majumder, M.; Chopra, N.; Andrews, R.; Hinds, B. J. Nanoscale hydrodynamics: Enhanced flow in carbon nanotubes. *Nature*, 438(7064):44–44, **2005**.
- [63] Holt, J. K.; Park, H. G.; Wang, Y.; Stadermann, M.; Artyukhin, A. B.; Grigoropoulos, C. P.; Noy, A.; Bakajin, O. Fast mass transport through sub-2-nanometer carbon nanotubes. *Science*, 312(5776):1034–1037, **2006**.
- [64] Whitby, M.; Cagnon, L.; Thanou, M.; Quirke, N. Enhanced fluid flow through nanoscale carbon pipes. *Nano Lett.*, 8(9):2632–2637, **2008**.
- [65] Sinha, S.; Rossi, M. P.; Mattia, D.; Gogotsi, Y.; Bau, H. H. Induction and measurement of minute flow rates through nanopipes. *Phys. Fluids*, 19(1):013603, **2007**.
- [66] Koplik, J.; Banavar, J. R.; Willemsen, J. F. Molecular dynamics of fluid flow at solid surfaces. *Phys. Fluids A.*, 1(5):781–794, **1989**.
- [67] Galea, T. M.; Attard, P. Molecular dynamics study of the effect of atomic roughness on the slip length at the fluid-solid boundary during shear flow. *Langmuir*, 20(8):3477–3482, **2004**.
- [68] Barrat, J.-L.; Bocquet, L. Large slip effect at a nonwetting fluid-solid interface. *Phys. Rev. Lett.*, 82(23):4671–4674, **1999**.
- [69] Cottin-Bizonne, C.; Barentin, C.; Charlaix, É.; Bocquet, L.; Barrat, J.-L. Dynamics of simple liquids at heterogeneous surfaces: Molecular-dynamics simulations and hydrodynamic description. *Eur. Phys. J. E*, 15(4):427–438, **2004**.
- [70] Sokhan, V. P.; Nicholson, D.; Quirke, N. Fluid flow in nanopores: Accurate boundary conditions for carbon nanotubes. *J. Chem. Phys.*, 117(18):8531–8539, **2002**.
- [71] Thomas, M.; Corry, B. Thermostat choice significantly influences water flow rates in molecular dynamics studies of carbon nanotubes. *Microfluid. Nanofluid.*, 18(1):41–47, **2014**.
- [72] Thompson, P. A.; Troian, S. M. A general boundary condition for liquid flow at solid surfaces. *Nature*, 389(6649):360–362, **1997**.
- [73] Hill, T. L. *An Introduction to Statistical Thermodynamics*. Dover Publications, Inc., New York, 2<sup>nd</sup> edition, **1986**.
- [74] Zwanzig, R. *Nonequilibrium Statistical Mechanics*. Oxford University Press, Oxford, **2001**.
- [75] Zimm, B. H. Dynamics of polymer molecules in dilute solution: Viscoelasticity, flow birefringence and dielectric loss. *J. Chem. Phys.*, 24(2):269–278, **1956**.
- [76] Bernstein, H. J.; Weisskopf, V. F. About liquids. *Am. J. Phys.*, 55(11):974–983, **1987**.
- [77] Bekker, H.; Dijkstra, E. J.; Renardus, M. K. R.; Berendsen, H. J. C. An efficient, box shape independent non-bonded force and virial algorithm for molecular dynamics. *Mol. Simulat.*, 14(3):137–151, **1995**.
- [78] Stone, J. *An Efficient Library for Parallel Ray Tracing and Animation*. Ph.D. thesis, Computer Science Department, University of Missouri-Rolla, **1998**.

- [79] Stone, J.; Gullingsrud, J.; Grayson, P.; Schulten, K. A system for interactive molecular dynamics simulation. In Hughes, J. F.; Séquin, C. H., eds., *2001 ACM Symposium on Interactive 3D Graphics*, pages 191–194. ACM SIGGRAPH, New York, **2001**.
- [80] Cheung, K. S.; Yip, S. Atomic-level stress in an inhomogeneous system. *J. Appl. Phys.*, 70(10):5688–5690, **1991**.
- [81] Saffman, P. G.; Delbrück, M. Brownian motion in biological membranes. *Proc. Nat. Acad. Sci. U. S. A.*, 72(8):3111–3113, **1975**.
- [82] Hazoglou, M. J.; Walther, V.; Dixit, P. D.; Dill, K. A. Communication: Maximum caliber is a general variational principle for nonequilibrium statistical mechanics. *J. Chem. Phys.*, 143(5):051104, **2015**.
- [83] Martyna, G. J.; Tobias, D. J.; Klein, M. L. Constant pressure molecular dynamics algorithms. *J. Chem. Phys.*, 101(5):4177–4189, **1994**.
- [84] E. A. Carter, G. C. Constrained reaction coordinate dynamics for the simulation of rare events. *Chem. Phys. Lett.*, 156(5):472–477, **1989**.
- [85] Ashurst, W. T.; Hoover, W. G. Dense-fluid shear viscosity via nonequilibrium molecular dynamics. *Phys. Rev. A*, 11(2):658–678, **1975**.
- [86] Groot, R. D.; Warren, P. B. Dissipative particle dynamics: Bridging the gap between atomistic and mesoscopic simulation. *J. Chem. Phys.*, 107(11):4423–4435, **1997**.
- [87] Koelman, J. M. V. A.; Hoogerbrugge, P. J. Dynamic simulations of hard-sphere suspensions under steady shear. *Europhys. Lett.*, 21(3):363, **1993**.
- [88] Plimpton, S. Fast parallel algorithms for short-range molecular dynamics. *J. Comput. Phys.*, 117(1):1–19, **1995**.
- [89] Onsager, L.; Machlup, S. Fluctuations and irreversible processes. *Phys. Rev.*, 91(6):1505–1512, **1953**.
- [90] Hardy, R. J. Formulas for determining local properties in molecular-dynamics simulations: Shock waves. *J. Chem. Phys.*, 76(1):622–628, **1982**.
- [91] Bonetto, F.; Lebowitz, J. L.; Rey-Bellet, L. Fourier’s law: A challenge for theorists. *arXiv*, math-ph/0002052, **2000**.
- [92] Thompson, A. P.; Plimpton, S. J.; Mattson, W. General formulation of pressure and stress tensor for arbitrary many-body interaction potentials under periodic boundary conditions. *J. Chem. Phys.*, 131(15):154107, **2009**.
- [93] Nosé, S.; Yonezawa, F. Isobaric–isothermal molecular dynamics study on the glass transition of a Lennard–Jones system. *Solid State Commun.*, 56(12):1005–1008, **1985**.
- [94] Nosé, S.; Yonezawa, F. Isothermal–isobaric computer simulations of melting and crystallization of a Lennard–Jones system. *J. Chem. Phys.*, 84(3):1803, **1986**.
- [95] York, D. Least-squares fitting of a straight line. *Can. J. Phys.*, 44(5):1079–1086, **1966**.

- [96] Heinbuch, U.; Fischer, J. Liquid flow in pores: Slip, no-slip, or multilayer sticking. *Phys. Rev. A*, 40(2):1144–1146, **1989**.
- [97] Branicio, P. S.; Srolovitz, D. J. Local stress calculation in simulations of multicomponent systems. *J. Comput. Phys.*, 228(22):8467–8479, **2009**.
- [98] Dewar, R. C. Maximum entropy production and the fluctuation theorem. *J. Phys. A.*, 38(21):L371–L381, **2005**.
- [99] Hoover, W. G.; Hoover, C. G.; Lutsko, J. F. Microscopic and macroscopic stress with gravitational and rotational forces. *Phys. Rev. E*, 79(3):036709, **2009**.
- [100] Hannon, L.; Lie, G. C.; Clementi, E. Molecular dynamics simulation of channel flow. *Phys. Lett. A.*, 119(4):174–177, **1986**.
- [101] Goldsmith, J.; Martens, C. C. Molecular dynamics simulation of salt rejection in model surface-modified nanopores. *J. Phys. Chem. Lett.*, 1(2):528–535, **2010**.
- [102] Xu, L.; Sahimi, M.; Tsotsis, T. T. Nonequilibrium molecular dynamics simulations of transport and separation of gas mixtures in nanoporous materials. *Phys. Rev. E*, 62(5):6942–6948, **2000**.
- [103] Ryckaert, J.-P.; Ciccotti, G.; Berendsen, H. J. C. Numerical integration of the cartesian equations of motion of a system with constraints: Molecular dynamics of n-alkanes. *J. Comput. Phys.*, 23(3):327–341, **1977**.
- [104] Clausius, R. On a mechanical theorem applicable to heat. *Philos. Mag.*, 40(265):122–127, **1870**.
- [105] Maxwell, J. C. On reciprocal figures, frames, and diagrams of forces. *Earth. Env. Sci. Trans. Roy. Soc. Edin.*, 26(01):1–40, **1870**.
- [106] Choi, Y.; Ree, T.; Ree, F. H. Phase diagram of a Lennard-Jones solid. *J. Chem. Phys.*, 99(12):9917, **1993**.
- [107] Martyna, G. J.; Tuckerman, M. E.; Tobias, D. J.; Klein, M. L. Explicit reversible integrators for extended systems dynamics. *Mol. Phys.*, 87(5):1117–1157, **1996**.
- [108] Heyes, D. M. Shear thinning and thickening of the Lennard-Jones liquid. A molecular dynamics study. *J. Chem. Soc. Faraday Trans. 2*, 82(9):1365, **1986**.
- [109] Heyes, D. M. Shear thinning of the Lennard-Jones fluid by molecular dynamics. *Physica A*, 133(3):473–496, **1985**.
- [110] Hoogerbrugge, P. J.; Koelman, J. M. V. A. Simulating microscopic hydrodynamic phenomena with dissipative particle dynamics. *Europhys. Lett.*, 19(3):155, **1992**.
- [111] Kirkwood, J. G. Statistical mechanics of fluid mixtures. *J. Chem. Phys.*, 3(5):300–313, **1935**.
- [112] Chandler, D. Statistical mechanics of isomerization dynamics in liquids and the transition state approximation. *J. Chem. Phys.*, 68(6):2959–2970, **1978**.

- [113] van Kampen, N. G. *Stochastic Processes in Physics and Chemistry*. Elsevier, Amsterdam, 3<sup>rd</sup> edition, **1992**.
- [114] Flannery, M. R. The enigma of nonholonomic constraints. *Am. J. Phys.*, 73(3):265–272, **2005**.
- [115] Hoover, W. G.; Posch, H. A.; Campbell, L. W. Thermal heat reservoirs via Gauss' principle of least constraint; Dissipation, chaos, and phase-space dimensionality loss in one-dimensional chains. *Chaos*, 3(3):325–332, **1993**.
- [116] Morriss, G. P.; Dettmann, C. P. Thermostats: Analysis and application. *Chaos*, 8(2):321–336, **1998**.
- [117] Gauss, C. F. Über ein neues allgemeines grundgesetz der mechanik. *J. Reine Angew. Math.*, 1829(4):232–235, **1829**.
- [118] York, D.; Evensen, N. M.; Martínez, M. L.; Delgado, J. D. B. Unified equations for the slope, intercept, and standard errors of the best straight line. *Am. J. Phys.*, 72(3):367–375, **2004**.
- [119] Maxwell, J. C. Van der Waals on the continuity of the gaseous and liquid states. *Nature*, 10:477–480, **1874**.
- [120] Chandler, D.; Weeks, J. D.; Andersen, H. C. Van der Waals picture of liquids, solids, and phase transformations. *Science*, 220(4599):787–794, **1983**.
- [121] Humphrey, W.; Dalke, A.; Schulten, K. VMD – visual molecular dynamics. *J. Mol. Graphics*, 14:33–38, **1996**.
- [122] Surwade, S. P.; Smirnov, S. N.; Vlassiouk, I. V.; Unocic, R. R.; Veith, G. M.; Dai, S.; Mahurin, S. M. Water desalination using nanoporous single-layer graphene. *Nat. Nanotechnol.*, 10(5):459–464, **2015**.
- [123] Cohen-Tanugi, D.; Grossman, J. C. Water permeability of nanoporous graphene at realistic pressures for reverse osmosis desalination. *J. Chem. Phys.*, 141(7):074704, **2014**.
- [124] Tocci, G.; Joly, L.; Michaelides, A. Friction of water on graphene and hexagonal boron nitride from ab initio methods: Very different slippage despite very similar interface structures. *Nano Lett.*, 14(12):6872–6877, **2014**.
- [125] Ma, M.; Grey, F.; Shen, L.; Urbakh, M.; Wu, S.; Liu, J. Z.; Liu, Y.; Zheng, Q. Water transport inside carbon nanotubes mediated by phonon-induced oscillating friction. *Nat. Nanotechnol.*, 10(8):692–695, **2015**.

## Chapter 3

### The Dynamics of Water in Porous Two-dimensional Crystals

Most of the contents of this chapter are reprinted, with permission, from

- (1) Strong, S. E.; Eaves, J. D. Atomistic hydrodynamics and the dynamical hydrophobic effect in porous graphene. *J. Phys. Chem. Lett.*, 7(10):1907–1912, **2016**
- (2) Strong, S. E.; Eaves, J. D. The dynamics of water in porous two-dimensional crystals. *J. Phys. Chem. B*, 121(1):189–207, **2017**
- (3) Strong, S. E.; Eaves, J. D. Linear response theory for water transport through dry nanopores. **2017**. Submitted

#### 3.1 Abstract

Porous 2d crystals offer many promises for applications in water desalination. For computer simulation to play a predictive role in this area, however, one needs to have reliable methods for simulating an atomistic system in hydrodynamic currents and the interpretative tools to relate microscopic interactions to emergent macroscopic dynamical quantities, like friction, slip length, and permeability. We use GD, the nonequilibrium MD method developed in Chapter 2, which provides microscopic insights into the interactions that control the flow of both simple liquids and liquid water through atomically small channels. We find that the wetting contact angle, a common measure of a membrane’s hydrophobicity, does not predict the permeability of a membrane. The contact angle can be tuned either through the polar interactions between the membrane and the water, or the van der Waals interactions. Experimentally, graphene can be doped or charged to

tune the polar interactions, while modulating the van der Waals interactions mimics changes in the membrane chemical composition. On neutral membranes, the hydrophobic effect is subtle, with both static and dynamic effects that can both help and hinder water transport through these materials. The competition between the static and dynamical hydrophobicity balances an atomic membrane's tendency to wet against hydrodynamic friction. To a reasonable approximation, the optimal contact angle depends only on the aspect ratio of the pore. On charged membranes, the permeability is instead governed by a crossover between two competing molecular transport mechanisms, and the permeability can be optimized by applying a voltage or chemically doping a membrane, or even by simple chemical termination of the pore with electron withdrawing groups. We also find that water molecules pass through the most hydrophobic membranes in a punctuated series of bursts that are separated by long pauses. A continuous-time Markov model of these data provides evidence of a molecular analogue to the clogging transition, a phenomenon observed in driven granular flows.

### 3.2 Background

The hydrophobic effect is one of the most important and elementary phenomena in chemistry.<sup>4–20</sup> On macroscopic scales, it is the driving force that partitions oily and aqueous solutions, and on molecular length scales it shapes the folding pathways of proteins and reinforces the stability of biomolecules.<sup>4,21</sup> Advancing the qualitative and conceptual underpinnings of the hydrophobic effect into quantitative theory remains a grand challenge in physical chemistry. The majority of work in this field has focused on solvation and aqueous chemistry, where the hydrophobic effect is thermodynamic in nature and depends solely on the statistical mechanics of intermolecular configurations.<sup>18–30</sup> In these aspects of chemistry, hydrophobicity derives from molecular statics. The simplest example comes from the wetting of solid surfaces, where one measures the surface's hydrophobicity through the contact angle.<sup>31–33</sup> For a droplet resting on a surface, the contact angle is a function of the liquid-solid surface tension.<sup>34,35</sup> But in dynamical contexts, quantifying the hydrophobic effect is more complicated. For a rolling droplet the contact angle depends on other

dynamical quantities, so that the surface tension becomes an incomplete predictor of wetting.<sup>33,36–38</sup>

In this Chapter, we bring new attention to the dynamical roles that the hydrophobic effect plays in aqueous transport. Motivated by applications to water desalination, we study aqueous flow through porous 2d crystals like graphene.<sup>39–42</sup> In water desalination, the size of the hydrated ion to be blocked dictates the size of the pore, so the throughput is bottlenecked by how fast one can push water across the membrane. One figure of merit that quantifies the throughput for a semipermeable membrane is the permeability, which is proportional to the slope of the mass flux versus applied pressure.<sup>43</sup> While the hydrodynamics appropriate for water desalination are at low Reynolds number ( $Re$ ) and transport takes place close to thermal equilibrium, computing the permeability from simulations at thermal equilibrium is computationally impractical.<sup>44</sup> To address this problem, we developed GD, which is an atomistic simulation method that allows one to simulate a fluid away from thermodynamic equilibrium and under flow, and is also faithful to statistical mechanics and hydrodynamics (Chapter 2).

We first study the dynamical hydrophobic effect in porous 2d crystals using electrically doped graphene (Section 3.5), which has a continuously tunable hydrophobicity<sup>45</sup> and is experimentally realizable.<sup>42,46,47</sup> Graphene has been the workhorse system for water desalination applications, but it is now feasible to produce high quality samples of other 2d crystals, like MoS<sub>2</sub> and BN.<sup>48–52</sup> It is possible that these materials could outperform graphene and it is therefore imperative to understand what types of intermolecular interactions lead to fast water transport through these emerging membranes. Therefore, we next cast a broader net and tune the intermolecular potentials between the water molecules and the surface parametrically so that we can answer general questions about what governs water transport through these materials (Section 3.6). We refer to these atomically thin model membranes as “atomic membranes.”

In our models, the intermolecular interactions come in two flavors, polar interactions and van der Waals interactions. These two classes of interactions between water and membrane atoms can both tune the wetting contact angle, but the dynamics of water passage depend sensitively on which class is dominant. Two membranes with different interaction types but with the same

contact angles, pore geometries, and pore sizes will not necessarily have the same permeabilities. Furthermore, the fluid flow endows the hydrophobic effect with both static and dynamic parts. The static contribution of the hydrophobic effect manifests as a tendency for the liquid to wet the pore, and can be understood in terms of equilibrium thermodynamics.<sup>20,21,27,53–56</sup> The dynamical aspects of hydrophobicity emerge as resistance, or friction, between the liquid and the solid surface. On electrically doped graphene, the observed behavior can even be more complex than either of these two contributions would predict. Understanding it requires a detailed picture of the microscopic transport mechanism, which we build using a Markov model.

Carbon nanotube (CNT) membranes have also been proposed for applications in RO, but simulations give wildly varying results for their permeability, with some even predicting frictionless flow.<sup>57–63</sup> Discrepancies between simulation methodologies, especially CNT rigidity and thermostatting, make them difficult to compare.<sup>57,58,61,64–70</sup> We study the effects of membrane flexibility and thermostatting in our atomic membranes to make connections to this controversy in the CNT literature (Section 3.7).

In Section 3.8, we find regimes where water transport deviates from a simple biased Markov random walk model, which is fundamental to the linear response theories that describe water transport near equilibrium.<sup>43</sup> We find that sharp bursts and long pauses dominate the mass current through the pores in the most hydrophobic membranes and we analyze these dynamics using a continuous time random walk (CTRW) model. The waiting-time distribution shows the onset of a power law decay and the burst-size distribution is an exponential. These two features are the signatures of the clogging transition observed in granular systems.<sup>71–75</sup> Interestingly, in this parameter space, the clogging phenomenon is a unique feature of the hydrogen bonding dynamics of water, and cannot be explained purely by the granular nature of water on a molecular scale.

In this clogged regime, large pressure drops are required to wet the pore and drive flow. These large pressure drops appear to push the system into the nonlinear regime, where linear response theory is not valid (Section 3.9). We use a macroscopic thermodynamic argument to show that such an apparently nonlinear relationship can be made to obey linear response in the right reference

state. This simple thermodynamic argument can, amazingly, capture both the equilibrium density of water inside a pore and the wetting pressure for the dry pores, even though the pores contain only about 3 water molecules at a time.

### 3.3 Methods

#### 3.3.1 Permeability

For a semipermeable membrane, the “osmotic permeability” quantifies the ease with which the solvent passes through a porous membrane.<sup>43</sup> The osmotic permeability,  $p$ , is the transport coefficient that relates a concentration difference to the osmotic current that it generates,

$$q_n = p\Delta C, \quad (3.1)$$

where  $\Delta C$  is the difference in solute concentration in moles per liter across a membrane that gives rise to a current of solvent,  $q_n = q/N_A$  in mol/s.<sup>43</sup> In a simulation it is much easier to drive a current with GD than it is with a concentration gradient, but to calculate  $p$ , we must make contact with eq. 3.1. Since we can compute the pressure drop in a simulation (Section 2.7), we replace the concentration difference in eq. 3.1 with the equivalent osmotic pressure that it would generate. For an ideal solution, the van't Hoff equation gives the osmotic pressure

$$\Delta P = N_A k_B T \Delta C. \quad (3.2)$$

Equations 3.1 and 3.2 yield our definition of the permeability

$$p = k_B T \frac{q}{\Delta P} \quad (3.3)$$

which expresses the relationship between the current,  $q$ , and the pressure drop,  $\Delta P$ . GD specifies the current and computes the pressure drop, while the pump method specifies the pressure drop and computes the current.<sup>76</sup> A detailed discussion of the calculation of  $\Delta P$  appears in Section 2.7. The permeability is analogous to an electrical conductivity, with the pressure drop playing the role of the voltage. Likewise, effective viscosity discussed in Section 2.8 is inversely related to the

permeability, and is analogous to an electrical resistance. The effective viscosity is normalized by the pore dimensions according to the Hagen-Poiseuille law to allow comparison between pores of different sizes. Here, we compare pores of only one size, so we use the more intuitive permeability instead of the effective viscosity.

We also calculate the permeability using an equilibrium linear response method, developed in Ref. 43. This method uses the collective variable  $n(t)$  (eq. 2.25). See Ref. 43 for details.

Because atomic membranes are so promising for next-generation RO, we also report the *approximate* “improvement factor”,  $p/p_0$ , over the permeability of conventional RO membranes,  $p_0$ . We use  $p_0 \approx 0.02$  liters of water filtered per  $\text{cm}^2$  of membrane per applied MPa per day,<sup>48</sup> and assume a membrane porosity of 10% by area<sup>40</sup> and a circular pore with diameter 7.4 Å. Note that in our simulations, the membrane is 3.9% porous by area.

### 3.3.2 Membranes

The atomic membranes have the same geometries as single-layer and double-layer graphene, and the membrane atoms remain fixed in space during the simulations. The pores in the membranes are designed to admit single-file water (Figure 3.1). We allow the membrane and oxygen atoms to interact through van der Waals forces, which we model with a LJ potential,  $U(r) = 4\epsilon[(\sigma/r)^{12} - (\sigma/r)^6]$ . Using graphene as a reference system, we tune the van der Waals part of the hydrophobicity by changing the  $\epsilon$  parameter for the carbon-oxygen LJ interaction while keeping  $\sigma$  fixed. Over the range of  $\epsilon$  values we study, Werder et al. found that the contact angle of a water drop on a double-layer 2d crystal varies linearly from about 30° to 140°.<sup>77</sup> By changing  $\epsilon$  and not  $\sigma$ , we aim to tune the hydrophobicity with the pore size fixed. In a statistical definition of the pore size based on, for example, the theory of Weeks, Chandler, and Andersen for a homogeneous fluid,<sup>78</sup> the effective hard-sphere diameter of the membrane atoms would vary with  $\epsilon$ , so the pore size would also depend on  $\epsilon$ . Because there are only a few water molecules in the pore and the environment there is anisotropic, we expect a mechanical criterion for the pore size to be more accurate. Mechanically, the pairwise membrane-water force goes to zero at  $2^{1/6}\sigma$ , and is independent of  $\epsilon$ . Regardless, if

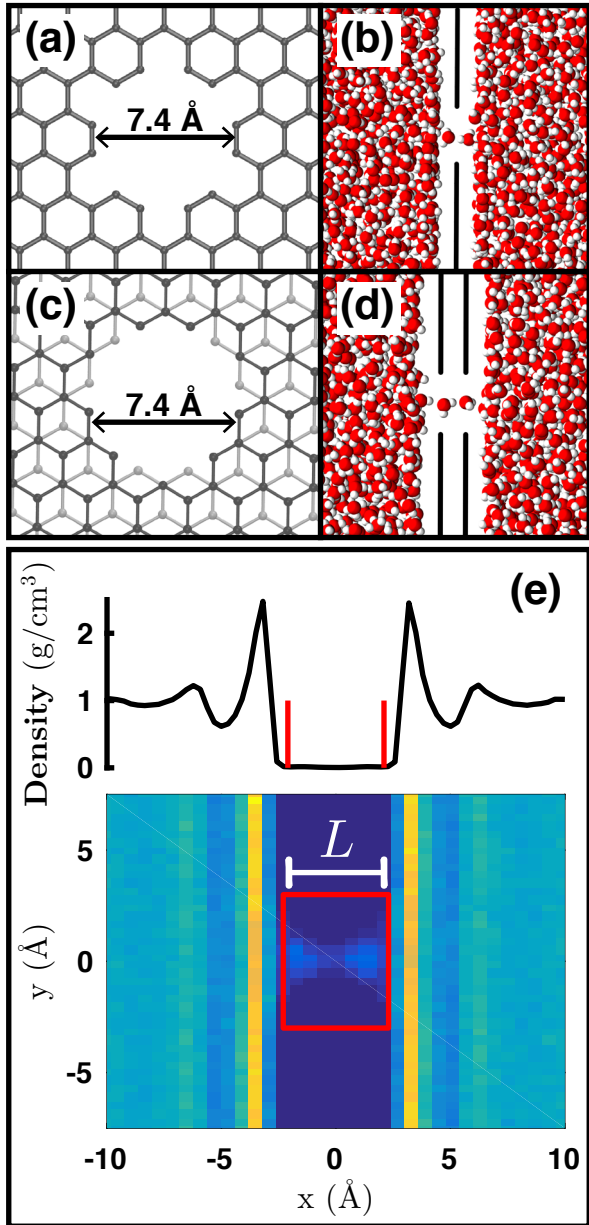


Figure 3.1: The single-layer membrane pore (a,b), and the double-layer membrane pore (c,d). The light gray atoms depict the bottom layer of the double-layer membrane. Nearly identical in shape, both pores have the same atom-to-atom distance ( $7.4 \text{ \AA}$ ). The pores are only wide enough to allow single-file water transport (b and d). We use the density of water in the vicinity of the pore (e) to define the length of the pore,  $L$  (eq. 3.5), and the region indicated by the red box is used to calculate  $n(t)$  (Section 2.4.2). This region has length  $L$  along the  $x$ -axis. The density scale is above, with red lines indicating the edges of the boxed region.

one were to employ the statistical criterion for the pore size, over the full range of  $\epsilon$  explored here, the channel diameter only changes by about 5%.

For the simulations of doped graphene, we use the graphene-water potential defined in case 28 of Table 2 in Ref. 77. This is the same potential that was used in Ref. 45, which showed that the hydrophobicity of graphene is tunable. This potential reproduces the wetting angle of water on graphite ( $\sim 90^\circ$ ), although now there is evidence that the wetting angle of water on graphene is significantly higher.<sup>79</sup>

We find the effective charge per carbon atom as a function of voltage from the dispersion relationship of graphene.<sup>45</sup> All carbon atoms have the same partial charge, with the charge placed at the atomic centers of each carbon. The excess charge per carbon atom,  $q_C$ , is

$$q_C = -aV^2 \operatorname{sgn}(V), \quad (3.4)$$

with  $a = 0.019336 \text{ e/volt}^2$ .<sup>45</sup>

### 3.3.3 Pore Dimensions

The calculations of the current through the pore (Section 2.4.2) and the pressure drop (Section 2.7) both require the definition of the length of the pore,  $L$ , or a “pore region”, where  $L$  is the length of the pore region in the direction of flow (Figures 2.2 and 3.1e). The edge of the pore is defined as the place where the equilibrium density profile,  $\rho(x)$ , has dropped by 90% of the total drop between the bulk and the pore (Figure 3.1e)

$$\rho(x_{\text{edge}}) = \rho_0 - 0.9(\rho_0 - \rho_{\text{pore}}), \quad (3.5)$$

where  $\rho_{\text{pore}}$  is the average density inside the pore and  $\rho_0 \approx 1 \text{ g/cm}^3$  is the bulk density of SPC/E water. Since the pore is symmetric about  $x = 0$ , the length of the pore is given by  $L = 2x_{\text{edge}}$ . In the  $y$  and  $z$  dimensions, the pore region is large enough to encompass all water molecules in the pore. The exact size is irrelevant because outside of the pore, molecules come within  $x_{\text{edge}}$  of the membrane exceedingly rarely.

### 3.3.4 Markov Model

We define the states of the Markov model using the definition of the pore region (Figure 3.1e). This region is divided into two halves by the plane of the membrane ( $x = 0$ ). When an oxygen atom is inside one of these two boxes, that box is occupied. The Markov states are defined using the occupation of these boxes: the “full” state corresponds to both boxes being occupied, etc (Figure 3.3). Since our Markov model assumes that each box can only be singly occupied or empty, the boxes must be small enough so that double occupation is rare. Using boxes defined as described, the boxes are doubly occupied less than 0.3% of the time.

We compute the Markov transition probabilities by simply counting the number of transitions between each state and normalizing by the total number of transitions.<sup>80</sup> We calculate the steady-state populations of the Markov process by diagonalizing the transition probability matrix and finding the eigenvector with unit eigenvalue. We then calculate the transition rates by converting the discrete Markov process into a continuous one using the sampling time step.

### 3.3.5 Reynolds Number

To compute the Reynolds number (eq. 2.26), we measure  $u_{\text{in}} = 2 \times 10^{-5} \text{ \AA/fs}$  explicitly in a GD simulation set at  $q = 11$  molecules/ns. Using values of  $\rho_0$  and  $\eta$  for SPC/E water from the literature:  $\rho_0 = 0.998 \text{ g/cm}^3$ ,<sup>81</sup>  $\eta = 0.729 \text{ mPa}\cdot\text{s}$ ,<sup>82</sup> and the “length” of the pore from eq. 3.5, the result is  $\text{Re} \approx 0.001$ .

### 3.3.6 Simulation Details

We model water using the rigid SPC/E potential.<sup>81,83</sup> The simulations start with 200 ps of bulk water equilibration at 1 atm and 298 K, at constant number, pressure, and temperature (NPT). We then add the atomic membrane and remove any water molecules that overlap it. We equilibrate the system again at NPT for 200 ps, only allowing expansion/contraction in the  $x$ -direction, because the atomic membrane in the  $yz$ -plane should not be deformed. After both of the NPT steps above, the box is linearly scaled over 100 ps to its average size during the NPT run. We then add an

initial COM momentum in the  $x$ -direction, turn on GD, and stabilize the system for at least 2 ns. The simulations of more hydrophobic membranes require 4, 7, or 9 ns of stabilization time. We then collect data for 5 ns. The simulation time step is 2 fs. The thermostat is a profile-unbiased Nosé-Hoover thermostat with a 200 fs damping time and boxes that contain an average of 4 molecules (Figure 2.1). The simulation box is about  $62 \times 37 \times 30 \text{ \AA}^3$  with 2060 water molecules for single-layer membranes, and  $68 \times 37 \times 30 \text{ \AA}^3$  with 2190 water molecules for double-layer membranes. The exact value of  $L_x$  and the number of water molecules vary because of the NPT equilibration and removal of water molecules when the membrane is added. The simulations are periodic in all dimensions. We use the particle-particle particle-mesh method to compute long range Coulombic forces.<sup>84</sup>

In the equilibrium simulations, we follow the same scheme as for the nonequilibrium simulations, except that we do not need to achieve steady state.

The membranes atoms are rigidly fixed in place in all simulations except those presented in Section 3.7. There, we use the DREIDING potential<sup>85</sup> to model flexible membranes.<sup>86</sup> We include bond interactions, angle interactions, and dihedral interactions between the membrane atoms. The DREIDING parameters are those for  $sp^2$  hybridized carbon atoms, as in graphene. The membrane atoms at the edge of the simulation box are fixed in space to prevent the membrane from moving with the flow. We use rRESPA to maintain energy conservation with a reasonable time step.<sup>87</sup> We use a 4 fs time step for the  $k$ -space Coulombic interactions, a 2 fs time step for the LJ interactions, a 1 fs time step for the dihedral interactions, and a 0.5 fs time step for the bond and angle interactions.

For each set of parameters, we run 96 simulations. We perform simulations at two different currents, 10 and 20 molecules/ns. To calculate  $p$ , we fit  $\Delta P$  versus  $q$  using all 96 data points at both currents by linear least-squares fitting with zero intercept, and substitute the slope of the best-fit line for  $q/\Delta P$  in eq. 3.3. The error bars in Figures 3.6, 3.7, and 3.5 correspond to the standard deviations of the best-fit slopes. Appendix B describes the software and computational resources used.

### 3.4 Tuning the Hydrophobicity

The bulk hydrophobicity, measured by the wetting contact angle that a droplet of water forms on a surface, is a macroscopic manifestation of the microscopic interactions between the surface and the water. These interactions can be divided into two categories: the interactions between the surface and the polar degrees of freedom in the water, and the interactions between the surface and the density degrees of freedom in the water, or van der Waals interactions. Here, we discuss the effect of both of these types of hydrophobicities on the permeability of water moving through an atomic membrane. To tune the polar part of the hydrophobicity we apply a voltage to the graphene sheet relative to the Fermi level.<sup>45</sup> The resulting electric field couples strongly to the polar degrees of freedom in water. The van der Waals interactions can be simply tuned with the LJ  $\epsilon$  parameter for the water-surface interaction. This separation between polar and van der Waals interactions is a conceptual device consistent with qualitative classes of intermolecular forces; it does not translate to a rigorous separation between the density and polar degrees of freedom in the liquid on all length scales. The statistics of density and polarization fields in liquid water are coupled, so tuning  $\epsilon$  will impact the polarization fluctuations, just as changing the voltage will modify the density fluctuations.

The contact angle is incredibly sensitive to changes in both types of interactions. Simulations have predicted that changing the voltage relative to the Fermi level by only  $\pm 0.35$  V decreases the contact angle by almost  $20^\circ$ .<sup>45</sup> This is an electrowetting effect completely dominated by collective polarization fluctuations.<sup>45</sup> Experimental work is consistent with these predictions.<sup>88,89</sup> The contact angle is likewise sensitive to changes in the van der Waals interaction strength. A  $0.2 k_B T$  change in the LJ  $\epsilon$  parameter, which tunes the van der Waals interactions between the membrane atoms and the water, changes the contact angle by  $130^\circ$ .<sup>77</sup>

Because a characteristic trait of liquid water is its ability to form extended hydrogen bonding networks, we also perform simulations with a model we call “apolar water”, which has the same mass, density, and steric interactions as the SPC/E water model, but that has no hydrogen bonds

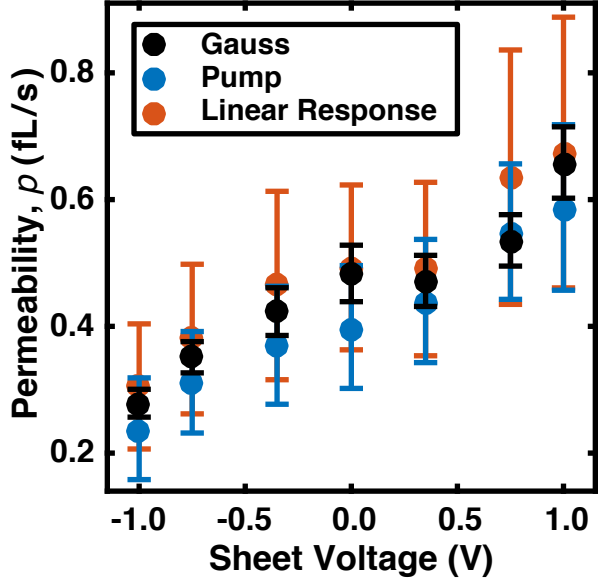


Figure 3.2: The permeability in femtoliters/second (eq. 3.3) of a single pore in a graphene sheet as a function of the voltage applied to the sheet, reported in volts. The hydrophobicity of the graphene sheet, calculated in Ref. 45, does not follow the permeability shown here.

or polar degrees of freedom.

### 3.5 Polar Interactions

We compute the permeability of porous single-layer graphene over a range of voltages applied to the sheet using GD, the pump method,<sup>76</sup> and linear response theory.<sup>43</sup> Using contact angle measurements, MD simulations of water droplets on graphene have shown that graphene becomes more hydrophilic at both positive and negative applied voltages.<sup>45</sup> In light of these simulations, our results show that the hydrophobicity of the sheet does not predict the permeability (Figure 3.2). The permeability of the sheet is higher at positive voltages (excess electrons) but lower at negative voltages (excess holes), even though the sheet is more hydrophilic in both regimes.<sup>45</sup> The size of the error bars illustrates the difficulty of converging these calculations, and it is only with GD that a statistically significant trend appears. For similar computational costs and for all simulations and quantities reported here, the standard errors are smaller for GD than for either of the other methods (Figs. 3.2 and 2.7d).

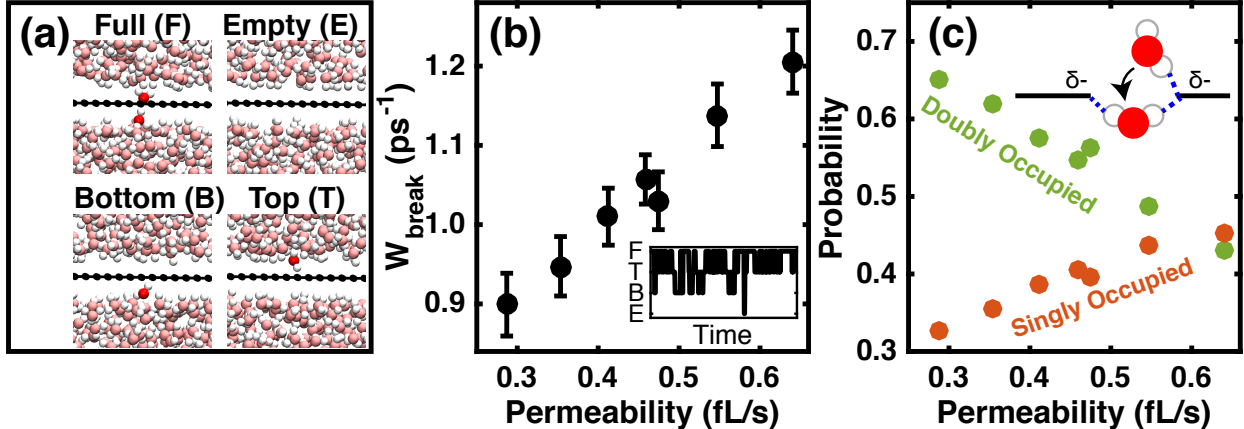


Figure 3.3: Panel (a) shows the four states used in the microscopic Markov model for transport. The inset to panel (b) shows 20 picoseconds of a time series of this Markov process, from which we compute the transition probabilities (Section 3.3.4). Panel (b) shows  $W_{\text{break}}$ , the rate at which a pair of molecules in the pore break their hydrogen-bond, which we interpret as a proxy for the evaporation-condensation transport rate (see text). Panel (c) shows the steady-state probabilities of singly (orange) and doubly (green) occupied states. Both  $W_{\text{break}}$  and the probability of a singly occupied state are correlated with the permeability, while the doubly occupied state is anticorrelated with it. The inset to panel (c) illustrates how the limber hydrogen atoms of a water molecule form contacts with a negatively charged sheet, enabling hydrogen-bond dissociation, single occupancy, and encouraging the evaporation-condensation mechanism.

The discrepancy between the permeability and the hydrophobicity suggests that passage dynamics are not dominated by a large-scale collective hydrophobic effect, like capillary wetting.<sup>90</sup> We instead suspect that microscopic motions control the transport dynamics in pores with dimensions comparable to a water molecule. To test this hypothesis, we coarse-grain the occupancy of the channel and develop a stochastic Markov model of the transport process. The pore is small enough that passage is single-file (Figure 3.1), so there are only four Markov states, depicted in Figure 3.3a. We run simulations at equilibrium and compute the transition probabilities and steady states of the Markov process directly from the time series (inset, Figure 3.3b).

We examine two mechanisms for water passage through the pore: As with single-file water in CNTs, water molecules can move through the pore in a translocation mechanism, crossing the membrane while maintaining an unbroken chain of hydrogen bonds.<sup>39,40,59,91–96</sup> In the case of an atomically thin channel, however, water molecules can also cross the sheet individually, severing

hydrogen bonds and moving through the pore in an evaporation-condensation mechanism.

To differentiate these mechanisms, we focus on the hydrogen-bond (H-bond) between two water molecules in the pore. The translocation mechanism relies on this H-bond staying intact, while the evaporation-condensation mechanism requires that this bond breaks. We approximate the breaking rate of this H-bond,  $W_{\text{break}}$ , as the Markov transition probability per unit time from a fully occupied pore to a singly occupied pore (Section 3.3.4),

$$W_{\text{break}} \approx W_{\text{full} \rightarrow \text{top}} + W_{\text{full} \rightarrow \text{bottom}}, \quad (3.6)$$

using the state labels in Figure 3.3a.  $W_{\text{break}}$  follows the permeability closely (Figure 3.3b); a larger  $W_{\text{break}}$  correlates to a higher permeability. This implies that the evaporation-condensation mechanism becomes more prevalent at higher permeability (positive voltages). The steady-state occupancies of the Markov process support this picture as well: the probability of observing a singly occupied pore correlates positively with the permeability, while the probability of observing a doubly occupied pore is anticorrelated with it (Figure 3.3c).

We propose the following picture to explain the results of the Markov model: When graphene is negatively charged (positive voltage), it functions as an H-bond acceptor and can form contacts with the positively charged hydrogens on the water molecules (inset, Figure 3.3c). With their H-bonds satisfied through contacts on the sheet, the water molecules can break their H-bonds with other water molecules more easily. A positive voltage thus facilitates H-bond breakage both between the water molecules in the channel and between the bulk and the channel waters, thereby lowering the barrier for the evaporation-condensation mechanism relative to the translocation one. Because water molecules pivot around a massive oxygen there is an intrinsic molecular asymmetry in the dynamics of passage, so that the hydrogens enter the channel first. We propose that the decrease in permeability at positive charge (negative voltage) is due to an increasing energetic penalty for the light and rotationally mobile hydrogen atoms to enter the pore.

The Markov model reveals that the asymmetry of the permeability as a function of voltage can be explained in molecular terms, by a transition from a concerted translocation transport mech-

anism to an evaporation-condensation mechanism. Because the transport process is bottlenecked by only a few water molecules for pores of these sizes, the collective aspects of hydrophobicity have little bearing on the dynamics of water passage. Instead, local interactions, in the form of hydrogen–membrane contacts, control the transport process.

### 3.5.1 H-bond Survival Time

One could argue that other processes should contribute to the Markov breaking rate

$$W_{\text{break}} \approx W_{\text{full} \rightarrow \text{top}} + W_{\text{full} \rightarrow \text{bottom}} + W_{\text{full} \rightarrow \text{empty}} + W_{\text{top} \rightarrow \text{empty}} + W_{\text{bottom} \rightarrow \text{empty}}. \quad (3.7)$$

This is a moot point for two reasons: First, the empty state is rare, so the transition probabilities to it are negligibly small. Second, these rates follow the same trend anyways.

To verify that  $W_{\text{break}}$  is a good proxy for the H-bond breaking rate, we calculate the breaking rate for H-bonds between two molecules in the pore explicitly. We define an H-bond as an O-O separation of 3.5 Å or less and a O-H-O angle of 30° or less.<sup>97</sup> We then compute the average time that an H-bond lasts between two molecules inside the pore. We ignore H-bonds which “break” because one of the molecules leaves the pore. The inverse of this survival time is the explicit breaking rate. This gives an independent estimate of the H-bond survival time, which is not influenced by any transport events. The explicit breaking rate follows the same trend as the Markov  $W_{\text{break}}$ , and is even quantitatively comparable (Figure 3.4). We conclude that the Markov estimate of the H-bond breaking rate accurately captures the H-bond dynamics

### 3.5.2 Pore Functionalization: Local versus Nonlocal Polar Interactions

The hypothesis that the local interactions between the pore and the water in the pore are responsible for trend in permeability can be further tested by applying a charge to the atoms at the edge of the pore only. This is also a simple model for chemical pore functionalization. Instead of studying a slew of possible chemical modifications to the pore edge, we model the effect by simply charging the carbon atoms at the edge of the pore (Figure 3.5, inset). While this is surely not

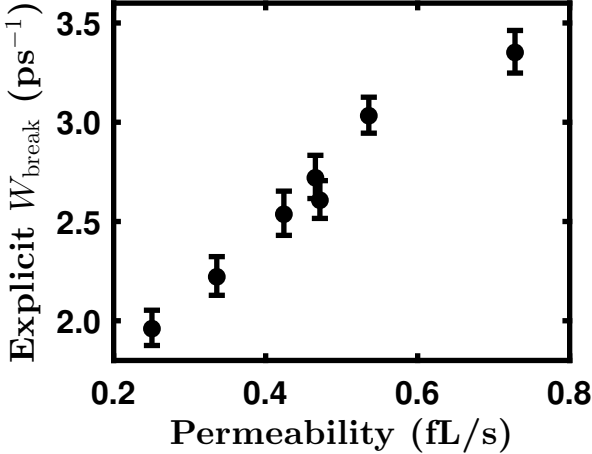


Figure 3.4: The survival time of an H-bond between two water molecules in the pore can be computed using an explicit definition of an H-bond, as discussed in the text. The explicit breaking rate is the inverse of this survival time, and is correlated with the permeability in the same way as the Markov  $W_{\text{break}}$ . The quantitative values are on the same order of magnitude as well. This supports the data in Figure 3.2b.

exhaustive, it gives an idea of the trends in permeability that might be discovered with chemically modified graphene pores. We report the applied charge as an “equivalent voltage” to make contact with Figure 3.2 and Ref. 45. At a given equivalent voltage, the charge on an edge carbon atom is equal to the charge per carbon atom at that voltage in Figure 3.2, but the other carbon atoms are neutral.

We find that the trend in permeability is qualitatively unchanged whether a voltage is applied to the sheet, tuning the bulk hydrophobicity, or only the local interactions are tuned, modeling pore functionalization (Figure 3.5). This supports the hypothesis presented in Section 3.5, that the shift in molecular transport mechanism responsible for the permeability trend observed is dominated by the local interactions between the water molecules and the pore. In other words, the molecular interactions in the vicinity of the pore overpower the collective polarization fluctuations in the bulk liquid. These local interactions could be tuned experimentally through pore functionalization, providing a useful handle for optimizing graphene membranes and other atomically thin membranes. Note that the trend is slightly weaker when only the edge carbon atoms are charged (Figure 3.5). This is likely because the next ring of carbon atoms around the pore also contributes to the local

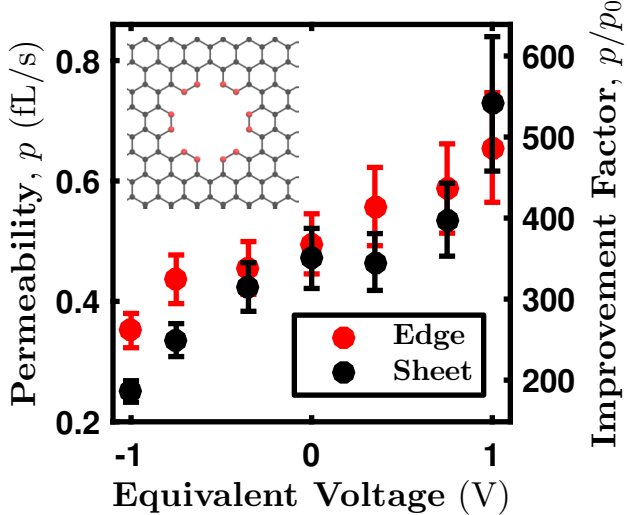


Figure 3.5: The permeability of porous single-layer graphene as a function of applied voltage (black points), compared to the permeability (red points) when only the carbon atoms on the edge are charged (red atoms, inset). This no longer corresponds to an applied voltage, so we report it as an “equivalent voltage.” The charge per carbon atom on the edge of the pore is equivalent to what it would be in a fully doped graphene sheet at the equivalent voltage. The trend is the same whether the entire membrane is charged or only the edge atoms are charged, reinforcing the evaporation-condensation mechanism facilitated by local hydrogen bonding. The improvement factor is the ratio of the permeability to that of conventional RO membranes (see text).

interactions, but were not charged in this study.

### 3.6 van der Waals Interactions

We now discuss the results of tuning the van der Waals part of the hydrophobicity through the LJ  $\epsilon$  parameter. We find that, as the atomic membranes become more hydrophobic, the permeability first increases slowly and then drops sharply (Figure 3.6a). The most noticeable part of the data in Figure 3.6a is the sharp drop in permeability, which occurs at different critical contact angles for single- and double-layer atomic membranes. As we show below, the thermodynamics of wetting describe this threshold behavior.

Just as the application of hydrodynamics to atomically small length scales is specious, so is the application of macroscopic thermodynamics, and for the same reasons. Nonetheless, we show that the thermodynamics of the dewetting transition does give a semi-quantitative description of

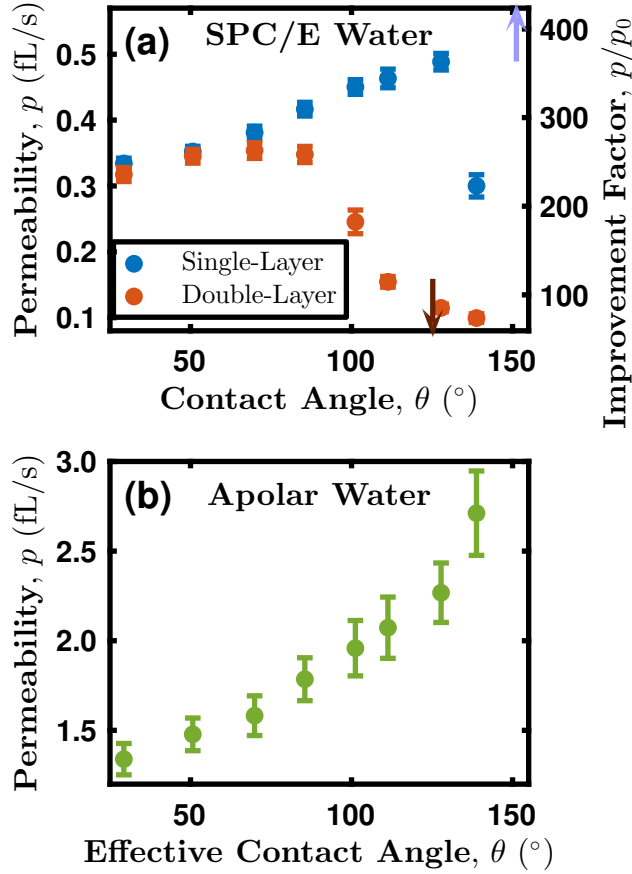


Figure 3.6: (a) The permeability as a function of contact angle on single-layer (blue) and double-layer (red) atomic membranes. We tune the contact angle by changing the membrane-water LJ interaction energy  $\epsilon$ .<sup>77</sup> As the membranes becomes more hydrophobic, the permeability initially increases due to decreasing friction and then decreases sharply due to dewetting. The arrows show the critical dewetting contact angles from macroscopic thermodynamics for both single-layer (dark red) and double-layer (light blue) membranes, reported in Table 3.1. (b) No dewetting transition is seen for apolar water because this model does not form a hydrogen bonding network. We report the LJ  $\epsilon$  parameter as the “effective” contact angle to make a connection to (a). The effective contact angle corresponds to the value of  $\epsilon$  that generates that contact angle for SPC/E water. The improvement factor is the ratio of the permeability to that of conventional RO membranes (see text).

the threshold phenomenon observed for the permeability of hydrophobic atomic membranes (Figure 3.6a). The dewetting transition is an equilibrium phenomenon that shares some similarities to homogeneous nucleation theory and capillary action. An early observation of the dewetting transition using computer simulations comes from the work of Wallqvist and Berne, who studied the spontaneous evaporation of liquid water between two paraffin plates.<sup>20</sup> The free energy of dewetting is a competition between bulk and surface terms associated with filling or emptying the pore.<sup>53</sup>

The pore in both single- and double-layer atomic membranes is roughly cylindrical. For a cylindrical pore with radius  $r$  and length  $L$ , consider the grand potential of the pore when it is occupied by liquid,  $\Omega_\ell$ , or vapor,  $\Omega_v$ ,<sup>27</sup>

$$\Omega_\ell = -P_\ell \pi r^2 L + 2\gamma_{s\ell} \pi r L \quad (3.8)$$

$$\Omega_v = -P_v \pi r^2 L + 2\gamma_{sv} \pi r L + 2\gamma_{v\ell} \pi r^2, \quad (3.9)$$

where  $P_v$  and  $P_\ell$  are the pressures of the respective phases, and  $\gamma_{sv}$ ,  $\gamma_{s\ell}$ , and  $\gamma_{v\ell}$  are the surface tensions. The free energy difference between the phases is

$$\Delta\Omega \equiv \Omega_v - \Omega_\ell = \Delta P_{\text{ph}} \pi r^2 L + 2\gamma_{v\ell} \pi r L \cos \theta + 2\gamma_{v\ell} \pi r^2, \quad (3.10)$$

where  $\Delta P_{\text{ph}} \equiv P_\ell - P_v$  is the pressure difference between the phases and  $\theta$  is the contact angle from Young's equation,  $\gamma_{v\ell} \cos \theta = \gamma_{sv} - \gamma_{s\ell}$ .<sup>35</sup> At the critical contact angle,  $\Delta\Omega = 0$ , which gives the relationship for the critical contact angle,  $\theta_c$ ,

$$-\cos \theta_c = \frac{\Delta P_{\text{ph}} r}{2\gamma_{v\ell}} + \frac{r}{L}. \quad (3.11)$$

Using the approximate values  $\Delta P_{\text{ph}} = 1$  atm and  $\gamma_{v\ell} = 72.1$  mJ/m<sup>2</sup>, we find

$$-\cos \theta_c = r \left( \frac{1}{1.4 \mu\text{m}} + \frac{1}{L} \right). \quad (3.12)$$

In our simulations,  $L$  is on the order of Å, so the first term is negligible and we can simplify the relation to

$$-\cos \theta_c \approx \frac{r}{L}. \quad (3.13)$$

	$r$ (Å)	$L$ (Å)	$\theta_c$ (°)
Single-Layer	3.7	4.2	152
Double-Layer	3.7	6.5	125

Table 3.1: The thermodynamic prediction of the critical wetting contact angle from eq. 3.13

The predictions of eq. 3.13 as a function of  $L$  for the critical angle on single- and double-layer atomic membranes are summarized in Table 3.1 and shown as arrows in Figure 3.6a. These predictions are surprisingly good given the macroscopic equilibrium nature of the free energy argument, but irrespective of their quantitative accuracy, they explain the qualitative decrease in  $\theta_c$  as the pore gets longer. It is interesting to note that eq. 3.13 predicts that the critical contact angle can never be smaller than 90°. Further, as long as the pore length is significantly smaller than one micron, well within the regime where macroscopic thermodynamics is valid, the critical contact angle only depends on the aspect ratio of the pore and is independent of the properties of the liquid and the membrane. The radius  $r$  used in Table 3.1 is the center-to-center distance between atoms in the geometry shown in Figures 3.1a and 3.1c, and the pore lengths,  $L$ , are determined using eq. 3.5, as discussed there. This choice of  $r$  reflects the ambiguity inherent in the thermodynamics behind eq. 3.13. With only a handful of molecules to distinguish between “vapor” and “liquid” phases inside the pore, there can be no rigorous classification of a thermodynamically stable interface in either putative phase. Nonetheless, thermodynamic dewetting calculations can be semi-quantitative for nanoscopic volumes.<sup>27</sup> Since the water density profile inside the pore is hourglass shaped (Figure 3.1e), an optimal cylinder to approximate the wetted interface for the pore would place  $r$  larger than the minimally accessible surface area that compensates for the excluded volume of the membrane atoms in the narrowest region of the channel. We simply use a value of  $r$  equivalent to the distance between atomic centers, partly because it is easy to determine from experiments. Section 3.9 generalizes this argument further.

The other important feature of the data in Figure 3.6a is the slow increase in the permeability as the membrane becomes more hydrophobic. This is due to friction between the water and the

membrane. On more hydrophilic membranes, the water-membrane interaction is more attractive, so the water molecules stick more strongly to the membrane, leading to more friction and lower permeability. This is a purely dynamical aspect of the passage process and has no counterpart at equilibrium.

While the dewetting transition observed for SPC/E water leads to a threshold behavior at intermediate hydrophobicities, the permeability of apolar water is a smooth and monotonically increasing function of the effective contact angle (Figure 3.6b). For apolar water, we report the LJ  $\epsilon$  parameter as the “effective” contact angle to make a connection to SPC/E water. The effective contact angle corresponds to the value of  $\epsilon$  that generates that contact angle for SPC/E water according to Ref. 77. We speculate that the lack of a dewetting transition in apolar water is due to the low vapor pressure and high surface tension of SPC/E water compared to apolar water. Because water forms hydrogen bond networks, it has a remarkably low vapor pressure and high surface tension for a low molecular weight substance. These features make the approximation in eq. 3.13 accurate for water. Apolar water cannot form hydrogen bonds, so it is far from liquid-vapor coexistence and its dewetting transition over this range of  $\epsilon$ . Removing the dewetting transition simplifies the analysis of the permeability because apolar water only experiences friction.

The dewetted pores also reveal a key difference between the pump method and GD. GD fixes the current, but admits fluctuations in the pressure drop. The pump method is the complementary method to GD, as it fixes the pressure drop but admits fluctuations in the current. For very small currents, flow becomes intermittent and equilibration to steady state very difficult. This gives rise to a discrepancy between the pump method and GD on very hydrophobic membranes (Figure 3.7). In order to allow sufficient passage to achieve steady state, one must apply exceedingly high pressures in the pump region. At very high pressures, it is not computationally feasible to converge the results with respect to the box length. While GD will also generate large pressures to maintain a given current, the external acceleration is not discontinuous as in the pump method, so shorter boxes can be used. Further, GD allows the user to specify how many passage events they want to observe in a simulation of a given length, and automatically finds the pressure drop that is necessary to

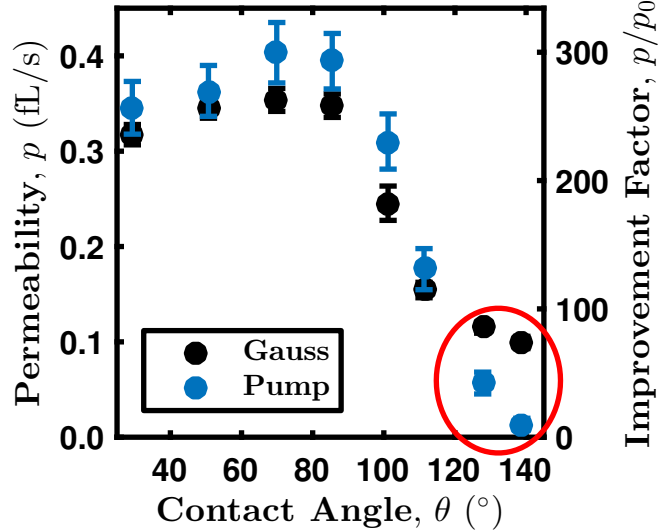


Figure 3.7: The permeability of a porous double-layer atomic membrane as a function of contact angle on a single-layer membrane. The pump method (blue) and GD (black) show the sharpest disagreement for the most hydrophobic membranes (circled in red), past the dewetting transition. The improvement factor is the ratio of the permeability to that of conventional RO membranes (see text).

generate that current. Practically, this eliminates the need for preliminary testing with the pump method to determine the pressure required to drive sufficient flow.

The general behavior we observe here when tuning the van der Waals part of the hydrophobicity is qualitatively different from that seen when tuning the hydrophobicity through polar interactions (Figure 3.6a). The molecular transport mechanism that was central to the behavior observed in Section 3.5 are overshadowed here by friction and dewetting. On detailed inspection, the contact angle alone is insufficient to fully characterize even the thermodynamic aspects of the hydrophobic effect; Ref. 90 also finds discrepancies between polar and nonpolar hydrophobicity in the statistics of interfacial fluctuations.

### 3.7 Flexible Membranes

We now turn to the effect of membrane flexibility on the permeability of atomically thin, porous membranes. As discussed in Chapter 2.9, there is a controversy in the literature regarding water flow through CNT.<sup>61</sup> Some of the disagreement is likely due to the differences in the rigidity

or flexibility of the CNTs. Only two studies have directly addressed the effect of rigidity.<sup>57,69</sup> They both found that flexible CNTs have about 20% higher permeability than rigid ones, but they do not explain why. Simulations by Ma et al. suggest that longitudinal phonon modes in CNTs contribute to the low friction observed there and could be the origin of the increased permeability.<sup>86</sup> In Section 2.9, however, we find that a 2d Lennard Jones fluid in Poiseuille flow between two walls has a smaller slip length, and therefore a smaller permeability, when the walls are flexible. This is the opposite of the results in CNTs. In Section 2.9, this result is attributed to the ability of the flexible walls to more efficiently absorb kinetic energy from the fluid, thereby reducing its velocity at the wall. Further, in these 2d simulations, the wall particles are separated by only  $1 \sigma$  so there is not space for significant longitudinal motion and the majority of the wall flexibility is transverse to the flow direction.

Here, as in the CNTs, most of the membrane motion is in the longitudinal direction, in the direction of the flow. We find that the permeabilities for the flexible membranes are systematically higher than for the rigid ones, though only by about 7% (Figure 3.8). Note that the permeabilities for the rigid membranes computed here are slightly higher than those reported in Section 3.6 because they are equilibrated 5 ns longer to ensure that the small difference between the flexible and rigid membranes is real.

We explore several possible origins for the increased permeability on a flexible membrane: pore stretching, dynamic correlations, and reorientation inside the pore. We look at the effect of pore stretching first. This is an effect unique to atomically thin membranes, where, as the pore atoms stretch downstream the pore enlarges to reduce the amount of bond stretching. In CNTs, on the other hand, these motions are longitudinal phonons that do not stretch the nanotube. We find that the density of water in the pore region (Section 3.3.3) extends slightly further from the center axis of the pore for a flexible membrane than a rigid one (Figure 3.8b). These densities are computed in the membrane frame, where the center of the pore region in the  $x$ -direction moves with the center of mass of the 12 atoms at the edge of the pore. Far from the center of the pore (large  $r$ ), where stretching is evident, the flux is zero, so stretching does not allow more water through

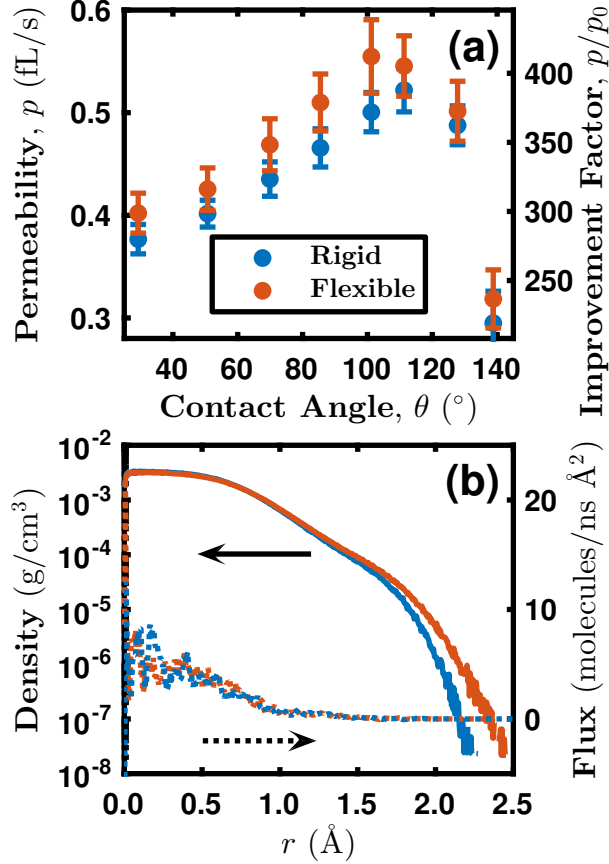


Figure 3.8: (a) The permeability of a single-layer atomic membrane is systematically larger when the membrane is flexible (orange) than when it is rigid (blue). (b, left axis) The density of water molecules in the pore region (Section 3.3.3) as a function of the distance from the center axis of the pore,  $r$  (solid lines). The slight increase in density at large  $r$  on flexible membranes indicates that the pore stretches by a very small amount. Note the log scale. (b, right axis) The flux through the pore as a function of  $r$  (dotted lines). The flux is zero for large  $r$ , where the excess density is, so the slight stretching does not allow more water through the pore.

the pore (Figure 3.8b). To test this, we compute the average position of the membrane when it is flexible and perform simulations with the membrane frozen at this average position. This yields the same permeability as the rigid and flat membrane, ruling out any effect due to steady-state pore stretching. This does not rule out the role of short lived stretching fluctuations, however, which we discuss next.

We test the hypothesis that the increased permeability is due to longitudinal motions of the membrane. Indeed, the fluctuations of the flow rate  $\dot{n}(t)$  are correlated with the fluctuations of

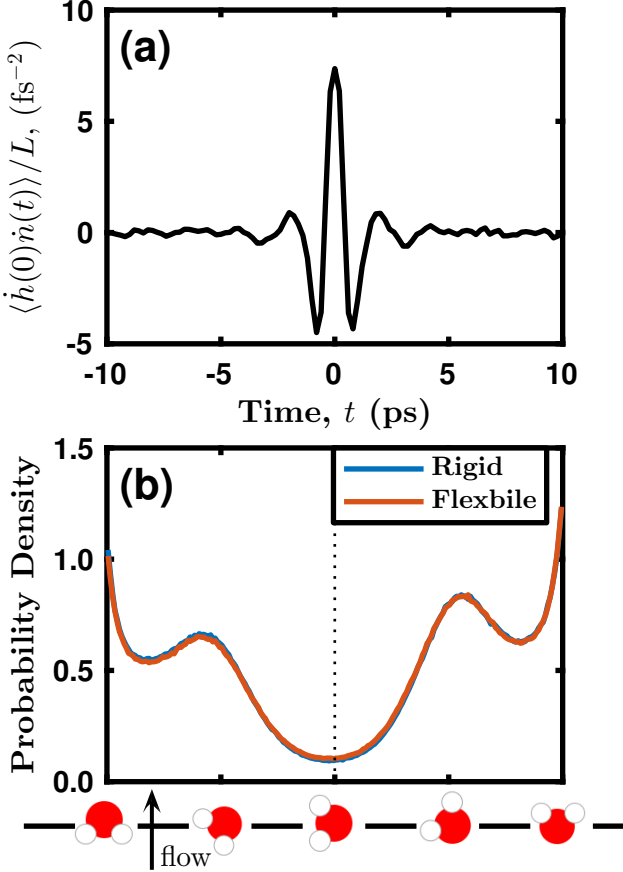


Figure 3.9: (a) The cross-correlation between the velocity of the pore in the direction of flow and the flow rate (see text). The nonzero correlation at time zero shows that the motion of the membrane is correlated with flux through it. (b) The steady-state orientational distribution of water molecules in the pore region (Section 3.3.3) as a function of the projection of the water dipole moment along the direction of flow,  $\mu_x$ . Various values of this projection are illustrated by the tick labels. The steady-state distribution is identical for rigid and flexible membranes. The reorientation probabilities described in the text refer to reorientations that cross the dotted black line.

the pore velocity in the longitudinal direction,  $\dot{h}(t)$ , where overdots indicate time derivatives (Figure 3.9a). Here,  $n(t)$  is the collective variable defined in Section 2.4.2, which effectively counts passage events.<sup>43</sup> Its time derivative  $\dot{n}(t)$  is the flow rate. Bearing in mind a pseudo stick boundary condition for the fluid in the pore, a Langevin description of the flow rate might include a coupling to the membrane velocity

$$\dot{n}(t) = v + \xi(n - vt) + c\dot{h}(t) + \sqrt{2D}\eta(t), \quad (3.14)$$

where  $v$  is the steady-state flux,  $\xi$  is the drag term,  $c$  is some proportionality constant,  $D$  is the generalized diffusion constant for  $n(t)$ , and  $\eta(t)$  is white noise.<sup>98</sup> In this case, the flow rate would be enhanced by an amount proportional to the integral of the cross-correlation function  $\int dt \langle \dot{h}(t) \dot{n}(0) \rangle$ . The integral of this cross-correlation function, shown in Figure 3.9, is zero, however, so this theory does not explain the increased permeability. One might expect that the increased permeability could be accounted for in the membrane frame, where the fluid velocity is taken relative to the membrane velocity. This is also not the case; the permeabilities are the same in both the lab and membrane frames. This holds true whether the permeability is computed away from equilibrium with GD, or at equilibrium with linear response theory.<sup>43</sup> Nonetheless, the nonzero correlation between the flow rate and the pore velocity could be the cause of the increased permeability, in some framework not captured by linear response theory.

Finally, we hypothesize that the reorientation dynamics are responsible for the difference in permeability between the flexible and rigid membranes. The steady-state orientation of water molecules in the pore is identical for both rigid and flexible membranes (Figure 3.9b). To study the reorientation dynamics, we compute the reorientation probability using a two state Markov model. The two states are differentiated by the projection of the water dipole moment along the direction of flow,  $\mu_x$ . The two states are  $\mu_x < 0$  and  $\mu_x \geq 0$ , which correspond to molecules oriented with their hydrogen atoms pointing upstream and downstream, respectively. We only consider trajectories of water molecules during successful passage events. A successful trajectory encompasses only a single excursion into the pore region (Section 3.3.3) that results in successful passage. During a successful passage event, however, a molecule can pass through the pore several times, without leaving the pore region. We construct a Markov time series where the “time steps” are delimited by passage events in which the molecule passes through the plane of the pore. During each Markov time step, the Markov state is determined by the average value of  $\mu_x$ , sampled every 0.2 ps.

We then compute the Markov transition probabilities from this time series (Figure 3.9b). The reorientation probability is given by the average of the  $(\mu_x < 0) \rightarrow (\mu_x \geq 0)$  and the  $(\mu_x \geq 0) \rightarrow (\mu_x < 0)$  probabilities. The reorientation probability is the same (19%) on both rigid and flexible

membranes (Figure 3.9b). This makes sense, considering that reorientation of water molecules is dominated by the hydrogen atoms and, in our simulations, the hydrogen atoms do not interact with the membrane, only the oxygen atoms do. So it is reasonable that the dynamics of the membrane are invisible to the hydrogen atoms and therefore to the reorientation of the water molecules.

While we have not been able to precisely determine the cause of the increased permeability on flexible membranes, we have ruled out a static explanation. The increase must be due to some dynamic effect, likely related to the correlation between membrane motion and passage events (Figure 3.9a).

Another possible explanation for the disagreement on the permeability of CNTs is the thermostatting methods used in simulations.<sup>61,69,70</sup> The thermostat can operate on the fluid, extracting heat from the fluid only, or the CNT walls, extracting heat from the walls only, or both (Section 2.9). With flexible membranes, we can now test the effect of the thermostat implementation in our system by thermostatting the membrane instead of the fluid. However, in simulations of single-file water flow through atomically thin membranes, we find that there is not sufficient thermal contact between the membrane and fluid to maintain steady state. The low frequency modes of the membrane do not couple efficiently to water's librational modes that account for most of the thermal energy in rigid water. As a result, the fluid heats at a rate of about  $10^9$  K/s, so we cannot make any reasonable comparisons between thermostatting methods.

### 3.8 Bursty Transport

An interesting observation in these systems is that the passage time series appears bursty, especially on the most hydrophobic membranes (Figure 3.10). The passage time series is the net number of molecules that have passed through the pore as a function of time. We compute the passage time series using the collective variable  $n(t)$  defined by Zhu et al. (eq. 2.25).<sup>43</sup> The traces in Figure 3.10 are the time series  $n(t)$ , which are computed using the pore region defined in Figure 3.1e according to eq. 3.5 and the equilibrium density considerations discussed there.

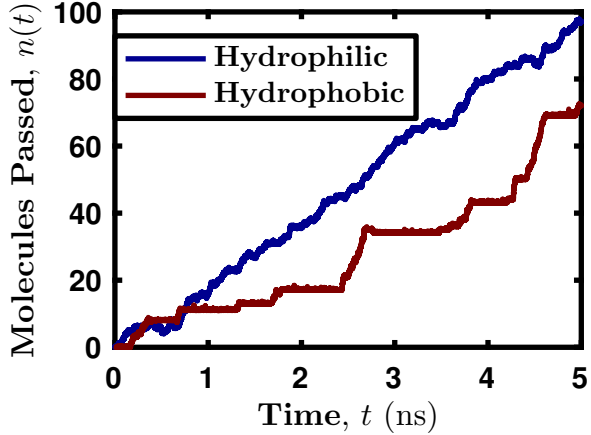


Figure 3.10: The net number of passage events as a function of time for single-layer membrane,  $n(t)$  (see text), transitions from a normal biased random walk in the most hydrophilic membrane (blue) to a transport process dominated by bursts and long pauses in the most hydrophobic membrane (red).

### 3.8.0.1 Continuous time random walk model

To understand the bursty behavior observed in Figure 3.10, we use a biased CTRW model, where a forward passage event is like a hop to the right on a 1d lattice, and a backward passage event is a hop to the left (Figure 3.11a). This model is a one-step Markovian process in a discrete state space. To map the continuous  $n(t)$  onto this discrete state space, we must discretize it. This can be done with varying complexity, but the simplest method of rounding to the nearest integer is adequate (Figure 3.11b). We test that the discretization procedure does not corrupt the data by checking that both  $n(t)$  and the discretized  $n(t)$  have the same mean-squared displacement at equilibrium and therefore yield the same collective diffusion coefficient.<sup>43</sup> The dynamics of an unbiased CTRW are completely determined by the waiting-time distribution,  $\psi(t)$ , which is the probability of observing a given waiting time between two consecutive hops, or passage events. For this system, the CTRW is biased because there is a net forward flux, so we must consider the forward and backward waiting-time distributions separately,  $\psi_f \neq \psi_b$  (Figure 3.11a). We compute the waiting times from the discretized  $n(t)$  as the elapsed time between each pair of consecutive passage events. The forward waiting times are those where the waiting time is terminated by a

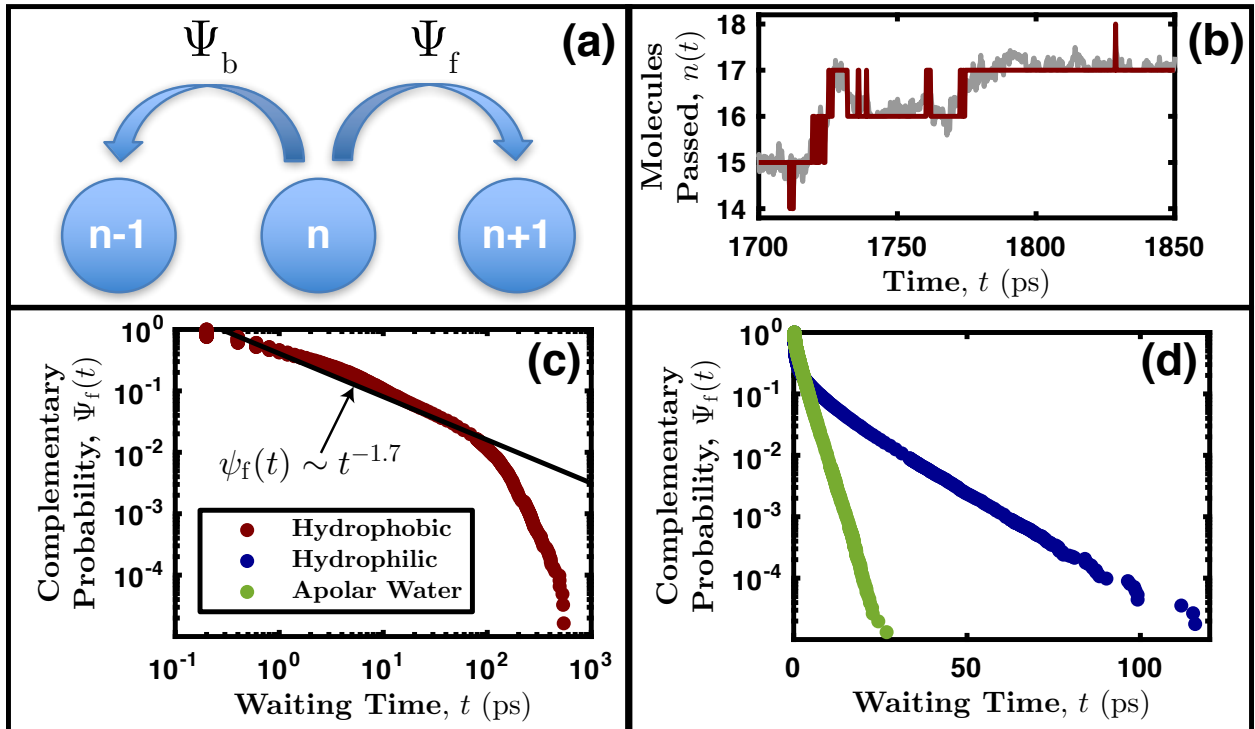


Figure 3.11: (a) We model the passage of water through atomic membranes as a CTRW that brings the system between states of different counts, illustrated in the coarse-graining (red line) of the time series  $n(t)$  (gray line) in (b). This time series is a segment of that shown in Figure 3.10. The model is fully described by the forward and backward complementary waiting-time distributions,  $\Psi_f(t)$  and  $\Psi_b(t)$ , the probabilities that no events have occurred either forwards or backward, respectively, between time zero and time  $t$ . (c) A log-log plot of  $\Psi_f(t)$  for the most hydrophobic single-layer membrane (red) shows that it follows a power law over about two decades with an exponential cutoff at long times. A power-law distribution of waiting times is one hallmark of a clogging transition.<sup>71</sup> The black line shows the power-law part of a fit by maximum likelihood estimation to eq. 3.18 (see text). The power-law exponent is 1.7, which indicates a divergent average waiting time (eq. 3.20). (d) A log-linear plot of  $\Psi_f(t)$  for the most hydrophilic single-layer membrane (blue) and apolar water on the most hydrophobic single-layer membrane (green) emphasizes the exponential decay. There is no significant power-law relaxation in either of these cases. Note the dramatic difference in the range of the  $x$ -axis in panels (c) and (d).

forward passage event, and likewise for the backward waiting times.

We plot the complementary cumulative waiting-time distributions to avoid errors associated with binning (Figures 3.11c,d).<sup>99</sup> The complementary cumulative probability

$$\Psi_f(t) = 1 - \int_0^t dt' \psi_f(t') \quad (3.15)$$

is the probability that there is no hop by time  $t$ . For brevity we refer to  $\Psi_f(t)$  as the complementary probability. We find that the forward waiting times appear to be power-law distributed for a couple of decades on the most hydrophobic membranes (Figure 3.11c), but are exponentially distributed on the hydrophilic membranes (Figure 3.11d). Note that for a power-law distribution,  $\psi(t) \sim t^{-\alpha}$ , the complementary distribution is also power-law, with an exponent that is shifted by one,  $\Psi(t) \sim t^{-\alpha+1}$ , so plots of either the distribution or the complementary distribution can be used to identify power-law behavior.

### 3.8.0.2 Maximum Likelihood Estimation

To characterize and quantify the power-law behavior, we fit the waiting-time distributions,  $\psi_f$ , to a series of model distributions: power-law, power-law with exponential cutoff (power-law-exp), exponential, biexponential, stretched-exponential, and log-normal. The power-law-exp distribution is defined as

$$\psi_f(t) \sim t^{-\alpha} e^{-\beta t}, \quad (3.16)$$

with the appropriate normalization factor. Unlike the pure power-law distribution, the complementary distribution to the power-law-exp distribution is not power-law-exp. Instead it is an upper incomplete Gamma function

$$\Psi_f(t) \sim \Gamma(1 - \alpha, \beta t), \quad (3.17)$$

which behaves asymptotically as  $t^{-\alpha+1}$  for  $\beta t \rightarrow 0$  and as  $t^{-\alpha} e^{\beta t}$  for  $\beta t \rightarrow \infty$ . So, while the complementary distribution of a power-law-exp distribution is not exactly power-law-exp, it asymptotically converges to a power-law-exp distribution for large and small  $\beta t$ . One can find a probability dis-

tribution for which the complementary distribution is exactly power-law-exp:

$$\psi_f(t) \sim t^{-\alpha} e^{-\beta t} (1 - \alpha - \beta t). \quad (3.18)$$

We also fit the data to this distribution, which is equivalent to fitting the complementary probability  $\Psi_f$  to a power-law-exp distribution.

We use the maximum likelihood estimation (MLE) method to find the best-fit parameters for each of these models. This gives significantly less biased estimates of the best-fit parameters than least-squares fitting methods.<sup>99</sup> For the power-law, exponential, and log-normal distributions there are closed-form solutions for the MLE parameters. For the other distributions, we numerically maximize the likelihood. The power-law and power-law-exp distributions diverge at  $t = 0$ , so they must have some short-time cutoff,  $t_c$ , below which they do not apply (Figure 3.12a). MLE cannot be used to find this cutoff parameter, because as  $t_c$  changes, the data set changes size. Instead, we numerically minimize a Kolmogorov-Smirnov statistic,  $D$ , to find the optimum  $t_c$ . Because we are interested in the behavior of the tail of the distribution, we use the Anderson-Darling statistic, which is weighted to be equally sensitive over the entire domain of the distribution,

$$D = \max_{t > t_c} \frac{|\Psi(t) - \hat{\Psi}(t)|}{\sqrt{\hat{\Psi}(t)(1 - \hat{\Psi}(t))}}, \quad (3.19)$$

where  $\hat{\Psi}(t)$  is the model distribution with the best-fit parameters from MLE.<sup>99</sup> We perform likelihood ratio tests as described in Ref. 99, which suggest that the power-law-exp distribution is the best model to describe our data of those listed above, but these tests are too noisy to make any conclusive statements in this case. Because eqs. 3.16 and 3.18 predict the same power-law behavior and lead to the same qualitative conclusions, we henceforth limit ourselves to the case where  $\Psi_f$  is power-law-exp (eq. 3.18).

### 3.8.0.3 Clogging Transition

To summarize the MLE results, we find that on the most hydrophobic membranes, the waiting-time distributions we measure are best fit by a power-law distribution cutoff by an expo-

ponential at long times (Figure 3.11c). On the more hydrophilic membranes, and with apolar water, regardless of the hydrophobicity, a power-law-exp distribution is still a good fit, but the exponential cutoff is at much shorter times,  $\beta^{-1} \approx 10$  ps, so that the power-law part of the distribution is never the dominating factor (Figure 3.11d). On the hydrophobic membranes, the exponential cutoff happens at very long times,  $\beta^{-1} \approx 100 - 200$  ps, much longer than the timescale of any relevant dynamics in water. A power-law distribution of waiting times is characteristic of clogging,<sup>71</sup> a common phenomena in granular flows.<sup>71-73,100,101</sup> For a true clogged process, the waiting-time distribution is purely power-law at long times, with an exponent  $\alpha \leq 2$ . This corresponds to a divergent average waiting time

$$\langle t \rangle = \int_{t_c}^{\infty} dt t \psi(t) = \int_{t_c}^{\infty} dt t^{1-\alpha} \rightarrow \infty \quad \text{if } 0 < \alpha \leq 2, \quad (3.20)$$

which corresponds to the intuition of clogging, that once a clog has formed, another passage event will not happen without some external influence. Here, the MLE fits predict  $\alpha \approx 1.7$ , which, without the exponential cutoff, would correspond to a divergent average waiting time. Without the exponential cutoff, the system would not be able to reach steady state because it would be nonergodic.<sup>102</sup> We postulate that the exponential cutoff is due to the finite size of the system, which limits the maximum wavelength of density fluctuations. Also, because the membrane is atomically thin, the capillary-wave fluctuations may be particularly relevant to transport across the pore. The pore could act as a window function that filters the power-law spectrum of the capillary waves, resulting in the power law with exponential cutoff that we observe.<sup>24,90</sup>

For clogged processes, the power-law waiting-time distribution should be accompanied by an exponential burst-size distribution.<sup>71-75,100</sup> The separation in timescales for the hydrophobic sheet in Figure 3.10 is evident. This time series is punctuated by long pauses and large jumps, or bursts. A burst is a set of events that occur without a pause time greater than  $t_c$  between consecutive events (Figure 3.12b).<sup>71</sup> Figure 3.12a shows  $t_c$  for a particular waiting-time distribution. In our data,  $t_c$  is always between 1 and 10 ps. The burst size is the net number of molecules that passed through the membrane during a burst. We find that the burst-size distribution is exponential,

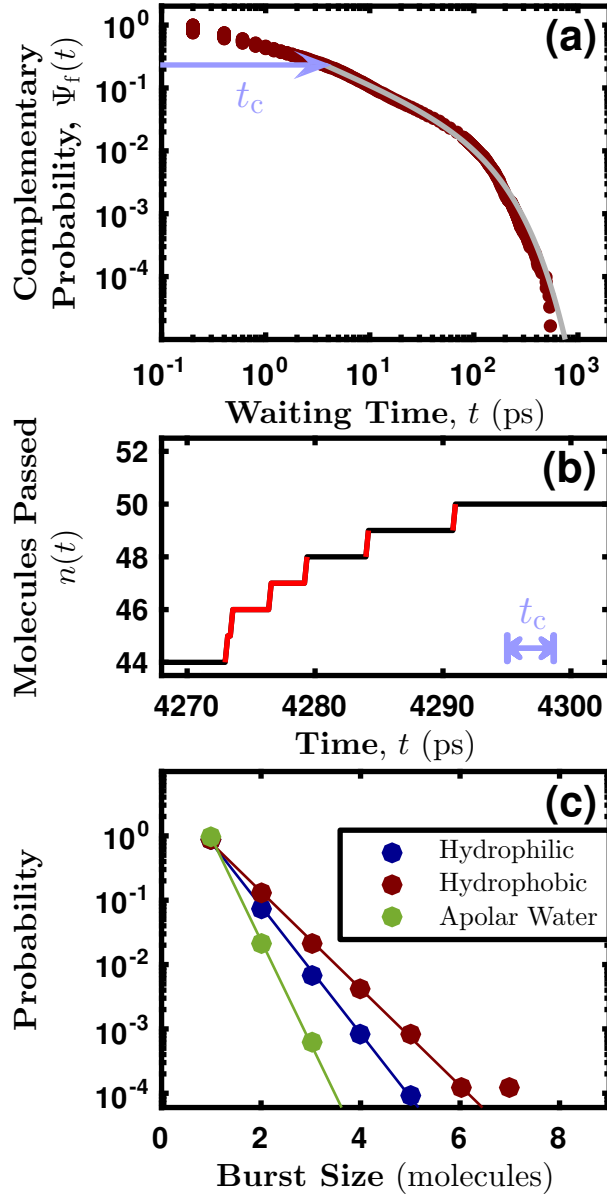


Figure 3.12: (a) The MLE fit (gray line) of eq. 3.18 to the complementary waiting-time distribution on the hydrophobic membrane shown in Figures 3.10 and 3.11c (black). The short time cutoff  $t_c$  is shown in blue. (b) Any waiting time that is longer than  $t_c$  (blue) starts a new burst (red). This shows two bursts of size one and one burst of size four. (c) The burst sizes are exponentially distributed for the same systems shown in Figures 3.11c,d: SPC/E water on a hydrophilic (blue) and hydrophobic (red) membrane, and apolar water on a hydrophobic membrane (green). This is another hallmark of a clogging transition.<sup>71</sup>

as expected for a clogged process (Figure 3.12c). The burst size can be zero or negative, but Figure 3.12c only shows the probability for positive burst sizes.

The clogging behavior we observe is commonplace in granular flows, but has never to our knowledge been observed in a molecular fluid. This behavior is not unreasonable given that, on the scale of the pore, water *is* granular. The behavior we observe, however, cannot be explained solely by the granular nature of water on these length scales. If that were the case, we would observe the same behavior for apolar water. Instead, we find no evidence of clogging in apolar water, even on the most hydrophobic membranes (Figure 3.11d). In granular flows, arch structures form at the opening, causing frustration and clogging.<sup>71,73,75</sup> Here, we postulate that the hydrogen bonding network in water causes long range frustration that leads to clogging. In apolar water, this long ranged hydrogen bonding network is not present, so clogging does not take place. It is also possible that hydrogen bonds stabilize arch structures in water that are unstable in apolar water at the same density. Further, our apolar water model is equivalent to a LJ fluid at  $T = 3.8 \epsilon/k_B$  and  $\rho = 1.0 \sigma^{-3}$ , which is deep into the regime of the supercritical fluid phase.<sup>103</sup> It is tempting to think that the absence of clogging is due to the low viscosity of a supercritical fluid, but in fact, its viscosity is comparable to or *higher* than that of the dense liquid phase.<sup>104</sup>

### 3.9 Linear Response Theory in Dry Nanopores

The permeability is related to a transport coefficient, and can therefore be computed using linear response theory.<sup>43</sup> Linear response theory is at the heart of nonequilibrium statistical mechanics, and uses the natural fluctuations around an equilibrium reference state to describe how the system behaves away from equilibrium.<sup>98,105</sup> For the least permeable sheets, the pressure differential is so large that the system could be pushed into the nonlinear regime (Figure 3.13). If one regards the permeability as the hydrodynamic analog of electrical conductivity, where voltage plays the role of the pressure differential, the current–pressure drop ( $q$ – $\Delta P$ ) relationship sketched in Figure 3.13 looks like the current-voltage characteristic of a diode, which is clearly nonlinear.<sup>106</sup> In this section, we turn again to thermodynamics to show that such an apparently nonlinear relationship can be

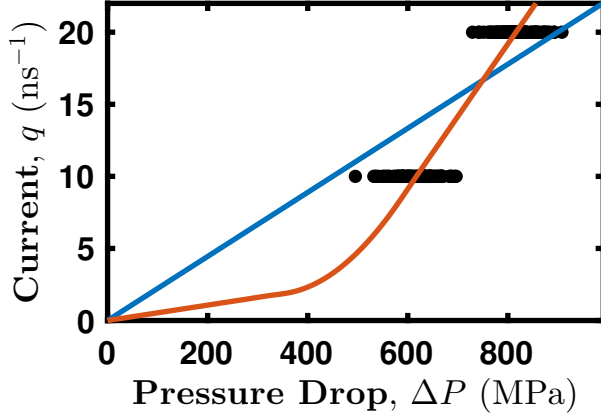


Figure 3.13: On a very hydrophobic ( $\theta = 128^\circ$ ) double-layer atomic membrane, the relationship between the current and the pressure drop is not linear with zero intercept. The black points show the results from 192 GD simulations. Naively applying eq. 3.3 to compute the permeability by fitting yields the conventional permeability (blue). The orange line shows an example of a nonlinear description for the relationship that fits both the data and the equilibrium system that necessarily has zero current and zero pressure drop.

made to obey linear response in the right reference state.<sup>107</sup>

Increasing the contact angle from about  $30^\circ$ , the permeability of an atomically thin membrane increases monotonically until the dewetting transition, where the channel dries and the permeability decreases abruptly. The terms dry and wet state are anecdotal, but in molecular scale systems like these, spontaneous transient fluctuations between the binary states do occur. The maximum permeability occurs near the critical dewetting contact angle, which depends on the channel geometry, particularly the aspect ratio. As the pore becomes drier, fluctuations into the wet state become more rare, and a larger applied pressure drop is required to induce the fluctuations into the wet state that allow transport. This pressure drop forces the system far from the equilibrium state, possibly into the nonlinear  $q-\Delta P$  regime (Figure 3.13). Were such a nonlinear description accurate, one would need to abandon basic linear response theory and describe the transport process with a differential permeability.

Linear response relies on the notion that a system that is fluctuating about a stable reference state cannot distinguish between an equilibrium fluctuation and a small external perturbation.

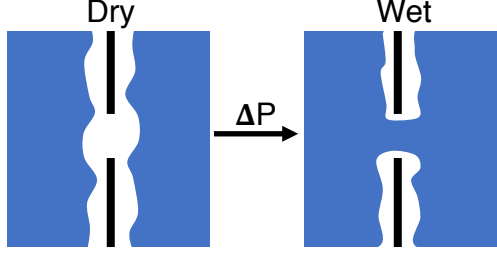


Figure 3.14: On hydrophobic membranes, past the dewetting transition, fluctuations into the wet state are rare, but a large enough applied pressure drop  $\Delta P$  wets the pore and allows passage.

Under the action of a generalized force  $f$  the nonequilibrium average  $\bar{A}$  is linear in  $f$ ,

$$\bar{A} = \langle A \rangle_{\text{ref}} + \chi_{\text{ref}} f, \quad (3.21)$$

where  $\langle \cdot \rangle_{\text{ref}}$  is an average in the reference (unperturbed) ensemble and  $\chi_{\text{ref}}$  is the susceptibility computed in the reference state. In this context, the observable is the current  $A \equiv q$  and the force is the applied pressure drop  $f \equiv \Delta P$ . For a very hydrophobic membrane, the reference state is ambiguous. Both wet and dry states are dynamically metastable and the transitions between them become more frequent as  $\Delta P$  becomes larger. An alternative to the nonlinear description of the  $q-\Delta P$  relationship sketched in Figure 3.13 is a two-step process for passage in which the pore must first wet under a large applied pressure drop  $\Delta P$  before passage can occur (Figure 3.14).

In the simplest possible manifestation of this two-step process, the transport is still in the linear regime after the initial wetting step. We apply this model to our nonequilibrium  $q-\Delta P$  data by fitting the  $q-\Delta P$  relationship to a line with nonzero intercept (Figure 3.15a). We call the slope of this line the “wet permeability”, because it is equivalent to the linear response permeability computed with respect to the wet reference state. Below the dewetting transition, the wet permeabilities match those from Section 3.6, as they should, since there is no dry state (Figure 3.15b). The small differences between the wet and conventional permeabilities here are simply due to errors in the fitting process. At the dewetting transition, the wet permeability decreases along with the conventional permeability, but then increases past the transition.

In the conventional picture, the  $q-\Delta P$  relationship is completely specified by a single pa-

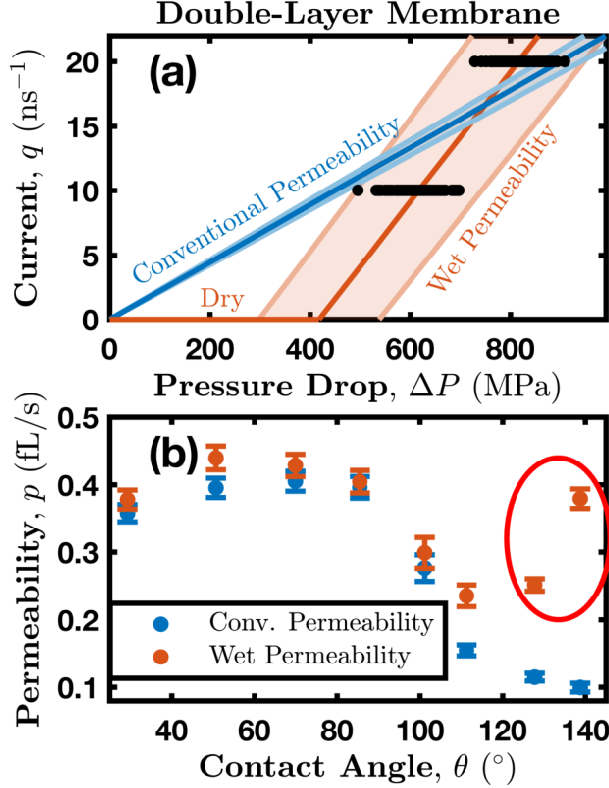


Figure 3.15: (a) On very hydrophobic ( $\theta = 128^\circ$ ) double-layer atomic membranes, the relationship between the current and the pressure drop is not linear with zero intercept. We fit the results from 192 GD simulations (black) to lines with zero (blue) and nonzero intercept (orange). The orange line describes a two-step process for passage (see the text). The pore first wets under a large applied pressure drop (orange “Dry” segment) and then passage occurs with the usual linear  $q-\Delta P$  relationship (“wet permeability”). The shaded regions show the standard error on the fits. (b) The slope of the blue line in (a) gives the conventional permeability used in Section 3.6 (eq. 3.3), while the slope of the orange line gives the wet permeabilities. The wet permeability follows the same trend as the conventional permeability below the dewetting transition, as it should, but above the dewetting transition, it increases.

parameter, the slope or permeability (eq. 3.3). The conventional permeability fundamentally cannot capture a nonlinear  $q-\Delta P$  relationship because, like a differential resistance, it depends on the range of values of  $q$  sampled in the simulations. For simulations that use the same values of  $q$  as in Section 3.6, the conventional permeability can still give a qualitative picture, in which increased resistance to passage results in a lower permeability, but it does not give the whole picture. An accurate description of the transport must recognize that it is a two-step process. This two-step process requires two parameters instead of one, the threshold pressure  $\Delta P_T$  which is the intercept

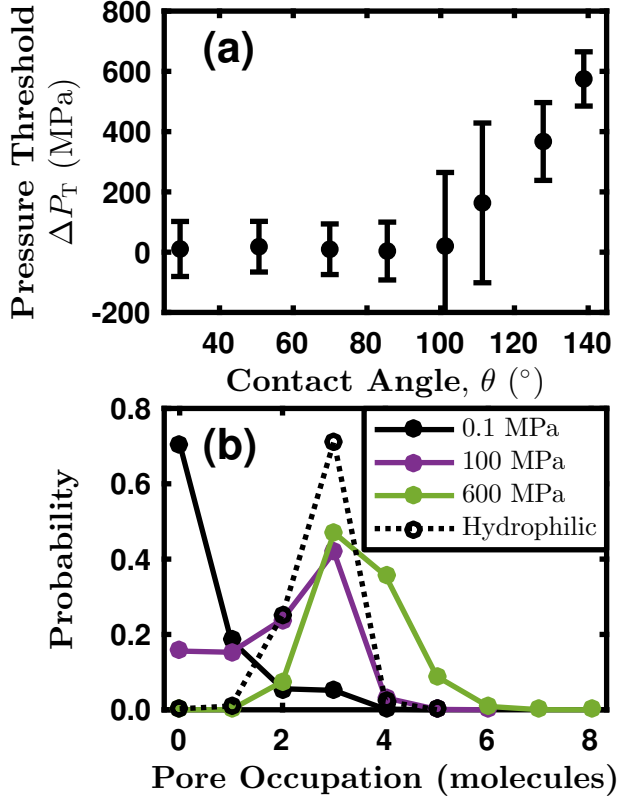


Figure 3.16: (a) The pressure threshold for a double-layer atomic membrane as a function of the contact angle computed from the intercept of the  $q-\Delta P$  relationship along the abscissa in Figure 3.15a. At the dewetting transition, this pressure threshold becomes nonzero. (b) The number of water molecules in the pore region (Section 3.3.3) as a function of the pressure at equilibrium. At 1 atm (0.1 MPa), the hydrophobic membrane ( $\theta = 128^{\circ}$ , solid black) is dry and the hydrophilic membrane ( $\theta = 29^{\circ}$ , dotted black) is wet. Increasing the external pressure (purple and green) wets the hydrophobic pore. While the dewetting transition is not sharp, it occurs near the pressure threshold shown in (a).

on the abscissa in Figure 3.15a, and the slope past  $\Delta P_T$ . The slope is related to the permeability in the usual way and  $\Delta P_T$  is the pressure threshold for wetting the pore away from equilibrium.

We compute the pressure threshold from the intercept of the linear fit to the nonequilibrium  $q-\Delta P$  data (Figure 3.15a). The pressure threshold is roughly zero below the dewetting transition, as expected, and then increases past it (Figure 3.16a). From a practical RO perspective, the wet permeabilities shown in Figure 3.15a imply that a very hydrophobic membrane ( $\theta \approx 140^{\circ}$ ) is almost as permeable as the optimal membrane with  $\theta \approx 80^{\circ}$ . This is misleading, however, because the performance of an RO device depends on the entire  $q-\Delta P$  relationship, not just its slope. For

an RO facility to take advantage of the high permeability of hydrophobic membranes, it would need to operate at applied pressures above the wetting pressure of the pores, which is clearly not feasible (Figure 3.16a). Note that the fluctuations in the pressure threshold peak at the dewetting transition, analogous to the susceptibility at a second order phase transition (Figure 3.16a).

Equilibrium simulations at varying pressures show that the nonequilibrium pressure threshold roughly corresponds to the equilibrium wetting pressure of the pore (Figure 3.16b). At 1 atm, a hydrophobic membrane is in a dry state at equilibrium, and the pore is most likely empty. As the external pressure increases, the peak in the pore occupation distribution shifts to three molecules, which corresponds to the wet state seen on hydrophilic membranes (Figure 3.16b). In these finite systems, where the difference between the wet and dry states depends on the occupation of three molecules, the dewetting transition is far from sharp. This makes it difficult to specify a precise equilibrium wetting pressure, but the equilibrium wetting pressures are on the order of 100s of MPa, similar to the nonequilibrium pressure thresholds (Figure 3.16a). The pressure intercept of the  $q-\Delta P$  relationship is a nonequilibrium pressure threshold for wetting the pore. It is an upper bound for the true equilibrium wetting pressure. The two are equal only when the transport process is reversible. Note that the occupation probabilities in Figure 3.16b are more broad than Poisson distributions, which is what one would expect if the number occupation statistics were independent and uncorrelated.

The two-step transport process describes a linear  $q-\Delta P$  relationship with nonzero intercept. At equilibrium, however, any system has both zero current and zero pressure drop, so any valid  $q-\Delta P$  relationship must go through the origin. The  $q-\Delta P$  relationship must therefore have two segments, one linear with nonzero intercept, and a flat segment that connects the origin to the pressure intercept (Figure 3.15a). The two segments of the  $q-\Delta P$  relationship correspond to the two steps in the passage process and the two possible reference states for linear response theory.

The linear response permeability with respect to the wet state is computed in an equilibrium system at a pressure above the wetting pressure (Figure 3.16b). For very hydrophobic pores, like those we study here, the equilibrium state at ambient pressure is the dry state, so the linear

response permeability with respect to the dry state is computed using equilibrium systems at ambient pressure. When computed in the wet reference state, permeabilities evaluated in linear response roughly match the nonequilibrium wet permeabilities shown in Figure 3.15b. The linear response permeabilities average poorly, which is the reason for studying them with nonequilibrium techniques (Section 3.5).

For a hypothetical macroscopic pore with a true thermodynamic dewetting transition, the linear response permeability computed with respect to the dry state would be vanishingly small because the probability for fluctuations that allow water to cross the dry pore tend towards zero in the thermodynamic limit. In this limit, the first segment of the  $q-\Delta P$  relationship has a slope near zero, as illustrated in Figure 3.15a. Our system, however, does not have a sharp thermodynamic dewetting transition. In the dry state, there are always fluctuations that wet the pore; there is almost a 30% chance of finding a molecule in the pore (Figure 3.16b). Some form of the nonlinear description shown in Figure 3.13 with a non-negligible initial slope is therefore always strictly correct. It remains to be shown that the large system limit and the corresponding simple linear  $q-\Delta P$  relationship in Figure 3.15a is in fact valid for these systems.

In these atomically thin membranes, with pores that admit only single file water, one might suspect that the large system limit (Figure 3.15a) of the general nonlinear relationship (Figure 3.13) is invalid. Indeed, the average pore occupation is around three molecules, a far cry from the thermodynamic limit (Figure 3.16b). In Section 3.6, we show that a simple macroscopic thermodynamic argument captures the dewetting contact angle surprisingly well, but this may not extend to more detailed observables like the wetting pressure. To justify the large system limit, we generalize this thermodynamic argument by allowing for more complex pore geometries.

For the thermodynamic analysis, we assume the pore volume is an hourglass shaped solid of revolution about the pore axis and symmetric about the plane of the membrane. The grand

potentials for the liquid and vapor phases inside the pore are<sup>27</sup>

$$\Omega_\ell = -P_\ell V + \gamma_{s\ell} A_{\text{side}} \quad (3.22)$$

$$\Omega_v = -P_v V + \gamma_{sv} A_{\text{side}} + 2\gamma_{\ell v} A_{\text{cap}} \quad (3.23)$$

where  $A_{\text{side}}$  is the area of the side of the solid of revolution,  $A_{\text{cap}}$  is the area of one of the caps on the end of the solid,  $V$  is the volume of the region (Figure 3.17a), the  $\gamma$ s are surface tensions, and  $P_\ell$  and  $P_v$  are the pressures of the two phases. The absolute free energies in eqs. 3.22 and 3.23 depend on quantities like  $P_v$  that are meaningless in systems like ours, where the “vapor phase” is defined by the absence of about three molecules. But at the dewetting transition, only the free energy difference  $\Delta\Omega \equiv \Omega_v - \Omega_\ell$  is important, and these ill-defined quantities appear in comparison with well defined ones. At the dewetting transition, we have  $\Delta\Omega = 0$ , so

$$P_\ell^* \approx -\frac{\gamma_{\ell v}}{V}(A_{\text{side}} \cos \theta + 2A_{\text{cap}}), \quad (3.24)$$

where we used Young’s equation,  $\gamma_{v\ell} \cos \theta = \gamma_{sv} - \gamma_{s\ell}$ <sup>35</sup>,  $P_\ell^*$  is the critical wetting pressure, and we have neglected  $P_v$ , because the vapor pressure of water is five orders of magnitude smaller than the wetting pressures in Figure 3.16a.

We compare the nonequilibrium pressure thresholds (Figure 3.16a) to the thermodynamic wetting pressures predicted by eq. 3.24. In Section 3.6, the pore was assumed to have a cylindrical volume with the length and radius determined by the pore size and equilibrium water density (Table 3.1). There, these assumptions gave a reasonable qualitative agreement with the critical contact angle observed in nonequilibrium simulation. Here, these assumptions reproduce the same qualitative trend in wetting pressure that we observe, but the agreement is unsatisfying (Figure 3.17b). We now explore more complex pore geometries, which are perhaps more faithful to the true “thermodynamic” surface. Further, instead of estimating the pore size from equilibrium density considerations, we turn the problem around, and ask the thermodynamics to predict the shape of the pore. To this end, we fit the pressure threshold data to the thermodynamic prediction to find the best-fit pore size parameters.

We fix the pore geometry to be the parabolic solid of revolution given by revolving

$$y(x) = ax^2 + r \quad (3.25)$$

about the  $x$ -axis. More complex solids require too many parameters and fits are underdefined by the simple form of the pressure threshold data (Figure 3.17b). The geometry of the pore defined by this revolved parabola depends on three parameters: its radius at the narrowest point  $r$ , its length  $L$ , and the curvature of the side wall  $a$ . The cylindrical case shown in Figure 3.17a corresponds to  $a = 0 \text{ \AA}^{-1}$ . We fit these parameters to the pressure threshold data in Figure 3.17b, treating a negative wetting pressure as a pressure threshold of zero. Since the nonzero data in Figure 3.17b appear linear, one might worry about fitting three parameters to these data, but with reasonable initial guesses, the fit converges well. Using  $\gamma_{\ell v} = 72.1 \text{ mJ/m}^2$  for water, the best fit pore geometry has  $L = 8.0 \text{ \AA}$ ,  $r = 1.3 \text{ \AA}$ , and  $a^{-1} = 64 \text{ \AA}$ , which describes the equilibrium water density in a wetted pore amazingly well (Figure 3.17c). It is phenomenal that a simple argument based on macroscopic thermodynamics can, in one stroke, capture both the equilibrium density of water inside the pore and the nonequilibrium wetting pressure for flow through the pore.

The surprising success of this macroscopic argument to capture the pressure threshold data suggests that the pressure threshold is indeed a valid concept in this system. If the wetting transition were not sharp, this would not be a valid concept, and we would be forced to understand the system in terms of the more complex nonlinear relationship presented in Figure 3.13. Instead, we find that the pressure threshold is valid, the transition is sharp, and the  $q - \Delta P$  relationship can be described by its slope and pressure intercept alone. While the nonlinear  $q - \Delta P$  relationship proposed in Figure 3.13 is strictly correct, this system is deep in the limit where the initial shallow slope is effectively zero, and the linear description is valid. This provides a simple, intuitive, and rich description of the passage process.

On single-layer membranes, there is not a sufficient distinction between the wet and dry states to perform a similar analysis. The critical dewetting contact angle is larger on single-layer membranes. As a result, the single-layer systems we explore in Section 3.6 do not exhibit a putative

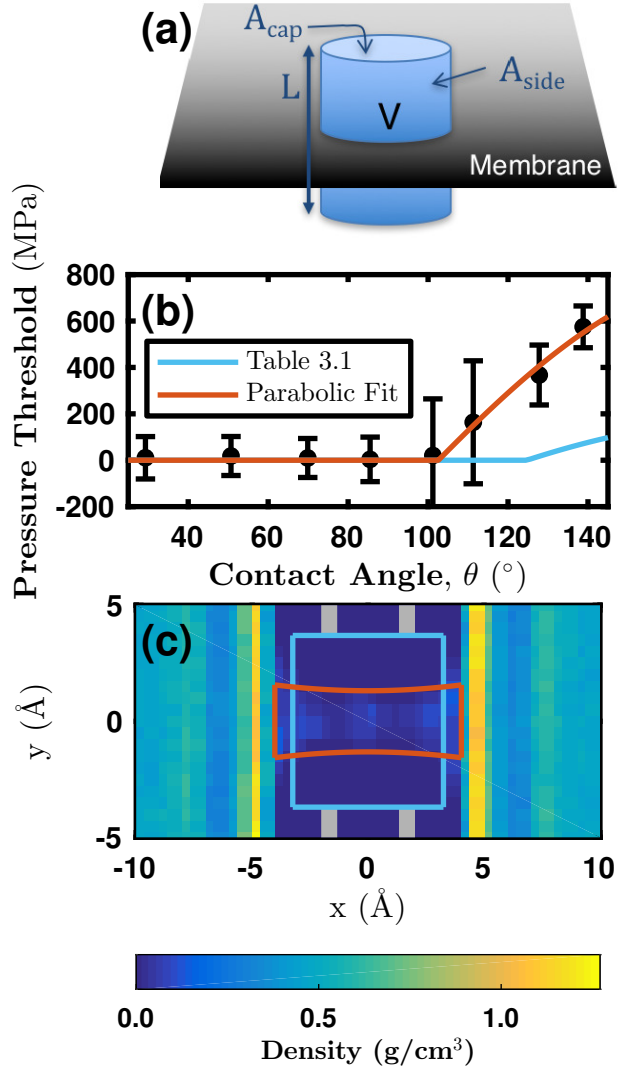


Figure 3.17: (a) A schematic showing a cylindrical pore volume with the area of the side  $A_{\text{side}}$ , the area of a cap  $A_{\text{cap}}$ , the volume  $V$ , and the length  $L$ . This can be easily generalized to an arbitrary solid of revolution, like the parabolic solid in panel (c). (b) The pressure threshold data shown in Figure 3.16a (black). The solid lines are predictions of the thermodynamic argument based on eq. 3.24 and panel (a). The blue line uses the pore geometry from Table 3.1 and illustrated in blue in panel (c). The red line uses a parabolic pore geometry (eq. 3.25) fit to the black points. The best fit geometry is shown in red in panel (c), with the equilibrium density of water in the background. The gray blocks in (c) are the edges of the pore in the membrane.

dry state. The existence of such a state, however, may be entirely washed out by fluctuations in a smaller single-layer pore volume. In either case, it is remarkable that this thermodynamic model captures the behavior of the double-layer membranes.

In very hydrophobic atomically thin porous membranes, the pores are dry at ambient pressure. Water transport in these membranes becomes a two-step process, where the externally applied pressure,  $\Delta P$  induces wetting, and transport occurs from the wet state. The water current is near zero until  $\Delta P > \Delta P_T$ . This two-step behavior is a simple nonlinearity with respect to the dry state at standard temperature and pressure. In the wet state, the system obeys linear response.

A similar explanation of, and resolution to, an apparently nonlinear phenomena has been proposed for aqueous solvation dynamics.<sup>107</sup> In the system we study, even with only three molecules in the pore, the pore is close enough to the macroscopic limit that the transition to the wet state is sharp and linear response theory about the wet state fully describes the transport process. This simple thermodynamic argument captures both the equilibrium density of water inside a pore and the wetting pressure for the dry pores.

From a naive perspective, a very hydrophobic pore has a high permeability. But in actual applications for reverse osmosis, one can only achieve this permeability after applying a pressure drop on the order of 0.5 GPa. Such large backing pressures are not only prohibitively large, they are likely to mechanically destroy the membranes.

### 3.10 Conclusion

In this Chapter, we employ our nonequilibrium MD tool, GD, to study the hydrodynamics of liquids moving through atomically small spaces. We probe the relationship between microscopic interactions and emergent macroscopic hydrodynamic quantities, like the slip length, channel permeability, and friction. These quantities are often material-specific inputs into hydrodynamic transport theories, and understanding their origin is critical for tailoring the chemistry of intermolecular interactions to control fluid flow on atomic and nanoscale dimensions. GD is a tool that may shed light on many interesting processes, but we focused attention on understanding how

water flows through porous 2d crystals because it is a process fundamental to next-generation RO membranes.<sup>39,40,42,48</sup>

The wetting contact angle is the most convenient measure of a substance's hydrophobicity, and here we use the wetting contact angle as a surrogate for the hydrophobicity. The contact angle is sensitive to the liquid-solid surface tension, and there are several equivalent ways to tune the surface tension that differ in their microscopic details. Doping a graphene sheet with electrons or holes both decrease the contact angle, yet the permeability is a monotonically decreasing function of the sheet's charge.<sup>45</sup> A Markov model reveals that the asymmetry of the permeability as a function of voltage can be explained in molecular terms, by a transition from a concerted translocation transport mechanism to an evaporation-condensation mechanism. Because the transport process is bottlenecked by only a few water molecules for pores of these sizes, the collective aspects of hydrophobicity have little bearing on the dynamics of water passage.

Electrical doping is an experimentally realizable method for tuning the hydrophobicity of graphene, but there are other 2d crystals that are promising in fluid separation applications, like MoS<sub>2</sub> and BN. We model the effect of changing a membrane's chemical composition by tuning the van der Waals interaction strength between membrane atoms and the water molecules in electrically neutral single- and double-layer membranes. Small changes of the LJ  $\epsilon$  parameter, on the order of fractions of  $k_B T$ , lead to dramatic changes in both the wetting contact angle and the permeability of atomic membranes. Just like charged membranes, the permeability is not a simple function of the contact angle. While the contact angle does not predict the permeability, the thermodynamic theory of dewetting does predict the observed onset of a threshold in the permeability.<sup>27</sup> The permeability increases dramatically if there is a thermodynamic driving force for the pore to wet, suggesting a tenuous connection to capillary action in this system. Once the pore wets, increasing the strength of the van der Waals attractions between the membrane and the water increases the friction and decreases the permeability. This competition, between the static hydrophobicity that drives wetting and the dynamical hydrophobicity that modulates friction, produces a "Goldilocks zone" for the optimum permeability as a function of the hydrophobicity of neutral atomic membranes. From a

practical perspective, for membranes that are much less than one micron in length, the optimal contact angle can simply be estimated from the aspect ratio of the channel in the membrane.

Finally, we find qualitative differences between the most hydrophilic and hydrophobic membranes for the statistics of water passage. In the extremely hydrophobic cases, water moves across the membrane in a series of fits and starts, punctuated by long pauses and rapid bursts. A continuous-time, one-step Markov model of the process shows that the waiting-time distribution exhibits a power-law decay over about two decades in time, from about 1–100 ps, with an exponential cutoff. The burst-size distribution exhibits an exponential decay. These two features, a power law in the waiting-time distribution and an exponential distribution of burst sizes, are both hallmarks of the clogging transition observed in a wide variety of systems, including driven granular flows.<sup>71–75,100</sup> The clogging we observe here, however, cannot be attributed entirely to the granular nature of water on these atomic length scales, because it is absent in “apolar water”, a simple liquid that has the same mass, density, temperature, and van der Waals parameters as SPC/E water, but no charges. Because apolar water cannot form hydrogen bonds, we postulate that the frustrated transport of water through very hydrophobic membranes is rooted in its hydrogen bond network rather than the kind of geometrical or steric crowding one observes in granular systems.

## Bibliography

- [1] Strong, S. E.; Eaves, J. D. Atomistic hydrodynamics and the dynamical hydrophobic effect in porous graphene. *J. Phys. Chem. Lett.*, 7(10):1907–1912, **2016**.
- [2] Strong, S. E.; Eaves, J. D. The dynamics of water in porous two-dimensional crystals. *J. Phys. Chem. B*, 121(1):189–207, **2017**.
- [3] Strong, S. E.; Eaves, J. D. Linear response theory for water transport through dry nanopores. **2017**. Submitted.
- [4] Chandler, D. Interfaces and the driving force of hydrophobic assembly. *Nature*, 437(7059):640–647, **2005**.
- [5] Patel, A. J.; Garde, S. Efficient method to characterize the context-dependent hydrophobicity of proteins. *J. Phys. Chem. B*, 118(6):1564–1573, **2014**.

- [6] Xi, E.; Patel, A. J. The hydrophobic effect, and fluctuations: The long and the short of it. *Proc. Nat. Acad. Sci. U. S. A.*, 113(17):4549–4551, **2016**.
- [7] Li, I. T. S.; Walker, G. C. Signature of hydrophobic hydration in a single polymer. *Proc. Nat. Acad. Sci. U. S. A.*, 108(40):16527–16532, **2011**.
- [8] Davis, J. G.; Gierszal, K. P.; Wang, P.; Ben-Amotz, D. Water structural transformation at molecular hydrophobic interfaces. *Nature*, 491(7425):582–585, **2012**.
- [9] Zhou, R.; Huang, X.; Margulis, C. J.; Berne, B. J. Hydrophobic collapse in multidomain protein folding. *Science*, 305(5690):1605–1609, **2004**.
- [10] Baldwin, R. L. Temperature dependence of the hydrophobic interaction in protein folding. *Proc. Nat. Acad. Sci. U. S. A.*, 83(21):8069–8072, **1986**.
- [11] Tanford, C. The hydrophobic effect and the organization of living matter. *Science*, 200(4345):1012–1018, **1978**.
- [12] Stillinger, F. H. Water revisited. *Science*, 209(4455):451–457, **1980**.
- [13] Zhang, X.; Zhu, Y.; Granick, S. Hydrophobicity at a Janus interface. *Science*, 295(5555):663–666, **2002**.
- [14] Petersen, C.; Tielrooij, K.-J.; Bakker, H. J. Strong temperature dependence of water reorientation in hydrophobic hydration shells. *J. Chem. Phys.*, 130(21):214511, **2009**.
- [15] Buchanan, P.; Aldiwan, N.; Soper, A. K.; Creek, J. L.; Koh, C. A. Decreased structure on dissolving methane in water. *Chem. Phys. Lett.*, 415(1–3):89–93, **2005**.
- [16] Laage, D.; Stirnemann, G.; Hynes, J. T. Why water reorientation slows without iceberg formation around hydrophobic solutes. *J. Phys. Chem. B*, 113(8):2428–2435, **2009**.
- [17] Raschke, T. M.; Levitt, M. Nonpolar solutes enhance water structure within hydration shells while reducing interactions between them. *Proc. Nat. Acad. Sci. U. S. A.*, 102(19):6777–6782, **2005**.
- [18] Matysiak, S.; Debenedetti, P. G.; Rossky, P. J. Dissecting the energetics of hydrophobic hydration of polypeptides. *J. Phys. Chem. B*, 115(49):14859–14865, **2011**.
- [19] Lee, C.-Y.; McCammon, J. A.; Rossky, P. J. The structure of liquid water at an extended hydrophobic surface. *J. Chem. Phys.*, 80(9):4448–4455, **1984**.
- [20] Wallqvist, A.; Berne, B. J. Computer simulation of hydrophobic hydration forces on stacked plates at short range. *J. Phys. Chem.*, 99(9):2893–2899, **1995**.
- [21] Lum, K.; Chandler, D.; Weeks, J. D. Hydrophobicity at small and large length scales. *J. Phys. Chem. B*, 103(22):4570–4577, **1999**.
- [22] Pratt, L. R.; Chandler, D. Theory of the hydrophobic effect. *J. Chem. Phys.*, 67(8):3683–3704, **1977**.
- [23] Hummer, G.; Garde, S.; García, A. E.; Pohorille, A.; Pratt, L. R. An information theory model of hydrophobic interactions. *Proc. Nat. Acad. Sci. U. S. A.*, 93(17):8951–8955, **1996**.

- [24] Vaikuntanathan, S.; Geissler, P. L. Putting water on a lattice: The importance of long wavelength density fluctuations in theories of hydrophobic and interfacial phenomena. *Phys. Rev. Lett.*, 112(2):020603, **2014**.
- [25] Vaikuntanathan, S.; Rotskoff, G.; Hudson, A.; Geissler, P. L. Necessity of capillary modes in a minimal model of nanoscale hydrophobic solvation. *Proc. Nat. Acad. Sci. U. S. A.*, 113(16):E2224–E2230, **2016**.
- [26] Wallqvist, A.; Gallicchio, E.; Levy, R. M. A model for studying drying at hydrophobic interfaces: Structural and thermodynamic properties. *J. Phys. Chem. B*, 105(28):6745–6753, **2001**.
- [27] Huang, X.; Margulis, C. J.; Berne, B. J. Dewetting-induced collapse of hydrophobic particles. *Proc. Nat. Acad. Sci. U. S. A.*, 100(21):11953–11958, **2003**.
- [28] Maibaum, L.; Dinner, A. R.; Chandler, D. Micelle formation and the hydrophobic effect. *J. Phys. Chem. B*, 108(21):6778–6781, **2004**.
- [29] Giovambattista, N.; Lopez, C. F.; Rossky, P. J.; Debenedetti, P. G. Hydrophobicity of protein surfaces: Separating geometry from chemistry. *Proc. Nat. Acad. Sci. U. S. A.*, 105(7):2274–2279, **2008**.
- [30] Giovambattista, N.; Debenedetti, P. G.; Rossky, P. J. Hydration behavior under confinement by nanoscale surfaces with patterned hydrophobicity and hydrophilicity. *J. Phys. Chem. C*, 111(3):1323–1332, **2007**.
- [31] Zhang, M.; Nguyen, Q. T.; Ping, Z. Hydrophilic modification of poly (vinylidene fluoride) microporous membrane. *J. Membrane Sci.*, 327(1–2):78–86, **2009**.
- [32] Hatakeyama, E. S.; Ju, H.; Gabriel, C. J.; Lohr, J. L.; Bara, J. E.; Noble, R. D.; Freeman, B. D.; Gin, D. L. New protein-resistant coatings for water filtration membranes based on quaternary ammonium and phosphonium polymers. *J. Membrane Sci.*, 330(1–2):104–116, **2009**.
- [33] Schellenberger, F.; Encinas, N.; Vollmer, D.; Butt, H.-J. How water advances on superhydrophobic surfaces. *Phys. Rev. Lett.*, 116(9):096101, **2016**.
- [34] de Gennes, P. G. Wetting: Statics and dynamics. *Rev. Mod. Phys.*, 57(3):827–863, **1985**.
- [35] Young, T. An essay on the cohesion of fluids. *Phil. Trans. R. Soc. Lond.*, 95:65–87, **1805**.
- [36] Joanny, J. F.; de Gennes, P. G. A model for contact angle hysteresis. *J. Chem. Phys.*, 81(1):552–562, **1984**.
- [37] Gao, L.; McCarthy, T. J. Contact angle hysteresis explained. *Langmuir*, 22(14):6234–6237, **2006**.
- [38] Law, K.-Y.; Zhao, H. What do contact angles measure? In *Surface Wetting*, pages 99–121. Springer International Publishing, **2016**.
- [39] Suk, M. E.; Aluru, N. R. Water transport through ultrathin graphene. *J. Phys. Chem. Lett.*, 1(10):1590–1594, **2010**.

- [40] Cohen-Tanugi, D.; Grossman, J. C. Water desalination across nanoporous graphene. *Nano Lett.*, 12(7):3602–3608, **2012**.
- [41] Cohen-Tanugi, D.; Grossman, J. C. Water permeability of nanoporous graphene at realistic pressures for reverse osmosis desalination. *J. Chem. Phys.*, 141(7):074704, **2014**.
- [42] Surwade, S. P.; Smirnov, S. N.; Vlassiouk, I. V.; Unocic, R. R.; Veith, G. M.; Dai, S.; Mahurin, S. M. Water desalination using nanoporous single-layer graphene. *Nat. Nanotechnol.*, 10(5):459–464, **2015**.
- [43] Zhu, F.; Tajkhorshid, E.; Schulten, K. Collective diffusion model for water permeation through microscopic channels. *Phys. Rev. Lett.*, 93(22):224501, **2004**.
- [44] Dashtpour, R.; Al-Zubaidy, S. N. Energy efficient reverse osmosis desalination process. *Int. J. Environ. Sci. Develop.*, 3(4):339, **2012**.
- [45] Ostrowski, J. H. J.; Eaves, J. D. The tunable hydrophobic effect on electrically doped graphene. *J. Phys. Chem. B*, 118(2):530–536, **2014**.
- [46] Farmer, D. B.; Golizadeh-Mojarad, R.; Perebeinos, V.; Lin, Y.-M.; Tulevski, G. S.; Tsang, J. C.; Avouris, P. Chemical doping and electron-hole conduction asymmetry in graphene devices. *Nano Lett.*, 9(1):388–392, **2009**.
- [47] Bao, W.; Myhro, K.; Zhao, Z.; Chen, Z.; Jang, W.; Jing, L.; Miao, F.; Zhang, H.; Dames, C.; Lau, C. N. In situ observation of electrostatic and thermal manipulation of suspended graphene membranes. *Nano Lett.*, 12(11):5470–5474, **2012**.
- [48] Heiranian, M.; Farimani, A. B.; Aluru, N. R. Water desalination with a single-layer MoS<sub>2</sub> nanopore. *Nat. Commun.*, 6:8616, **2015**.
- [49] Xue, M.; Qiu, H.; Guo, W. Exceptionally fast water desalination at complete salt rejection by pristine graphyne monolayers. *Nanotechnology*, 24(50):505720, **2013**.
- [50] Lei, W.; Portehault, D.; Liu, D.; Qin, S.; Chen, Y. Porous boron nitride nanosheets for effective water cleaning. *Nat. Commun.*, 4:1777, **2013**.
- [51] Garnier, L.; Szymczyk, A.; Malfreyt, P.; Ghoufi, A. Physics behind water transport through nanoporous boron nitride and graphene. *J. Phys. Chem. Lett.*, pages 3371–3376, **2016**.
- [52] Miró, P.; Audiffred, M.; Heine, T. An atlas of two-dimensional materials. *Chem. Soc. Rev.*, 43(18):6537, **2014**.
- [53] Huang, X.; Zhou, R.; Berne, B. J. Drying and hydrophobic collapse of paraffin plates. *J. Phys. Chem. B*, 109(8):3546–3552, **2005**.
- [54] Lum, K.; Luzar, A. Pathway to surface-induced phase transition of a confined fluid. *Phys. Rev. E*, 56(6):R6283–R6286, **1997**.
- [55] Bolhuis, P. G.; Chandler, D. Transition path sampling of cavitation between molecular scale solvophobic surfaces. *J. Chem. Phys.*, 113(18):8154–8160, **2000**.
- [56] Brovchenko, I.; Geiger, A.; Oleinikova, A. Water in nanopores: II. The liquid-vapour phase transition near hydrophobic surfaces. *J. Phys.: Condens. Matter*, 16(45):S5345, **2004**.

- [57] Joseph, S.; Aluru, N. R. Why are carbon nanotubes fast transporters of water? *Nano Lett.*, 8(2):452–458, **2008**.
- [58] Liu, L.; Patey, G. N. Simulated conduction rates of water through a (6,6) carbon nanotube strongly depend on bulk properties of the model employed. *J. Chem. Phys.*, 144(18):184502, **2016**.
- [59] Kalra, A.; Garde, S.; Hummer, G. Osmotic water transport through carbon nanotube membranes. *Proc. Nat. Acad. Sci. U. S. A.*, 100(18):10175–10180, **2003**.
- [60] Thomas, J. A.; McGaughey, A. J. H. Reassessing fast water transport through carbon nanotubes. *Nano Lett.*, 8(9):2788–2793, **2008**.
- [61] Kannam, S. K.; Todd, B. D.; Hansen, J. S.; Daivis, P. J. How fast does water flow in carbon nanotubes? *J. Chem. Phys.*, 138(9):094701, **2013**.
- [62] Walther, J. H.; Ritos, K.; Cruz-Chu, E. R.; Megaridis, C. M.; Koumoutsakos, P. Barriers to superfast water transport in carbon nanotube membranes. *Nano Lett.*, 13(5):1910–1914, **2013**.
- [63] Falk, K.; Sedlmeier, F.; Joly, L.; Netz, R. R.; Bocquet, L. Molecular origin of fast water transport in carbon nanotube membranes: Superlubricity versus curvature dependent friction. *Nano Lett.*, 10(10):4067–4073, **2010**.
- [64] Kannam, S. K.; Todd, B. D.; Hansen, J. S.; Daivis, P. J. Slip length of water on graphene: Limitations of non-equilibrium molecular dynamics simulations. *J. Chem. Phys.*, 136(2):024705, **2012**.
- [65] Koplik, J.; Banavar, J. R.; Willemsen, J. F. Molecular dynamics of fluid flow at solid surfaces. *Phys. Fluids A.*, 1(5):781–794, **1989**.
- [66] Galea, T. M.; Attard, P. Molecular dynamics study of the effect of atomic roughness on the slip length at the fluid-solid boundary during shear flow. *Langmuir*, 20(8):3477–3482, **2004**.
- [67] Barrat, J.-L.; Bocquet, L. Large slip effect at a nonwetting fluid-solid interface. *Phys. Rev. Lett.*, 82(23):4671–4674, **1999**.
- [68] Cottin-Bizonne, C.; Barentin, C.; Charlaix, É.; Bocquet, L.; Barrat, J.-L. Dynamics of simple liquids at heterogeneous surfaces: Molecular-dynamics simulations and hydrodynamic description. *Eur. Phys. J. E*, 15(4):427–438, **2004**.
- [69] Sokhan, V. P.; Nicholson, D.; Quirke, N. Fluid flow in nanopores: Accurate boundary conditions for carbon nanotubes. *J. Chem. Phys.*, 117(18):8531–8539, **2002**.
- [70] Thomas, M.; Corry, B. Thermostat choice significantly influences water flow rates in molecular dynamics studies of carbon nanotubes. *Microfluid. Nanofluid.*, 18(1):41–47, **2014**.
- [71] Zuriguel, I.; Parisi, D. R.; Hidalgo, R. C.; Lozano, C.; Janda, A.; Gago, P. A.; Peralta, J. P.; Ferrer, L. M.; Pugnaloni, L. A.; Clément, E.; et al. Clogging transition of many-particle systems flowing through bottlenecks. *Sci. Rep.*, 4:7324, **2014**.
- [72] Lafond, P. G.; Gilmer, M. W.; Koh, C. A.; Sloan, E. D.; Wu, D. T.; Sum, A. K. Orifice jamming of fluid-driven granular flow. *Phys. Rev. E*, 87(4):042204, **2013**.

- [73] To, K.; Lai, P.-Y.; Pak, H. K. Jamming of granular flow in a two-dimensional hopper. *Phys. Rev. Lett.*, 86(1):71–74, **2001**.
- [74] Helbing, D.; Johansson, A.; Mathiesen, J.; Jensen, M. H.; Hansen, A. Analytical approach to continuous and intermittent bottleneck flows. *Phys. Rev. Lett.*, 97(16):168001, **2006**.
- [75] Masuda, T.; Nishinari, K.; Schadschneider, A. Critical bottleneck size for jamless particle flows in two dimensions. *Phys. Rev. Lett.*, 112(13):138701, **2014**.
- [76] Zhu, F.; Tajkhorshid, E.; Schulten, K. Pressure-induced water transport in membrane channels studied by molecular dynamics. *Biophys. J.*, 83(1):154–160, **2002**.
- [77] Werder, T.; Walther, J. H.; Jaffe, R. L.; Halicioglu, T.; Koumoutsakos, P. On the water-carbon interaction for use in molecular dynamics simulations of graphite and carbon nanotubes. *J. Phys. Chem. B*, 107(6):1345–1352, **2003**.
- [78] Weeks, J. D.; Chandler, D.; Andersen, H. C. Role of repulsive forces in determining the equilibrium structure of simple liquids. *J. Chem. Phys.*, 54(12):5237–5247, **1971**.
- [79] Taherian, F.; Marcon, V.; van der Vegt, N. F. A.; Leroy, F. What is the contact angle of water on graphene? *Langmuir*, 29(5):1457–1465, **2013**.
- [80] van Kampen, N. G. *Stochastic Processes in Physics and Chemistry*. Elsevier, Amsterdam, 3<sup>rd</sup> edition, **1992**.
- [81] Berendsen, H. J. C.; Grigera, J. R.; Straatsma, T. P. The missing term in effective pair potentials. *J. Phys. Chem.*, 91(24):6269–6271, **1987**.
- [82] González, M. A.; Abascal, J. L. F. The shear viscosity of rigid water models. *J. Chem. Phys.*, 132(9):096101, **2010**.
- [83] Ryckaert, J.-P.; Ciccotti, G.; Berendsen, H. J. C. Numerical integration of the cartesian equations of motion of a system with constraints: Molecular dynamics of n-alkanes. *J. Comput. Phys.*, 23(3):327–341, **1977**.
- [84] Hockney, R. W.; Eastwood, J. W. *Computer Simulation Using Particles*. Taylor & Francis, New York, **1989**.
- [85] Mayo, S. L.; Olafson, B. D.; Goddard, W. A. DREIDING: A generic force field for molecular simulations. *J. Phys. Chem.*, 94(26):8897–8909, **1990**.
- [86] Ma, M.; Grey, F.; Shen, L.; Urbakh, M.; Wu, S.; Liu, J. Z.; Liu, Y.; Zheng, Q. Water transport inside carbon nanotubes mediated by phonon-induced oscillating friction. *Nat. Nanotechnol.*, 10(8):692–695, **2015**.
- [87] Tuckerman, M.; Berne, B. J.; Martyna, G. J. Reversible multiple time scale molecular dynamics. *J. Chem. Phys.*, 97(3):1990–2001, **1992**.
- [88] Hong, G.; Han, Y.; Schutzius, T. M.; Wang, Y.; Pan, Y.; Hu, M.; Jie, J.; Sharma, C. S.; Müller, U.; Poulikakos, D. On the mechanism of hydrophilicity of graphene. *Nano Lett.*, 16(7):4447–4453, **2016**.

- [89] Ashraf, A.; Wu, Y.; Wang, M. C.; Yong, K.; Sun, T.; Jing, Y.; Haasch, R. T.; Aluru, N. R.; Nam, S. Doping-induced tunable wettability and adhesion of graphene. *Nano Lett.*, 16(7):4708–4712, **2016**.
- [90] Willard, A. P.; Chandler, D. The molecular structure of the interface between water and a hydrophobic substrate is liquid-vapor like. *J. Chem. Phys.*, 141(18):18C519, **2014**.
- [91] Berezhkovskii, A.; Hummer, G. Single-file transport of water molecules through a carbon nanotube. *Phys. Rev. Lett.*, 89(6):064503, **2002**.
- [92] Chou, T. How fast do fluids squeeze through microscopic single-file pores? *Phys. Rev. Lett.*, 80(1):85–88, **1998**.
- [93] Corry, B. Designing carbon nanotube membranes for efficient water desalination. *J. Phys. Chem. B*, 112(5):1427–1434, **2008**.
- [94] Hummer, G.; Rasaiah, J. C.; Noworyta, J. P. Water conduction through the hydrophobic channel of a carbon nanotube. *Nature*, 414(6860):188–190, **2001**.
- [95] Mukherjee, B.; Maiti, P. K.; Dasgupta, C.; Sood, A. K. Single-file diffusion of water inside narrow carbon nanorings. *ACS Nano*, 4(2):985–991, **2010**.
- [96] Casieri, C.; Monaco, A.; De Luca, F. Evidence of temperature-induced subdiffusion of water on the micrometer scale in a Nafion membrane. *Macromolecules*, 43(2):638–642, **2010**.
- [97] Luzar, A.; Chandler, D. Effect of environment on hydrogen bond dynamics in liquid water. *Phys. Rev. Lett.*, 76(6):928–931, **1996**.
- [98] Zwanzig, R. *Nonequilibrium Statistical Mechanics*. Oxford University Press, Oxford, **2001**.
- [99] Clauset, A.; Shalizi, C.; Newman, M. Power-law distributions in empirical data. *SIAM Rev.*, 51(4):661–703, **2009**.
- [100] Zuriguel, I.; Pugnaloni, L. A.; Garcimartín, A.; Maza, D. Jamming during the discharge of grains from a silo described as a percolating transition. *Phys. Rev. E*, 68(3):030301, **2003**.
- [101] Saloma, C.; Perez, G. J.; Tapang, G.; Lim, M.; Palmes-Saloma, C. Self-organized queuing and scale-free behavior in real escape panic. *Proc. Nat. Acad. Sci. U. S. A.*, 100(21):11947–11952, **2003**.
- [102] Metzler, R.; Klafter, J. The random walk’s guide to anomalous diffusion: A fractional dynamics approach. *Phys. Rep.*, 339(1):1–77, **2000**.
- [103] Hansen, J.-P.; Verlet, L. Phase transitions of the Lennard-Jones system. *Phys. Rev.*, 184(1):151–161, **1969**.
- [104] Rowley, R. L.; Painter, M. M. Diffusion and viscosity equations of state for a Lennard-Jones fluid obtained from molecular dynamics simulations. *Int. J. Thermophys.*, 18(5):1109–1121, **1997**.
- [105] Frenkel, D.; Smit, B. *Understanding Molecular Simulation: From Algorithms to Applications*. Academic Press, San Diego, 2<sup>nd</sup> edition, **2001**.

- [106] Kittel, C. *Introduction to Solid State Physics*. Wiley, New York, 2nd edition, **1963**.
- [107] Geissler, P. L.; Chandler, D. Importance sampling and theory of nonequilibrium solvation dynamics in water. *J. Chem. Phys.*, 113(21):9759–9765, **2000**.
- [108] Hill, T. L. *An Introduction to Statistical Thermodynamics*. Dover Publications, Inc., New York, 2<sup>nd</sup> edition, **1986**.
- [109] Nosé, S. A molecular dynamics method for simulations in the canonical ensemble. *Mol. Phys.*, 52(2):255–268, **1984**.
- [110] Davis, J. G.; Rankin, B. M.; Gierszal, K. P.; Ben-Amotz, D. On the cooperative formation of non-hydrogen-bonded water at molecular hydrophobic interfaces. *Nat. Chem.*, 5(9):796–802, **2013**.
- [111] Majumder, M.; Chopra, N.; Andrews, R.; Hinds, B. J. Nanoscale hydrodynamics: Enhanced flow in carbon nanotubes. *Nature*, 438(7064):44–44, **2005**.
- [112] Holt, J. K.; Park, H. G.; Wang, Y.; Stadermann, M.; Artyukhin, A. B.; Grigoropoulos, C. P.; Noy, A.; Bakajin, O. Fast mass transport through sub-2-nanometer carbon nanotubes. *Science*, 312(5776):1034–1037, **2006**.
- [113] Sinha, S.; Rossi, M. P.; Mattia, D.; Gogotsi, Y.; Bau, H. H. Induction and measurement of minute flow rates through nanopipes. *Phys. Fluids*, 19(1):013603, **2007**.
- [114] Whitby, M.; Cagnon, L.; Thanou, M.; Quirke, N. Enhanced fluid flow through nanoscale carbon pipes. *Nano Lett.*, 8(9):2632–2637, **2008**.
- [115] Tocci, G.; Joly, L.; Michaelides, A. Friction of water on graphene and hexagonal boron nitride from ab initio methods: Very different slippage despite very similar interface structures. *Nano Lett.*, 14(12):6872–6877, **2014**.
- [116] Daub, C. D.; Bratko, D.; Leung, K.; Luzar, A. Electrowetting at the nanoscale. *J. Phys. Chem. C*, 111(2):505–509, **2007**.
- [117] Widom, B. Line tension and the shape of a sessile drop. *J. Phys. Chem.*, 99(9):2803–2806, **1995**.
- [118] Li, J.; Morrone, J. A.; Berne, B. J. Are hydrodynamic interactions important in the kinetics of hydrophobic collapse? *J. Phys. Chem. B*, 116(37):11537–11544, **2012**.
- [119] Smirnov, S.; Vlassiouk, I.; Takmakov, P.; Rios, F. Water confinement in hydrophobic nanopores. Pressure-induced wetting and drying. *ACS Nano*, 4(9):5069–5075, **2010**.
- [120] Shenogina, N.; Godawat, R.; Keblinski, P.; Garde, S. How wetting and adhesion affect thermal conductance of a range of hydrophobic to hydrophilic aqueous interfaces. *Phys. Rev. Lett.*, 102(15):156101, **2009**.
- [121] Sigal, G. B.; Mrksich, M.; Whitesides, G. M. Effect of surface wettability on the adsorption of proteins and detergents. *J. Am. Chem. Soc.*, 120(14):3464–3473, **1998**.

- [122] Montroll, E. W.; Shlesinger, M. F. On the wonderful world of random walks. In *Nonequilibrium Phenomena II: From Stochastics to Hydrodynamics*, volume 9, pages 5–46. North-Holland Physics Publishing, Amsterdam, **1984**.
- [123] Vajna, S.; Tóth, B.; Kertész, J. Modelling bursty time series. *New J. Phys.*, 15(10):103023, **2013**.
- [124] Newman, M. E. J. Power laws, Pareto distributions and Zipf's law. *Contemp. Phys.*, 46(5):323–351, **2005**.
- [125] Drahushuk, L. W.; Wang, L.; Koenig, S. P.; Bunch, J. S.; Strano, M. S. Analysis of time-varying, stochastic gas transport through graphene membranes. *ACS Nano*, 10(1):786–795, **2016**.
- [126] Jain, T.; Rasera, B. C.; Guerrero, R. J. S.; Boutilier, M. S. H.; O'Hern, S. C.; Idrobo, J.-C.; Karnik, R. Heterogeneous sub-continuum ionic transport in statistically isolated graphene nanopores. *Nat. Nanotechnol.*, 10(12):1053–1057, **2015**.
- [127] Brovchenko, I.; Geiger, A.; Oleinikova, A. Water in nanopores. I. Coexistence curves from Gibbs ensemble Monte Carlo simulations. *J. Chem. Phys.*, 120(4):1958–1972, **2004**.
- [128] Brovchenko, I.; Oleinikova, A. Water in nanopores: III. Surface phase transitions of water on hydrophilic surfaces. *J. Phys. Chem. C*, 111(43):15716–15725, **2007**.
- [129] Aghigh, A.; Alizadeh, V.; Wong, H. Y.; Islam, M. S.; Amin, N.; Zaman, M. Recent advances in utilization of graphene for filtration and desalination of water: A review. *Desalination*, 365:389–397, **2015**.
- [130] Huang, C.; Choi, P. Y. K.; Kostiuk, L. W. A method for creating a non-equilibrium NT( $P_1 - P_2$ ) ensemble in molecular dynamics simulation. *Phys. Chem. Chem. Phys.*, 13(46):20750, **2011**.
- [131] Stone, J. *An Efficient Library for Parallel Ray Tracing and Animation*. Ph.D. thesis, Computer Science Department, University of Missouri-Rolla, **1998**.
- [132] Du, X.; Skachko, I.; Barker, A.; Andrei, E. Y. Approaching ballistic transport in suspended graphene. *Nat. Nanotechnol.*, 3(8):491–495, **2008**.
- [133] Stone, J.; Gullingsrud, J.; Grayson, P.; Schulten, K. A system for interactive molecular dynamics simulation. In Hughes, J. F.; Séquin, C. H., eds., *2001 ACM Symposium on Interactive 3D Graphics*, pages 191–194. ACM SIGGRAPH, New York, **2001**.
- [134] Liu, H.; Liu, Y.; Zhu, D. Chemical doping of graphene. *J. Mater. Chem.*, 21(10):3335–3345, **2011**.
- [135] Willard, A. P.; Chandler, D. Coarse-grained modeling of the interface between water and heterogeneous surfaces. *Faraday Discuss.*, 141:209–220, **2009**.
- [136] Meric, I.; Han, M. Y.; Young, A. F.; Ozyilmaz, B.; Kim, P.; Shepard, K. L. Current saturation in zero-bandgap, top-gated graphene field-effect transistors. *Nat. Nanotechnol.*, 3(11):654–659, **2008**.

- [137] Vega, C.; Sanz, E.; Abascal, J. L. F.; Noya, E. G. Determination of phase diagrams via computer simulation: Methodology and applications to water, electrolytes and proteins. *J. Phys.: Condens. Matter*, 20(15):153101, **2008**.
- [138] Lin, Y.-M.; Chiu, H.-Y.; Jenkins, K.; Farmer, D. B.; Avouris, P.; Valdes-Garcia, A. Dual-gate graphene FETs with  $f_T$  of 50 GHz. *IEEE Electr. Device Lett.*, 31(1):68–70, **2010**.
- [139] Zhu, A.; Christofides, P. D.; Cohen, Y. Effect of stream mixing on RO energy cost minimization. *Desalination*, 261(3):232–239, **2010**.
- [140] Zhu, A.; Christofides, P. D.; Cohen, Y. Effect of thermodynamic restriction on energy cost optimization of RO membrane water desalination. *Ind. Eng. Chem. Res.*, 48(13):6010–6021, **2009**.
- [141] Eaves, J. D.; Tokmakoff, A.; Geissler, P. L. Electric field fluctuations drive vibrational dephasing in water. *J. Phys. Chem. A*, 109(42):9424–9436, **2005**.
- [142] Chandler, D. Electron transfer in water and other polar environments, how it happens. In Berne, B. J.; Ciccotti, G.; Coker, D. F., eds., *Classical and Quantum Dynamics in Condensed Phase Simulations*, pages 25–49. World Scientific, Singapore, **1998**.
- [143] Smith, J. D.; Cappa, C. D.; Wilson, K. R.; Messer, B. M.; Cohen, R. C.; Saykally, R. J. Energetics of hydrogen bond network rearrangements in liquid water. *Science*, 306(5697):851–853, **2004**.
- [144] Chong, T. H.; Loo, S.-L.; Krantz, W. B. Energy-efficient reverse osmosis desalination process. *J. Membr. Sci.*, 473:177–188, **2015**.
- [145] Bennett, C. H. Exact defect calculations in model substances. In Nowick, A.; Burton, J., eds., *Diffusion in Solids: Recent Developments*, pages 73–113. Academic Press, New York, **1975**.
- [146] Martyna, G. J.; Tuckerman, M. E.; Tobias, D. J.; Klein, M. L. Explicit reversible integrators for extended systems dynamics. *Mol. Phys.*, 87(5):1117–1157, **1996**.
- [147] Kim, M.; Safron, N. S.; Han, E.; Arnold, M. S.; Gopalan, P. Fabrication and characterization of large-area, semiconducting nanoperforated graphene materials. *Nano Lett.*, 10(4):1125–1131, **2010**.
- [148] Plimpton, S. Fast parallel algorithms for short-range molecular dynamics. *J. Comput. Phys.*, 117(1):1–19, **1995**.
- [149] Castillo-Tejas, J.; Rojas-Morales, A.; López-Medina, F.; Alvarado, J. F. J.; Luna-Bárcenas, G.; Bautista, F.; Manero, O. Flow of linear molecules through a 4:1:4 contraction–expansion using non-equilibrium molecular dynamics: Extensional rheology and pressure drop. *J. Non-Newton. Fluid.*, 161(1–3):48–59, **2009**.
- [150] Onsager, L.; Machlup, S. Fluctuations and irreversible processes. *Phys. Rev.*, 91(6):1505–1512, **1953**.
- [151] Sagle, A.; Freeman, B. Fundamentals of membranes for water treatment. In *The Future of Desalination in Texas*, volume 2, pages 137–154. Texas Water Development Board, **2004**.

- [152] El-Dessouky, H. T.; Ettouney, H. M. *Fundamentals of Salt Water Desalination*. Elsevier, **2002**.
- [153] Dameron, A. A.; Davidson, S. D.; Burton, B. B.; Garcia, P. F.; McLean, R. S.; George, S. M. Gas diffusion barriers on polymers using multilayers fabricated by Al<sub>2</sub>O<sub>3</sub> and rapid SiO<sub>2</sub> atomic layer deposition. *J. Phys. Chem. C*, 112(12):4573–4580, **2008**.
- [154] Garaj, S.; Hubbard, W.; Reina, A.; Kong, J.; Branton, D.; Golovchenko, J. A. Graphene as a subnanometre trans-electrode membrane. *Nature*, 467(7312):190–193, **2010**.
- [155] Schrier, J. Helium separation using porous graphene membranes. *J. Phys. Chem. Lett.*, 1(15):2284–2287, **2010**.
- [156] Eaves, J. D.; Loparo, J. J.; Fecko, C. J.; Roberts, S. T.; Tokmakoff, A.; Geissler, P. L. Hydrogen bonds in liquid water are broken only fleetingly. *Proc. Nat. Acad. Sci. U. S. A.*, 102(37):13019–13022, **2005**.
- [157] Chandler, D. Hydrophobicity: Two faces of water. *Nature*, 417(6888):491–491, **2002**.
- [158] Willard, A. P.; Chandler, D. Instantaneous liquid interfaces. *J. Phys. Chem. B*, 114(5):1954–1958, **2010**.
- [159] Taherian, F.; Leroy, F.; van der Vegt, N. F. A. Interfacial tension does not drive asymmetric nanoscale electrowetting on graphene. *Langmuir*, 31(16):4686–4695, **2015**.
- [160] York, D. Least-squares fitting of a straight line. *Can. J. Phys.*, 44(5):1079–1086, **1966**.
- [161] Purcell, E. M. Life at low Reynolds number. *Am. J. Phys.*, 45(1):3–11, **1977**.
- [162] Bao, W.; Liu, G.; Zhao, Z.; Zhang, H.; Yan, D.; Deshpande, A.; LeRoy, B.; Lau, C. N. Lithography-free fabrication of high quality substrate-supported and freestanding graphene devices. *Nano Res.*, 3(2):98–102, **2010**.
- [163] Falconer, J. L.; George, S. M.; Ott, A. W.; Klaus, J. W.; Noble, R. D.; Funke, H. H. Modification of zeolite or molecular sieve membranes using atomic layer controlled chemical vapor deposition. U. S. Patent 6043177 A, **2000**.
- [164] Funke, H. H.; Klaus, J. W.; George, S. M.; Ott, A. W.; Falconer, J. L.; Noble, R. D. Modified zeolite membrane. U. S. Patent 6051517 A, **2000**.
- [165] Goldsmith, J.; Martens, C. C. Molecular dynamics simulation of salt rejection in model surface-modified nanopores. *J. Phys. Chem. Lett.*, 1(2):528–535, **2010**.
- [166] Skouidas, A. I. Molecular dynamics simulations of gas diffusion in metal-organic frameworks: Argon in CuBTC. *J. Am. Chem. Soc.*, 126(5):1356–1357, **2004**.
- [167] Takaba, H.; Onumata, Y.; Nakao, S.-I. Molecular simulation of pressure-driven fluid flow in nanoporous membranes. *J. Chem. Phys.*, 127(5):054703, **2007**.
- [168] Vieira-Linhares, A. M.; Seaton, N. A. Non-equilibrium molecular dynamics simulation of gas separation in a microporous carbon membrane. *Chem. Eng. Sci.*, 58(18):4129–4136, **2003**.

- [169] Noah-Vanhoucke, J.; Geissler, P. L. On the fluctuations that drive small ions toward, and away from, interfaces between polar liquids and their vapors. *Proc. Nat. Acad. Sci. U. S. A.*, 106(36):15125–15130, **2009**.
- [170] Bieri, M.; Treier, M.; Cai, J.; Aït-Mansour, K.; Ruffieux, P.; Gröning, O.; Gröning, P.; Kastler, M.; Rieger, R.; Feng, X.; et al. Porous graphenes: Two-dimensional polymer synthesis with atomic precision. *Chem. Commun.*, 45:6919–6921, **2009**.
- [171] Bell, D. C.; Lemme, M. C.; Stern, L. A.; Williams, J. R.; Marcus, C. M. Precision cutting and patterning of graphene with helium ions. *Nanotechnology*, 20(45):455301, **2009**.
- [172] Andersen, H. C. RATTLE: A “velocity” version of the SHAKE algorithm for molecular dynamics calculations. *J. Comput. Phys.*, 52(1):24–34, **1983**.
- [173] Bae, S.; Kim, H.; Lee, Y.; Xu, X.; Park, J.-S.; Zheng, Y.; Balakrishnan, J.; Lei, T.; Ri Kim, H.; Song, Y. I.; et al. Roll-to-roll production of 30-inch graphene films for transparent electrodes. *Nat. Nanotechnol.*, 5(8):574–578, **2010**.
- [174] Koenig, S. P.; Wang, L.; Pellegrino, J.; Bunch, J. S. Selective molecular sieving through porous graphene. *Nat. Nanotechnol.*, 7(11):728–732, **2012**.
- [175] Konatham, D.; Yu, J.; Ho, T. A.; Striolo, A. Simulation insights for graphene-based water desalination membranes. *Langmuir*, 29(38):11884–11897, **2013**.
- [176] Ballenegger, V.; Arnold, A.; Cerdà, J. J. Simulations of non-neutral slab systems with long-range electrostatic interactions in two-dimensional periodic boundary conditions. *J. Chem. Phys.*, 131(9):094107, **2009**.
- [177] Lin, S.; Elimelech, M. Staged reverse osmosis operation: Configurations, energy efficiency, and application potential. *Desalination*, 366:9–14, **2015**.
- [178] Evans, D. J.; Morriss, G. *Statistical Mechanics of Nonequilibrium Liquids*. Cambridge University Press, Cambridge, 2<sup>nd</sup> edition, **2008**.
- [179] Mahnke, R.; Pieret, N. Stochastic master-equation approach to aggregation in freeway traffic. *Phys. Rev. E*, 56(3):2666–2671, **1997**.
- [180] Mark, P.; Nilsson, L. Structure and dynamics of the TIP3P, SPC, and SPC/E water models at 298 K. *J. Phys. Chem. A*, 105(43):9954–9960, **2001**.
- [181] Stillinger, F. H. Structure in aqueous solutions of nonpolar solutes from the standpoint of scaled-particle theory. *J. Solution Chem.*, 2(2–3):141–158, **1973**.
- [182] Wei, D.; Liu, Y.; Wang, Y.; Zhang, H.; Huang, L.; Yu, G. Synthesis of N-doped graphene by chemical vapor deposition and its electrical properties. *Nano Lett.*, 9(5):1752–1758, **2009**.
- [183] Panchakarla, L. S.; Subrahmanyam, K. S.; Saha, S. K.; Govindaraj, A.; Krishnamurthy, H. R.; Waghmare, U. V.; Rao, C. N. R. Synthesis, structure, and properties of boron- and nitrogen-doped graphene. *Adv. Mater.*, 21(46):4726–4730, **2009**.
- [184] Elimelech, M.; Phillip, W. A. The future of seawater desalination: Energy, technology, and the environment. *Science*, 333(6043):712–717, **2011**.

- [185] Zhu, F.; Tajkhorshid, E.; Schulten, K. Theory and simulation of water permeation in aquaporin-1. *Biophys. J.*, 86(1):50–57, **2004**.
- [186] Safran, S. A.; Pincus, P.; Andelman, D. Theory of spontaneous vesicle formation in surfactant mixtures. *Science*, 248(4953):354–356, **1990**.
- [187] Halgren, T. A. The representation of van der Waals (vdW) interactions in molecular mechanics force fields: Potential form, combination rules, and vdW parameters. *J. Am. Chem. Soc.*, 114(20):7827–7843, **1992**.
- [188] Spiegler, K. S.; Kedem, O. Thermodynamics of hyperfiltration (reverse osmosis): Criteria for efficient membranes. *Desalination*, 1(4):311–326, **1966**.
- [189] Bernardi, S.; Todd, B. D.; Searles, D. J. Thermostating highly confined fluids. *J. Chem. Phys.*, 132(24):244706, **2010**.
- [190] Frentrup, H.; Avendaño, C.; Horsch, M.; Salih, A.; Müller, E. A. Transport diffusivities of fluids in nanopores by non-equilibrium molecular dynamics simulation. *Mol. Simulat.*, 38(7):540–553, **2012**.
- [191] Bird, R. B.; Stewart, W. E.; Lightfoot, E. N. *Transport Phenomena*. John Wiley & Sons, Inc., New York, 2<sup>nd</sup> edition, **2006**.
- [192] Han, Y.; Xu, Z.; Gao, C. Ultrathin graphene nanofiltration membrane for water purification. *Adv. Funct. Mater.*, 23(29):3693–3700, **2013**.
- [193] York, D.; Evensen, N. M.; Martínez, M. L.; Delgado, J. D. B. Unified equations for the slope, intercept, and standard errors of the best straight line. *Am. J. Phys.*, 72(3):367–375, **2004**.
- [194] Nair, R. R.; Wu, H. A.; Jayaram, P. N.; Grigorieva, I. V.; Geim, A. K. Unimpeded permeation of water through helium-leak-tight graphene-based membranes. *Science*, 335(6067):442–444, **2012**.
- [195] Chandler, D.; Weeks, J. D.; Andersen, H. C. Van der Waals picture of liquids, solids, and phase transformations. *Science*, 220(4599):787–794, **1983**.
- [196] Zhao, L.; He, R.; Rim, K. T.; Schiros, T.; Kim, K. S.; Zhou, H.; Gutiérrez, C.; Chockalingam, S. P.; Arguello, C. J.; Pálová, L.; et al. Visualizing individual nitrogen dopants in monolayer graphene. *Science*, 333(6045):999–1003, **2011**.
- [197] Humphrey, W.; Dalke, A.; Schulten, K. VMD – visual molecular dynamics. *J. Mol. Graphics*, 14:33–38, **1996**.
- [198] Willard, A. P.; Reed, S. K.; Madden, P. A.; Chandler, D. Water at an electrochemical interface—a simulation study. *Faraday Discuss.*, 141:423–441, **2009**.
- [199] Karagiannis, I. C.; Soldatos, P. G. Water desalination cost literature: Review and assessment. *Desalination*, 223(1–3):448–456, **2008**.
- [200] Wang, E. N.; Karnik, R. Water desalination: Graphene cleans up water. *Nat. Nanotechnol.*, 7(9):552–554, **2012**.

## Chapter 4

### Tetracene Aggregation on Polar and Nonpolar Surfaces

The contents of this chapter are reprinted, with permission, from

Strong, S. E.; Eaves, J. D. Tetracene aggregation on polar and nonpolar surfaces: Implications for singlet fission. *J. Phys. Chem. Lett.*, 6(7):1209–1215, **2015**

#### 4.1 Abstract

In molecular crystals that exhibit singlet fission, quantum yields depend strongly on intermolecular configurations that control the relevant electronic couplings. Here, we explore how non-covalent interactions between molecules and surfaces stabilize intermolecular structures with strong singlet fission couplings. Using MD simulations, we study the aggregation patterns of tetracene molecules on a solid surface as a function of surface polarity. Even at low surface concentrations, we find that tetracene self-assembles into nanocrystallites where about 10–20% of the clustered molecules are part of at least one herringbone structure. The herringbone structure is the native structure of crystalline tetracene, which exhibits a high singlet fission quantum yield. Increasing the polarity of the surface reduces both the amount of clustering and the relative number of herringbone configurations, but only when the dipoles on the surface are orientationally disordered. These results have implications for the application of singlet fission in dye-sensitized solar cells.

## 4.2 Background

Singlet fission (SF), a process where one singlet excited state relaxes into two triplets, is a fundamentally interesting electronic process that can address an important loss mechanism in conventional single-junction solar cells.<sup>2</sup> In such a cell, electrons excited by the absorption of photons with energies greater than the optical gap dissipate this excess energy as heat.<sup>3</sup> A solar cell with both a SF chromophore and a conventional chromophore absorbs those high-energy photons and splits them into two electrons, preventing heat loss. A device using this mechanism could break the Shockley-Queisser detailed balance limit that bounds the efficiency of single-chromophore/single-junction solar cells.<sup>2,3</sup> In many ways, such a device would function as a multiple-junction solar cell without the current-matching constraint.<sup>2</sup> A dye-sensitized solar cell (DSSC), in which both SF and conventional chromophores adsorb onto the surface of semiconducting nanoparticles, is one concrete realization of such a device that resonates closely with the work presented here.<sup>2,4–6</sup>

For SF to occur with high efficiency, the singlet and two triplet states must have comparable energy and be coupled sufficiently strongly.<sup>7–11</sup> The large exchange energy present in acene molecules satisfies the energy-matching criterion.<sup>7,8</sup> The electronic couplings, however, depend strongly on intermolecular geometry.<sup>7,8,12–46</sup> Many studies find a variety of geometries that promote SF, but these geometries depend on the molecular system.<sup>11,13–21</sup> While the precise intermolecular orientations that maximize SF are unknown, both calculations and experiments suggest that SF can occur with high efficiency in acenes when the molecules adopt a herringbone structure (Figure 4.1a).<sup>7,8,22,24,42</sup> Since this is the structure found in many crystalline acenes at ambient conditions, it is natural that SF was first discovered in them.<sup>2</sup> In a DSSC, however, the intermolecular structures of the molecules at noncrystalline densities determine the efficiency of SF. These structures depend, in complex ways, on the molecular structures of the aggregating molecules and on the interactions of those molecules with the surface.<sup>47–50</sup>

A large body of work, on both dimers and crystals, has manipulated the intermolecular structure of pentacene and tetracene derivatives through synthetic modifications to covalent architec-

tures.<sup>9,11,14,15,18,19,29,31,51,52</sup> We pursue a complementary approach that examines how noncovalent interactions guide the self-assembly of intermolecular structures. In particular, we study how interactions with the surface promote the assembly of aggregates that can undergo SF. Experiments have found that the absorption spectrum of tetracene adsorbed to amorphous silica exhibits a splitting similar to the Davydov splitting in bulk crystalline tetracene, even at low surface concentration (1–2% of a monolayer).<sup>50</sup> This suggests that the structures of the adsorbed aggregates are similar to those in the bulk crystal, but this is, so far, an untested hypothesis. Our work examines this hypothesis and addresses a knowledge gap between the bulk (crystalline) and molecular (solution-phase) structural properties of acenes.

The chemical, electronic, and topological properties of a surface all play a role in aggregation.<sup>53–56</sup> Here, we investigate the effects of surface polarity using a model that encompasses both microscopically and macroscopically polar surfaces. A microscopically polar surface is one that is polar on atomic length scales but macroscopically nonpolar because of symmetry or disorder. Our motivations for studying the effects of surface polarity are as follows: Recent work has found that SF is only competitive with singlet electron injection in a DSSC when a spacer layer between the chromophores and the semiconductor surface slows down electron injection.<sup>6</sup> Tailoring the intermolecular interactions between the substrate and the chromophores in a DSSC by adjusting the polarity of the spacer layer might offer considerable design flexibility. Surface polarity is also an important feature in materials such as amorphous silica, which was used in the experiments by Dabestani and co-workers,<sup>50</sup> and titanium dioxide, a semiconductor frequently used in DSSCs.<sup>4,57</sup> Silica has both a microscopically disordered polarity from the random orientations of the Si–O bonds at the surface and an ordered polarity from passivation by hydrogen.<sup>58</sup> In crystalline titanium dioxide, the most stable surfaces are not macroscopically polar,<sup>59</sup> even though the Ti–O bond is polar on microscopic length scales. Surface passivation can also render many nonpolar surfaces polar. For example, silicon passivated with Al<sub>2</sub>O<sub>3</sub> exhibits a macroscopically polar surface.<sup>60</sup> Finally, during solar cell operation, space-charge regions form at the interfaces between materials, creating electric fields similar to those from a polar surface.<sup>61,62</sup> In this work, we use the term

“surface polarity” to encompass cases in which the surface is polar on macroscopic length scales and those in which the surface is polar on molecular length scales but nonpolar on macroscopic ones. This differs from the usual convention that uses the term surface polarity only to describe surfaces that are macroscopically polar.<sup>59,63</sup>

### 4.3 Methods

To study the aggregation of tetracene on a surface, we perform classical MD simulations with replica exchange to aid equilibration.<sup>64</sup> The surface is in the  $xy$ -plane and is modeled by a slab of point particles with LJ dispersion interactions with each atom on the tetracene molecules. In all simulations, there are 10 tetracene molecules on the surface. We perform two simulations, one with a  $7 \times 7 \times 2.5 \text{ nm}^3$  box, and another with a larger,  $9.7 \times 9.7 \times 2.5 \text{ nm}^3$  box. Using the area of the crystal  $ab$ -plane as the area of a unit cell in a monolayer,<sup>65</sup> this gives a surface coverage of  $\sim 4.9\%$  of a monolayer for the small box and  $\sim 2.5\%$  for the large box. These are larger than the surface concentrations used in the Dabestani experiments (1–2%),<sup>50</sup> but a smaller concentration in these simulations is too expensive and gives poor statistics.

The DREIDING force field<sup>66</sup> with atomic charges from crystal DFT calculations<sup>67</sup> describes the inter- and intramolecular tetracene interactions. There are qualitative differences between atomic charges from a vacuum monomer calculation<sup>68</sup> and those from the crystal calculations.<sup>69</sup> It is unclear, *a priori*, which are more appropriate to use. To test this, we also perform simulations using atomic charges from vacuum monomer calculations<sup>70</sup> and notice no qualitative differences. The DREIDING force field has been shown to qualitatively reproduce two experimental polymorph structures of pentacene at room temperature and pressure,<sup>71</sup> so should work for tetracene as well.

The LJ parameters for the interaction between surface particles and the carbon atoms of the tetracene molecules are the same as those for the carbon-carbon interactions. This choice ensures that the tetracene molecules attract one another with approximately the same strength as the surface. The LJ interaction between the surface atoms and the hydrogen atoms is determined using a geometric mean combination rule for the bond energies and an arithmetic mean combination rule

for the bond lengths. The surface is the (001) face of a face-centered-cubic (fcc) lattice of particles, with the lattice parameter set at the minimum of the LJ potential well ( $R_0 = 3.9 \text{ \AA}$ ). The surface particles are fixed during the simulation.

To model the polarity of the surface, we place a point dipole at the center of each particle with a random orientation. The random orientation is determined by picking the  $x$ ,  $y$ , and  $z$  components independently from a uniform distribution on  $[-0.5, 0.5]$ . The magnitude of these dipoles is a proxy for the polarity of the surface. To measure the effects of surface polarity, we run simulations using 0.0, 0.2, 0.4, 0.6, 0.8, and 1.0 D dipoles. For reference, the dipole moment of water is about 2 D.

To get more data per simulation, we simulate tetracene molecules on both sides of a slab of surface particles, using a simulation box twice as long in the  $z$ -direction ( $7 \times 7 \times 5 \text{ nm}^3$ ). The slab is 7.8 Å thick in the  $z$ -direction. We verify that this is thick enough to eliminate interactions between tetracene molecules on opposite sides by averaging the total energy of one-sided and two-sided simulations over 100 ps. If the two sides of a slab are non-interacting, the energy of the two-sided simulation should be exactly double that of a one sided simulation. This is true to 1 part in 100,000. Because of the surface, these simulations are not periodic in the  $z$ -direction. To prevent interactions between periodic images in the  $z$ -direction, we use the conventional slab geometry, in which a vacuum layer is added between periodic images in the  $z$ -direction.<sup>72</sup> The thickness of the vacuum layer is three times the length of the simulation box (15 nm). This thickness gives errors in the forces on the order of 1 part in 1,000,000.

Long-range electrostatics are computed using the Ewald method modified for the slab geometry.<sup>72</sup> Dispersion interactions are cut off at 12 Å. We use the rRESPA multi-timescale integrator<sup>73</sup> to treat the bond, angle, dihedral, improper, pairwise, and  $k$ -space interactions with time steps of 0.25, 0.25, 0.5, 0.5, 1, and 2 fs, respectively.

Straightforward MD simulations are slow to equilibrate, so we use replica exchange molecular dynamics (REMD).<sup>64</sup> REMD is an MD scheme in which multiple replicas of a simulation are run at varying temperatures. The replicas attempt to exchange with each other every 1 ps, and exchange success is dictated by the metropolis condition.<sup>64</sup> We use four replicas with temperatures of 280,

296, 312, and 330 K; these are distributed exponentially to give an exchange success rate of  $\sim$ 10%. The temperature is held constant in each replica using the Nosé-Hoover thermostat.<sup>74,75</sup> All data are based on the 296 K replica.

The tetracene molecules are initially arranged separated from one another and laying flat on the surface at a distance of  $R_0$  from the surface. Each simulation is composed of 0.5 ns for equilibration followed by 0.5 ns for data collection. To measure equilibration, we look for aging in the autocorrelation functions of the number of clustered molecules. In an equilibrated time series, the autocorrelation function for the first and second halves of the data should be the same. These autocorrelation functions are very noisy due to the small number of clustered molecules, so instead of comparing autocorrelation functions, we compare the decay times of these autocorrelation functions. We use 12 independent REMD simulations to generate each data point: 6 simulations each with two sides of the slab.

The diffusion data and tetracene-surface interaction energy data are generated from simulations with only one molecule on only one side of the slab. REMD is not used. The simulations are equilibrated for 100 ps followed by 100 ps of data collection. All other settings are the same. Squared-displacements are averaged over 1000 trajectories, each with a different configuration of randomly oriented dipoles.

#### 4.4 Results and Discussion

Because tetracene is a canonical SF chromophore, we explore the aggregation patterns of tetracene molecules on surfaces as a function of surface polarity. We model the surface by a slab of LJ particles with point dipoles at their centers, oriented either uniformly or randomly, to mimic an ordered or disordered polar surface, respectively. We report surface polarity in units of the magnitude of the dipole moment of the surface particles.

Even at low concentrations (5% of a monolayer), between 40 and 75% of the molecules are in clusters of size two or larger (Figure 4.2a). Of those molecules in clusters, between 10 and 20% of them are in at least one herringbone configuration (Figure 4.2a). The fraction of molecules in

clusters is independent of polarity on ordered polar surfaces (Figure 4.2b). On disordered polar surfaces, however, the polarity has a qualitative impact on both the clustering statistics (Figures 4.2a and 4.3) and the number of herringbone structures observed in clusters (Figure 4.2a). On these disordered polar surfaces, diffusion constants decrease exponentially with polarity (Figure 4.4), implying that energetic roughness on a disordered polar surface provides some degree of trapping.

Snapshots from simulations show both herringbone structures and  $\pi$ -stacked structures, in which the molecules lie flat on one another (Figure 4.1a,b). While the experimental evidence supporting the notion that the herringbone configuration promotes efficient SF is overwhelming, some calculations have predicted that the  $\pi$ -stacked structures also promote SF.<sup>7,8,17,21,46</sup> The stacking angle, defined as the angle between the vectors normal to the molecular planes, distinguishes these two configurations. The stacking angle alone cannot, however, unambiguously identify either configuration. It does not resolve rotations about the normal axis of either molecule, nor does it resolve a slip along the long or short molecular axis. The molecular COM distance, in conjunction with the stacking angle, helps resolve these ambiguities. We construct the Helmholtz free energy surface as a function of the COM distance,  $R_{\text{COM}}$ , and the cosine of the stacking angle,  $\cos \theta$ , by measuring the probability of observing a given configuration,  $P(R_{\text{COM}}, \cos \theta)$ , through histogramming. Ignoring physically irrelevant constants, the Helmholtz free energy density is

$$F(R_{\text{COM}}, \cos \theta) = -k_B T \ln \left( \frac{P(R_{\text{COM}}, \cos \theta)}{R_{\text{COM}}^2} \right) \quad (4.1)$$

where  $T$  is the absolute temperature, 296 K, and  $k_B$  is Boltzmann's constant.<sup>77</sup> We normalize by  $R^2$  so that the COM free energy density reduces to the potential of mean force in three dimensions when  $\cos \theta$  is integrated out of  $P(R_{\text{COM}}, \cos \theta)$ .<sup>77</sup> Figure 4.1c shows the free energy surface along with the expected minima corresponding to the experimental crystal structure.

Figure 4.1c also shows the geometric criteria that we use to identify clusters and to assign intermolecular herringbone structures. To quantify clustering, we define a cluster as a group of molecules connected by neighbors for which  $R_{\text{COM}}$  is less than 5.5 Å (blue dashed line in Figure 4.1c). This definition includes both the first and second peaks in the radial distribution function

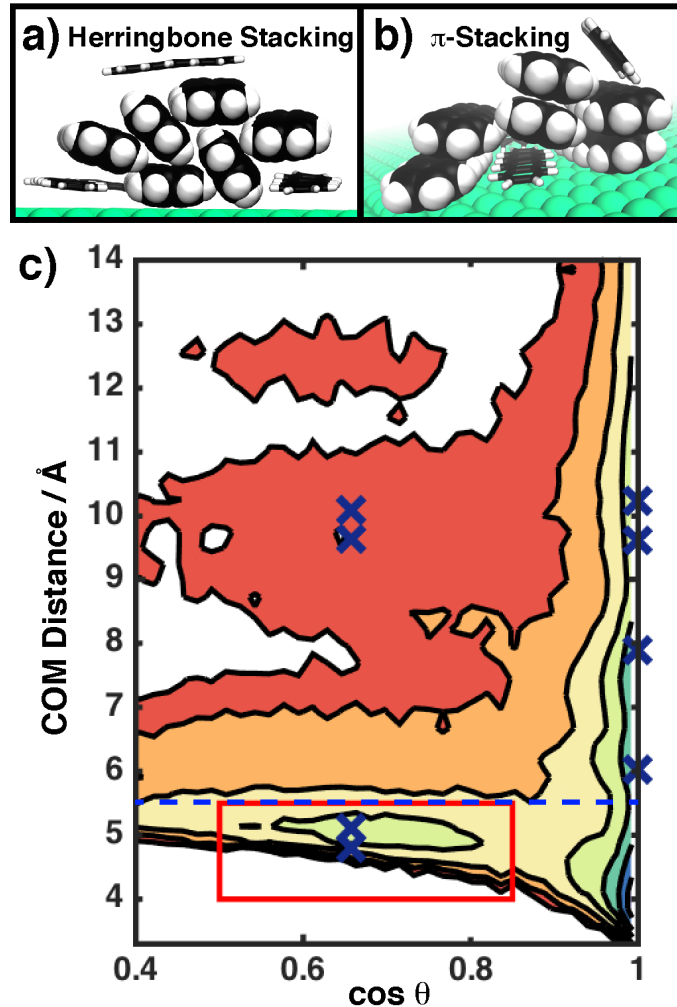


Figure 4.1: Snapshots from simulations of tetracene show space-filled molecules in (a) herringbone and (b)  $\pi$ -stacked configurations according to our geometric criteria. (c) The Helmholtz free energy density for tetracene on a nonpolar surface as a function of the center-of-mass (COM) distance between two molecules and the cosine of their stacking angle, as described in the text. The free energy does not change qualitatively as a function of surface polarity. The contours are spaced by  $1 k_B T$ , with free energy decreasing toward the cooler colors. It is important to analyze the data in the cosine of the angle rather than in the angle itself to avoid singularities in the Jacobian.<sup>76</sup> The blue dashed line is the cutoff used to identify neighbors in the clustering calculation, and the red box illustrates the geometric criterion that we use to identify herringbone structures. The blue  $\times$ s indicate the minima of the free energy for the experimental structure of crystalline tetracene.<sup>65</sup> The red box surrounds the herringbone signatures in the crystal phase and the associated basin in the free energy for clusters. The  $\pi$ -stacked configurations in (b) correspond to the minimum in the free energy at  $\cos \theta = 1$  and a COM distance of  $\sim 4 \text{ \AA}$ .

of the aggregates. The first peak corresponds to  $\pi$ -stacked and similar configurations, which are not present in the crystal, while the second corresponds to the herringbone configuration. We define a herringbone configuration as a pair of molecules for which  $R_{\text{COM}}$  is less than 5.5 Å and  $\cos \theta$  is between 0.5 and 0.85. The red box in Figure 4.1c shows this region. We define  $p_H$  as the conditional probability that a molecule is in a herringbone configuration with at least one neighbor provided that it is also in a cluster. We compute  $p_H$  by averaging the number of molecules in at least one herringbone configuration and dividing by the total number of clustered molecules.

Figure 4.2a shows that both the fraction of molecules in clusters and  $p_H$  decrease with increasing surface polarity, but only when the dipoles are oriented randomly. When the dipoles were all aligned perpendicular to the surface, clustering is independent of surface polarity (Figure 4.2b). To investigate the effects of surface concentration and finite system size, we perform simulations with a fixed number of molecules on both a large and a small slab: low and high surface concentration, respectively. From equilibrium arguments, one would expect the fraction of clustered molecules to scale inversely with the area for a fixed number of molecules, so the fraction of clustered molecules multiplied by the surface area should be the same for any size slab. This is true, except on the small slab at high polarities, where the results saturate to a minimum clustering fraction for that slab size (Figure 4.2b).

To gain deeper insight into how polarity impacts clustering, we compute probability distribution functions of cluster size for various surface polarities. Figure 4.3 shows these distributions and hints at some degree of cooperativity during clustering. To model cooperativity, we consider a null hypothesis of noncooperativity. In the noncooperative picture, all molecules in clusters of all sizes behave in exactly the same way; each molecule in the cluster can dissociate from the cluster at any time, with a rate  $k_d$ , and any molecule in the cluster can associate with a new molecule at any time, with a rate  $k_a$ . Ignoring events in which larger pieces (dimers, trimers, etc.) associate or dissociate simultaneously, which should be rare at the low concentrations studied here, clusters can only change size by one molecule at a time. For  $n > 1$ , the following master equation describes

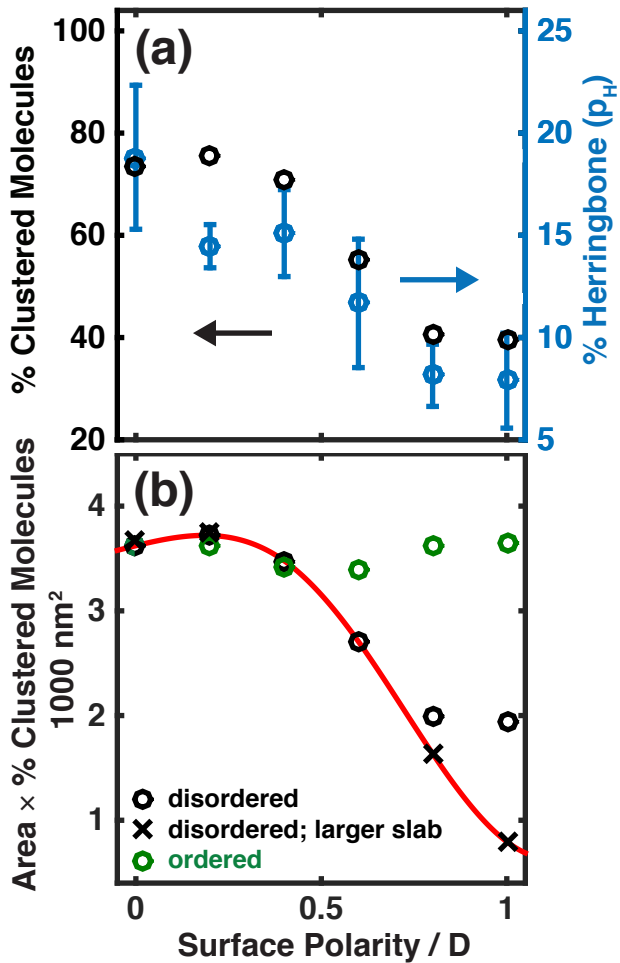


Figure 4.2: (a; left axis) The fraction of clustered molecules decreases as a function of surface polarity when the orientations of the dipoles on the surface are disordered. (a; right axis) Of molecules in clusters, the fraction in herringbone structures,  $p_H$ , also decreases as a function of surface polarity. (b) The fraction of clustered molecules multiplied by the surface area for both random (black) and uniform dipoles (green) in simulations with a fixed number of molecules on a small slab ( $\circ$ ) and a large slab ( $\times$ ). Multiplying the fraction of clustered molecules by the surface area should put the large and small slab simulations on the same curve. The red line is a guide for the eye that follows this curve. The data for the small slab do not fall on the red curve for polarities larger than 0.6  $D$  because the size of the slab limits the minimum clustering fraction. The fraction of molecules in a cluster do not depend on the surface polarity when dipoles are uniformly oriented either parallel or perpendicular to the slab (green  $\circ$ ). Note that for a nonpolar surface (0  $D$ ), the distinction between ordered and disordered polarity is meaningless. All absolute error bars are less than  $\pm 10\%$  or  $500 \text{ nm}^2$ .

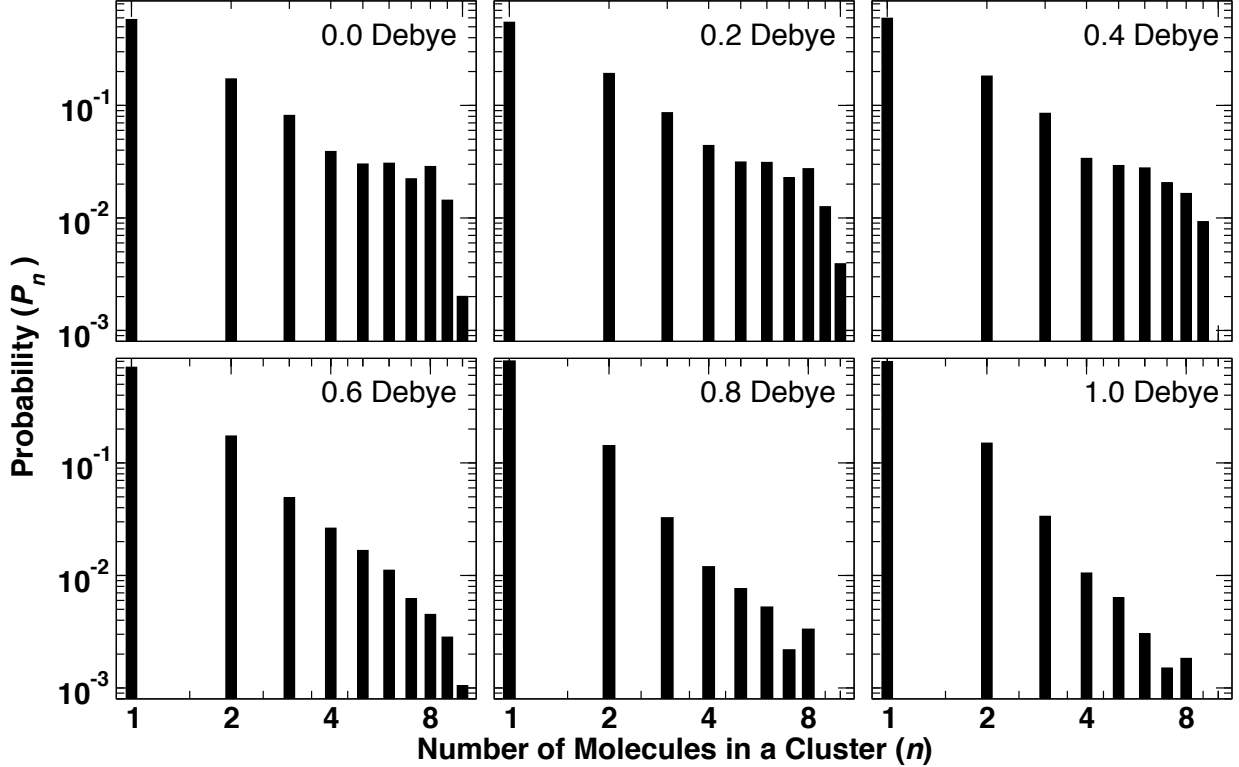


Figure 4.3: The probability of observing a cluster containing  $n$  molecules for various values of polarity on a disordered surface. Large cluster sizes occur with a much lower frequency than a noncooperative model would predict, especially for polarities above 0.4 D. To account for this observation, we explore two mechanisms: anticooperative cluster growth and monomer trapping to the surface.

this scenario

$$\frac{dP_n(t)}{dt} = k_a(n-1)P_{n-1}(t) + k_d(n+1)P_{n+1}(t) - (k_d + k_a)nP_n(t) \quad (4.2)$$

where  $P_n(t)$  is the probability of finding a cluster of  $n$  molecules at time  $t$ . At steady state,  $\frac{dP_n(t)}{dt} = 0$ , we find the equilibrium clustering probabilities,  $P_n$ , by solving the recurrence relation

$$K(n-1)P_{n-1} + (n+1)P_{n+1} - (1+K)nP_n = 0 \quad (4.3)$$

where  $K \equiv k_a/k_d$  is the equilibrium constant. The solution can be found using the ansatz  $nP_n = z^n$ , with appropriate boundary conditions, and is

$$P_n = \frac{1-K^n}{n} \left( \frac{P_1}{1-K} \right) \quad (4.4)$$

While the numerator tends to unity exponentially fast,  $P_n$  goes as a power law,  $n^{-1}$ , for asymptotically large  $n$ . Our data decay faster than the  $n^{-1}$  expectation from the noncooperative model at all polarities, but especially for polarities above 0.4 D where the decay law is closer to  $n^{-3}$ . This could mean that clustering becomes increasingly anticooperative as surface polarity increases; that is, the larger a cluster grows, the more it resists growth. But there is an alternate scenario where the surface plays a pivotal role. The fluctuations in polarity on disordered surfaces give molecules opportunities to find pockets on the surface to which they strongly attract, effectively trapping them and making it more difficult for them to join clusters.

To distinguish between these two mechanisms, we study the hypothesis that trapping inhibits clustering by calculating the diffusion constant of one molecule on a surface. We compute the 2d diffusion constant,  $D_{2d}$ , from the mean-squared displacement of a single tetracene molecule's COM projected onto the plane of the surface. The mean-squared displacement is averaged over many trajectories and realizations of the disorder.  $D_{2d}$  decreases exponentially with polarity on a disordered surface (Figure 4.4), confirming that the tetracene molecules adhere more strongly to the surface at higher polarities.

To cast this observation in the theoretical framework of diffusion in disordered media, one must translate the dependence of  $D_{2d}$  on the polarity to its dependence on the potential energy. The fluctuations in the potential are more drastic when the randomly oriented dipoles have larger magnitudes, so the variance of the potential fluctuations should scale with the polarity. There are, unfortunately, few theories that relate the quenched disorder of a potential to the renormalization of the diffusion constant without resorting to the phenomenology of continuous time random walks.<sup>78,79</sup> In one dimension, Zwanzig showed that the diffusion constant depends exponentially on the variance of the potential energy when the fluctuations are drawn from a Gaussian distribution.<sup>80</sup> To see if our data fit this trend, we compute the variance of the interaction energy between a tetracene molecule and the surface. While the variance increases monotonically with polarity, the relationship is not linear, so  $D_{2d}$  is not exponential in the variance. The connection here is tenuous: our system is not one-dimensional, and the fluctuations in the potential are not necessarily

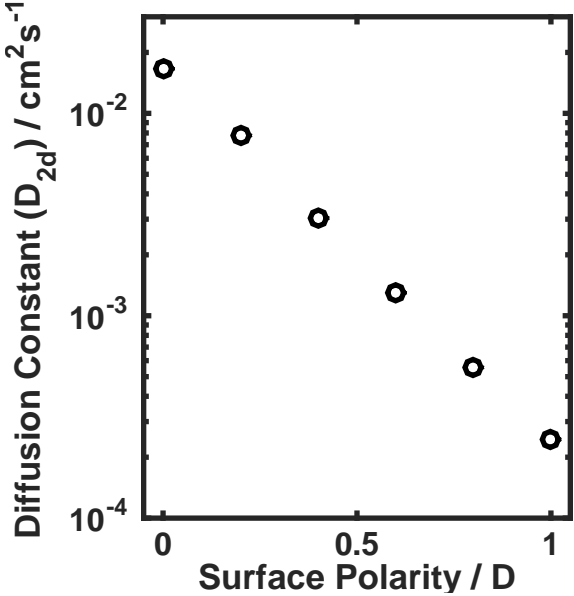


Figure 4.4: Diffusion constants decrease exponentially with polarity on disordered surfaces. Diffusion constants are calculated using the mean-squared displacement of a molecule’s center-of-mass projected onto the slab. Error bars are smaller than the data markers.

Gaussian. The near-perfect exponential decay of the diffusion constant with polarity in Figure 4.4 is, however, striking.

For our results to have bearing on SF, the clustered structures must persist for time scales that are comparable to or longer than the time scale for SF. Because the herringbone well in the free energy surface is shallow, about  $1 k_B T$  deep (Figure 4.1a), fluctuations away from the herringbone structure are facile. One might worry that the putative herringbone structure is nothing more than a fleeting fluctuation. We estimate the persistence time of the herringbone structures by measuring the time correlation function for a herringbone order parameter, which is unity when a given molecule is in a herringbone structure with at least one neighbor and zero otherwise.<sup>81,82</sup> Decay times of the time correlation function average poorly at our concentrations, but we estimate that herringbone structures survive on time scales from 10 to 100 ps. Estimates for the SF rate range from sub-ps to 100 ps,<sup>8,22,40,83,84</sup> therefore, it is likely that the herringbone structures identified here are stable on the time scale of SF. The lifetime of a cluster is longer: at least 1 ns. This is

why REMD is necessary to achieve equilibrium.

Singlet fission could be the key to next-generation solar cells, but it is still difficult to establish design principles for cost-effective and robust devices. One of the most conceptually simple implementations of a SF device is a DSSC, but the functionality of a DSSC depends on the chromophore molecules aggregating in geometries that are suitable for SF. We find that a significant fraction of tetracene molecules on a surface do indeed self-assemble into herringbone structures at surface concentrations as small as a few percent of a monolayer. This result supports the hypothesis that herringbone structures in small aggregates give rise to the Davydov splitting seen in the absorption spectra of tetracene on silica at low surface coverage.<sup>50</sup> Further, the semiconductor surface can play an important role in both aggregation and SF; a recent study has found that SF in a DSSC requires a spacer layer on the semiconductor surface.<sup>6</sup> This layer could introduce a polar surface and allow for experimental tuning of the polarity. We find that when the surface is microscopically polar, the roughness in the potential between the molecules and the surface lets the molecules adhere to pockets on the surface more strongly, resulting in less clustering, smaller clusters, and fewer molecules in herringbone structures. When the surface is macroscopically polar, the roughness in the potential disappears, and surprisingly, the polarity does not affect clustering or herringbone formation statistics. The role of polarity is therefore subtle, and our results run counter to the expectation that clustering statistics arise from a microscopic version of phase separation, where nonpolar acene molecules form clusters as they retreat from a polar surface. Though our simulation results apply to tetracene, it is likely that the qualitative conclusions drawn here apply to other acene molecules that engage in singlet fission, like pentacene.

## Bibliography

- [1] Strong, S. E.; Eaves, J. D. Tetracene aggregation on polar and nonpolar surfaces: Implications for singlet fission. *J. Phys. Chem. Lett.*, 6(7):1209–1215, **2015**.
- [2] Hanna, M. C.; Nozik, A. J. Solar conversion efficiency of photovoltaic and photoelectrolysis cells with carrier multiplication absorbers. *J. of Appl. Phys.*, 100(7):074510–8, **2006**.

- [3] Shockley, W.; Queisser, H. J. Detailed balance limit of efficiency of  $p - n$  junction solar cells. *J. Appl. Phys.*, 32(3):510–519, **1961**.
- [4] O'Regan, B.; Grätzel, M. A low-cost, high-efficiency solar cell based on dye-sensitized colloidal  $TiO_2$  films. *Nature*, 353(6346):737–740, **1991**.
- [5] Teichen, P. E.; Eaves, J. D. A microscopic model of singlet fission. *J. Phys. Chem. B*, 116(37):11473–11481, **2012**.
- [6] Schrauben, J. N.; Zhao, Y.; Mercado, C.; Dron, P. I.; Ryerson, J. L.; Michl, J.; Zhu, K.; Johnson, J. C. Photocurrent enhanced by singlet fission in a dye-sensitized solar cell. *ACS Appl. Mater. Interfaces*, 7(4):2286–2293, **2015**.
- [7] Smith, M. B.; Michl, J. Singlet fission. *Chem. Rev.*, 110(11):6891–6936, **2010**.
- [8] Smith, M. B.; Michl, J. Recent advances in singlet fission. *Ann. Rev. Phys. Chem.*, 64:361–386, **2013**.
- [9] Paci, I.; Johnson, J. C.; Chen, X.; Rana, G.; Popović, D.; David, D. E.; Nozik, A. J.; Ratner, M. A.; Michl, J. Singlet fission for dye-sensitized solar cells: Can a suitable sensitizer be found? *J. Am. Chem. Soc.*, 128(51):16546–16553, **2006**.
- [10] Akdag, A.; Havlas, Z.; Michl, J. Search for a small chromophore with efficient singlet fission: Biradicaloid heterocycles. *J. Am. Chem. Soc.*, 134(35):14624–14631, **2012**.
- [11] Greyson, E. C.; Stepp, B. R.; Chen, X.; Schwerin, A. F.; Paci, I.; Smith, M. B.; Akdag, A.; Johnson, J. C.; Nozik, A. J.; Michl, J.; et al. Singlet exciton fission for solar cell applications: Energy aspects of interchromophore coupling. *J. Phys. Chem. B*, 114(45):14223–14232, **2009**.
- [12] Greyson, E. C.; Vura-Weis, J.; Michl, J.; Ratner, M. A. Maximizing singlet fission in organic dimers: Theoretical investigation of triplet yield in the regime of localized excitation and fast coherent electron transfer. *J. Phys. Chem. B*, 114(45):14168–14177, **2010**.
- [13] Johnson, J. C.; Nozik, A. J.; Michl, J. High triplet yield from singlet fission in a thin film of 1,3-diphenylisobenzofuran. *J. Am. Chem. Soc.*, 132(46):16302–16303, **2010**.
- [14] Johnson, J. C.; Nozik, A. J.; Michl, J. The role of chromophore coupling in singlet fission. *Acc. Chem. Res.*, 46(6):1290–1299, **2013**.
- [15] Roberts, S. T.; McAnally, R. E.; Mastron, J. N.; Webber, D. H.; Whited, M. T.; Brutchey, R. L.; Thompson, M. E.; Bradforth, S. E. Efficient singlet fission discovered in a disordered acene film. *J. Am. Chem. Soc.*, 134(14):6388–6400, **2012**.
- [16] Piland, G. B.; Burdett, J. J.; Kurunthu, D.; Bardeen, C. J. Magnetic field effects on singlet fission and fluorescence decay dynamics in amorphous rubrene. *J. Phys. Chem. C*, 117(3):1224–1236, **2012**.
- [17] Wang, L.; Olivier, Y.; Prezhdo, O. V.; Beljonne, D. Maximizing singlet fission by intermolecular packing. *J. Phys. Chem. Lett.*, 5(19):3345–3353, **2014**.
- [18] Müller, A. M.; Avlasevich, Y. S.; Schoeller, W. W.; Müllen, K.; Bardeen, C. J. Exciton fission and fusion in bis(tetracene) molecules with different covalent linker structures. *J. Am. Chem. Soc.*, 129(46):14240–14250, **2007**.

- [19] Ma, L.; Zhang, K.; Kloc, C.; Sun, H.; Michel-Beyerle, M. E.; Gurzadyan, G. G. Singlet fission in rubrene single crystal: Direct observation by femtosecond pump-probe spectroscopy. *Phys. Chem. Chem. Phys.*, 14(23):8307, **2012**.
- [20] Yost, S. R.; Lee, J.; Wilson, M. W. B.; Wu, T.; McMahon, D. P.; Parkhurst, R. R.; Thompson, N. J.; Congreve, D. N.; Rao, A.; Johnson, K.; et al. A transferable model for singlet-fission kinetics. *Nat. Chem.*, 6(6):492–497, **2014**.
- [21] Liu, H.; Nichols, V. M.; Shen, L.; Jahanousz, S.; Chen, Y.; Hanson, K. M.; Bardeen, C. J.; Li, X. Synthesis and photophysical properties of a “face-to-face” stacked tetracene dimer. *Phys. Chem. Chem. Phys.*, **2015**.
- [22] Burdett, J. J.; Mueller, A. M.; Gosztola, D.; Bardeen, C. J. Excited state dynamics in solid and monomeric tetracene: The roles of superradiance and exciton fission. *J. Chem. Phys.*, 133(14):144506, **2010**.
- [23] Ryerson, J. L.; Schrauben, J. N.; Ferguson, A. J.; Sahoo, S. C.; Naumov, P.; Havlas, Z.; Michl, J.; Nozik, A. J.; Johnson, J. C. Two thin film polymorphs of the singlet fission compound 1,3-diphenylisobenzofuran. *J. Phys. Chem. C*, 118(23):12121–12132, **2014**.
- [24] Lee, J.; Jadhav, P.; Baldo, M. A. High efficiency organic multilayer photodetectors based on singlet exciton fission. *Appl. Phys. Lett.*, 95(3):033301, **2009**.
- [25] Marciak, H.; Fiebig, M.; Huth, M.; Schiefer, S.; Nickel, B.; Selmaier, F.; Lochbrunner, S. Ultrafast exciton relaxation in microcrystalline pentacene films. *Phys. Rev. Lett.*, 99(17):176402, **2007**.
- [26] Kuhlman, T. S.; Kongsted, J.; Mikkelsen, K. V.; Møller, K. B.; Sølling, T. I. Interpretation of the ultrafast photoinduced processes in pentacene thin films. *J. Am. Chem. Soc.*, 132(10):3431–3439, **2010**.
- [27] Havenith, R. W.; de Gier, H. D.; Broer, R. Explorative computational study of the singlet fission process. *Mol. Phys.*, 110(19–20):2445–2454, **2012**.
- [28] Zimmerman, P. M.; Bell, F.; Casanova, D.; Head-Gordon, M. Mechanism for singlet fission in pentacene and tetracene: From single exciton to two triplets. *J. Am. Chem. Soc.*, 133(49):19944–19952, **2011**.
- [29] Ramanan, C.; Smeigh, A. L.; Anthony, J. E.; Marks, T. J.; Wasielewski, M. R. Competition between singlet fission and charge separation in solution-processed blend films of 6,13-bis(triisopropylsilyl)ethynylpentacene with sterically-encumbered perylene-3,4:9,10-bis(dicarboximide)s. *J. Am. Chem. Soc.*, 134(1):386–397, **2011**.
- [30] Eaton, S. W.; Shoer, L. E.; Karlen, S. D.; Dyar, S. M.; Margulies, E. A.; Veldkamp, B. S.; Ramanan, C.; Hartzler, D. A.; Savikhin, S.; Marks, T. J.; et al. Singlet exciton fission in polycrystalline thin films of a slip-stacked perylenediimide. *J. Am. Chem. Soc.*, 135(39):14701–14712, **2013**.
- [31] Müller, A. M.; Avlasevich, Y. S.; Müllen, K.; Bardeen, C. J. Evidence for exciton fission and fusion in a covalently linked tetracene dimer. *Chem. Phys. Lett.*, 421(4–6):518–522, **2006**.

- [32] Quarti, C.; Fazzi, D.; Del Zoppo, M. A computational investigation on singlet and triplet exciton couplings in acene molecular crystals. *Phys. Chem. Chem. Phys.*, 13(41):18615, **2011**.
- [33] Marciak, H.; Pugliesi, I.; Nickel, B.; Lochbrunner, S. Ultrafast singlet and triplet dynamics in microcrystalline pentacene films. *Phys. Rev. B*, 79(23):235318, **2009**.
- [34] Johnson, J. C.; Akdag, A.; Zamadar, M.; Chen, X.; Schwerin, A. F.; Paci, I.; Smith, M. B.; Havlas, Z.; Miller, J. R.; Ratner, M. A.; et al. Toward designed singlet fission: Solution photophysics of two indirectly coupled covalent dimers of 1,3-diphenylisobenzofuran. *J. Phys. Chem. B*, 117(16):4680–4695, **2013**.
- [35] Michl, J.; Nozik, A. J.; Chen, X.; Johnson, J. C.; Rana, G.; Akdag, A.; Schwerin, A. F. Toward singlet fission for excitonic solar cells. In *SPIE Proceedings: Organic Photovoltaics*, volume 6656, pages 66560E–66560E–9. **2007**.
- [36] Schwob, H. P.; Williams, D. F. Charge transfer exciton fission in anthracene crystals. *J. Chem. Phys.*, 58(4):1542–1547, **1973**.
- [37] Ryasnyanskiy, A.; Biaggio, I. Triplet exciton dynamics in rubrene single crystals. *Phys. Rev. B*, 84(19):193203, **2011**.
- [38] Najafov, H.; Lee, B.; Zhou, Q.; Feldman, L. C.; Podzorov, V. Observation of long-range exciton diffusion in highly ordered organic semiconductors. *Nat. Mater.*, 9(11):938–943, **2010**.
- [39] Chen, Y.; Lee, B.; Fu, D.; Podzorov, V. The origin of a 650 nm photoluminescence band in rubrene. *Adv. Mater.*, 23(45):5370–5375, **2011**.
- [40] Burdett, J. J.; Gosztola, D.; Bardeen, C. J. The dependence of singlet exciton relaxation on excitation density and temperature in polycrystalline tetracene thin films: Kinetic evidence for a dark intermediate state and implications for singlet fission. *J. Chem. Phys.*, 135(21):214508, **2011**.
- [41] Berkelbach, T. C.; Hybertsen, M. S.; Reichman, D. R. Microscopic theory of singlet exciton fission. I. General formulation. *J. Chem. Phys.*, 138(11):114102, **2013**.
- [42] Berkelbach, T. C.; Hybertsen, M. S.; Reichman, D. R. Microscopic theory of singlet exciton fission. II. Application to pentacene dimers and the role of superexchange. *J. Chem. Phys.*, 138(11):114103, **2013**.
- [43] Berkelbach, T. C.; Hybertsen, M. S.; Reichman, D. R. Microscopic theory of singlet exciton fission. III. Crystalline pentacene. *J. Chem. Phys.*, 141(7):074705, **2014**.
- [44] Schwerin, A. F.; Johnson, J. C.; Smith, M. B.; Sreearunothai, P.; Popović, D.; Černý, J.; Havlas, Z.; Paci, I.; Akdag, A.; MacLeod, M. K.; et al. Toward designed singlet fission: Electronic states and photophysics of 1,3-diphenylisobenzofuran. *J. Phys. Chem. A*, 114(3):1457–1473, **2009**.
- [45] Renaud, N.; Sherratt, P. A.; Ratner, M. A. Mapping the relation between stacking geometries and singlet fission yield in a class of organic crystals. *J. Phys. Chem. Lett.*, 4(7):1065–1069, **2013**.

- [46] Feng, X.; Luzanov, A. V.; Krylov, A. I. Fission of entangled spins: An electronic structure perspective. *J. Phys. Chem. Lett.*, 4(22):3845–3852, **2013**.
- [47] Anthony, J. E. The larger acenes: Versatile organic semiconductors. *Angew. Chem. Int. Ed.*, 47(3):452–483, **2008**.
- [48] Anthony, J. E.; Eaton, D. L.; Parkin, S. R. A road map to stable, soluble, easily crystallized pentacene derivatives. *Organic Lett.*, 4(1):15–18, **2001**.
- [49] Maly, K. E. Acenes vs N-heteroacenes: The effect of N-substitution on the structural features of crystals of polycyclic aromatic hydrocarbons. *Cryst. Growth Des.*, 11(12):5628–5633, **2011**.
- [50] Dabestani, R.; Nelson, M.; Sigman, M. E. Photochemistry of tetracene adsorbed on dry silica: Products and mechanism. *Photochem. Photobiol.*, 64(1):80–86, **1996**.
- [51] Alguire, E. C.; Subotnik, J. E.; Damrauer, N. H. Exploring non-condon effects in a covalent tetracene dimer: How important are vibrations in determining the electronic coupling for singlet fission? *J. Phys. Chem. A*, 119(2):299–311, **2014**.
- [52] Walker, B. J.; Musser, A. J.; Beljonne, D.; Friend, R. H. Singlet exciton fission in solution. *Nat. Chem.*, 5(12):1019–1024, **2013**.
- [53] Willard, A. P.; Chandler, D. Coarse-grained modeling of the interface between water and heterogeneous surfaces. *Faraday Discuss.*, 141:209–220, **2009**.
- [54] Willard, A. P.; Reed, S. K.; Madden, P. A.; Chandler, D. Water at an electrochemical interface—a simulation study. *Faraday Discuss.*, 141:423–441, **2009**.
- [55] Chandler, D. Interfaces and the driving force of hydrophobic assembly. *Nature*, 437(7059):640–647, **2005**.
- [56] Willard, A. P.; Chandler, D. The molecular structure of the interface between water and a hydrophobic substrate is liquid-vapor like. *J. Chem. Phys.*, 141(18):18C519, **2014**.
- [57] Hagfeldt, A.; Boschloo, G.; Sun, L.; Kloo, L.; Pettersson, H. Dye-sensitized solar cells. *Chem. Rev.*, 110(11):6595–6663, **2010**.
- [58] Hair, M. L. Hydroxyl groups on silica surface. *J. Non-Cryst. Solids*, 19:299–309, **1975**.
- [59] Diebold, U. The surface science of titanium dioxide. *Surf. Sci. Rep.*, 48(5–8):53–229, **2003**.
- [60] Hoex, B.; Schmidt, J.; Pohl, P.; van de Sanden, M. C. M.; Kessels, W. M. M. Silicon surface passivation by atomic layer deposited Al<sub>2</sub>O<sub>3</sub>. *J. Appl. Phys.*, 104(4):044903, **2008**.
- [61] Kroemer, H. Nobel lecture: Quasielectric fields and band offsets: Teaching electrons new tricks. *Rev. mod. phy*, 73(3):783–793, **2001**.
- [62] Sweeney, M. C.; Eaves, J. D. Carrier transport in heterojunction nanocrystals under strain. *J. Phys. Chem. Lett.*, 3(6):791–795, **2011**.
- [63] Noguera, C. Polar oxide surfaces. *J. Phys.: Condens. Mat.*, 12(31):R367, **2000**.
- [64] Sugita, Y.; Okamoto, Y. Replica-exchange molecular dynamics method for protein folding. *Chem. Phys. Lett.*, 314(1–2):141–151, **1999**.

- [65] Campbell, R. B.; Robertson, J. M.; Trotter, J. The crystal structure of hexacene, and a revision of the crystallographic data for tetracene. *Acta Crystallogr.*, 15(3):289–290, **1962**.
- [66] Mayo, S. L.; Olafson, B. D.; Goddard, W. A. DREIDING: A generic force field for molecular simulations. *J. Phys. Chem.*, 94(26):8897–8909, **1990**.
- [67] Della Valle, R. G.; Venuti, E.; Brillante, A.; Girlando, A. Do computed crystal structures of nonpolar molecules depend on the electrostatic interactions? The case of tetracene. *J. Phys. Chem. A*, 112(5):1085–1089, **2008**.
- [68] Deng, W.-Q.; Goddard, W. A. Predictions of hole mobilities in oligoacene organic semiconductors from quantum mechanical calculations. *J. Phys. Chem. B*, 108(25):8614–8621, **2004**.
- [69] Giannozzi, P.; Baroni, S.; Bonini, N.; Calandra, M.; Car, R.; Cavazzoni, C.; Davide Ceresoli; Chiarotti, G. L.; Cococcioni, M.; Dabo, I.; et al. QUANTUM ESPRESSO: A modular and open-source software project for quantum simulations of materials. *J. Phys.: Condens. Matter*, 21(39):395502, **2009**.
- [70] Schmidt, M. W.; Baldridge, K. K.; Boatz, J. A.; Elbert, S. T.; Gordon, M. S.; Jensen, J. H.; Koseki, S.; Matsunaga, N.; Nguyen, K. A.; Su, S.; et al. General atomic and molecular electronic structure system. *J. Comput. Chem.*, 14(11):1347–1363, **1993**.
- [71] Mattheus, C. C.; de Wijs, G. A.; de Groot, R. A.; Palstra, T. T. M. Modeling the polymorphism of pentacene. *J. Am. Chem. Soc.*, 125(20):6323–6330, **2003**.
- [72] Yeh, I.-C.; Berkowitz, M. L. Ewald summation for systems with slab geometry. *J. Chem. Phys.*, 111(7):3155–3162, **1999**.
- [73] Tuckerman, M.; Berne, B. J.; Martyna, G. J. Reversible multiple time scale molecular dynamics. *J. Chem. Phys.*, 97(3):1990–2001, **1992**.
- [74] Hoover, W. G. Canonical dynamics: Equilibrium phase-space distributions. *Phys. Rev. A*, 31(3):1695–1697, **1985**.
- [75] Nosé, S. A unified formulation of the constant temperature molecular dynamics methods. *J. Chem. Phys.*, 81(1):511–519, **1984**.
- [76] Eaves, J. D.; Tokmakoff, A.; Geissler, P. L. Electric field fluctuations drive vibrational dephasing in water. *J. Phys. Chem. A*, 109(42):9424–9436, **2005**.
- [77] Chandler, D. *Introduction to Modern Statistical Mechanics*. Oxford University Press, New York, 1<sup>st</sup> edition, **1987**.
- [78] Bouchaud, J.-P.; Georges, A. Anomalous diffusion in disordered media: Statistical mechanisms, models and physical applications. *Phys. Rep.*, 195(4–5):127–293, **1990**.
- [79] Banerjee, S.; Biswas, R.; Seki, K.; Bagchi, B. Diffusion on a rugged energy landscape with spatial correlations. *J. Chem. Phys.*, 141(12):124105, **2014**.
- [80] Zwanzig, R. Diffusion in a rough potential. *Proc. Nat. Acad. Sci. U. S. A.*, 85(7):2029–2030, **1988**.

- [81] Bennett, C. H. Exact defect calculations in model substances. In Nowick, A.; Burton, J., eds., *Diffusion in Solids: Recent Developments*, pages 73–113. Academic Press, New York, **1975**.
- [82] Chandler, D. Statistical mechanics of isomerization dynamics in liquids and the transition state approximation. *J. Chem. Phys.*, 68(6):2959–2970, **1978**.
- [83] Chan, W.-L.; Ligges, M.; Jailaubekov, A.; Kaake, L.; Miaja-Avila, L.; Zhu, X.-Y. Observing the multiexciton state in singlet fission and ensuing ultrafast multielectron transfer. *Science*, 334(6062):1541–1545, **2011**.
- [84] Burdett, J. J.; Bardeen, C. J. The dynamics of singlet fission in crystalline tetracene and covalent analogs. *Acc. Chem. Res.*, 46(6):1312–1320, **2013**.
- [85] Yokoi, K. Empirical atom-atom potential for a naphthalene crystal and transferability to other polyacene crystals. *Mol. Phys.*, 85(3):449–462, **1995**.
- [86] Raiteri, P.; Martoňák, R.; Parrinello, M. Exploring polymorphism: The case of benzene. *Angew. Chem. Int. Ed.*, 44(24):3769–3773, **2005**.
- [87] Mattheus, C. C.; Dros, A. B.; Baas, J.; Meetsma, A.; de Boer, J. L.; Palstra, T. T. M. Polymorphism in pentacene. *Acta Crystallogr. Sect. C Cryst. Struct. Commun.*, 57(8):939–941, **2001**.
- [88] Yokoi, B. K.; Nishikawa, T. Revised intermolecular potential with parameters depending on partial atomic charges for aromatic molecular systems. *Mol. Phys.*, 90(5):705–712, **1997**.
- [89] Nabok, D.; Puschnig, P.; Ambrosch-Draxl, C.; Werzer, O.; Resel, R.; Smilgies, D.-M. Crystal and electronic structures of pentacene thin films from grazing-incidence x-ray diffraction and first-principles calculations. *Phys. Rev. B*, 76(23):235322, **2007**.
- [90] Della Valle, R. G.; Venuti, E.; Brillante, A.; Girlando, A. Inherent structures of crystalline pentacene. *J. Chem. Phys.*, 118(2):807–815, **2003**.
- [91] Yoneya, M.; Kawasaki, M.; Ando, M. Are pentacene monolayer and thin-film polymorphs really substrate-induced? A molecular dynamics simulation study. *J. Phys. Chem. C*, 116(1):791–795, **2012**.
- [92] Venuti, E.; Della Valle, R. G.; Brillante, A.; Masino, M.; Girlando, A. Probing pentacene polymorphs by lattice dynamics calculations. *J. Am. Chem. Soc.*, 124(10):2128–2129, **2002**.
- [93] Yoshida, H.; Sato, N. Crystallographic and electronic structures of three different polymorphs of pentacene. *Phys. Rev. B*, 77(23):235205, **2008**.
- [94] Holmes, D.; Kumaraswamy, S.; Matzger, A. J.; Vollhardt, K. P. C. On the nature of nonplanarity in the [N]phenylenes. *Chem. Eur. J.*, 5(11):3399–3412, **1999**.
- [95] Mattheus, C. C.; Dros, A. B.; Baas, J.; Oostergetel, G. T.; Meetsma, A.; de Boer, J. L.; Palstra, T. T. Identification of polymorphs of pentacene. *Synth. Met.*, 138(3):475–481, **2003**.
- [96] Zingg, S. P.; Sigman, M. E. Influence of an SiO<sub>2</sub>/cyclohexane interface on the photochemistry of anthracene. *Photochem. Photobiol.*, 57(3):453–459, **1993**.

- [97] Schatschneider, B.; Monaco, S.; Tkatchenko, A.; Liang, J.-J. Understanding the structure and electronic properties of molecular crystals under pressure: Application of dispersion corrected DFT to oligoacenes. *J. Phys. Chem. A*, 117(34):8323–8331, **2013**.
- [98] Barbas, J. T.; Dabestani, R.; Sigman, M. F. A mechanistic study of photodecomposition of acenaphthylene on a dry silica surface. *J. Photochem. Photobiol. A*, 80(1–3):103–111, **1994**.
- [99] Debestani, R.; Ellis, K. J.; Sigman, M. E. Photodecomposition of anthracene on dry surfaces: Products and mechanism. *J. Photochem. Photobiol. A*, 86(1–3):231–239, **1995**.
- [100] Campbell, R. B.; Robertson, J. M.; Trotter, J. The crystal and molecular structure of pentacene. *Acta Crystallogr.*, 14(7):705–711, **1961**.
- [101] Della Valle, R. G.; Venuti, E.; Brillante, A.; Girlando, A. Inherent structures of crystalline tetracene. *J. Phys. Chem. A*, 110(37):10858–10862, **2006**.
- [102] Farina, L.; Brillante, A.; Della Valle, R. G.; Venuti, E.; Amboage, M.; Syassen, K. Pressure-induced phase transition in pentacene. *Chem. Phys. Lett.*, 375(5–6):490–494, **2003**.
- [103] Kasha, M. Characterization of electronic transitions in complex molecules. *Faraday Discuss.*, 9:14–19, **1950**.
- [104] Tang, J.; Ge, G.; Brus, L. E. Gas-liquid-solid phase transition model for two-dimensional nanocrystal self-assembly on graphite. *J. Phys. Chem. B*, 106(22):5653–5658, **2002**.
- [105] Swope, W. C.; Andersen, H. C.; Berens, P. H.; Wilson, K. R. A computer simulation method for the calculation of equilibrium constants for the formation of physical clusters of molecules: Application to small water clusters. *J. Chem. Phys.*, 76(1):637–649, **1982**.
- [106] Witten, T. A.; Sander, L. M. Diffusion-limited aggregation. *Phys. Rev. B*, 27(9):5686–5697, **1983**.
- [107] Witten, T. A.; Sander, L. M. Diffusion-limited aggregation, a kinetic critical phenomenon. *Phys. Rev. Lett.*, 47(19):1400–1403, **1981**.
- [108] Meakin, P.; Vicsek, T.; Family, F. Dynamic cluster-size distribution in cluster-cluster aggregation: Effects of cluster diffusivity. *Phys. Rev. B*, 31(1):564–569, **1985**.
- [109] Würthner, F.; Kaiser, T. E.; Saha-Möller, C. R. J-aggregates: From serendipitous discovery to supramolecular engineering of functional dye materials. *Angew. Chem. Int. Ed.*, 50(15):3376–3410, **2011**.
- [110] Eisfeld, A.; Briggs, J. S. The J- and H-bands of organic dye aggregates. *Chem. Phys.*, 324(2–3):376–384, **2006**.
- [111] Kasha, M.; Rawls, H. R.; Ashraf, E.-B. M. The exciton model in molecular spectroscopy. *Pure Appl. Chem.*, 11(3–4):371–392, **2009**.
- [112] Beljonne, D.; Cornil, J.; Silbey, R.; Millié, P.; Brédas, J. L. Interchain interactions in conjugated materials: The exciton model versus the supermolecular approach. *J. Chem. Phys.*, 112(10):4749–4758, **2000**.

- [113] Spano, F. C. Emission from aggregates of oligo-phenylene vinylenes: A recipe for superradiant H-aggregates. *Chem. Phys. Lett.*, 331(1):7–13, **2000**.
- [114] Troisi, A. Charge transport in high mobility molecular semiconductors: Classical models and new theories. *Chem. Soc. Rev.*, 40(5):2347–2358, **2011**.
- [115] Singh, S.; Jones, W. J.; Siebrand, W.; Stoicheff, B. P.; Schneider, W. G. Laser generation of excitons and fluorescence in anthracene crystals. *J. Chem. Phys.*, 42(1):330–342, **1965**.
- [116] Troisi, A.; Orlandi, G. Band structure of the four pentacene polymorphs and effect on the hole mobility at low temperature. *J. Phys. Chem. B*, 109(5):1849–1856, **2005**.
- [117] Ambrosio, F.; Troisi, A. Singlet fission in linear chains of molecules. *J. Chem. Phys.*, 141(20):204703, **2014**.
- [118] Aryanpour, K.; Muñoz, J. A.; Mazumdar, S. Does singlet fission enhance the performance of organic solar cells? *J. Phys. Chem. C*, 117(10):4971–4979, **2013**.
- [119] Chan, W.-L.; Tritsch, J. R.; Zhu, X.-Y. Harvesting singlet fission for solar energy conversion one- versus two-electron transfer from the quantum mechanical superposition. *J. Am. Chem. Soc.*, **2012**.
- [120] Grumstrup, E. M.; Johnson, J. C.; Damrauer, N. H. Enhanced triplet formation in polycrystalline tetracene films by femtosecond optical-pulse shaping. *Phys. Rev. Lett.*, 105(25):257403, **2010**.
- [121] Yamagata, H.; Norton, J.; Hontz, E.; Olivier, Y.; Beljonne, D.; Brédas, J. L.; Silbey, R. J.; Spano, F. C. The nature of singlet excitons in oligoacene molecular crystals. *J. Chem. Phys.*, 134(20):204703–204703–11, **2011**.
- [122] Bässler, H.; Köhler, A. Charge transport in organic semiconductors. *Top. Curr. Chem.*, 312:1–65, **2012**.
- [123] Coropceanu, V.; Cornil, J.; da Silva Filho, D. A.; Olivier, Y.; Silbey, R.; Brédas, J.-L. Charge transport in organic semiconductors. *Chem. Rev.*, 107(4):926–952, **2007**.
- [124] Kolomeisky, A. B.; Feng, X.; Krylov, A. I. A simple kinetic model for singlet fission: A role of electronic and entropic contributions to macroscopic rates. *J. Phys. Chem. C*, 118(10):5188–5195, **2014**.
- [125] Geacintov, N.; Pope, M.; Vogel, F. Effect of magnetic field on the fluorescence of tetracene crystals: Exciton fission. *Phys. Rev. Lett.*, 22(12):593–596, **1969**.
- [126] Kaake, L. G.; Barbara, P. F.; Zhu, X.-Y. Intrinsic charge trapping in organic and polymeric semiconductors: A physical chemistry perspective. *J. Phys. Chem. Lett.*, 1(3):628–635, **2010**.
- [127] Rivnay, J.; Jimison, L. H.; Northrup, J. E.; Toney, M. F.; Noriega, R.; Lu, S.; Marks, T. J.; Facchetti, A.; Salleo, A. Large modulation of carrier transport by grain-boundary molecular packing and microstructure in organic thin films. *Nat. Mater.*, 8(12):952–958, **2009**.
- [128] Lim, S.-H.; Bjorklund, T. G.; Spano, F. C.; Bardeen, C. J. Exciton delocalization and superradiance in tetracene thin films and nanoaggregates. *Phys. Rev. Lett.*, 92(10):107402, **2004**.

- [129] Grätzel, M. Solar energy conversion by dye-sensitized photovoltaic cells. *Inorg. Chem.*, 44(20):6841–6851, **2005**.
- [130] Roberts, S. T.; Schlenker, C. W.; Barlier, V.; McAnally, R. E.; Zhang, Y.; Mastron, J. N.; Thompson, M. E.; Bradforth, S. E. Observation of triplet exciton formation in a platinum-sensitized organic photovoltaic device. *J. Phys. Chem. Lett.*, 2(2):48–54, **2010**.
- [131] Akimov, A. V.; Prezhdo, O. V. Nonadiabatic dynamics of charge transfer and singlet fission at the pentacene/C<sub>60</sub> interface. *J. Am. Chem. Soc.*, 136(4):1599–1608, **2014**.
- [132] Parker, S. M.; Seideman, T.; Ratner, M. A.; Shiozaki, T. Model hamiltonian analysis of singlet fission from first principles. *J. Phys. Chem. C*, 118(24):12700–12705, **2014**.
- [133] Wilson, M. W. B.; Rao, A.; Clark, J.; Kumar, R. S. S.; Brida, D.; Cerullo, G.; Friend, R. H. Ultrafast dynamics of exciton fission in polycrystalline pentacene. *J. Am. Chem. Soc.*, 133(31):11830–11833, **2011**.
- [134] Vallett, P. J.; Snyder, J. L.; Damrauer, N. H. Tunable electronic coupling and driving force in structurally well-defined tetracene dimers for molecular singlet fission: A computational exploration using density functional theory. *J. Phys. Chem. A*, 117(42):10824–10838, **2013**.
- [135] Chan, W.-L.; Ligges, M.; Zhu, X. Y. The energy barrier in singlet fission can be overcome through coherent coupling and entropic gain. *Nat. Chem.*, 4(10):840–845, **2012**.
- [136] Aberle, A. G. Surface passivation of crystalline silicon solar cells: A review. *Prog. Photovoltaics*, 8(5):473–487, **2000**.
- [137] Tasker, P. W. The stability of ionic crystal surfaces. *J. Phys. C*, 12(22):4977, **1979**.
- [138] Fenner, D. B.; Biegelsen, D. K.; Bringans, R. D. Silicon surface passivation by hydrogen termination: A comparative study of preparation methods. *J. Appl. Phys.*, 66(1):419–424, **1989**.
- [139] Hukushima, K.; Nemoto, K. Exchange Monte Carlo method and application to spin glass simulations. *J. Phys. Soc. Jpn.*, 65(6):1604–1608, **1996**.
- [140] Löwdin, P.-O. On the nonorthogonality problem. In *Advances in Quantum Chemistry*, volume 5, pages 185–199. Academic Press, **1970**.
- [141] Sanchez-Portal, D.; Artacho, E.; Soler, J. M. Projection of plane-wave calculations into atomic orbitals. *Solid State Commun.*, 95(10):685–690, **1995**.
- [142] Ballenegger, V.; Arnold, A.; Cerdà, J. J. Simulations of non-neutral slab systems with long-range electrostatic interactions in two-dimensional periodic boundary conditions. *J. Chem. Phys.*, 131(9):094107, **2009**.
- [143] van Kampen, N. G. *Stochastic Processes in Physics and Chemistry*. Elsevier, Amsterdam, 3<sup>rd</sup> edition, **1992**.
- [144] Hockney, R. W.; Eastwood, J. W. *Computer Simulation Using Particles*. Taylor & Francis, New York, **1989**.

## Chapter 5

### Complete Bibliography

This is a compilation of all the works consulted in the preparation of this Thesis. Works cited within a chapter are referenced to the bibliography at the end of that chapter.

Standard tables for reference solar spectral irradiances: Direct normal and hemispherical on 37° tilted surface. Technical Report G173–03, ASTM International, **2012**.

Summary for policymakers. In Edenhofer, O.; Pichs-Madruga, R.; Farahani, E.; Kadner, S.; Seyboth, K.; Adler, A.; Baum, I.; Brunner, S.; Eickemeier, P.; Kriemann, B.; et al., eds., *Climate Change 2014: Mitigation of Climate Change. Contribution of Working Group III to the Fifth Assessment Report of the Intergovernmental Panel on Climate Change*, pages 1–30. Cambridge University Press, Cambridge, **2014**.

Abdul-Hamid, O. S.; Odulaja, A.; Hassani, H.; Christodoulides, P.; Stöger, K.; Kalirai, H.; Moudasir, M.; Pospiech, R.; Gredinger, A.; Hamamciyan, L.-S.; et al. OPEC annual statistical bulletin. Technical Report ESA/P/WP.242, OPEC, **2016**.

Aberle, A. G. Surface passivation of crystalline silicon solar cells: A review. *Prog. Photovoltaics*, 8(5):473–487, **2000**.

Aghigh, A.; Alizadeh, V.; Wong, H. Y.; Islam, M. S.; Amin, N.; Zaman, M. Recent advances in utilization of graphene for filtration and desalination of water: A review. *Desalination*, 365:389–397, **2015**.

Akdag, A.; Havlas, Z.; Michl, J. Search for a small chromophore with efficient singlet fission: Biradicaloid heterocycles. *J. Am. Chem. Soc.*, 134(35):14624–14631, **2012**.

Akimov, A. V.; Prezhdo, O. V. Nonadiabatic dynamics of charge transfer and singlet fission at the pentacene/C<sub>60</sub> interface. *J. Am. Chem. Soc.*, 136(4):1599–1608, **2014**.

Alder, B. J.; Wainwright, T. E. Studies in molecular dynamics. I. General method. *J. Chem. Phys.*, 31(2):459–466, **1959**.

Alder, B. J.; Wainwright, T. E. Velocity autocorrelations for hard spheres. *Phys. Rev. Lett.*, 18(23):988–990, **1967**.

- Alder, B. J.; Wainwright, T. E. Decay of the velocity autocorrelation function. *Phys. Rev. A*, 1(1):18–21, **1970**.
- Alguire, E. C.; Subotnik, J. E.; Damrauer, N. H. Exploring non-condon effects in a covalent tetracene dimer: How important are vibrations in determining the electronic coupling for singlet fission? *J. Phys. Chem. A*, 119(2):299–311, **2014**.
- Ambrosio, F.; Troisi, A. Singlet fission in linear chains of molecules. *J. Chem. Phys.*, 141(20):204703, **2014**.
- Andersen, H. C. RATTLE: A “velocity” version of the SHAKE algorithm for molecular dynamics calculations. *J. Comput. Phys.*, 52(1):24–34, **1983**.
- Anthony, J. E. The larger acenes: Versatile organic semiconductors. *Angew. Chem. Int. Ed.*, 47(3):452–483, **2008**.
- Anthony, J. E.; Eaton, D. L.; Parkin, S. R. A road map to stable, soluble, easily crystallized pentacene derivatives. *Organic Lett.*, 4(1):15–18, **2001**.
- Aryanpour, K.; Muñoz, J. A.; Mazumdar, S. Does singlet fission enhance the performance of organic solar cells? *J. Phys. Chem. C*, 117(10):4971–4979, **2013**.
- Ashraf, A.; Wu, Y.; Wang, M. C.; Yong, K.; Sun, T.; Jing, Y.; Haasch, R. T.; Aluru, N. R.; Nam, S. Doping-induced tunable wettability and adhesion of graphene. *Nano Lett.*, 16(7):4708–4712, **2016**.
- Ashurst, W. T.; Hoover, W. G. Dense-fluid shear viscosity via nonequilibrium molecular dynamics. *Phys. Rev. A*, 11(2):658–678, **1975**.
- Bae, S.; Kim, H.; Lee, Y.; Xu, X.; Park, J.-S.; Zheng, Y.; Balakrishnan, J.; Lei, T.; Ri Kim, H.; Song, Y. I.; et al. Roll-to-roll production of 30-inch graphene films for transparent electrodes. *Nat. Nanotechnol.*, 5(8):574–578, **2010**.
- Baldwin, R. L. Temperature dependence of the hydrophobic interaction in protein folding. *Proc. Nat. Acad. Sci. U. S. A.*, 83(21):8069–8072, **1986**.
- Ballenegger, V.; Arnold, A.; Cerdà, J. J. Simulations of non-neutral slab systems with long-range electrostatic interactions in two-dimensional periodic boundary conditions. *J. Chem. Phys.*, 131(9):094107, **2009**.
- Banerjee, S.; Biswas, R.; Seki, K.; Bagchi, B. Diffusion on a rugged energy landscape with spatial correlations. *J. Chem. Phys.*, 141(12):124105, **2014**.
- Bao, W.; Liu, G.; Zhao, Z.; Zhang, H.; Yan, D.; Deshpande, A.; LeRoy, B.; Lau, C. N. Lithography-free fabrication of high quality substrate-supported and freestanding graphene devices. *Nano Res.*, 3(2):98–102, **2010**.
- Bao, W.; Myhro, K.; Zhao, Z.; Chen, Z.; Jang, W.; Jing, L.; Miao, F.; Zhang, H.; Dames, C.; Lau, C. N. In situ observation of electrostatic and thermal manipulation of suspended graphene membranes. *Nano Lett.*, 12(11):5470–5474, **2012**.
- Barbas, J. T.; Dabestani, R.; Sigman, M. F. A mechanistic study of photodecomposition of ace-naphthylene on a dry silica surface. *J. Photochem. Photobiol. A*, 80(1–3):103–111, **1994**.

- Barrat, J.-L.; Bocquet, L. Large slip effect at a nonwetting fluid-solid interface. *Phys. Rev. Lett.*, 82(23):4671–4674, **1999**.
- Bässler, H.; Köhler, A. Charge transport in organic semiconductors. *Top. Curr. Chem.*, 312:1–65, **2012**.
- Bekker, H.; Dijkstra, E. J.; Renardus, M. K. R.; Berendsen, H. J. C. An efficient, box shape independent non-bonded force and virial algorithm for molecular dynamics. *Mol. Simulat.*, 14(3):137–151, **1995**.
- Beljonne, D.; Cornil, J.; Silbey, R.; Millié, P.; Brédas, J. L. Interchain interactions in conjugated materials: The exciton model versus the supermolecular approach. *J. Chem. Phys.*, 112(10):4749–4758, **2000**.
- Bell, D. C.; Lemme, M. C.; Stern, L. A.; Williams, J. R.; Marcus, C. M. Precision cutting and patterning of graphene with helium ions. *Nanotechnology*, 20(45):455301, **2009**.
- Bennett, C. H. Exact defect calculations in model substances. In Nowick, A.; Burton, J., eds., *Diffusion in Solids: Recent Developments*, pages 73–113. Academic Press, New York, **1975**.
- Berendsen, H. J. C.; Grigera, J. R.; Straatsma, T. P. The missing term in effective pair potentials. *J. Phys. Chem.*, 91(24):6269–6271, **1987**.
- Berendsen, H. J. C.; Postma, J. P. M.; van Gunsteren, W. F.; Hermans, J. Interaction models for water in relation to protein hydration. In Pullman, B., ed., *Intermolecular Forces*, volume 14 of *The Jerusalem Symposia on Quantum Chemistry and Biochemistry*, pages 331–342. Springer, Netherlands, **1981**.
- Berezhkovskii, A.; Hummer, G. Single-file transport of water molecules through a carbon nanotube. *Phys. Rev. Lett.*, 89(6):064503, **2002**.
- Berkelbach, T. C.; Hybertsen, M. S.; Reichman, D. R. Microscopic theory of singlet exciton fission. I. General formulation. *J. Chem. Phys.*, 138(11):114102, **2013**.
- Berkelbach, T. C.; Hybertsen, M. S.; Reichman, D. R. Microscopic theory of singlet exciton fission. II. Application to pentacene dimers and the role of superexchange. *J. Chem. Phys.*, 138(11):114103, **2013**.
- Berkelbach, T. C.; Hybertsen, M. S.; Reichman, D. R. Microscopic theory of singlet exciton fission. III. Crystalline pentacene. *J. Chem. Phys.*, 141(7):074705, **2014**.
- Bernardi, S.; Todd, B. D.; Searles, D. J. Thermostating highly confined fluids. *J. Chem. Phys.*, 132(24):244706, **2010**.
- Bernstein, H. J.; Weisskopf, V. F. About liquids. *Am. J. Phys.*, 55(11):974–983, **1987**.
- Bieri, M.; Treier, M.; Cai, J.; Aït-Mansour, K.; Ruffieux, P.; Gröning, O.; Gröning, P.; Kastler, M.; Rieger, R.; Feng, X.; et al. Porous graphenes: Two-dimensional polymer synthesis with atomic precision. *Chem. Commun.*, 45:6919–6921, **2009**.
- Bird, R. B.; Stewart, W. E.; Lightfoot, E. N. *Transport Phenomena*. John Wiley & Sons, Inc., New York, 2<sup>nd</sup> edition, **2006**.

- Bolhuis, P. G.; Chandler, D. Transition path sampling of cavitation between molecular scale solvophobic surfaces. *J. Chem. Phys.*, 113(18):8154–8160, **2000**.
- Bonetto, F.; Lebowitz, J. L.; Rey-Bellet, L. Fourier’s law: A challenge for theorists. *arXiv*, math-ph/0002052, **2000**.
- Bouchaud, J.-P.; Georges, A. Anomalous diffusion in disordered media: Statistical mechanisms, models and physical applications. *Phys. Rep.*, 195(4–5):127–293, **1990**.
- Branicio, P. S.; Srolovitz, D. J. Local stress calculation in simulations of multicomponent systems. *J. Comput. Phys.*, 228(22):8467–8479, **2009**.
- Brovchenko, I.; Geiger, A.; Oleinikova, A. Water in nanopores. I. Coexistence curves from Gibbs ensemble Monte Carlo simulations. *J. Chem. Phys.*, 120(4):1958–1972, **2004**.
- Brovchenko, I.; Geiger, A.; Oleinikova, A. Water in nanopores: II. The liquid-vapour phase transition near hydrophobic surfaces. *J. Phys.: Condens. Matter*, 16(45):S5345, **2004**.
- Brovchenko, I.; Oleinikova, A. Water in nanopores: III. Surface phase transitions of water on hydrophilic surfaces. *J. Phys. Chem. C*, 111(43):15716–15725, **2007**.
- Buchanan, P.; Aldiwan, N.; Soper, A. K.; Creek, J. L.; Koh, C. A. Decreased structure on dissolving methane in water. *Chem. Phys. Lett.*, 415(1–3):89–93, **2005**.
- Burdett, J. J.; Bardeen, C. J. The dynamics of singlet fission in crystalline tetracene and covalent analogs. *Acc. Chem. Res.*, 46(6):1312–1320, **2013**.
- Burdett, J. J.; Gosztola, D.; Bardeen, C. J. The dependence of singlet exciton relaxation on excitation density and temperature in polycrystalline tetracene thin films: Kinetic evidence for a dark intermediate state and implications for singlet fission. *J. Chem. Phys.*, 135(21):214508, **2011**.
- Burdett, J. J.; Mueller, A. M.; Gosztola, D.; Bardeen, C. J. Excited state dynamics in solid and monomeric tetracene: The roles of superradiance and exciton fission. *J. Chem. Phys.*, 133(14):144506, **2010**.
- Campbell, R. B.; Robertson, J. M.; Trotter, J. The crystal and molecular structure of pentacene. *Acta Crystallogr.*, 14(7):705–711, **1961**.
- Campbell, R. B.; Robertson, J. M.; Trotter, J. The crystal structure of hexacene, and a revision of the crystallographic data for tetracene. *Acta Crystallogr.*, 15(3):289–290, **1962**.
- Casieri, C.; Monaco, A.; De Luca, F. Evidence of temperature-induced subdiffusion of water on the micrometer scale in a Nafion membrane. *Macromolecules*, 43(2):638–642, **2010**.
- Castillo-Tejas, J.; Rojas-Morales, A.; López-Medina, F.; Alvarado, J. F. J.; Luna-Bárcenas, G.; Bautista, F.; Manero, O. Flow of linear molecules through a 4:1:4 contraction-expansion using non-equilibrium molecular dynamics: Extensional rheology and pressure drop. *J. Non-Newton. Fluid.*, 161(1–3):48–59, **2009**.
- Chan, W.-L.; Ligges, M.; Jaijalaubekov, A.; Kaake, L.; Miaja-Avila, L.; Zhu, X.-Y. Observing the multiexciton state in singlet fission and ensuing ultrafast multielectron transfer. *Science*, 334(6062):1541–1545, **2011**.

- Chan, W.-L.; Ligges, M.; Zhu, X. Y. The energy barrier in singlet fission can be overcome through coherent coupling and entropic gain. *Nat. Chem.*, 4(10):840–845, **2012**.
- Chan, W.-L.; Tritsch, J. R.; Zhu, X.-Y. Harvesting singlet fission for solar energy conversion one-versus two-electron transfer from the quantum mechanical superposition. *J. Am. Chem. Soc.*, **2012**.
- Chandler, D. Statistical mechanics of isomerization dynamics in liquids and the transition state approximation. *J. Chem. Phys.*, 68(6):2959–2970, **1978**.
- Chandler, D. *Introduction to Modern Statistical Mechanics*. Oxford University Press, New York, 1<sup>st</sup> edition, **1987**.
- Chandler, D. Electron transfer in water and other polar environments, how it happens. In Berne, B. J.; Ciccotti, G.; Coker, D. F., eds., *Classical and Quantum Dynamics in Condensed Phase Simulations*, pages 25–49. World Scientific, Singapore, **1998**.
- Chandler, D. Hydrophobicity: Two faces of water. *Nature*, 417(6888):491–491, **2002**.
- Chandler, D. Interfaces and the driving force of hydrophobic assembly. *Nature*, 437(7059):640–647, **2005**.
- Chandler, D.; Weeks, J. D.; Andersen, H. C. Van der Waals picture of liquids, solids, and phase transformations. *Science*, 220(4599):787–794, **1983**.
- Chen, Y.; Lee, B.; Fu, D.; Podzorov, V. The origin of a 650 nm photoluminescence band in rubrene. *Adv. Mater.*, 23(45):5370–5375, **2011**.
- Cheung, K. S.; Yip, S. Atomic-level stress in an inhomogeneous system. *J. Appl. Phys.*, 70(10):5688–5690, **1991**.
- Choi, Y.; Ree, T.; Ree, F. H. Phase diagram of a Lennard-Jones solid. *J. Chem. Phys.*, 99(12):9917, **1993**.
- Chong, T. H.; Loo, S.-L.; Krantz, W. B. Energy-efficient reverse osmosis desalination process. *J. Membr. Sci.*, 473:177–188, **2015**.
- Chou, T. How fast do fluids squeeze through microscopic single-file pores? *Phys. Rev. Lett.*, 80(1):85–88, **1998**.
- Church, J.; Clark, P.; Cazenave, A.; Gregory, J.; Jevrejeva, S.; Levermann, A.; Merrifield, M.; Milne, G.; Nerem, R.; Nunn, P.; et al. Sea level change. In Stocker, T.; Qin, D.; Plattner, G.-K.; Tignor, M.; Allen, S.; Boschung, J.; Nauels, A.; Xia, Y.; Bex, V.; Midgley, P., eds., *Climate Change 2013: The Physical Science Basis. Contribution of Working Group I to the Fifth Assessment Report of the Intergovernmental Panel on Climate Change*, pages 1137–1216. Cambridge University Press, Cambridge, **2013**.
- Clauset, A.; Shalizi, C.; Newman, M. Power-law distributions in empirical data. *SIAM Rev.*, 51(4):661–703, **2009**.
- Clausius, R. On a mechanical theorem applicable to heat. *Philos. Mag.*, 40(265):122–127, **1870**.

- Cohen-Tanugi, D.; Grossman, J. C. Water desalination across nanoporous graphene. *Nano Lett.*, 12(7):3602–3608, **2012**.
- Cohen-Tanugi, D.; Grossman, J. C. Water permeability of nanoporous graphene at realistic pressures for reverse osmosis desalination. *J. Chem. Phys.*, 141(7):074704, **2014**.
- Coropceanu, V.; Cornil, J.; da Silva Filho, D. A.; Olivier, Y.; Silbey, R.; Brédas, J.-L. Charge transport in organic semiconductors. *Chem. Rev.*, 107(4):926–952, **2007**.
- Corry, B. Designing carbon nanotube membranes for efficient water desalination. *J. Phys. Chem. B*, 112(5):1427–1434, **2008**.
- Cottin-Bizonne, C.; Barentin, C.; Charlaix, É.; Bocquet, L.; Barrat, J.-L. Dynamics of simple liquids at heterogeneous surfaces: Molecular-dynamics simulations and hydrodynamic description. *Eur. Phys. J. E*, 15(4):427–438, **2004**.
- Cronström, C.; Raita, T. On nonholonomic systems and variational principles. *J. Math. Phys.*, 50(4):042901, **2009**.
- Dabestani, R.; Nelson, M.; Sigman, M. E. Photochemistry of tetracene adsorbed on dry silica: Products and mechanism. *Photochem. Photobiol.*, 64(1):80–86, **1996**.
- Dameron, A. A.; Davidson, S. D.; Burton, B. B.; Garcia, P. F.; McLean, R. S.; George, S. M. Gas diffusion barriers on polymers using multilayers fabricated by Al<sub>2</sub>O<sub>3</sub> and rapid SiO<sub>2</sub> atomic layer deposition. *J. Phys. Chem. C*, 112(12):4573–4580, **2008**.
- Dashtpour, R.; Al-Zubaidy, S. N. Energy efficient reverse osmosis desalination process. *Int. J. Environ. Sci. Develop.*, 3(4):339, **2012**.
- Daub, C. D.; Bratko, D.; Leung, K.; Luzar, A. Electrowetting at the nanoscale. *J. Phys. Chem. C*, 111(2):505–509, **2007**.
- Davis, J. G.; Gierszal, K. P.; Wang, P.; Ben-Amotz, D. Water structural transformation at molecular hydrophobic interfaces. *Nature*, 491(7425):582–585, **2012**.
- Davis, J. G.; Rankin, B. M.; Gierszal, K. P.; Ben-Amotz, D. On the cooperative formation of non-hydrogen-bonded water at molecular hydrophobic interfaces. *Nat. Chem.*, 5(9):796–802, **2013**.
- de Gennes, P. G. Wetting: Statics and dynamics. *Rev. Mod. Phys.*, 57(3):827–863, **1985**.
- Debestani, R.; Ellis, K. J.; Sigman, M. E. Photodecomposition of anthracene on dry surfaces: Products and mechanism. *J. Photochem. Photobiol. A*, 86(1–3):231–239, **1995**.
- Della Valle, R. G.; Venuti, E.; Brillante, A.; Girlando, A. Inherent structures of crystalline tetracene. *J. Phys. Chem. A*, 110(37):10858–10862, **2006**.
- Della Valle, R. G.; Venuti, E.; Brillante, A.; Girlando, A. Do computed crystal structures of nonpolar molecules depend on the electrostatic interactions? The case of tetracene. *J. Phys. Chem. A*, 112(5):1085–1089, **2008**.
- Della Valle, R. G.; Venuti, E.; Brillante, A.; Girlando, A. Inherent structures of crystalline pentacene. *J. Chem. Phys.*, 118(2):807–815, **2003**.

- Deng, W.-Q.; Goddard, W. A. Predictions of hole mobilities in oligoacene organic semiconductors from quantum mechanical calculations. *J. Phys. Chem. B*, 108(25):8614–8621, **2004**.
- Department of Economic and Social Affairs, Population Division. World population prospects: The 2015 revision, methodology of the United Nations population estimates and projections. Technical Report ESA/P/WP.242, United Nations, **2015**.
- Dewar, R. C. Maximum entropy production and the fluctuation theorem. *J. Phys. A.*, 38(21):L371–L381, **2005**.
- Diebold, U. The surface science of titanium dioxide. *Surf. Sci. Rep.*, 48(5–8):53–229, **2003**.
- Docherty, S. Y.; Nicholls, W. D.; Borg, M. K.; Lockerby, D. A.; Reese, J. M. Boundary conditions for molecular dynamics simulations of water transport through nanotubes. *Proc. Inst. Mech. Eng. C.*, 228(1):186–195, **2014**.
- Drahushuk, L. W.; Wang, L.; Koenig, S. P.; Bunch, J. S.; Strano, M. S. Analysis of time-varying, stochastic gas transport through graphene membranes. *ACS Nano*, 10(1):786–795, **2016**.
- Du, X.; Skachko, I.; Barker, A.; Andrei, E. Y. Approaching ballistic transport in suspended graphene. *Nat. Nanotechnol.*, 3(8):491–495, **2008**.
- E. A. Carter, G. C. Constrained reaction coordinate dynamics for the simulation of rare events. *Chem. Phys. Lett.*, 156(5):472–477, **1989**.
- Eaton, S. W.; Shoer, L. E.; Karlen, S. D.; Dyar, S. M.; Margulies, E. A.; Veldkamp, B. S.; Ramanan, C.; Hartzler, D. A.; Savikhin, S.; Marks, T. J.; et al. Singlet exciton fission in polycrystalline thin films of a slip-stacked perylenediimide. *J. Am. Chem. Soc.*, 135(39):14701–14712, **2013**.
- Eaves, J. D.; Loparo, J. J.; Fecko, C. J.; Roberts, S. T.; Tokmakoff, A.; Geissler, P. L. Hydrogen bonds in liquid water are broken only fleetingly. *Proc. Nat. Acad. Sci. U. S. A.*, 102(37):13019–13022, **2005**.
- Eaves, J. D.; Tokmakoff, A.; Geissler, P. L. Electric field fluctuations drive vibrational dephasing in water. *J. Phys. Chem. A*, 109(42):9424–9436, **2005**.
- Edberg, R.; Evans, D. J.; Morriss, G. P. Constrained molecular dynamics: Simulations of liquid alkanes with a new algorithm. *J. Chem. Phys.*, 84(12):6933–6939, **1986**.
- Eisfeld, A.; Briggs, J. S. The J- and H-bands of organic dye aggregates. *Chem. Phys.*, 324(2–3):376–384, **2006**.
- El-Dessouky, H. T.; Ettouney, H. M. *Fundamentals of Salt Water Desalination*. Elsevier, **2002**.
- Elimelech, M.; Phillip, W. A. The future of seawater desalination: Energy, technology, and the environment. *Science*, 333(6043):712–717, **2011**.
- Evans, D. J. Computer “experiment” for nonlinear thermodynamics of Couette flow. *J. Chem. Phys.*, 78(6):3297–3302, **1983**.
- Evans, D. J.; Hoover, W. G.; Failor, B. H.; Moran, B.; Ladd, A. J. C. Nonequilibrium molecular dynamics via Gauss’s principle of least constraint. *Phys. Rev. A*, 28(2):1016–1021, **1983**.

- Evans, D. J.; Morriss, G. P. Non-Newtonian molecular dynamics. *Comput. Phys. Rep.*, 1(6):297–343, **1984**.
- Evans, D. J.; Morriss, G. *Statistical Mechanics of Nonequilibrium Liquids*. Cambridge University Press, Cambridge, 2<sup>nd</sup> edition, **2008**.
- Evans, D. J.; Morriss, G. P. Shear thickening and turbulence in simple fluids. *Phys. Rev. Lett.*, 56(20):2172–2175, **1986**.
- Falconer, J. L.; George, S. M.; Ott, A. W.; Klaus, J. W.; Noble, R. D.; Funke, H. H. Modification of zeolite or molecular sieve membranes using atomic layer controlled chemical vapor deposition. U. S. Patent 6043177 A, **2000**.
- Falk, K.; Sedlmeier, F.; Joly, L.; Netz, R. R.; Bocquet, L. Molecular origin of fast water transport in carbon nanotube membranes: Superlubricity versus curvature dependent friction. *Nano Lett.*, 10(10):4067–4073, **2010**.
- Farina, L.; Brillante, A.; Della Valle, R. G.; Venuti, E.; Amboage, M.; Syassen, K. Pressure-induced phase transition in pentacene. *Chem. Phys. Lett.*, 375(5–6):490–494, **2003**.
- Farmer, D. B.; Golizadeh-Mojarad, R.; Perebeinos, V.; Lin, Y.-M.; Tulevski, G. S.; Tsang, J. C.; Avouris, P. Chemical doping and electron-hole conduction asymmetry in graphene devices. *Nano Lett.*, 9(1):388–392, **2009**.
- Feng, X.; Luzanov, A. V.; Krylov, A. I. Fission of entangled spins: An electronic structure perspective. *J. Phys. Chem. Lett.*, 4(22):3845–3852, **2013**.
- Fenner, D. B.; Biegelsen, D. K.; Bringans, R. D. Silicon surface passivation by hydrogen termination: A comparative study of preparation methods. *J. Appl. Phys.*, 66(1):419–424, **1989**.
- Fermi, E.; Pasta, J.; Ulam, S. Studies of non linear problems. Technical Report LA-1940, Los Alamos National Laboratory, **1955**.
- Flannery, M. R. The enigma of nonholonomic constraints. *Am. J. Phys.*, 73(3):265–272, **2005**.
- Flannery, M. R. The elusive d'Alembert-Lagrange dynamics of nonholonomic systems. *Am. J. Phys.*, 79(9):932–944, **2011**.
- Frenkel, D.; Smit, B. *Understanding Molecular Simulation: From Algorithms to Applications*. Academic Press, San Diego, 2<sup>nd</sup> edition, **2001**.
- Frentrup, H.; Avendaño, C.; Horsch, M.; Salih, A.; Müller, E. A. Transport diffusivities of fluids in nanopores by non-equilibrium molecular dynamics simulation. *Mol. Simulat.*, 38(7):540–553, **2012**.
- Funke, H. H.; Klaus, J. W.; George, S. M.; Ott, A. W.; Falconer, J. L.; Noble, R. D. Modified zeolite membrane. U. S. Patent 6051517 A, **2000**.
- Galea, T. M.; Attard, P. Molecular dynamics study of the effect of atomic roughness on the slip length at the fluid-solid boundary during shear flow. *Langmuir*, 20(8):3477–3482, **2004**.
- Gao, L.; McCarthy, T. J. Contact angle hysteresis explained. *Langmuir*, 22(14):6234–6237, **2006**.

- Garaj, S.; Hubbard, W.; Reina, A.; Kong, J.; Branton, D.; Golovchenko, J. A. Graphene as a subnanometre trans-electrode membrane. *Nature*, 467(7312):190–193, **2010**.
- Garnier, L.; Szymczyk, A.; Malfreyt, P.; Ghoufi, A. Physics behind water transport through nanoporous boron nitride and graphene. *J. Phys. Chem. Lett.*, pages 3371–3376, **2016**.
- Gauss, C. F. Über ein neues allgemeines grundgesetz der mechanik. *J. Reine Angew. Math.*, 1829(4):232–235, **1829**.
- Geacintov, N.; Pope, M.; Vogel, F. Effect of magnetic field on the fluorescence of tetracene crystals: Exciton fission. *Phys. Rev. Lett.*, 22(12):593–596, **1969**.
- Geissler, P. L.; Chandler, D. Importance sampling and theory of nonequilibrium solvation dynamics in water. *J. Chem. Phys.*, 113(21):9759–9765, **2000**.
- Giannozzi, P.; Baroni, S.; Bonini, N.; Calandra, M.; Car, R.; Cavazzoni, C.; Davide Ceresoli; Chiarotti, G. L.; Cococcioni, M.; Dabo, I.; et al. QUANTUM ESPRESSO: A modular and open-source software project for quantum simulations of materials. *J. Phys.: Condens. Matter*, 21(39):395502, **2009**.
- Giovambattista, N.; Debenedetti, P. G.; Rossky, P. J. Hydration behavior under confinement by nanoscale surfaces with patterned hydrophobicity and hydrophilicity. *J. Phys. Chem. C*, 111(3):1323–1332, **2007**.
- Giovambattista, N.; Lopez, C. F.; Rossky, P. J.; Debenedetti, P. G. Hydrophobicity of protein surfaces: Separating geometry from chemistry. *Proc. Nat. Acad. Sci. U. S. A.*, 105(7):2274–2279, **2008**.
- Goldsmith, J.; Martens, C. C. Molecular dynamics simulation of salt rejection in model surface-modified nanopores. *J. Phys. Chem. Lett.*, 1(2):528–535, **2010**.
- Goldstein, H.; Poole, C. P., Jr.; Safko, J. L. *Classical Mechanics*. Pearson, San Francisco, 3<sup>rd</sup> edition, **2001**.
- González, M. A.; Abascal, J. L. F. The shear viscosity of rigid water models. *J. Chem. Phys.*, 132(9):096101, **2010**.
- Grätzel, M. Solar energy conversion by dye-sensitized photovoltaic cells. *Inorg. Chem.*, 44(20):6841–6851, **2005**.
- Green, M. A.; Emery, K.; Hishikawa, Y.; Warta, W.; Dunlop, E. D. Solar cell efficiency tables (version 48). *Prog. Photovoltaics*, 24(7):905–913, **2016**.
- Greyson, E. C.; Stepp, B. R.; Chen, X.; Schwerin, A. F.; Paci, I.; Smith, M. B.; Akdag, A.; Johnson, J. C.; Nozik, A. J.; Michl, J.; et al. Singlet exciton fission for solar cell applications: Energy aspects of interchromophore coupling. *J. Phys. Chem. B*, 114(45):14223–14232, **2009**.
- Greyson, E. C.; Vura-Weis, J.; Michl, J.; Ratner, M. A. Maximizing singlet fission in organic dimers: Theoretical investigation of triplet yield in the regime of localized excitation and fast coherent electron transfer. *J. Phys. Chem. B*, 114(45):14168–14177, **2010**.
- Groot, R. D.; Warren, P. B. Dissipative particle dynamics: Bridging the gap between atomistic and mesoscopic simulation. *J. Chem. Phys.*, 107(11):4423–4435, **1997**.

- Grumstrup, E. M.; Johnson, J. C.; Damrauer, N. H. Enhanced triplet formation in polycrystalline tetracene films by femtosecond optical-pulse shaping. *Phys. Rev. Lett.*, 105(25):257403, **2010**.
- Hafskjold, B.; Ikeshoji, T. Microscopic pressure tensor for hard-sphere fluids. *Phys. Rev. E*, 66(1):011203, **2002**.
- Hagen, G. Ueber die bewegung des wassers in engen cylindrischen röhren. *Ann. Phys. (Leipzig)*, 122(3):423–442, **1839**.
- Hagfeldt, A.; Boschloo, G.; Sun, L.; Kloo, L.; Pettersson, H. Dye-sensitized solar cells. *Chem. Rev.*, 110(11):6595–6663, **2010**.
- Hair, M. L. Hydroxyl groups on silica surface. *J. Non-Cryst. Solids*, 19:299–309, **1975**.
- Halgren, T. A. The representation of van der Waals (vdW) interactions in molecular mechanics force fields: Potential form, combination rules, and vdW parameters. *J. Am. Chem. Soc.*, 114(20):7827–7843, **1992**.
- Han, Y.; Xu, Z.; Gao, C. Ultrathin graphene nanofiltration membrane for water purification. *Adv. Funct. Mater.*, 23(29):3693–3700, **2013**.
- Hanna, M. C.; Nozik, A. J. Solar conversion efficiency of photovoltaic and photoelectrolysis cells with carrier multiplication absorbers. *J. Appl. Phys.*, 100(7):074510–8, **2006**.
- Hannon, L.; Lie, G. C.; Clementi, E. Molecular dynamics simulation of channel flow. *Phys. Lett. A.*, 119(4):174–177, **1986**.
- Hansen, J.-P.; Verlet, L. Phase transitions of the Lennard-Jones system. *Phys. Rev.*, 184(1):151–161, **1969**.
- Hardy, R. J. Formulas for determining local properties in molecular-dynamics simulations: Shock waves. *J. Chem. Phys.*, 76(1):622–628, **1982**.
- Harvey, S. C.; Tan, R. K.-Z.; Cheatham, T. E. The flying ice cube: Velocity rescaling in molecular dynamics leads to violation of energy equipartition. *J. Comput. Chem.*, 19(7):726–740, **1998**.
- Hatakeyama, E. S.; Ju, H.; Gabriel, C. J.; Lohr, J. L.; Bara, J. E.; Noble, R. D.; Freeman, B. D.; Gin, D. L. New protein-resistant coatings for water filtration membranes based on quaternary ammonium and phosphonium polymers. *J. Membrane Sci.*, 330(1–2):104–116, **2009**.
- Havenith, R. W.; de Gier, H. D.; Broer, R. Explorative computational study of the singlet fission process. *Mol. Phys.*, 110(19–20):2445–2454, **2012**.
- Hazoglou, M. J.; Walther, V.; Dixit, P. D.; Dill, K. A. Communication: Maximum caliber is a general variational principle for nonequilibrium statistical mechanics. *J. Chem. Phys.*, 143(5):051104, **2015**.
- Heinbuch, U.; Fischer, J. Liquid flow in pores: Slip, no-slip, or multilayer sticking. *Phys. Rev. A*, 40(2):1144–1146, **1989**.
- Heinz, H. Calculation of local and average pressure tensors in molecular simulations. *Mol. Simulat.*, 33(9–10):747–758, **2007**.

- Heiranian, M.; Farimani, A. B.; Aluru, N. R. Water desalination with a single-layer MoS<sub>2</sub> nanopore. *Nat. Commun.*, 6:8616, **2015**.
- Helbing, D.; Johansson, A.; Mathiesen, J.; Jensen, M. H.; Hansen, A. Analytical approach to continuous and intermittent bottleneck flows. *Phys. Rev. Lett.*, 97(16):168001, **2006**.
- Heyes, D. M.; Morriss, G. P.; Evans, D. J. Nonequilibrium molecular dynamics study of shear flow in soft disks. *J. Chem. Phys.*, 83(9):4760–4766, **1985**.
- Heyes, D. M. Shear thinning of the Lennard-Jones fluid by molecular dynamics. *Physica A*, 133(3):473–496, **1985**.
- Heyes, D. M. Shear thinning and thickening of the Lennard-Jones liquid. A molecular dynamics study. *J. Chem. Soc. Faraday Trans. 2*, 82(9):1365, **1986**.
- Hill, T. L. *An Introduction to Statistical Thermodynamics*. Dover Publications, Inc., New York, 2<sup>nd</sup> edition, **1986**.
- Hockney, R. W.; Eastwood, J. W. *Computer Simulation Using Particles*. Taylor & Francis, New York, **1989**.
- Hoex, B.; Schmidt, J.; Pohl, P.; van de Sanden, M. C. M.; Kessels, W. M. M. Silicon surface passivation by atomic layer deposited Al<sub>2</sub>O<sub>3</sub>. *J. Appl. Phys.*, 104(4):044903, **2008**.
- Holmes, D.; Kumaraswamy, S.; Matzger, A. J.; Vollhardt, K. P. C. On the nature of nonplanarity in the [N]phenylenes. *Chem. Eur. J.*, 5(11):3399–3412, **1999**.
- Holt, J. K.; Park, H. G.; Wang, Y.; Stadermann, M.; Artyukhin, A. B.; Grigoropoulos, C. P.; Noy, A.; Bakajin, O. Fast mass transport through sub-2-nanometer carbon nanotubes. *Science*, 312(5776):1034–1037, **2006**.
- Hong, G.; Han, Y.; Schutzius, T. M.; Wang, Y.; Pan, Y.; Hu, M.; Jie, J.; Sharma, C. S.; Müller, U.; Poulikakos, D. On the mechanism of hydrophilicity of graphene. *Nano Lett.*, 16(7):4447–4453, **2016**.
- Hoogerbrugge, P. J.; Koelman, J. M. V. A. Simulating microscopic hydrodynamic phenomena with dissipative particle dynamics. *Europhys. Lett.*, 19(3):155, **1992**.
- Hoover, W. G. Canonical dynamics: Equilibrium phase-space distributions. *Phys. Rev. A*, 31(3):1695–1697, **1985**.
- Hoover, W. G.; Ladd, A. J. C.; Moran, B. High-strain-rate plastic flow studied via nonequilibrium molecular dynamics. *Phys. Rev. Lett.*, 48(26):1818–1820, **1982**.
- Hoover, W. G.; Posch, H. A.; Campbell, L. W. Thermal heat reservoirs via Gauss' principle of least constraint; Dissipation, chaos, and phase-space dimensionality loss in one-dimensional chains. *Chaos*, 3(3):325–332, **1993**.
- Hoover, W. G.; Hoover, C. G.; Lutsko, J. F. Microscopic and macroscopic stress with gravitational and rotational forces. *Phys. Rev. E*, 79(3):036709, **2009**.
- Huang, C.; Choi, P. Y. K.; Kostiuk, L. W. A method for creating a non-equilibrium NT(P<sub>1</sub>–P<sub>2</sub>) ensemble in molecular dynamics simulation. *Phys. Chem. Chem. Phys.*, 13(46):20750, **2011**.

- Huang, C.; Nandakumar, K.; Choi, P. Y. K.; Kostiuk, L. W. Molecular dynamics simulation of a pressure-driven liquid transport process in a cylindrical nanopore using two self-adjusting plates. *J. Chem. Phys.*, 124(23):234701, **2006**.
- Huang, X.; Margulis, C. J.; Berne, B. J. Dewetting-induced collapse of hydrophobic particles. *Proc. Nat. Acad. Sci. U. S. A.*, 100(21):11953–11958, **2003**.
- Huang, X.; Zhou, R.; Berne, B. J. Drying and hydrophobic collapse of paraffin plates. *J. Phys. Chem. B*, 109(8):3546–3552, **2005**.
- Hukushima, K.; Nemoto, K. Exchange Monte Carlo method and application to spin glass simulations. *J. Phys. Soc. Jpn.*, 65(6):1604–1608, **1996**.
- Hummer, G.; Garde, S.; García, A. E.; Pohorille, A.; Pratt, L. R. An information theory model of hydrophobic interactions. *Proc. Nat. Acad. Sci. U. S. A.*, 93(17):8951–8955, **1996**.
- Hummer, G.; Rasaiah, J. C.; Noworyta, J. P. Water conduction through the hydrophobic channel of a carbon nanotube. *Nature*, 414(6860):188–190, **2001**.
- Humphrey, W.; Dalke, A.; Schulten, K. VMD – visual molecular dynamics. *J. Mol. Graphics*, 14:33–38, **1996**.
- Irving, J. H.; Kirkwood, J. G. The statistical mechanical theory of transport processes. IV. The equations of hydrodynamics. *J. Chem. Phys.*, 18(6):817–829, **1950**.
- Jain, T.; Rasera, B. C.; Guerrero, R. J. S.; Boutilier, M. S. H.; O'Hern, S. C.; Idrobo, J.-C.; Karnik, R. Heterogeneous sub-continuum ionic transport in statistically isolated graphene nanopores. *Nat. Nanotechnol.*, 10(12):1053–1057, **2015**.
- Joanny, J. F.; de Gennes, P. G. A model for contact angle hysteresis. *J. Chem. Phys.*, 81(1):552–562, **1984**.
- Johnson, J. C.; Akdag, A.; Zamadar, M.; Chen, X.; Schwerin, A. F.; Paci, I.; Smith, M. B.; Havlas, Z.; Miller, J. R.; Ratner, M. A.; et al. Toward designed singlet fission: Solution photo-physics of two indirectly coupled covalent dimers of 1,3-diphenylisobenzofuran. *J. Phys. Chem. B*, 117(16):4680–4695, **2013**.
- Johnson, J. C.; Nozik, A. J.; Michl, J. High triplet yield from singlet fission in a thin film of 1,3-diphenylisobenzofuran. *J. Am. Chem. Soc.*, 132(46):16302–16303, **2010**.
- Johnson, J. C.; Nozik, A. J.; Michl, J. The role of chromophore coupling in singlet fission. *Acc. Chem. Res.*, 46(6):1290–1299, **2013**.
- Joseph, S.; Aluru, N. R. Why are carbon nanotubes fast transporters of water? *Nano Lett.*, 8(2):452–458, **2008**.
- Kaake, L. G.; Barbara, P. F.; Zhu, X.-Y. Intrinsic charge trapping in organic and polymeric semiconductors: A physical chemistry perspective. *J. Phys. Chem. Lett.*, 1(3):628–635, **2010**.
- Kalra, A.; Garde, S.; Hummer, G. Osmotic water transport through carbon nanotube membranes. *Proc. Nat. Acad. Sci. U. S. A.*, 100(18):10175–10180, **2003**.

- Kannam, S. K.; Todd, B. D.; Hansen, J. S.; Daivis, P. J. Slip length of water on graphene: Limitations of non-equilibrium molecular dynamics simulations. *J. Chem. Phys.*, 136(2):024705, **2012**.
- Kannam, S. K.; Todd, B. D.; Hansen, J. S.; Daivis, P. J. How fast does water flow in carbon nanotubes? *J. Chem. Phys.*, 138(9):094701, **2013**.
- Karagiannis, I. C.; Soldatos, P. G. Water desalination cost literature: Review and assessment. *Desalination*, 223(1–3):448–456, **2008**.
- Karplus, M.; Levitt, M.; Warshel, A. Nobel prize in chemistry 2013. [http://www.nobelprize.org/nobel\\_prizes/chemistry/laureates/2013/](http://www.nobelprize.org/nobel_prizes/chemistry/laureates/2013/), **2013**. Accessed: 2017-03-25.
- Kasha, M.; Rawls, H. R.; Ashraf, E.-B. M. The exciton model in molecular spectroscopy. *Pure Appl. Chem.*, 11(3–4):371–392, **2009**.
- Kasha, M. Characterization of electronic transitions in complex molecules. *Faraday Discuss.*, 9:14–19, **1950**.
- Kim, M.; Safron, N. S.; Han, E.; Arnold, M. S.; Gopalan, P. Fabrication and characterization of large-area, semiconducting nanoporous graphene materials. *Nano Lett.*, 10(4):1125–1131, **2010**.
- Kirkwood, J. G. Statistical mechanics of fluid mixtures. *J. Chem. Phys.*, 3(5):300–313, **1935**.
- Kittel, C. *Introduction to Solid State Physics*. Wiley, New York, 2nd edition, **1963**.
- Koelman, J. M. V. A.; Hoogerbrugge, P. J. Dynamic simulations of hard-sphere suspensions under steady shear. *Europhys. Lett.*, 21(3):363, **1993**.
- Koenig, S. P.; Wang, L.; Pellegrino, J.; Bunch, J. S. Selective molecular sieving through porous graphene. *Nat. Nanotechnol.*, 7(11):728–732, **2012**.
- Kolomeisky, A. B.; Feng, X.; Krylov, A. I. A simple kinetic model for singlet fission: A role of electronic and entropic contributions to macroscopic rates. *J. Phys. Chem. C*, 118(10):5188–5195, **2014**.
- Konatham, D.; Yu, J.; Ho, T. A.; Striolo, A. Simulation insights for graphene-based water desalination membranes. *Langmuir*, 29(38):11884–11897, **2013**.
- Koplik, J.; Banavar, J. R.; Willemsen, J. F. Molecular dynamics of fluid flow at solid surfaces. *Phys. Fluids A.*, 1(5):781–794, **1989**.
- Kroemer, H. Nobel lecture: Quasielectric fields and band offsets: Teaching electrons new tricks. *Rev. mod. phy.*, 73(3):783–793, **2001**.
- Kuhlman, T. S.; Kongsted, J.; Mikkelsen, K. V.; Møller, K. B.; Sølling, T. I. Interpretation of the ultrafast photoinduced processes in pentacene thin films. *J. Am. Chem. Soc.*, 132(10):3431–3439, **2010**.
- Laage, D.; Stirnemann, G.; Hynes, J. T. Why water reorientation slows without iceberg formation around hydrophobic solutes. *J. Phys. Chem. B*, 113(8):2428–2435, **2009**.

- Lafond, P. G.; Gilmer, M. W.; Koh, C. A.; Sloan, E. D.; Wu, D. T.; Sum, A. K. Orifice jamming of fluid-driven granular flow. *Phys. Rev. E*, 87(4):042204, **2013**.
- Law, K.-Y.; Zhao, H. What do contact angles measure? In *Surface Wetting*, pages 99–121. Springer International Publishing, **2016**.
- Lee, C.-Y.; McCammon, J. A.; Rossky, P. J. The structure of liquid water at an extended hydrophobic surface. *J. Chem. Phys.*, 80(9):4448–4455, **1984**.
- Lee, J.; Jadhav, P.; Baldo, M. A. High efficiency organic multilayer photodetectors based on singlet exciton fission. *Appl. Phys. Lett.*, 95(3):033301, **2009**.
- Lee, K. P.; Arnot, T. C.; Mattia, D. A review of reverse osmosis membrane materials for desalination—Development to date and future potential. *J. Membrane Sci.*, 370(1–2):1–22, **2011**.
- Lei, W.; Portehault, D.; Liu, D.; Qin, S.; Chen, Y. Porous boron nitride nanosheets for effective water cleaning. *Nat. Commun.*, 4:1777, **2013**.
- Li, I. T. S.; Walker, G. C. Signature of hydrophobic hydration in a single polymer. *Proc. Nat. Acad. Sci. U. S. A.*, 108(40):16527–16532, **2011**.
- Li, J.; Morrone, J. A.; Berne, B. J. Are hydrodynamic interactions important in the kinetics of hydrophobic collapse? *J. Phys. Chem. B*, 116(37):11537–11544, **2012**.
- Lim, S.-H.; Bjorklund, T. G.; Spano, F. C.; Bardeen, C. J. Exciton delocalization and superradiance in tetracene thin films and nanoaggregates. *Phys. Rev. Lett.*, 92(10):107402, **2004**.
- Lin, S.; Elimelech, M. Staged reverse osmosis operation: Configurations, energy efficiency, and application potential. *Desalination*, 366:9–14, **2015**.
- Lin, Y.-M.; Chiu, H.-Y.; Jenkins, K.; Farmer, D. B.; Avouris, P.; Valdes-Garcia, A. Dual-gate graphene FETs with  $f_T$  of 50 GHz. *IEEE Electr. Device Lett.*, 31(1):68–70, **2010**.
- Liu, H.; Nichols, V. M.; Shen, L.; Jahanousz, S.; Chen, Y.; Hanson, K. M.; Bardeen, C. J.; Li, X. Synthesis and photophysical properties of a “face-to-face” stacked tetracene dimer. *Phys. Chem. Chem. Phys.*, **2015**.
- Liu, H.; Liu, Y.; Zhu, D. Chemical doping of graphene. *J. Mater. Chem.*, 21(10):3335–3345, **2011**.
- Liu, L.; Patey, G. N. Simulated conduction rates of water through a (6,6) carbon nanotube strongly depend on bulk properties of the model employed. *J. Chem. Phys.*, 144(18):184502, **2016**.
- Löwdin, P.-O. On the nonorthogonality problem. In *Advances in Quantum Chemistry*, volume 5, pages 185–199. Academic Press, **1970**.
- Lum, K.; Chandler, D.; Weeks, J. D. Hydrophobicity at small and large length scales. *J. Phys. Chem. B*, 103(22):4570–4577, **1999**.
- Lum, K.; Luzar, A. Pathway to surface-induced phase transition of a confined fluid. *Phys. Rev. E*, 56(6):R6283–R6286, **1997**.
- Luzar, A.; Chandler, D. Effect of environment on hydrogen bond dynamics in liquid water. *Phys. Rev. Lett.*, 76(6):928–931, **1996**.

- Ma, L.; Zhang, K.; Kloc, C.; Sun, H.; Michel-Beyerle, M. E.; Gurzadyan, G. G. Singlet fission in rubrene single crystal: Direct observation by femtosecond pump-probe spectroscopy. *Phys. Chem. Chem. Phys.*, 14(23):8307, **2012**.
- Ma, M.; Grey, F.; Shen, L.; Urbakh, M.; Wu, S.; Liu, J. Z.; Liu, Y.; Zheng, Q. Water transport inside carbon nanotubes mediated by phonon-induced oscillating friction. *Nat. Nanotechnol.*, 10(8):692–695, **2015**.
- Mahnke, R.; Pieret, N. Stochastic master-equation approach to aggregation in freeway traffic. *Phys. Rev. E*, 56(3):2666–2671, **1997**.
- Maibaum, L.; Dinner, A. R.; Chandler, D. Micelle formation and the hydrophobic effect. *J. Phys. Chem. B*, 108(21):6778–6781, **2004**.
- Majumder, M.; Chopra, N.; Andrews, R.; Hinds, B. J. Nanoscale hydrodynamics: Enhanced flow in carbon nanotubes. *Nature*, 438(7064):44–44, **2005**.
- Maly, K. E. Acenes vs N-heteroacenes: The effect of N-substitution on the structural features of crystals of polycyclic aromatic hydrocarbons. *Cryst. Growth Des.*, 11(12):5628–5633, **2011**.
- Marciniak, H.; Fiebig, M.; Huth, M.; Schiefer, S.; Nickel, B.; Selmaier, F.; Lochbrunner, S. Ultrafast exciton relaxation in microcrystalline pentacene films. *Phys. Rev. Lett.*, 99(17):176402, **2007**.
- Marciniak, H.; Pugliesi, I.; Nickel, B.; Lochbrunner, S. Ultrafast singlet and triplet dynamics in microcrystalline pentacene films. *Phys. Rev. B*, 79(23):235318, **2009**.
- Mark, P.; Nilsson, L. Structure and dynamics of the TIP3P, SPC, and SPC/E water models at 298 K. *J. Phys. Chem. A*, 105(43):9954–9960, **2001**.
- Martyna, G. J.; Tobias, D. J.; Klein, M. L. Constant pressure molecular dynamics algorithms. *J. Chem. Phys.*, 101(5):4177–4189, **1994**.
- Martyna, G. J.; Tuckerman, M. E.; Tobias, D. J.; Klein, M. L. Explicit reversible integrators for extended systems dynamics. *Mol. Phys.*, 87(5):1117–1157, **1996**.
- Masuda, T.; Nishinari, K.; Schadschneider, A. Critical bottleneck size for jamless particle flows in two dimensions. *Phys. Rev. Lett.*, 112(13):138701, **2014**.
- Mattheus, C. C.; de Wijs, G. A.; de Groot, R. A.; Palstra, T. T. M. Modeling the polymorphism of pentacene. *J. Am. Chem. Soc.*, 125(20):6323–6330, **2003**.
- Mattheus, C. C.; Dros, A. B.; Baas, J.; Meetsma, A.; de Boer, J. L.; Palstra, T. T. M. Polymorphism in pentacene. *Acta Crystallogr. Sect. C Cryst. Struct. Commun.*, 57(8):939–941, **2001**.
- Mattheus, C. C.; Dros, A. B.; Baas, J.; Oostergetel, G. T.; Meetsma, A.; de Boer, J. L.; Palstra, T. T. Identification of polymorphs of pentacene. *Synth. Met.*, 138(3):475–481, **2003**.
- Matysiak, S.; Debenedetti, P. G.; Rossky, P. J. Dissecting the energetics of hydrophobic hydration of polypeptides. *J. Phys. Chem. B*, 115(49):14859–14865, **2011**.
- Maxwell, J. C. On reciprocal figures, frames, and diagrams of forces. *Earth. Env. Sci. Trans. Roy. Soc. Edin.*, 26(01):1–40, **1870**.

- Maxwell, J. C. Van der Waals on the continuity of the gaseous and liquid states. *Nature*, 10:477–480, **1874**.
- Mayo, S. L.; Olafson, B. D.; Goddard, W. A. DREIDING: A generic force field for molecular simulations. *J. Phys. Chem.*, 94(26):8897–8909, **1990**.
- Meakin, P.; Vicsek, T.; Family, F. Dynamic cluster-size distribution in cluster-cluster aggregation: Effects of cluster diffusivity. *Phys. Rev. B*, 31(1):564–569, **1985**.
- Meric, I.; Han, M. Y.; Young, A. F.; Ozyilmaz, B.; Kim, P.; Shepard, K. L. Current saturation in zero-bandgap, top-gated graphene field-effect transistors. *Nat. Nanotechnol.*, 3(11):654–659, **2008**.
- Metropolis, N.; Ulam, S. The Monte Carlo method. *J. Am. Stat. Assoc.*, 44(247):335–341, **1949**.
- Metzler, R.; Klafter, J. The random walk’s guide to anomalous diffusion: A fractional dynamics approach. *Phys. Rep.*, 339(1):1–77, **2000**.
- Michl, J.; Nozik, A. J.; Chen, X.; Johnson, J. C.; Rana, G.; Akdag, A.; Schwerin, A. F. Toward singlet fission for excitonic solar cells. In *SPIE Proceedings: Organic Photovoltaics*, volume 6656, pages 66560E–66560E–9. **2007**.
- Miró, P.; Audiffred, M.; Heine, T. An atlas of two-dimensional materials. *Chem. Soc. Rev.*, 43(18):6537, **2014**.
- Montroll, E. W.; Shlesinger, M. F. On the wonderful world of random walks. In *Nonequilibrium Phenomena II: From Stochastics to Hydrodynamics*, volume 9, pages 5–46. North-Holland Physics Publishing, Amsterdam, **1984**.
- Morriss, G. P.; Dettmann, C. P. Thermostats: Analysis and application. *Chaos*, 8(2):321–336, **1998**.
- Morriss, G. P.; Evans, D. J. A constraint algorithm for the computer simulation of complex molecular liquids. *Comput. Phys. Commun.*, 62(2–3):267–278, **1991**.
- Mukherjee, B.; Maiti, P. K.; Dasgupta, C.; Sood, A. K. Single-file diffusion of water inside narrow carbon nanorings. *ACS Nano*, 4(2):985–991, **2010**.
- Müller, A. M.; Avlasevich, Y. S.; Müllen, K.; Bardeen, C. J. Evidence for exciton fission and fusion in a covalently linked tetracene dimer. *Chem. Phys. Lett.*, 421(4–6):518–522, **2006**.
- Müller, A. M.; Avlasevich, Y. S.; Schoeller, W. W.; Müllen, K.; Bardeen, C. J. Exciton fission and fusion in bis(tetracene) molecules with different covalent linker structures. *J. Am. Chem. Soc.*, 129(46):14240–14250, **2007**.
- Müller-Plathe, F. A simple nonequilibrium molecular dynamics method for calculating the thermal conductivity. *J. Chem. Phys.*, 106(14):6082–6085, **1997**.
- Nabok, D.; Puschnig, P.; Ambrosch-Draxl, C.; Werzer, O.; Resel, R.; Smilgies, D.-M. Crystal and electronic structures of pentacene thin films from grazing-incidence x-ray diffraction and first-principles calculations. *Phys. Rev. B*, 76(23):235322, **2007**.

- Nair, R. R.; Wu, H. A.; Jayaram, P. N.; Grigorieva, I. V.; Geim, A. K. Unimpeded permeation of water through helium-leak-tight graphene-based membranes. *Science*, 335(6067):442–444, **2012**.
- Najafov, H.; Lee, B.; Zhou, Q.; Feldman, L. C.; Podzorov, V. Observation of long-range exciton diffusion in highly ordered organic semiconductors. *Nat. Mater.*, 9(11):938–943, **2010**.
- Newman, M. E. J. Power laws, Pareto distributions and Zipf's law. *Contemp. Phys.*, 46(5):323–351, **2005**.
- Noah-Vanhoucke, J.; Geissler, P. L. On the fluctuations that drive small ions toward, and away from, interfaces between polar liquids and their vapors. *Proc. Nat. Acad. Sci. U. S. A.*, 106(36):15125–15130, **2009**.
- Noguera, C. Polar oxide surfaces. *J. Phys.: Condens. Mat.*, 12(31):R367, **2000**.
- Nosé, S.; Yonezawa, F. Isobaric–isothermal molecular dynamics study on the glass transition of a Lennard–Jones system. *Solid State Commun.*, 56(12):1005–1008, **1985**.
- Nosé, S. A molecular dynamics method for simulations in the canonical ensemble. *Mol. Phys.*, 52(2):255–268, **1984**.
- Nosé, S. A unified formulation of the constant temperature molecular dynamics methods. *J. Chem. Phys.*, 81(1):511–519, **1984**.
- Nosé, S.; Yonezawa, F. Isothermal–isobaric computer simulations of melting and crystallization of a Lennard–Jones system. *J. Chem. Phys.*, 84(3):1803, **1986**.
- Onsager, L.; Machlup, S. Fluctuations and irreversible processes. *Phys. Rev.*, 91(6):1505–1512, **1953**.
- O'Regan, B.; Grätzel, M. A low-cost, high-efficiency solar cell based on dye-sensitized colloidal TiO<sub>2</sub> films. *Nature*, 353(6346):737–740, **1991**.
- Ostrowski, J. H. J.; Eaves, J. D. The tunable hydrophobic effect on electrically doped graphene. *J. Phys. Chem. B*, 118(2):530–536, **2014**.
- Paci, I.; Johnson, J. C.; Chen, X.; Rana, G.; Popović, D.; David, D. E.; Nozik, A. J.; Ratner, M. A.; Michl, J. Singlet fission for dye-sensitized solar cells: Can a suitable sensitizer be found? *J. Am. Chem. Soc.*, 128(51):16546–16553, **2006**.
- Panchakarla, L. S.; Subrahmanyam, K. S.; Saha, S. K.; Govindaraj, A.; Krishnamurthy, H. R.; Waghmare, U. V.; Rao, C. N. R. Synthesis, structure, and properties of boron- and nitrogen-doped graphene. *Adv. Mater.*, 21(46):4726–4730, **2009**.
- Parker, S. M.; Seideman, T.; Ratner, M. A.; Shiozaki, T. Model hamiltonian analysis of singlet fission from first principles. *J. Phys. Chem. C*, 118(24):12700–12705, **2014**.
- Patel, A. J.; Garde, S. Efficient method to characterize the context-dependent hydrophobicity of proteins. *J. Phys. Chem. B*, 118(6):1564–1573, **2014**.
- Petersen, C.; Tielrooij, K.-J.; Bakker, H. J. Strong temperature dependence of water reorientation in hydrophobic hydration shells. *J. Chem. Phys.*, 130(21):214511, **2009**.

- Piland, G. B.; Burdett, J. J.; Kurunthu, D.; Bardeen, C. J. Magnetic field effects on singlet fission and fluorescence decay dynamics in amorphous rubrene. *J. Phys. Chem. C*, 117(3):1224–1236, **2012**.
- Plimpton, S. Fast parallel algorithms for short-range molecular dynamics. *J. Comput. Phys.*, 117(1):1–19, **1995**.
- Poiseuille, J. L. *Comptes rendus hebdomadaires des séances de l'Académie des Sciences*, 11:961 and 1041, **1840**.
- Poiseuille, J. L. *Comptes rendus hebdomadaires des séances de l'Académie des Sciences*, 12:112, **1841**.
- Pomeau, Y.; Resibois, P. Time dependent correlation functions and mode-mode coupling theories. *Phys. Rep.*, 19(2):63–139, **1975**.
- Pratt, L. R.; Chandler, D. Theory of the hydrophobic effect. *J. Chem. Phys.*, 67(8):3683–3704, **1977**.
- Purcell, E. M. Life at low Reynolds number. *Am. J. Phys.*, 45(1):3–11, **1977**.
- Quarti, C.; Fazzi, D.; Del Zoppo, M. A computational investigation on singlet and triplet exciton couplings in acene molecular crystals. *Phys. Chem. Chem. Phys.*, 13(41):18615, **2011**.
- Rahman, A. Correlations in the motion of atoms in liquid argon. *Phys. Rev.*, 136(2A):A405–A411, **1964**.
- Raiteri, P.; Martoňák, R.; Parrinello, M. Exploring polymorphism: The case of benzene. *Angew. Chem. Int. Ed.*, 44(24):3769–3773, **2005**.
- Ramanan, C.; Smeigh, A. L.; Anthony, J. E.; Marks, T. J.; Wasielewski, M. R. Competition between singlet fission and charge separation in solution-processed blend films of 6,13-bis(triisopropylsilyl)ethynyl)pentacene with sterically-encumbered perylene-3,4:9,10-bis(dicarboximide)s. *J. Am. Chem. Soc.*, 134(1):386–397, **2011**.
- Raschke, T. M.; Levitt, M. Nonpolar solutes enhance water structure within hydration shells while reducing interactions between them. *Proc. Nat. Acad. Sci. U. S. A.*, 102(19):6777–6782, **2005**.
- Renaud, N.; Sherratt, P. A.; Ratner, M. A. Mapping the relation between stacking geometries and singlet fission yield in a class of organic crystals. *J. Phys. Chem. Lett.*, 4(7):1065–1069, **2013**.
- Rivnay, J.; Jimison, L. H.; Northrup, J. E.; Toney, M. F.; Noriega, R.; Lu, S.; Marks, T. J.; Facchetti, A.; Salleo, A. Large modulation of carrier transport by grain-boundary molecular packing and microstructure in organic thin films. *Nat. Mater.*, 8(12):952–958, **2009**.
- Roberts, S. T.; McAnally, R. E.; Mastron, J. N.; Webber, D. H.; Whited, M. T.; Brutchey, R. L.; Thompson, M. E.; Bradforth, S. E. Efficient singlet fission discovered in a disordered acene film. *J. Am. Chem. Soc.*, 134(14):6388–6400, **2012**.
- Roberts, S. T.; Schlenker, C. W.; Barlier, V.; McAnally, R. E.; Zhang, Y.; Mastron, J. N.; Thompson, M. E.; Bradforth, S. E. Observation of triplet exciton formation in a platinum-sensitized organic photovoltaic device. *J. Phys. Chem. Lett.*, 2(2):48–54, **2010**.

- Rowley, R. L.; Painter, M. M. Diffusion and viscosity equations of state for a Lennard-Jones fluid obtained from molecular dynamics simulations. *Int. J. Thermophys.*, 18(5):1109–1121, **1997**.
- Ryasnyanskiy, A.; Biaggio, I. Triplet exciton dynamics in rubrene single crystals. *Phys. Rev. B*, 84(19):193203, **2011**.
- Ryckaert, J.-P.; Ciccotti, G.; Berendsen, H. J. C. Numerical integration of the cartesian equations of motion of a system with constraints: Molecular dynamics of n-alkanes. *J. Comput. Phys.*, 23(3):327–341, **1977**.
- Ryerson, J. L.; Schrauben, J. N.; Ferguson, A. J.; Sahoo, S. C.; Naumov, P.; Havlas, Z.; Michl, J.; Nozik, A. J.; Johnson, J. C. Two thin film polymorphs of the singlet fission compound 1,3-diphenylisobenzofuran. *J. Phys. Chem. C*, 118(23):12121–12132, **2014**.
- Saffman, P. G.; Delbrück, M. Brownian motion in biological membranes. *Proc. Nat. Acad. Sci. U. S. A.*, 72(8):3111–3113, **1975**.
- Safran, S. A.; Pincus, P.; Andelman, D. Theory of spontaneous vesicle formation in surfactant mixtures. *Science*, 248(4953):354–356, **1990**.
- Sagle, A.; Freeman, B. Fundamentals of membranes for water treatment. In *The Future of Desalination in Texas*, volume 2, pages 137–154. Texas Water Developement Board, **2004**.
- Saloma, C.; Perez, G. J.; Tapang, G.; Lim, M.; Palmes-Saloma, C. Self-organized queuing and scale-free behavior in real escape panic. *Proc. Nat. Acad. Sci. U. S. A.*, 100(21):11947–11952, **2003**.
- Sanchez-Portal, D.; Artacho, E.; Soler, J. M. Projection of plane-wave calculations into atomic orbitals. *Solid State Commun.*, 95(10):685–690, **1995**.
- Schatschneider, B.; Monaco, S.; Tkatchenko, A.; Liang, J.-J. Understanding the structure and electronic properties of molecular crystals under pressure: Application of dispersion corrected DFT to oligoacenes. *J. Phys. Chem. A*, 117(34):8323–8331, **2013**.
- Schellenberger, F.; Encinas, N.; Vollmer, D.; Butt, H.-J. How water advances on superhydrophobic surfaces. *Phys. Rev. Lett.*, 116(9):096101, **2016**.
- Schmidt, M. W.; Baldridge, K. K.; Boatz, J. A.; Elbert, S. T.; Gordon, M. S.; Jensen, J. H.; Koseki, S.; Matsunaga, N.; Nguyen, K. A.; Su, S.; et al. General atomic and molecular electronic structure system. *J. Comput. Chem.*, 14(11):1347–1363, **1993**.
- Schrauben, J. N.; Zhao, Y.; Mercado, C.; Dron, P. I.; Ryerson, J. L.; Michl, J.; Zhu, K.; Johnson, J. C. Photocurrent enhanced by singlet fission in a dye-sensitized solar cell. *ACS Appl. Mater. Interfaces*, 7(4):2286–2293, **2015**.
- Schriger, J. Helium separation using porous graphene membranes. *J. Phys. Chem. Lett.*, 1(15):2284–2287, **2010**.
- Schwerin, A. F.; Johnson, J. C.; Smith, M. B.; Sreearunothai, P.; Popović, D.; Černý, J.; Havlas, Z.; Paci, I.; Akdag, A.; MacLeod, M. K.; et al. Toward designed singlet fission: Electronic states and photophysics of 1,3-diphenylisobenzofuran. *J. Phys. Chem. A*, 114(3):1457–1473, **2009**.

- Schwob, H. P.; Williams, D. F. Charge transfer exciton fission in anthracene crystals. *J. Chem. Phys.*, 58(4):1542–1547, **1973**.
- Shenogina, N.; Godawat, R.; Kebinski, P.; Garde, S. How wetting and adhesion affect thermal conductance of a range of hydrophobic to hydrophilic aqueous interfaces. *Phys. Rev. Lett.*, 102(15):156101, **2009**.
- Shockley, W.; Queisser, H. J. Detailed balance limit of efficiency of  $p - n$  junction solar cells. *J. Appl. Phys.*, 32(3):510–519, **1961**.
- Sigal, G. B.; Mrksich, M.; Whitesides, G. M. Effect of surface wettability on the adsorption of proteins and detergents. *J. Am. Chem. Soc.*, 120(14):3464–3473, **1998**.
- Singh, S.; Jones, W. J.; Siebrand, W.; Stoicheff, B. P.; Schneider, W. G. Laser generation of excitons and fluorescence in anthracene crystals. *J. Chem. Phys.*, 42(1):330–342, **1965**.
- Sinha, S.; Rossi, M. P.; Mattia, D.; Gogotsi, Y.; Bau, H. H. Induction and measurement of minute flow rates through nanopipes. *Phys. Fluids*, 19(1):013603, **2007**.
- Skouidas, A. I. Molecular dynamics simulations of gas diffusion in metal-organic frameworks: Argon in CuBTC. *J. Am. Chem. Soc.*, 126(5):1356–1357, **2004**.
- Smirnov, S.; Vlassiouk, I.; Takmakov, P.; Rios, F. Water confinement in hydrophobic nanopores. Pressure-induced wetting and drying. *ACS Nano*, 4(9):5069–5075, **2010**.
- Smith, J. D.; Cappa, C. D.; Wilson, K. R.; Messer, B. M.; Cohen, R. C.; Saykally, R. J. Energetics of hydrogen bond network rearrangements in liquid water. *Science*, 306(5697):851–853, **2004**.
- Smith, M. B.; Michl, J. Singlet fission. *Chem. Rev.*, 110(11):6891–6936, **2010**.
- Smith, M. B.; Michl, J. Recent advances in singlet fission. *Ann. Rev. Phys. Chem.*, 64:361–386, **2013**.
- Sokhan, V. P.; Nicholson, D.; Quirke, N. Fluid flow in nanopores: Accurate boundary conditions for carbon nanotubes. *J. Chem. Phys.*, 117(18):8531–8539, **2002**.
- Spano, F. C. Emission from aggregates of oligo-phenylene vinylenes: A recipe for superradiant H-aggregates. *Chem. Phys. Lett.*, 331(1):7–13, **2000**.
- Spiegler, K. S.; Kedem, O. Thermodynamics of hyperfiltration (reverse osmosis): Criteria for efficient membranes. *Desalination*, 1(4):311–326, **1966**.
- Stillinger, F. H. Water revisited. *Science*, 209(4455):451–457, **1980**.
- Stillinger, F. H. Structure in aqueous solutions of nonpolar solutes from the standpoint of scaled-particle theory. *J. Solution Chem.*, 2(2–3):141–158, **1973**.
- Stone, J. *An Efficient Library for Parallel Ray Tracing and Animation*. Ph.D. thesis, Computer Science Department, University of Missouri-Rolla, **1998**.
- Stone, J.; Gullingsrud, J.; Grayson, P.; Schulten, K. A system for interactive molecular dynamics simulation. In Hughes, J. F.; Séquin, C. H., eds., *2001 ACM Symposium on Interactive 3D Graphics*, pages 191–194. ACM SIGGRAPH, New York, **2001**.

- Strong, S. E.; Eaves, J. D. Tetracene aggregation on polar and nonpolar surfaces: Implications for singlet fission. *J. Phys. Chem. Lett.*, 6(7):1209–1215, **2015**.
- Strong, S. E.; Eaves, J. D. Atomistic hydrodynamics and the dynamical hydrophobic effect in porous graphene. *J. Phys. Chem. Lett.*, 7(10):1907–1912, **2016**.
- Strong, S. E.; Eaves, J. D. The dynamics of water in porous two-dimensional crystals. *J. Phys. Chem. B*, 121(1):189–207, **2017**.
- Strong, S. E.; Eaves, J. D. Linear response theory for water transport through dry nanopores. **2017**. Submitted.
- Sugita, Y.; Okamoto, Y. Replica-exchange molecular dynamics method for protein folding. *Chem. Phys. Lett.*, 314(1–2):141–151, **1999**.
- Suk, M. E.; Aluru, N. R. Water transport through ultrathin graphene. *J. Phys. Chem. Lett.*, 1(10):1590–1594, **2010**.
- Surwade, S. P.; Smirnov, S. N.; Vlassiouk, I. V.; Unocic, R. R.; Veith, G. M.; Dai, S.; Mahurin, S. M. Water desalination using nanoporous single-layer graphene. *Nat. Nanotechnol.*, 10(5):459–464, **2015**.
- Sweeney, M. C.; Eaves, J. D. Carrier transport in heterojunction nanocrystals under strain. *J. Phys. Chem. Lett.*, 3(6):791–795, **2011**.
- Swope, W. C.; Andersen, H. C.; Berens, P. H.; Wilson, K. R. A computer simulation method for the calculation of equilibrium constants for the formation of physical clusters of molecules: Application to small water clusters. *J. Chem. Phys.*, 76(1):637–649, **1982**.
- Taherian, F.; Leroy, F.; van der Vegt, N. F. A. Interfacial tension does not drive asymmetric nanoscale electrowetting on graphene. *Langmuir*, 31(16):4686–4695, **2015**.
- Taherian, F.; Marcon, V.; van der Vegt, N. F. A.; Leroy, F. What is the contact angle of water on graphene? *Langmuir*, 29(5):1457–1465, **2013**.
- Takaba, H.; Onumata, Y.; Nakao, S.-I. Molecular simulation of pressure-driven fluid flow in nanoporous membranes. *J. Chem. Phys.*, 127(5):054703, **2007**.
- Tanford, C. The hydrophobic effect and the organization of living matter. *Science*, 200(4345):1012–1018, **1978**.
- Tang, J.; Ge, G.; Brus, L. E. Gas-liquid-solid phase transition model for two-dimensional nanocrystal self-assembly on graphite. *J. Phys. Chem. B*, 106(22):5653–5658, **2002**.
- Tasker, P. W. The stability of ionic crystal surfaces. *J. Phys. C*, 12(22):4977, **1979**.
- Teichen, P. E.; Eaves, J. D. A microscopic model of singlet fission. *J. Phys. Chem. B*, 116(37):11473–11481, **2012**.
- Thomas, J. A.; McGaughey, A. J. H. Reassessing fast water transport through carbon nanotubes. *Nano Lett.*, 8(9):2788–2793, **2008**.

- Thomas, M.; Corry, B. Thermostat choice significantly influences water flow rates in molecular dynamics studies of carbon nanotubes. *Microfluid. Nanofluid.*, 18(1):41–47, **2014**.
- Thompson, A. P.; Plimpton, S. J.; Mattson, W. General formulation of pressure and stress tensor for arbitrary many-body interaction potentials under periodic boundary conditions. *J. Chem. Phys.*, 131(15):154107, **2009**.
- Thompson, P. A.; Troian, S. M. A general boundary condition for liquid flow at solid surfaces. *Nature*, 389(6649):360–362, **1997**.
- To, K.; Lai, P.-Y.; Pak, H. K. Jamming of granular flow in a two-dimensional hopper. *Phys. Rev. Lett.*, 86(1):71–74, **2001**.
- Tocci, G.; Joly, L.; Michaelides, A. Friction of water on graphene and hexagonal boron nitride from ab initio methods: Very different slippage despite very similar interface structures. *Nano Lett.*, 14(12):6872–6877, **2014**.
- Todd, B. D.; Evans, D. J.; Daivis, P. J. Pressure tensor for inhomogeneous fluids. *Phys. Rev. E*, 52(2):1627–1638, **1995**.
- Troisi, A. Charge transport in high mobility molecular semiconductors: Classical models and new theories. *Chem. Soc. Rev.*, 40(5):2347–2358, **2011**.
- Troisi, A.; Orlandi, G. Band structure of the four pentacene polymorphs and effect on the hole mobility at low temperature. *J. Phys. Chem. B*, 109(5):1849–1856, **2005**.
- Tuckerman, M.; Berne, B. J.; Martyna, G. J. Reversible multiple time scale molecular dynamics. *J. Chem. Phys.*, 97(3):1990–2001, **1992**.
- Turgman-Cohen, S.; Araque, J. C.; Hoek, E. M. V.; Escobedo, F. A. Molecular dynamics of equilibrium and pressure-driven transport properties of water through LTA-type zeolites. *Langmuir*, 29(40):12389–12399, **2013**.
- Vaikuntanathan, S.; Geissler, P. L. Putting water on a lattice: The importance of long wavelength density fluctuations in theories of hydrophobic and interfacial phenomena. *Phys. Rev. Lett.*, 112(2):020603, **2014**.
- Vaikuntanathan, S.; Rotskoff, G.; Hudson, A.; Geissler, P. L. Necessity of capillary modes in a minimal model of nanoscale hydrophobic solvation. *Proc. Nat. Acad. Sci. U. S. A.*, 113(16):E2224–E2230, **2016**.
- Vajna, S.; Tóth, B.; Kertész, J. Modelling bursty time series. *New J. Phys.*, 15(10):103023, **2013**.
- Vallett, P. J.; Snyder, J. L.; Damrauer, N. H. Tunable electronic coupling and driving force in structurally well-defined tetracene dimers for molecular singlet fission: A computational exploration using density functional theory. *J. Phys. Chem. A*, 117(42):10824–10838, **2013**.
- van Kampen, N. G. *Stochastic Processes in Physics and Chemistry*. Elsevier, Amsterdam, 3<sup>rd</sup> edition, **1992**.
- Vega, C.; Sanz, E.; Abascal, J. L. F.; Noya, E. G. Determination of phase diagrams via computer simulation: Methodology and applications to water, electrolytes and proteins. *J. Phys.: Condens. Matter*, 20(15):153101, **2008**.

- Venuti, E.; Della Valle, R. G.; Brillante, A.; Masino, M.; Girlando, A. Probing pentacene polymorphs by lattice dynamics calculations. *J. Am. Chem. Soc.*, 124(10):2128–2129, **2002**.
- Vieira-Linhares, A. M.; Seaton, N. A. Non-equilibrium molecular dynamics simulation of gas separation in a microporous carbon membrane. *Chem. Eng. Sci.*, 58(18):4129–4136, **2003**.
- Vörösmarty, C. J.; McIntyre, P. B.; Gessner, M. O.; Dudgeon, D.; Prusevich, A.; Green, P.; Glidden, S.; Bunn, S. E.; Sullivan, C. A.; Liermann, C. R.; et al. Global threats to human water security and river biodiversity. *Nature*, 467(7315):555–561, **2010**.
- Walker, B. J.; Musser, A. J.; Beljonne, D.; Friend, R. H. Singlet exciton fission in solution. *Nat. Chem.*, 5(12):1019–1024, **2013**.
- Wallqvist, A.; Berne, B. J. Computer simulation of hydrophobic hydration forces on stacked plates at short range. *J. Phys. Chem.*, 99(9):2893–2899, **1995**.
- Wallqvist, A.; Gallicchio, E.; Levy, R. M. A model for studying drying at hydrophobic interfaces: Structural and thermodynamic properties. *J. Phys. Chem. B*, 105(28):6745–6753, **2001**.
- Walther, J. H.; Ritos, K.; Cruz-Chu, E. R.; Megaridis, C. M.; Koumoutsakos, P. Barriers to superfast water transport in carbon nanotube membranes. *Nano Lett.*, 13(5):1910–1914, **2013**.
- Wang, E. N.; Karnik, R. Water desalination: Graphene cleans up water. *Nat. Nanotechnol.*, 7(9):552–554, **2012**.
- Wang, L.; Olivier, Y.; Prezhdo, O. V.; Beljonne, D. Maximizing singlet fission by intermolecular packing. *J. Phys. Chem. Lett.*, 5(19):3345–3353, **2014**.
- Weeks, J. D.; Chandler, D.; Andersen, H. C. Role of repulsive forces in determining the equilibrium structure of simple liquids. *J. Chem. Phys.*, 54(12):5237–5247, **1971**.
- Wei, D.; Liu, Y.; Wang, Y.; Zhang, H.; Huang, L.; Yu, G. Synthesis of N-doped graphene by chemical vapor deposition and its electrical properties. *Nano Lett.*, 9(5):1752–1758, **2009**.
- Werder, T.; Walther, J. H.; Jaffe, R. L.; Halicioglu, T.; Koumoutsakos, P. On the water-carbon interaction for use in molecular dynamics simulations of graphite and carbon nanotubes. *J. Phys. Chem. B*, 107(6):1345–1352, **2003**.
- Whitby, M.; Cagnon, L.; Thanou, M.; Quirke, N. Enhanced fluid flow through nanoscale carbon pipes. *Nano Lett.*, 8(9):2632–2637, **2008**.
- Widom, B. Line tension and the shape of a sessile drop. *J. Phys. Chem.*, 99(9):2803–2806, **1995**.
- Willard, A. P.; Chandler, D. Coarse-grained modeling of the interface between water and heterogeneous surfaces. *Faraday Discuss.*, 141:209–220, **2009**.
- Willard, A. P.; Chandler, D. Instantaneous liquid interfaces. *J. Phys. Chem. B*, 114(5):1954–1958, **2010**.
- Willard, A. P.; Chandler, D. The molecular structure of the interface between water and a hydrophobic substrate is liquid-vapor like. *J. Chem. Phys.*, 141(18):18C519, **2014**.

- Willard, A. P.; Reed, S. K.; Madden, P. A.; Chandler, D. Water at an electrochemical interface—a simulation study. *Faraday Discuss.*, 141:423–441, **2009**.
- Wilson, M. W. B.; Rao, A.; Clark, J.; Kumar, R. S. S.; Brida, D.; Cerullo, G.; Friend, R. H. Ultrafast dynamics of exciton fission in polycrystalline pentacene. *J. Am. Chem. Soc.*, 133(31):11830–11833, **2011**.
- Witten, T. A.; Sander, L. M. Diffusion-limited aggregation, a kinetic critical phenomenon. *Phys. Rev. Lett.*, 47(19):1400–1403, **1981**.
- Witten, T. A.; Sander, L. M. Diffusion-limited aggregation. *Phys. Rev. B*, 27(9):5686–5697, **1983**.
- Würthner, F.; Kaiser, T. E.; Saha-Möller, C. R. J-aggregates: From serendipitous discovery to supramolecular engineering of functional dye materials. *Angew. Chem. Int. Ed.*, 50(15):3376–3410, **2011**.
- Xi, E.; Patel, A. J. The hydrophobic effect, and fluctuations: The long and the short of it. *Proc. Nat. Acad. Sci. U. S. A.*, 113(17):4549–4551, **2016**.
- Xu, L.; Sahimi, M.; Tsotsis, T. T. Nonequilibrium molecular dynamics simulations of transport and separation of gas mixtures in nanoporous materials. *Phys. Rev. E*, 62(5):6942–6948, **2000**.
- Xu, L.; Tsotsis, T. T.; Sahimi, M. Nonequilibrium molecular dynamics simulation of transport and separation of gases in carbon nanopores. I. Basic results. *J. Chem. Phys.*, 111(7):3252–3264, **1999**.
- Xue, M.; Qiu, H.; Guo, W. Exceptionally fast water desalination at complete salt rejection by pristine graphyne monolayers. *Nanotechnology*, 24(50):505720, **2013**.
- Yamagata, H.; Norton, J.; Hontz, E.; Olivier, Y.; Beljonne, D.; Brédas, J. L.; Silbey, R. J.; Spano, F. C. The nature of singlet excitons in oligoacene molecular crystals. *J. Chem. Phys.*, 134(20):204703–204703–11, **2011**.
- Yeh, I.-C.; Berkowitz, M. L. Ewald summation for systems with slab geometry. *J. Chem. Phys.*, 111(7):3155–3162, **1999**.
- Ying-Hua, Q.; Kun, L.; Wei-Yu, C.; Wei, S.; Qi-Yan, T.; Yun-Fei, C. Ion and water transport in charge-modified graphene nanopores. *Chinese Phys. B*, 24(10):108201, **2015**.
- Yokoi, B. K.; Nishikawa, T. Revised intermolecular potential with parameters depending on partial atomic charges for aromatic molecular systems. *Mol. Phys.*, 90(5):705–712, **1997**.
- Yokoi, K. Empirical atom-atom potential for a naphthalene crystal and transferability to other polyacene crystals. *Mol. Phys.*, 85(3):449–462, **1995**.
- Yoneya, M.; Kawasaki, M.; Ando, M. Are pentacene monolayer and thin-film polymorphs really substrate-induced? A molecular dynamics simulation study. *J. Phys. Chem. C*, 116(1):791–795, **2012**.
- York, D. Least-squares fitting of a straight line. *Can. J. Phys.*, 44(5):1079–1086, **1966**.
- York, D.; Evensen, N. M.; Martínez, M. L.; Delgado, J. D. B. Unified equations for the slope, intercept, and standard errors of the best straight line. *Am. J. Phys.*, 72(3):367–375, **2004**.

- Yoshida, H.; Sato, N. Crystallographic and electronic structures of three different polymorphs of pentacene. *Phys. Rev. B*, 77(23):235205, **2008**.
- Yost, S. R.; Lee, J.; Wilson, M. W. B.; Wu, T.; McMahon, D. P.; Parkhurst, R. R.; Thompson, N. J.; Congreve, D. N.; Rao, A.; Johnson, K.; et al. A transferable model for singlet-fission kinetics. *Nat. Chem.*, 6(6):492–497, **2014**.
- Young, T. An essay on the cohesion of fluids. *Phil. Trans. R. Soc. Lond.*, 95:65–87, **1805**.
- Zhang, M.; Nguyen, Q. T.; Ping, Z. Hydrophilic modification of poly (vinylidene fluoride) microporous membrane. *J. Membrane Sci.*, 327(1–2):78–86, **2009**.
- Zhang, X.; Zhu, Y.; Granick, S. Hydrophobicity at a Janus interface. *Science*, 295(5555):663–666, **2002**.
- Zhao, L.; He, R.; Rim, K. T.; Schiros, T.; Kim, K. S.; Zhou, H.; Gutiérrez, C.; Chockalingam, S. P.; Arguello, C. J.; Pálová, L.; et al. Visualizing individual nitrogen dopants in monolayer graphene. *Science*, 333(6045):999–1003, **2011**.
- Zhou, R.; Huang, X.; Margulis, C. J.; Berne, B. J. Hydrophobic collapse in multidomain protein folding. *Science*, 305(5690):1605–1609, **2004**.
- Zhu, A.; Christofides, P. D.; Cohen, Y. Effect of thermodynamic restriction on energy cost optimization of RO membrane water desalination. *Ind. Eng. Chem. Res.*, 48(13):6010–6021, **2009**.
- Zhu, A.; Christofides, P. D.; Cohen, Y. On RO membrane and energy costs and associated incentives for future enhancements of membrane permeability. *J. Membrane Sci.*, 344(1–2):1–5, **2009**.
- Zhu, A.; Christofides, P. D.; Cohen, Y. Effect of stream mixing on RO energy cost minimization. *Desalination*, 261(3):232–239, **2010**.
- Zhu, F.; Tajkhorshid, E.; Schulten, K. Pressure-induced water transport in membrane channels studied by molecular dynamics. *Biophys. J.*, 83(1):154–160, **2002**.
- Zhu, F.; Tajkhorshid, E.; Schulten, K. Collective diffusion model for water permeation through microscopic channels. *Phys. Rev. Lett.*, 93(22):224501, **2004**.
- Zhu, F.; Tajkhorshid, E.; Schulten, K. Theory and simulation of water permeation in aquaporin-1. *Biophys. J.*, 86(1):50–57, **2004**.
- Zimm, B. H. Dynamics of polymer molecules in dilute solution: Viscoelasticity, flow birefringence and dielectric loss. *J. Chem. Phys.*, 24(2):269–278, **1956**.
- Zimmerman, J. A.; Webb, E. B., III; Hoyt, J. J.; Jones, R. E.; Klein, P. A.; Bammann, D. J. Calculation of stress in atomistic simulation. *Model. Simul. Mater. Eng.*, 12(4):S319, **2004**.
- Zimmerman, P. M.; Bell, F.; Casanova, D.; Head-Gordon, M. Mechanism for singlet fission in pentacene and tetracene: From single exciton to two triplets. *J. Am. Chem. Soc.*, 133(49):19944–19952, **2011**.
- Zingg, S. P.; Sigman, M. E. Influence of an SiO<sub>2</sub>/cyclohexane interface on the photochemistry of anthracene. *Photochem. Photobiol.*, 57(3):453–459, **1993**.

Zuriguel, I.; Parisi, D. R.; Hidalgo, R. C.; Lozano, C.; Janda, A.; Gago, P. A.; Peralta, J. P.; Ferrer, L. M.; Pugnaloni, L. A.; Clément, E.; et al. Clogging transition of many-particle systems flowing through bottlenecks. *Sci. Rep.*, 4:7324, **2014**.

Zuriguel, I.; Pugnaloni, L. A.; Garcimartín, A.; Maza, D. Jamming during the discharge of grains from a silo described as a percolating transition. *Phys. Rev. E*, 68(3):030301, **2003**.

Zwanzig, R. Diffusion in a rough potential. *Proc. Nat. Acad. Sci. U. S. A.*, 85(7):2029–2030, **1988**.

Zwanzig, R. *Nonequilibrium Statistical Mechanics*. Oxford University Press, Oxford, **2001**.

## Appendix A

### Derivation of Gaussian Dynamics with an Isokinetic Thermostat

Here we derive eq. 2.14, and show that the flow, temperature, and geometry constraints separate completely. Consider the same system discussed in Section 2.3. We follow the prescription for Gauss's principal of least constraint found in Ref. 1. The Gaussian cost function is

$$C(\{\mathbf{r}, \dot{\mathbf{r}}, \ddot{\mathbf{r}}\}) = \frac{1}{2} \sum_{i=1}^N m_i \left( \ddot{\mathbf{r}}_i - \frac{\mathbf{F}_i}{m_i} \right)^2 + \lambda_T \dot{g}_T(\{\mathbf{r}, \dot{\mathbf{r}}, \ddot{\mathbf{r}}\}) + \boldsymbol{\lambda}_f \cdot \dot{\mathbf{g}}_f(\{\ddot{\mathbf{r}}\}) + \lambda_m \ddot{g}_m(\{\mathbf{r}, \dot{\mathbf{r}}, \ddot{\mathbf{r}}\}), \quad (\text{A.1})$$

which is identical to eq. 2.5 with an added constraint on molecular geometries,  $g_m$ . We do not treat the geometry constraint explicitly here because it is well known, and its use in conjunction with a temperature constraint is also well known.<sup>2–5</sup> Here, we need only show that the flow constraint  $\dot{\mathbf{g}}_f$  separates completely from the geometry constraint  $g_m$ . Since  $\dot{\mathbf{g}}_f$  applies a uniform acceleration to all particles (eq. 2.14), it cannot distort any bonds or angles, and therefore cannot impact the implementation of  $g_m$ . So, from here on out, we only consider  $\mathbf{g}_f$  and  $g_T$ .

The temperature and flow constraints are given in eqs. 2.4 and 2.1. They are repeated here for clarity.

$$\mathbf{g}_f(\{\dot{\mathbf{r}}\}) = \frac{1}{M} \sum_{i=1}^N m_i \dot{\mathbf{r}}_i - \mathbf{u}_{\text{COM}} = 0 \quad (\text{A.2})$$

$$g_T(\{\mathbf{r}, \dot{\mathbf{r}}\}) = \sum_{i=1}^N \frac{1}{2} m_i (\dot{\mathbf{r}}_i - \mathbf{u}(\mathbf{r}_i))^2 - \frac{d(N - N_u) k_B T}{2} = 0, \quad (\text{A.3})$$

These are both nonholonomic constraints, since they depend on the velocities, so to find the form that depends on the accelerations we take one time derivative

$$\dot{g}_T = \sum_{i=1}^N m_i (\dot{\mathbf{r}}_i - \mathbf{u}(\mathbf{r}_i)) \cdot \ddot{\mathbf{r}}_i = 0 \quad (\text{A.4})$$

$$\dot{\mathbf{g}}_f = \sum_{i=1}^N m_i \ddot{\mathbf{r}}_i = 0, \quad (A.5)$$

where we have used the fact that at steady state, the streaming velocity is time independent. The Gaussian cost function (eq. A.1) now reads

$$C(\{\ddot{\mathbf{r}}\}) = \frac{1}{2} \sum_{i=1}^N m_i \left( \ddot{\mathbf{r}}_i - \frac{\mathbf{F}_i}{m_i} \right)^2 + \lambda_T \sum_{i=1}^N m_i (\dot{\mathbf{r}}_i - \mathbf{u}(\mathbf{r}_i)) \cdot \ddot{\mathbf{r}}_i + \boldsymbol{\lambda}_f \cdot \sum_{i=1}^N m_i \ddot{\mathbf{r}}_i. \quad (A.6)$$

We find the accelerations that minimize this cost function

$$\frac{\partial}{\partial \ddot{\mathbf{r}}_i} C(\{\ddot{\mathbf{r}}\}) = m_i \left( \ddot{\mathbf{r}}_i - \frac{\mathbf{F}_i}{m_i} \right) + \lambda_T m_i (\dot{\mathbf{r}}_i - \mathbf{u}(\mathbf{r}_i)) + \boldsymbol{\lambda}_f m_i = 0. \quad (A.7)$$

This gives the equation of motion

$$m_i \ddot{\mathbf{r}}_i = \mathbf{F}_i - \lambda_T m_i (\dot{\mathbf{r}}_i - \mathbf{u}(\mathbf{r}_i)) - \boldsymbol{\lambda}_f m_i. \quad (A.8)$$

To solve for the temperature multiplier,  $\lambda_T$ , we take the scalar product of eq. A.8 with  $(\dot{\mathbf{r}}_i - \mathbf{u}(\mathbf{r}_i))$ , and then sum over all particles

$$\sum_{i=1}^N m_i (\dot{\mathbf{r}}_i - \mathbf{u}(\mathbf{r}_i)) \cdot \ddot{\mathbf{r}}_i = \sum_{i=1}^N (\dot{\mathbf{r}}_i - \mathbf{u}(\mathbf{r}_i)) \cdot \mathbf{F}_i - \lambda_T \sum_{i=1}^N m_i (\dot{\mathbf{r}}_i - \mathbf{u}(\mathbf{r}_i))^2 - \boldsymbol{\lambda}_f \sum_{i=1}^N m_i (\dot{\mathbf{r}}_i - \mathbf{u}(\mathbf{r}_i)). \quad (A.9)$$

The term on the left hand side is zero, due to eq. A.4, and the  $\boldsymbol{\lambda}_f$  term on the right is zero due to eq. A.2. We can now solve for  $\lambda_T$

$$\lambda_T = \frac{\sum_{i=1}^N (\dot{\mathbf{r}}_i - \mathbf{u}(\mathbf{r}_i)) \cdot \mathbf{F}_i}{\sum_{i=1}^N m_i (\dot{\mathbf{r}}_i - \mathbf{u}(\mathbf{r}_i))^2}. \quad (A.10)$$

This is the well known result for the Gaussian isokinetic thermostat.<sup>1,6-8</sup> It is profile-unbiased, meaning that it is applied on the peculiar velocities of the system, with the local streaming velocity removed.<sup>9</sup>

We now solve for the flow multiplier,  $\boldsymbol{\lambda}_f$ , by summing eq. A.8 over all particles:

$$\sum_{i=1}^N m_i \ddot{\mathbf{r}}_i = \sum_{i=1}^N \mathbf{F}_i - \lambda_T \sum_{i=1}^N m_i (\dot{\mathbf{r}}_i - \mathbf{u}(\mathbf{r}_i)) - \boldsymbol{\lambda}_f \sum_{i=1}^N m_i. \quad (A.11)$$

The term on the left hand side is zero due to eq. A.5, and the  $\lambda_T$  term on the right hand side is zero due to eq. A.2. So, we can solve for  $\boldsymbol{\lambda}_f$

$$\boldsymbol{\lambda}_f = \frac{1}{M} \sum_{i=1}^N \mathbf{F}_i, \quad (A.12)$$

where we have defined  $M \equiv \sum_{i=1}^N m_i$  as the total mass of the system. The resulting equation of motion is

$$m_i \ddot{\mathbf{r}}_i = \mathbf{F}_i - m_i \mathbf{I} - m_i \xi (\dot{\mathbf{r}}_i - \mathbf{u}(\mathbf{r}_i)), \quad (\text{A.13})$$

where we have made the definitions

$$\mathbf{I} \equiv \boldsymbol{\lambda}_{\text{f}} = \frac{1}{M} \sum_{i=1}^N \mathbf{F}_i, \quad (\text{A.14})$$

$$\xi \equiv \lambda_{\text{T}} = \frac{\sum_{i=1}^N (\dot{\mathbf{r}}_i - \mathbf{u}(\mathbf{r}_i)) \cdot \mathbf{F}_i}{\sum_{i=1}^N m_i (\dot{\mathbf{r}}_i - \mathbf{u}(\mathbf{r}_i))^2}. \quad (\text{A.15})$$

Including the geometry constraints simply adds another term to the equation,  $\mathbf{f}_i$ ,<sup>1–3</sup>

$$m_i \ddot{\mathbf{r}}_i = \mathbf{F}_i - m_i \mathbf{I} - m_i \xi (\dot{\mathbf{r}}_i - \mathbf{u}(\mathbf{r}_i)) + \mathbf{f}_i, \quad (\text{A.16})$$

By solving for the temperature and flow Gaussian multipliers independently we have shown that these constraints separate completely. The geometry constraint separates because the uniform acceleration applied by the flow constraint cannot change any relative geometries.

## Bibliography

- [1] Evans, D. J.; Morriss, G. *Statistical Mechanics of Nonequilibrium Liquids*. Cambridge University Press, Cambridge, 2<sup>nd</sup> edition, **2008**.
- [2] Edberg, R.; Evans, D. J.; Morriss, G. P. Constrained molecular dynamics: Simulations of liquid alkanes with a new algorithm. *J. Chem. Phys.*, 84(12):6933–6939, **1986**.
- [3] Morriss, G. P.; Evans, D. J. A constraint algorithm for the computer simulation of complex molecular liquids. *Comput. Phys. Commun.*, 62(2–3):267–278, **1991**.
- [4] Nosé, S. A unified formulation of the constant temperature molecular dynamics methods. *J. Chem. Phys.*, 81(1):511–519, **1984**.
- [5] Hoover, W. G. Canonical dynamics: Equilibrium phase-space distributions. *Phys. Rev. A*, 31(3):1695–1697, **1985**.
- [6] Hoover, W. G.; Ladd, A. J. C.; Moran, B. High-strain-rate plastic flow studied via nonequilibrium molecular dynamics. *Phys. Rev. Lett.*, 48(26):1818–1820, **1982**.
- [7] Evans, D. J. Computer “experiment” for nonlinear thermodynamics of Couette flow. *J. Chem. Phys.*, 78(6):3297–3302, **1983**.

- [8] Evans, D. J.; Hoover, W. G.; Failor, B. H.; Moran, B.; Ladd, A. J. C. Nonequilibrium molecular dynamics via Gauss's principle of least constraint. *Phys. Rev. A*, 28(2):1016–1021, **1983**.
- [9] Evans, D. J.; Morriss, G. P. Shear thickening and turbulence in simple fluids. *Phys. Rev. Lett.*, 56(20):2172–2175, **1986**.

## Appendix B

### Funding and Computer Resources

This thesis utilized the Janus supercomputer, which is supported by the National Science Foundation (Grant No. CNS-0821794) and the University of Colorado Boulder. The Janus supercomputer is a joint effort of the University of Colorado Boulder, the University of Colorado Denver and the National Center for Atmospheric Research. This thesis is based upon work supported by the National Science Foundation under Grant No. 1455365 and a Graduate Research Fellowship under Grant No. DGE-1144083. All simulations were done with the LAMMPS package,<sup>1</sup> and all simulation snapshots were generated with the VMD and Tachyon packages.<sup>2,3</sup>

### Bibliography

- [1] Plimpton, S. Fast parallel algorithms for short-range molecular dynamics. *J. Comput. Phys.*, 117(1):1–19, **1995**.
- [2] Humphrey, W.; Dalke, A.; Schulten, K. VMD – visual molecular dynamics. *J. Mol. Graphics*, 14:33–38, **1996**.
- [3] Stone, J. *An Efficient Library for Parallel Ray Tracing and Animation*. Ph.D. thesis, Computer Science Department, University of Missouri-Rolla, **1998**.

## Appendix C

### Hagen-Poiseuille Law

The Hagen-Poiseuille (HP) law assumes the following:<sup>1-4</sup>

- (1) The fluid is incompressible.
- (2) The flow is at low Re.
- (3) The flow is at steady state.
- (4) The fluid is Newtonian.
- (5) The fluid acts as a continuum.
- (6) There is no-slip at the walls.
- (7) The channel is long enough that the flow profile is well developed.

In the systems discussed in Chapter 2.8, some of these are good assumptions

- (1) The fluid is relatively incompressible; the density only changes by a few percent in our simulations (Section 2.6).
- (2) We are at low enough Re that the flow is not turbulent ( $\text{Re} \lesssim 10$ ).
- (3) We ensure steady-state as discussed in Section 2.4.2.

But some are bad assumptions:

- (4) Lennard-Jones fluids are Newtonian at low shear rates, but non-Newtonian at high shear rates.<sup>5-7</sup>
- (5) An atomic system is not a continuum.

- (6) Exact no-slip boundary conditions are impossible in an atomic simulation, though simulations with flexible walls can approach no-slip (Figure 2.9b).
- (7) The channels are at most  $100 \sigma$  long, very short relative to the engineering applications for which the HP law was intended.

Clearly, we should not expect the HP law to hold in this application. If it were quantitative, all the data in Figure 2.7d would lie on the same point. It does, however, provide a means by which to compare the relationship of the flux to the pressure drop for a variety of channel geometries. Note that in Figure 2.7d, the effective viscosity appears to be converging to some value as  $\text{Re}$  increases. This is probably because  $\text{Re}$  is proportional to  $L$ , and as  $L$  increases, the HP law becomes more accurate. This is not meaningful, since we are not interested in quantitative accuracy of the HP law.

### C.1 Derivation of Hagen-Poiseuille Law in 2d

We now derive the HP law in 2d for the channel geometry shown in Figure 2.7a. The continuity equation is

$$\frac{\partial \rho(\mathbf{r}, t)}{\partial t} + \nabla \cdot \mathbf{J}(\mathbf{r}, t) = 0. \quad (\text{C.1})$$

Both the assumptions of steady state and incompressibility give

$$\frac{\partial \rho(\mathbf{r}, t)}{\partial t} = 0. \quad (\text{C.2})$$

Equations C.1 and C.2 combine to give

$$\frac{\partial u_x}{\partial x} + \frac{\partial u_y}{\partial y} = 0, \quad (\text{C.3})$$

where  $u_x$  and  $u_y$  are the components of the velocity field. We know that  $u_y = 0$ , so  $\partial u_y / \partial y = 0$ , and therefore  $\partial u_x / \partial x = 0$  as well. The Navier-Stokes equation for an incompressible fluid at low Reynolds number is<sup>4</sup>

$$\rho \frac{\partial \mathbf{u}}{\partial t} = -\nabla P + \rho \mathbf{g} + \eta \nabla^2 \mathbf{u}. \quad (\text{C.4})$$

From here on out, we ignore the gravity term. The flow is at steady state, so  $\partial \mathbf{u} / \partial t = 0$ . There is only a pressure drop along the direction of flow, so only the  $x$ -component of  $\nabla P$  is non-zero. The  $x$ -component of eq. C.4 is

$$\frac{\partial P}{\partial x} = \eta \left( \frac{\partial^2 u_x}{\partial x^2} + \frac{\partial^2 u_x}{\partial y^2} \right) \quad (\text{C.5})$$

$$= \eta \frac{\partial^2 u_x}{\partial y^2}, \quad (\text{C.6})$$

where we used the fact that  $\partial u_x / \partial x = 0$ . Since  $u_x$  is not a function of  $x$ , we can easily integrate both sides with respect to  $x$ :

$$P(x) = c_1 x + c_2. \quad (\text{C.7})$$

We now use the boundary conditions at the ends of the channel:  $P(0) = P_1$  and  $P(L) = P_2$ , with  $\Delta P \equiv P_1 - P_2$ ,

$$P(x) = P_1 - \frac{\Delta P}{L} x. \quad (\text{C.8})$$

Plugging this into eq. C.6 gives

$$-\frac{\Delta P}{\eta L} = \frac{\partial^2 u_x}{\partial y^2}. \quad (\text{C.9})$$

We integrate both sides of the equation with respect to  $y$  twice

$$u_x(y) = -\frac{\Delta P}{2\eta L} y^2 + k_1 y + k_2 \quad (\text{C.10})$$

and apply the no-slip boundary conditions  $u_x(-h/2) = u_x(h/2) = 0$  giving

$$u_x(y) = \frac{\Delta P}{2\eta L} \left[ \left( \frac{h}{2} \right)^2 - y^2 \right]. \quad (\text{C.11})$$

The mass flow rate  $Q$  is the product of the density and the velocity, integrated over the width of the pore. For an incompressible fluid, the density is constant in space, so the flow rate is given by

$$Q \equiv \rho \int_{-h/2}^{h/2} u_x(y) dy \quad (\text{C.12})$$

$$= \rho \int_{-h/2}^{h/2} \frac{\Delta P}{2\eta L} \left[ \left( \frac{h}{2} \right)^2 - y^2 \right] dy \quad (\text{C.13})$$

$$= \frac{\Delta P \rho h^3}{12\eta L}. \quad (\text{C.14})$$

We can now define the mass flux,  $J$ , as the flow rate through a cross-sectional area (length, in 2d),

$$J = \frac{Q}{h}. \quad (\text{C.15})$$

The result is

$$J = \frac{\Delta P \rho h^2}{12\eta L}. \quad (\text{C.16})$$

This is the Hagen-Poiseuille law in 2d. Expressed in terms of the flux  $J$ , it is identical to the Hagen-Poiseuille law in 3d.<sup>4</sup> Note that this is not the case if it is expressed in terms of the flow rate  $Q$ .

## Bibliography

- [1] Hagen, G. Ueber die bewegung des wassers in engen cylindrischen röhren. *Ann. Phys. (Leipzig)*, 122(3):423–442, **1839**.
- [2] Poiseuille, J. L. *Comptes rendus hebdomadaires des séances de l'Académie des Sciences*, 11:961 and 1041, **1840**.
- [3] Poiseuille, J. L. *Comptes rendus hebdomadaires des séances de l'Académie des Sciences*, 12:112, **1841**.
- [4] Bird, R. B.; Stewart, W. E.; Lightfoot, E. N. *Transport Phenomena*. John Wiley & Sons, Inc., New York, 2<sup>nd</sup> edition, **2006**.
- [5] Ashurst, W. T.; Hoover, W. G. Dense-fluid shear viscosity via nonequilibrium molecular dynamics. *Phys. Rev. A*, 11(2):658–678, **1975**.
- [6] Heyes, D. M. Shear thinning of the Lennard-Jones fluid by molecular dynamics. *Physica A*, 133(3):473–496, **1985**.
- [7] Heyes, D. M. Shear thinning and thickening of the Lennard-Jones liquid. A molecular dynamics study. *J. Chem. Soc. Faraday Trans. 2*, 82(9):1365, **1986**.